Phd Thesis

Analytical study of subwavelength imaging for terahertz radiation
(サブ波長構造を用いたテラヘルツ波イメージングに関する解析的研究)

Graduate School of Science,
Tohoku University
Department of Physics

Piyawath Tapsanit

2015

Analytical study of subwavelength imaging for terahertz radiation
(サブ波長構造を用いたテラヘルツ波イメージングに関する解析的研究)

Piyawath Tapsanit
Department of Physics, Graduate School of Science, Tohoku university

Abstract

The imaging resolution of the terahertz (THz) radiation is restricted approximately to the wavelength (λ) of the THz due to the diffraction limit. The subwavelength objects can be imaged by using the artificial structures called the hyperbolic metamaterials (HMMs). The cylindrical HMMs or the hyperlens can magnify the subwavelength objects into the far-field image, and also focus the far-field light into the subwavelength spot. Here, we develop the analytical solutions of the hyperlens made by alternating metal/dielectric layers with finite dielectric constants. The analytical solutions are consistent with the FDTD, but they are about three order faster than the FDTD. As the dielectric constant of the metals becomes infinitely large in the THz band, the new HMMs made by stacked grating/dielectric layers have been proposed. Thanks to the spoof surface plasmons of the grating, we can analytically demonstrate the subwavelength imaging of the array of slits with size 1 μm and the separation distance 5 μm at the THz frequency about 1 THz (λ=300 μm) over the long distance 33 mm. The effective parameters at this frequency show that the structures are type-II HMMs. Therefore, the stacked grating/dielectric layers can be used to make the hyperlens for the THz. The analytical solutions may also lead to the novel two-dimensional subwavelength imaging devices by replacing the grating with the hole array.

Keywords : terahertz, diffraction limit, subwavelength imaging, hyperbolic metamaterials, hyperlens, gratings, spoof surface plasmons

1. Introduction

The terahertz (THz, 1 THz=10^{12} 1/s) radiation locates in between the microwave and the infrared radiation. The emergence of THz sources and detectors leads to many applications of the THz in our daily life such as non-invasive food quality control, homeland security, and biomedical imaging. However, the THz needs to go beyond the diffraction limit if we want to use it to image the objects smaller than the wavelength (λ) of the THz. The diffraction limit results from the lost of the near-fields or evanescent waves which carry fine details of the objects without propagating to the far-field region. The diffraction limit can be overcome by the hyperbolic media (HMs) that allow the propagation of the evanescent waves via their hyperbolic equi-frequency contour (EFC). The HMs can be artificially made by alternating negative and positive dielectric constant layers. These structures are called the hyperbolic metamaterials (HMMs). The HMMs are type-I or type-II if the major axis of the hyperbolic EFC is parallel to the normal component of the wavevector, or the tangential component of the wavevector, respectively. The negative dielectric constant layers are usually the noble metals that can support the surface plasmons (SPs) on their surfaces. The cylindrical HMMs or the hyperlens can be made by bending the HMMs into the cylindrical shape. The subwavelength objects placed inside the core of the hyperlens are magnified into the far-field region by the conservation of the angular momentum of light if the hyperlens is properly designed. However, the finite difference time domain (FDTD) method as conventionally employed to optimize the hyperlens is time-consuming and inaccurate when the hyperlens becomes much more smaller than the λ of the THz.

In this study, the analytical solutions (AN) of the cylindrical HMMs made by alternating metal/dielectric layers with the finite dielectric constants have been developed [1]. As the dielectric constant of the metals becomes infinitely large in the THz band, we develop new HMMs for the THz by employing the spoof surface plasmons (SSPs) on the metallic grating surfaces. We analytically demonstrate the subwavelength imaging of the new HMMs and compare the results with the effective medium model. The THz cylindrical HMMs can be realized by bending these structures into the cylindrical shape. The analytical solutions also lead to the realizations of the ultra-sensitive subwavelength-film sensors, and the THz subwavelength focusing [2].

2. Results

2.1 Cylindrical HMM (Hyperlens)

The hyperlens is made by the *N* number of concentric cylindrical layers (CCLs) as schematically drawn in Fig. 1(a). The hyperlens can work in two processes : the magnifying process and the focusing process. In the magnifying process, the subwavelength objects which are placed inside the core of the hyperlens are modelled as the collection of point sources as indicated by the blue circles. In the focusing process, the subwavelength apertures which couple the incident light in the outer region to the large wavevector waves of the hyperlens are modelled as the collection of point sources as indicated

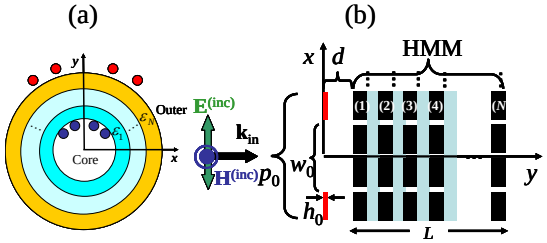

Fig. 1. (a) Schematic view of the cylindrical HMM (hyperlens). (b) . Schematic view of the new HMM for the THz with the testing object $h_0 = 1\ \mu$m and $p_0 = 5\ \mu$m .

by the red circles. The electromagnetic fields in both processes are obtained by solving the inhomogeneous Helmholtz's equation with the Green's function analysis. We check the AN with the FDTD by using the finite and negative dielectric constant of Ag in the UV band that is -3.11+0.123*i* at λ=368 nm. We use the Al_2O_3 with dielectric constant 3.2 so that the alternating Ag/Al_2O_3 CCLs form the type-I HMM according to the traditional effective medium approximation. The core and the outer regions are defined as air, the innermost radius is 100 nm, the thickness of each CCL is 10 nm, and the number of CCLs is 10. In the magnifying process, the two point sources are placed in the core, on the innermost curve, and at the azimuthal angles 57.05° and 122.95° so that the sources are separated by the angular distance $\lambda/3.2$. In the focusing process, the two point sources are put in the outer region, on the outermost curve, and at the azimuthal angles 45° and 135°. The intensity profiles obtained by the AN and the FDTD are compared in Fig. 2(a) for the magnifying process and Fig. 2(b) for the focusing process. We see that the FDTD profiles approach the AN profiles by increasing the FDTD resolutions from 2 pix/nm to 4 pix/nm. This means that

the AN are consistent with the FDTD with high resolution. The FDTD profiles with the resolutions 2 pix/nm and 4 pix/nm. take 4 hours and 2 days, respectively, to compute, while the AN profiles take only a few minute to obtain. This means that the AN are about three order faster than the FDTD simulation.

2.2 New HMMs for the THz

In the THz band, we employ the SSPs on the metallic grating surfaces to build the new HMMs by staking the grating/dielectric layers as schematically shown in Fig. 1(b). The subwavelength imaging using these structures can be analytically demonstrated by introducing another grating in front of the structures as indicated by the red grating. With the assumptions that the metals

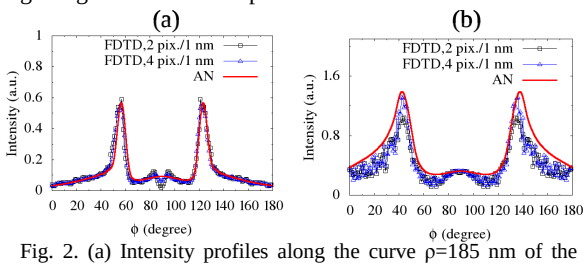

Fig. 2. (a) Intensity profiles along the curve ρ=185 nm of the magnifying process. (b) Intensity profiles along the curve ρ=100 nm of the focusing process.

are perfect electric conductors which is valid for the THz and lower frequency bands and the slit width is much more smaller than the λ, the AN of these structures can be derived by applying the coupled-mode analysis and the transfer matrix method. After checking the solutions with the FDTD using simple parameters, we then apply the AN to the deep-subwavelength HMM. Each grating comprising the HMM has the period 1 μm, the slit width 0.2 μm, and the slit height 150 μm. The SSPs at the edges of the first Brillouin zone of the grating are at the frequency about 0.997 THz. The electric field of these SSPs is localized on the grating surfaces with the decay length 144 nm. The distance between the object and the HMM is optimized as 100 nm to obtain large amplitude of the electric field behind the grating due to the excitation of the quasi-waveguide resonance (QWR) inside the air gap between the object and the first grating of the HMM at the frequency only 4 GHz lower than that of the SSPs. The number of gratings in the HMM is N=220, the gratings are separated by air with the optimized separation distance 80 nm so that L=33,017.52 μm, and then we obtain the amplitude of the electric field as shown in Fig. 3 (a)-(c) for w_0 =1-3 μm, respectively. We obtain the sharp images in all cases, and the differences in the field distributions indicate that these signals come from the objects.

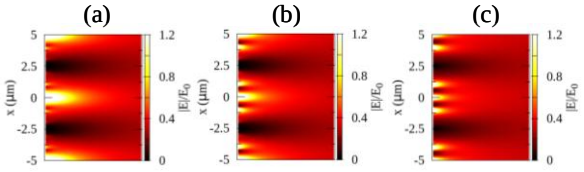

Fig. 3. The $|\mathbf{E}|/E_0$ at the frequency 0.997 THz behind the HMM over the distance 2 μm for (a) w_0 =1 μm, (b) w_0 =2 μm, and (c) w_0 =3 μm.

The full width at half maximums of the $|\mathbf{E}|/E_0$ at the distance 0.398 μm away from the interface of the HMM are 1.346 μm, 2.778 μm, and 3.260 μm for w_0=1-3 μm, respectively. The effective parameters of this structure are $\varepsilon_x^{(\text{eff})} = -8.95\times10^{-3}$, $\varepsilon_y^{(\text{eff})} = 1.94\times10^{3}$, and $\mu_z^{(\text{eff})} = 7.47\times10^{-5}$, which indicate that this structure is type-II HMM. The critical angle of the Poynting vector $\theta_c = \pm 0.1229^\circ$ with respect to the y-axis of this HMM indicates that the central image at x=0 does not really come from the object at x=0, but it comes from two objects located at $x = \pm 70\ \mu$m , and the same consideration explains the images at $x = \pm 5\ \mu$m . The effect of the oblique propagation of the optical energy can be more clearly seen in the N=10 and N=14 HMMs when the images are not perfectly focused. Fig. 4(a)-(c) show the $|\mathbf{E}|/E_0$ distributions over two unit cells along the x-axis and 2 μm behind the end interfaces of the N=10 HMM, N=14 HMM, and N=16 HMM, respectively, for the object with size one micron. The images are out of focus in the N=10 HMM and N=14 HMM, but they are sharply focused in the N=16 HMM. Consider the peak positions of the $|\mathbf{E}|/E_0$ profile along the end interface of the N=10 HMM. The peak positions of the i1 and i2 images in the positive unit cell (x>0) are located at x=1.988 μm and x=3.012 μm, respectively. The critical angle of the Poynting vector in this medium is $\theta_c = \pm 0.1152^\circ$ according to our effective medium model. Therefore, the images of the object at x=0 will be formed at the distance ±3.017 μm from the y-axis. This position is only 5 nm larger than the position of the i2 image in the positive unit cell, and the i1 image in the negative unit cell. Therefore, the i2 image in the positive unit cell and the i1 image in the negative unit cell come from the object at x=0. With the same consideration, the i1 image in the positive unit cell comes from the object at x=+5 μm, and the i2 image in the negative unit cell comes from the object at x=-5 μm. By increasing N, the images are formed in the larger distance from the y-axis because of the longer length of the HMMs, and perfect focusing is obtained at N=16. Therefore, the subwavelength imaging can be satisfyingly explained by the effective medium model.

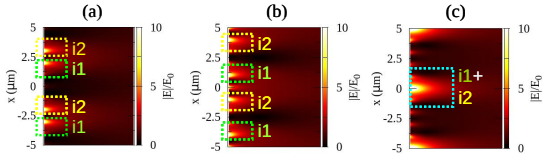

Fig. 4 (a) The $|\mathbf{E}|/E_0$ at the frequency 0.997 THz behind the HMMs over the distance 2 μm for (a) N=10, N=14, and (c) N=16. The parameters of the objects are $w_0 = 1\ \mu$m , $h_0 = 1\ \mu$m and $p_0 = 5\ \mu$m .

3. Conclusion

The new analytical solutions of the cylindrical HMMs made by alternating metal/dielectric layers with finite dielectric constants which are more efficient than the FDTD have been developed. As the dielectric constants of the metals are infinite in the THz band, the new HMMs made by stacked grating/dielectric layers have been proposed for the THz. The subwavelength imaging over the long distance 33 mm of one micron size object has been analytically demonstrated at the wavelength about 300 μm using the new HMM.

References

[1] P. Tapsanit, M. Yamashita, C. Otani, Opt. Express **22**, 229-238 (2014).

[2] P. Tapsanit, M. Yamashita, C. Otani, Engineering Journal **20**, 61-70 (2016).

Acknowledgement

I have been studying at Tohoku university already 5 years and half. I am indebted to the Development and Promotion of Science and Technology Talent Project (DPST) of the Kingdom of Thailand that kindly awarded me the scholarship to pursue the master and doctor of philosophy in Physics at the Tohoku university. Located on the Aobayama mountain, the department of Physics of Tohoku university is surrounded by trees and spirits. It is because of this that makes this place a good place for learning and growing up. I have the best luck to graduate from here, and I will bring my knowledge and my experience back to develop the science and technology in my country. I would like to express my gratitude to many people who contribute to this thesis, both directly and indirectly. Without their spirit and their kindness, the thesis cannot be finally completed.

I am deeply grateful to Prof. Chiko Otani who supports and advices me throughout the period of my study in the doctor course. His words are invaluable things for me and I really cannot forget what he taught. Working is hard, but he seems to turn it to be something interesting and challenge, and that keep pushing me forward. I thanks Mr. Masatsugu Yamashita or Yamashita-san who must be very patient with me since 3 years and half ago. I started learning about the concept of hyperlens with Yamashita-san knowing nothing about it. We tried many ways to make the hyperlens working for the terahertz, discussed many things, such as doped-semiconductors and rod arrays, which mostly didn't work. The failing works which are not shown up in this thesis are not the failures, but they serve me as the scientific steps that I have to learn how to surpass and to learn from them to achieve the best one. Yamashita-san is an experimentalist, and he does not familiar with the theory at all. What I learned from Yamashita-san is the practical thinking. He showed me to make new structures which can be realized in the experiments available at the present day. Moreover, the structures must be better than all previous structures which have been already demonstrated. That notion is now with me. Living in Japan is hard, especially for the person who didn't learn Japanese language seriously. Therefore, without the help of the secretariats, Sasada-san, Yamada-san, and the former secretariat Wakui-san, of the Otani lab. at RIKEN, I would not survive until today. I am very thankful to them. I also thanks my friends Suzuki-san, Yamada-san, Ikeda-san, and Ishida-san, who give me the advices concerning living in Japan. They always cheer me up in doing my research. The cheering may be a small thing, but it mentally helps when I stuck with the problems. I am grateful to Prof. Teruya Ishihara who taught me to make a concrete story for this thesis. Without his guidance, the thesis cannot be completed.

Lastly, I thanks my family who always keep asking me to finish this thesis as soon as possible and just go back home. Now, their dream come true. I am quite sure that they will never understand this thesis. They are just happy because they know that I have finally finished what I want to do. I wish that someday I will show them the real working hyperlens and tell them that this is what I started doing in Sendai. They would be more happy, I hope.

Table of Content

Chapter 1
Introduction

1.1 Preface

Scientists had applied lenses to see objects with light beyond the capability of human eyes. The famous story was the invention of refracting telescope by Galileo in 17th century which allowed him to observe stars and planets 30 times larger than seen by naked eyes [1]. The observation convinced him that earth was not the centre of the universe as believed at that time, but just normal planet circulating one star. Later in the same century, the lenses also allowed biologists to see microscopic world with light microscopes followed by the discovering of cell by Robert Hooke [2]. Although both telescopes and microscopes allowed the observations of tiny objects but the limitation of the smallest sizes in which these instruments could resolve remained unsolved in this century due to the lack of compelling theory of light. The interference phenomenon of light demonstrated in the early 19th century firmly confirmed the notion of light. Then, the classical wave theory was applied to analyze the propagation of light wave in lens and apertures located far from the source analytically, and the diffraction limit of the optical instruments was discovered by Ernst Karl Abbe in 1873, and similar equation by Lord Rayleigh in 1879 [3]. This law stated that the minimum distance between two objects in which light can resolve was limited approximately by the wavelength of light. The law remained valid, unbeaten, until the complete theory of light wave as the electromagnetic waves was formulated by James Clerk Maxwell. The equations are now known as the Maxwell's equations which give the correct description of classical light containing many photons. The Maxwell's equations had been applied to study light-matter interaction at nanoscale. We became understand that the diffraction limit was associated with the decay of near fields carrying fine information from the objects. With this understanding in mind, the diffraction limit was finally beaten in the previous century. Thanks to both the Maxwell's equation and advanced photonic technology. There are two main techniques to beat the diffraction limit : (i) localized surface plasmons (LSPs) in nanoparticles or scanning probes, and (ii) metamaterials. In this section, we describe how these two approaches beat the diffraction limit and explain why using the metamaterials is more promising than using the scanning probes. Finally, we discuss the problem that we interest in this thesis.

Metallic nanoparticles, apertures, edges and tips support the localized oscillations of electronic plasma which can be coupled to the external radiation to form quasi-particles called LSPs [4-8]. LSPs generated at the probe surface create large electric field enhancement corresponding to the near field with high spatial frequencies. The near field generated by LSPs on an nano-aperture surface is the earliest structure that can beat the diffraction limit [6]. In this technique, the aperture was prepared by coating metallic layer onto a fibre and an metallized aperture was created at the end of the fibre. Then, light was sent down a fibre which now became a waveguide, and the near field was created at the aperture surface. The aperture was brought close to a sample to allow the near field to interact with the sample, then it was raster-scanned over the sample to obtain the image in the far field. The resolution of this technique was restricted by the aperture diameter. However, the working wavelength directly proportional to the aperture diameter and therefore this aperture-type works only in short wavelength.

This technique was followed by aperture-less type which use the tip to create the stronger near field at the top apex by allowing it to scatter with the incident light [9-12]. These experiments rely on the optical interaction between large near field, which is at the tip apex, and the vibrational modes of targeted nano-molecules to enhance the signal. The tip can be regarded as an nano-antenna which converts propagating waves into evanescent waves and vice versa. The tip-type scanning near-field microscope has been brought from visible region to THz radiation bans (THz, 1 THz=10^{12} Hz) [13]. However, the tips as the probes are very fragile, non-reproducible, and invasive to the samples which severely prevent its practical use [14]. Therefore, new optical structures which can convert the near field into the far field to be detected by a detector are needed.

Wherever they come from, the near fields are already here, but they are too weak due to their evanescent nature. This is more strict argument than saying that they are completely lost. What we need to do is to amplify their signal with negative refraction material if we want to see them. This is the concept of the perfect lens proposed by J. B. Pendry and marked the true beginning of metamaterial (MMs) research [15]. The negative refraction was first demonstrated in microwave region by R. A. Shelby et al. [16]. In their demonstration, the MM comprised periodic array of split ring resonators designed to possess, simultaneously, negative effective permeability and metallic rods designed to possess effective dielectric at the resonant frequency, and therefore the effective negative index of this MM must be chosen as predicted by Veselago [17] resulting in the negative refraction. J. B. Pendry also predicted that the subwavelength metallic slab with only negative dielectric constant could also magnify the near field signal, and this prediction was confirmed in ultraviolet region by N. Fang et al. [18]. The lens with either dielectric constant or magnetic permeability is negative is called superlens [18]. By alternating metallic layers and dielectric layers, the effective dielectric constants become anisotropic medium whose components of effective dielectric constant tensor have different sign [19-23]. This metamaterial is called hyperbolic metamaterials (HMMs) following its hyperbolic equi-frequency contour. The HMMs support the propagation of large k-vectors (corresponding to near field) but it doesn't amplify the near field like superlens. Instead, the cylindrical HMMs can magnify small objects into larger objects by allowing the near field placed close to this device, inside the inner core, to propagate with magnification process into the outer region to be later detected by detector [19,20]. The cylindrical HMMs can function in both magnifying and focusing processes [24]. The planar HMMs show the potential in subwavelength focusing with flat surface in the optical regime [21]. The high ohmic loss in the planar HMMs in visible band can be overcome by working only on the structured metallic surface called the metasurfaces which also exhibit hyperbolic equi-frequency contour [25]. The hyperbolic material does exist in nature, but currently found only in hexagonal boron nitride (h-BN) in the mid-infrared band [26-28]. In the THz band, metals behave as perfect electrical conductor and graphene was proposed to substitute the metals, but this device has yet experimentally demonstrated [29]. The tapered fibre comprising indium rod array embedded in low loss Zeonex polymer has been experimentally demonstrated to work as focusing and magnifying THz hyperlens over the long distance [30]. Due to the negatively large effective dielectric constant along the fibre axis, all transverse components of wavevectors can propagate from one side to another side at the Faby-Perot resonance. Researchers can achieve the focal spot size about 143 μm at the frequency 75 GHz

(λ=4000 μm) in this experiment. The focal spot size is limited by the ratio between sizes of apertures on both sides of the tapered fibre and the resonant loss. This structure is promising in biomedical imaging as the THz radiation provides non-ionizing radiation in diagnostic. S. J. Oh et al have demonstrated using THz radiation to differentiate between brain tumour regions and normal regions in reflection-type THz imaging using water-sensitive property of THz [31]. However, the signal to noise ratio is poor and image processing technique is employed to obtain useful image. Furthermore, the imaging technique cannot study tumour tissues more deeper because of the diffraction limit. The resolution of a few microns should be more useful in biomedical imaging with THz radiation.

1.2 Purpose of the study

In this thesis, we develop the analytical solutions of hyperbolic metamaterials (HMMs) to efficiently optimize the subwavelength imaging beyond the diffraction limit using the THz radiation. First, the analytical solutions of the cylindrical HMMs made by alternating metal/dielectric layers with the finite dielectric constants working in both magnifying and focusing processes have been developed based on the Green's function analysis and the transfer matrix method. As the dielectric constant of the metals becomes infinitely large in the THz radiation band, we develop the new HMMs for the THz radiation. The new HMMs are the stacked grating/dielectric layers and the analytical solutions of these structures have been developed by applying the coupled-mode analysis and the transfer matrix method.

The analytical solutions are much more efficient than the finite difference time domain method (FDTD) simulation. The electromagnetic fields in the structures with sizes much more smaller than the wavelength of light can be rapidly obtained by using the analytical solutions, while it is impossible to obtain these solutions by using the FDTD simulation run on a single PC. Any finite dielectric constants of the dielectric layers, real or complex numbers, can be studied by the analytical solutions. The mathematical expressions given by the analytical solutions allow us to study the optical mechanism in the structures.

We show that the analytical solutions of the cylindrical HMMs are three order faster than the FDTD simulation. We can analytically demonstrate the THz subwavelength imaging by using the stacked gratings/dielectric layers over the long distance about 33 mm at the frequency about 1 THz (λ=300 μm). The analytical solutions allow us to study the effective optical properties of the stacked grating/dielectric layers. These effective optical properties show that the stacked grating/dielectric layers are HMMs, and therefore they can be used to build the cylindrical HMMs. The analytical solutions not only close the gap due to the large difference in the length-scale between the wavelength of THz light and the subwavelength imaging devices, but they also lead to the novel devices such as the subwavelength-film sensing devices.

1.3 Organization

We organize the thesis as follows. In the following section of this chapter, the backgrounds in which we will refer to frequently in later chapters will be given. In the chapter 2, we describe the Green's function analysis applied to the cylindrical hyperlens made by alternating metal/dielectric layers with finite dielectric constants. We will describe how to obtain the HMMs for the THz light using the combination between the metallic grating and the dielectric layers in the chapter 3. The coupled-mode analysis will be used in this chapter because it gives superb consistency with FDTD simulation in the case of only the bare grating whose analytical solutions are already known. By applying the coupled-mode analysis of the bare grating and the transfer matrix method, the analytical solutions of the dielectrics/grating/dielectrics are formulated in the chapter 3. The analytical solutions of these structures lead to the new HMMs for the THz light and the novel devices for the subwavelength-film sensing. We describe the novel devices for the subwavelength-film sensing in the chapter 3, and the new HMMs are described in the chapter 4 and 5. The chapter 4 explains the analytical solutions of the stacked grating/dielectric layers as the new HMMs for the THz light. The scheme of the analytical demonstration of the subwaveelngth imaging is also introduced in the chapter 4. The long-distance subwavelength imaging is analytically demonstrated in this chapter. Lastly, the chapter 5 explains the effective medium model of the stacked grating/dielectric layers. The optical properties such as the equi-frequency contour (EFC), the effective parameters, and the critical angles, of the stacked grating/dielectric layers are discussed in this chapter. The thesis is summarized after the chapter 5. The analytical solutions are translated into the FORTRAN programming language in order to extract the useful physical quantities such as the intensity and field distributions from them. The FORTRAN codes of each chapter are provided in the CD-ROM, and the details of the programs are described in the appendix.

1.4 Backgrounds

1.4.1 Terahertz radiation

The terahertz (THz) radiation lies in the technological gap between the microwave and the infrared light as shown in Fig. 1.1 which is shrinking fast thanks to the technological progress of powerful THz sources and highly sensitive detectors. It is roughly located at 1-10 THz [32], where 1 THz is 10^{12} Hz which is equivalent to the wavelength 300 μm, and to the energy 4.14 meV or 33.3 cm^{-1}.

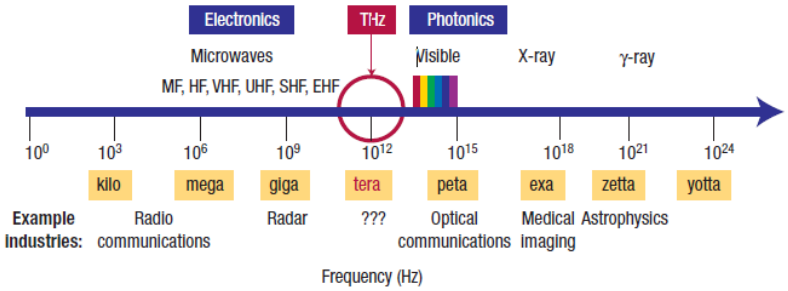

Fig. 1.1. Spectral location of THz in electromagnetic spectrum [32].

The THz band is called the gap because its sources and detectors are much less developed than its neighbours. The broadband THz radiation pulse is usually generated by transient photocurrents in photoconductive antenna which is excited by optical femtosecond laser pulse in terahertz time-domain spectroscopy (THz-TDS) [33]. The use of femtosecond laser makes the set up of THz-TDS bulky which requires table top experiment. The more compact source is THz quantum cascade laser (THz-QCL) [34]. THz-QCL yields THz continuous wave with high output power, but it works only at low temperature. Therefore, the THz-TDS is more commonly used than the THz-QCL in imaging and material characterization because the former can operates at room temperature. Researchers have been developing more compact THz source with low cost because of potential applications of THz radiation spanning from enhancing communication bandwidth [35], food quality control [36], biomedical imaging [31,37], homeland security [38-40], to fundamental science [41]. Especially, the THz light is attractive for non-invasive sensing and imaging of biomedical objects, e.g. tumors detection, due to its relatively low energy. Recently, S. J. Oh et al have demonstrated using THz light to differentiate between brain tumour regions and normal regions in reflection-type THz imaging [31]. The THz is sensitive to water content in the tissues. The tumour regions with lower water content reflect more THz light than normal regions, and therefore they can be distinguished from normal regions by observing reflectance scattered from the samples as shown in Fig. 1.2. However, the THz light is highly absorbed by water and this limits the penetration depth into the tissues. The long wavelength of THz light also makes low contrast and restricts details in the tissues that can be resolved with THz light. This thesis tackles the latter problem by studying new artificial structures that can beat this natural law which restricts the imaging resolution. In the next section, we will describe about the origin of this law which is known as the diffraction limit. Once we understand where this law comes from, we will give the concept of how to go beyond this limit.

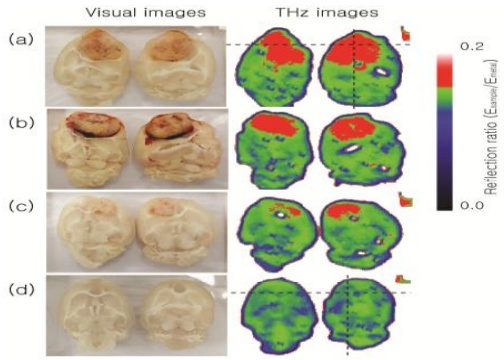

Fig. 1.2. Brain tumour regions differentiated by THz radiation in THz reflection-type imaging [31].

1.4.2 Diffraction limit

When lens is employed to collect light from an object, the image on the screen appears bigger. For simplicity, let's consider a single distant point source as an our object, e.g., a star, and an aperture of lens is circular with diameter *D*. The lens aperture will diffract the incident light coming from the point source and focus some part of the diffracted light onto the screen placed at the focal spot behind the lens. The focal length of the lens is much larger than the wavelength of light, and only the so called "far-fields" can reach the screen. By integrating all the far-fields diffracted from the lens aperture, the far-field intensity at distance r from the centre of the image plane is written as [42]

$$I(r) = I(0)\left[\frac{2J_1(kar/l_f)}{kar/l_f}\right], \tag{1.1}$$

where $I(0)$ is the intensity at the centre of the image plane, $J_1(x)$ is first-order Bessel function, $k = 2\pi/\lambda$, $a = D/2$, and l_f is focal length. The intensity is azimuthally symmetric with the brightest intensity at the centre. The intensity decreases as the radial distance increases from the centre. By looking top-down on two-dimensional plane, the intensity distribution about the centre forms a disk surrounded by several narrow dark and bright rings as shown in Fig. 1.3 (a). The central disk is known as Airy disk which was first proposed by G. B. Airy (1801-1892). The first dark ring has the radius determined by the first zero of $J_1(kar/l_f)$. This radius is equal to

$$r_1 = \frac{1.22 l_f \lambda}{D}. \tag{1.2}$$

If there are two point sources, two Airy disks associated with each point source are created on the screen. L. Rayleigh (1841-1919) described that if r_1 of one Airy disk overlaps with the centre of the other Airy disk, then two objects are said to be just resolved as shown in Fig. 1.3 (b) [3]. Therefore, the minimum distance $(\Delta l)_{\min}$ between two point sources that can be resolved is defined by the r_1 given by Eq. (2) : $(\Delta l)_{\min} = 1.22 l_f \lambda / D$. This condition is called **Rayleigh's criterion** and well known as the diffraction limit. Two objects separated by distance greater than $(\Delta l)_{\min}$ are clearly resolved, but they cannot be resolved if their separation distance is smaller than $(\Delta l)_{\min}$ as shown in Fig. 1.3 (c). Another formula of the diffraction limit is called **Abbe's criterion** derived by E. A. Abbe (1840-1905) when he

was finding the limitation of the optical microscope. The diffraction limit in the Abbe's criterion is expressed as [8]

$$(\Delta l)_{\min} = \frac{0.61\lambda}{NA}, \tag{1.3}$$

where $NA = n\sin\alpha$ is the numerical aperture of the objective lens, n is the background medium of the optical set up, and α is the acceptance angle. From both criterions, the resolution is better by reducing the focal length and increasing the size of aperture (increasing the numerical aperture). But this approach leads to bigger instrument. Another way is to reduce the wavelength of light. But the optical energy will also be higher which may ionize the sample. Is there another way to go beyond these criterions? We will later describe that there is actually the way to use long wavelength and achieving better resolution than that restricted by the diffraction limit. Before describing how to beat the diffraction limit, we will explain more why the resolution is limited by the wavelength of light.

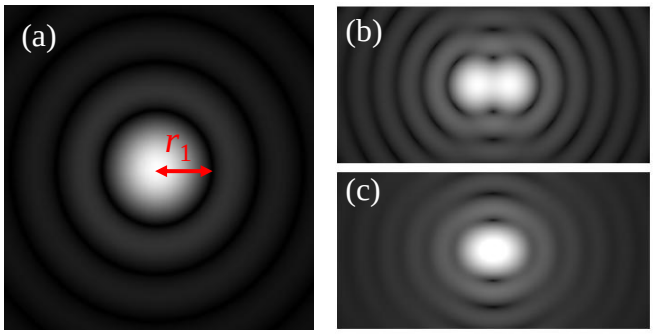

Fig. 1.3. (a) Airy disk of one point source, (b) Two Airy disks are just resolved at the Rayleigh's criterion, (c) Two Airy disks are not resolved below the Rayleigh's criterion.

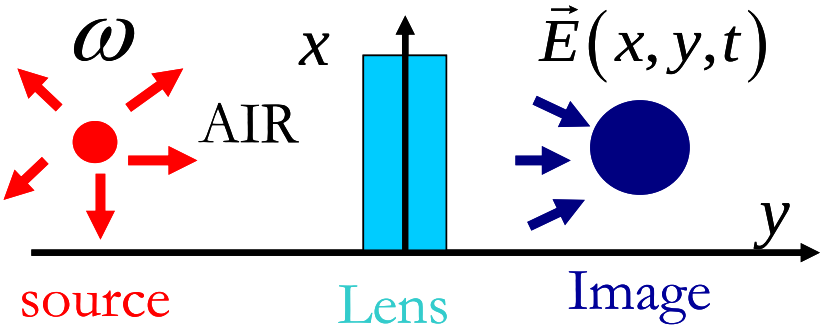

Fig. 1.4. A simple model used to describe the limitation of relation on wavelength

We consider a distant point source radiating continuous wave with angular frequency ω along the y-axis as schematically shown in Fig. 1.4. The electric fields from the point source are collected by an infinitely large lens which form an image on the screen. The electric field at the space-time position (y,x,t) can be written as the infinitely summation of many electromagnetic field modes, each mode is represented by wavevector $\mathbf{k} = (k_x, k_y)$ where k_x is tangential component, and k_y is normal component. This can be expressed in terms of an equation as

$$\vec{E}(x,y,t) = \sum_{k_x}\sum_{k_y} E(k_x,k_y)\exp\left[i\left(k_x x + k_y x - \omega t\right)\right], \tag{1.4}$$

where $E\left(k_x, k_y\right)$ is field amplitude corresponding to the electromagnetic mode $\mathbf{k} = \left(k_x, k_y\right)$. The tangential component k_x contains the resolution of the source, and the normal component k_y controls the propagation of the image. The k_x and k_y must satisfy the dispersion relation of the air medium in which the source and our optical set up are embedded, that is

$$k_x^2 + k_y^2 = \left(\omega / c\right)^2 \text{, or } k_y = \sqrt{\left(\omega / c\right)^2 - k_x^2} \,. \tag{1.5}$$

When $k_x < \omega / c$, k_y is real number. This mode can propagate from the source to the screen at which we can detect its signal. The electromagnetic waves satisfying this condition are called propagating waves or far-field. However, when $k_x > \omega / c$, k_y becomes imaginary. We cannot detect the signal of this electromagnetic mode on the screen because it rapidly decays from the source due to the exponentially decaying function. The electromagnetic waves satisfying to the latter condition are called evanescent waves or near-fields. Therefore, the cut-off k_x determines the resolution of the infinitely large aperture lens. The resolution is defined as

$$\left(\Delta l\right)_{\min} = \frac{2\pi}{\omega / c} = \lambda \,. \tag{1.6}$$

Eq. (1.6) shows that the resolution is limited by the wavelength of light even in the case of very large lens. The restriction evidently emerges from the lack of evanescent waves on the screen. This is the origin of the diffraction limit as derived by L. Rayleigh and E. A. Abbe. The evanescent waves are forced to decay because the air medium supports only the propagating waves with small wavevectors. In order to overcome the diffraction limit, we need to make new media which allow the propagation of large wavevectors. Another approach is to recover the evanescent waves by amplifying their signals. These approach rely on the qausi-particles found in metals. These quasi-paticles have large wavevectors so they can fulfil our requirement. The quasi-particles are surface plasmons.

1.4.3 Plasmons and surface plasmons

Free electrons in bulk metals collectively oscillate (all electrons are described by one unique position vector) relative to positive charges when they are driven by some external radiation. The collective oscillation has zero momentum, at which the dielectric constant is exactly zero, and it is parallel to the propagation direction of light [43]. This state of oscillation is known as **plasmon** which occurs at particular frequency called plasma frequency. The plasma frequency is found by deriving dielectric constant function of a metal excited by external light, and then the plasma frequency is obtained by forcing dielectric constant to become zero. The dielectric constant model of metals which is well consistent with experiment is the Drude model written as a function of angular frequency ω of incident light as [44]

$$\tilde{\varepsilon} = \varepsilon_\infty - \frac{\left(Ne^2 / \varepsilon_0 m\right)}{\omega^2 + i\omega / \tau} \,, \tag{1.7}$$

where ε_∞ is dielectric constant of the positive background, N is electron density, m is electron mass, and τ is electron relaxation time. The imaginary part of the dielectric constant arises due to the scattering of electrons which introduces damping force $-\langle p \rangle / \tau$ into the equation of motion. By neglecting this term and restrict $\tilde{\varepsilon} = 0$, then the angular plasma frequency becomes

$$\omega_p = \sqrt{\frac{Ne^2}{\varepsilon_0 \varepsilon_\infty m}} . \tag{1.8}$$

The plasma frequencies of all metals lie in ultraviolet region due to their large electron density. For example, the plasma frequencies of gold and silver are 9.03 eV and 9.01 eV, respectively [45]. The plasma frequency gives the border between the opacity and the transparency of the metal. If the frequency of incident light is lower than the plasma frequency of the metal, the light will decay inside the metal as it propagates through the metal because the dielectric constant of the metal is negative leading to complex refractive index. The decay length is characterized by the decay of light intensity by $1/e$ known as skin depth δ_d. The skin depth is explicitly written in terms of real part (ε') and imaginary part (ε'') of the dielectric constant as

$$\delta_d = \frac{\lambda}{4\pi} \sqrt{\frac{2}{-\varepsilon' + \sqrt{\varepsilon'^2 + \varepsilon''^2}}} . \tag{1.9}$$

For example, the skin depths of gold and silver at 1 THz are equal to 61 nm and 55 nm, respectively. If a metal slab has thickness larger than its skin depth and the incident light has lower energy than the plasma frequency of the metal, then the incident light will be all reflected. But the incident light can propagate to the other side of the metal if it has energy beyond the plasma frequency of the metal because the dielectric constant become positive. This is the reason why bulk silver mirrors reflect visible light (and lower energy light) and why radio signal is reflected from ionosphere. We plot real part and imaginary part of gold dielectric constant in THz band using parameters of Drude model from Ref. 45 in Fig. 1.5. The real part and imaginary part of the gold dielectric constant are in the forth order and sixth order, respectively, in THz band. The absolute values of both quantities keep rising in lower frequency band. The large dielectric constant results in the large conductivity. Therefore, gold including other noble metals are considered as perfect electrical conductor (PEC) in the THz and lower frequency band. The PEC approximation forces metals to have no losses, and it also eases the modelling of metals which we will see in chapter 3 for the case of metallic grating.

One may expect that there must be something special occurring at the front interface of a metal where it is hit by an incident light which later decays through the metal for frequency of the incident light lower than the plasma frequency of the metal. The study of an electromagnetic modes at this interface gives rise to new quasi-particles called **surface plasmons**.

The electromagnetic modes of surface plasmons are described by the dispersion relation which contains the information of allowed wavevectors parallel to interface between dielectric medium and metal at given frequency of the incident light. This dispersion relation can be obtained by considering reflection and transmission from the interface excited by transverse-magnetic (TM) polarized light in which the magnetic field is perpendicular to the propagation direction.

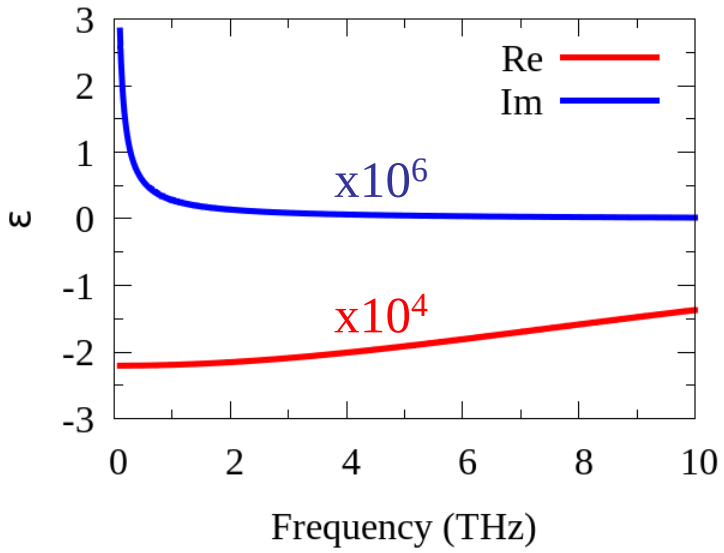

Fig. 1.5. Dielectric constant of gold in THz band obtained from the Drude model.

The magnetic field has only *z*-component and the electric fields are obtained by the magnetic field using Faraday's law in the Maxwell equations (to be described in section 1.4.7). After applying the continuities of H_z and E_x , the 0th-order reflection and transmission coefficients of TM-mode are written as

$$r_0 = \frac{\varepsilon_m k_y^{(d)} - \varepsilon_d k_y^{(m)}}{\varepsilon_m k_y^{(d)} + \varepsilon_d k_y^{(m)}}, \quad t_0 = \frac{2\varepsilon_m k_y^{(d)}}{\varepsilon_m k_y^{(d)} + \varepsilon_d k_y^{(m)}}, \tag{1.10}$$

where ε_d and ε_m are dielectric constants of dielectric medium and metals, respectively, and $k_y^{(j)} = \sqrt{\varepsilon_j (\omega/c)^2 - k_x^2}$ is normal component of wavevector in medium *j*. Notice that r_0 and t_0 have common denominator. By forcing this denominator to be zero and follow straightforward algebra, the well known dispersion relation of SPs is obtained

$$k_x = \sqrt{\frac{\varepsilon_d \varepsilon_m}{\varepsilon_d + \varepsilon_m}} \frac{\omega}{c}. \tag{1.11}$$

k_x satisfying Eq. (1.11) is regarded as SP wavenumber : k_{SP} . According the Eq. (1.11), the wavenumber of SP deviates from that of the light line as schematically shown in Fig. 1.6 (a). It can be seen that the SP has larger wavenumber comparing to the light in vacuum. This means that it is evanescent wave or near-field, localized only to the interface of the metal. An intuitive picture of SPs is shown in Fig. 1.6 (b) which illustrates the collective oscillation of electron cloud relative to positive background at the metallic surface. The SPs are coupled with non-radiating light and these states of couplings are known as surface plasmon polaritons (SPPs). Researchers tend to discard the term polaritons and use only surface plasmons with the coupling between light and collective oscillations of free electrons understood. In this thesis, we will also use only the term surface plasmons or SPs hereafter.

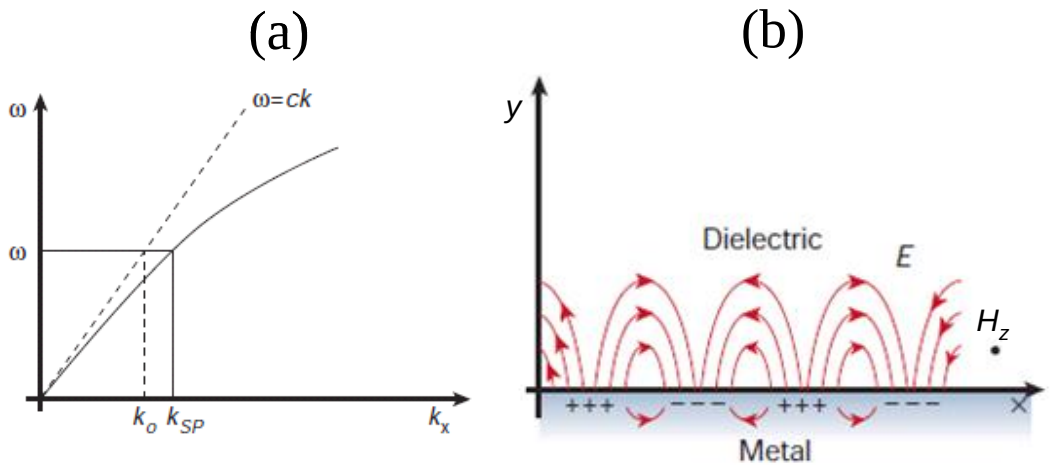

Fig. 1.6. (a) Schematically drawing of dispersion relation of SPs (solid line) comparing to the light line (dashed line). (b) An intuitive picture of SPs showing the collective oscillation of free electrons coupling with light [46].

Due to the large wavenumber of SPs, they cannot be directly excited by the external radiation. The near-field generated by the internal total reflection (ITR) effect on the prism surface is commonly used to excite the SPs in optical region as schematically drawn in Fig. 1.7 (a) [47]. Another scheme uses the near-field from the sharp edges to excite and to collect the SPs as schematically drawn in 1.7 (b) [48]. The diffraction grating can also be used to excite the SPs via Bloch-Floquet waves as schematically drawn in 1.7 (c) [47]. These methods have one thing in common that is they create large wavevector waves to excite the SPs which must already exist on the surface of the metal.

Once the SPs are excited on the interface of a metal slab, it seems impossible that the same SPs will appear on another interface of the metal. However, T. W. Ebbesen et al showed that the SPs could emerge on another side of the metal slab by making hole array on them [49]. The coupling of the SPs on two faces of the hole array results in large transmission called extraordinary optical transmission (EOT) effect at resonant wavelength larger than lattice constant as shown in Fig. 1.8 (b). The wavevectors of the SPs approximately satisfy the following phase matching condition

$$\mathbf{k}_{\mathrm{SP}} = \mathbf{k}_{\mathrm{in}} + \mathbf{k}_R, \tag{1.12}$$

where $\mathbf{k}_{\mathrm{SP}}$ is SP wavevector, $\mathbf{k}_{\mathrm{in}}$ is tangential component of the incident wavevector, and $\mathbf{k}_R$ is reciprocal lattice vector of the hole array which is $\mathbf{k}_R = \hat{x}n2\pi/a + \hat{y}m2\pi/a$ for square lattice where n and m are integer, and a is the lattice constant. The complete theory of the EOT effect is the coupled-mode theory [50] which gives us the clear picture of the coupled-SPs as shown in Fig. 1.8 (c). The EOT effect has sparked the interest in subwavelength sensing with THz radiation [51, 52].

New electromagnetic modes also appear in metallic nanoparticles such as spherical and cylindrical nanoparticles. These modes are known as localized surface plasmons (LSPs) which are heavily studied in visible regime due to its potential in ultrasensitive sensing and enhanced spectroscopy [53]. The calculation of dispersion relations and electromagnetic fields in these structures are complicated because of non-flat boundaries. The incident light must be expanded in terms of spherical waves and cylindrical waves for spherical and cylindrical nanoparticles, respectively, and the solutions in all regions are expressed in terms of these basis functions. For example, the Mie's theory

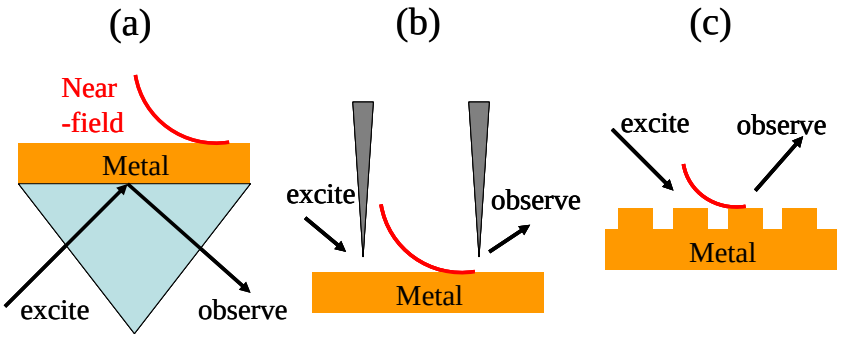

Fig. 1.7. Some schemes of exciting SPs (a) prism coupling (b) edge coupling, and (c) grating coupling.

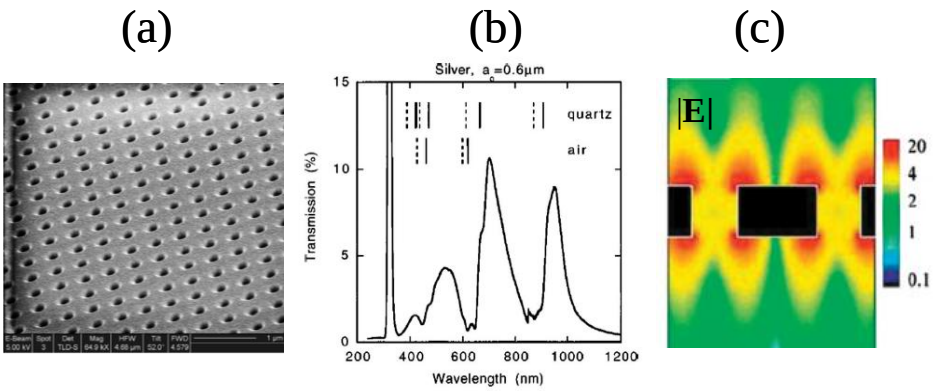

Fig. 1.8. Extraordinary optical transmission (EOT) effect in hole array. (a) Circular hole array milled in gold film with film thickness 260 nm, hole diameter 150 nm, and lattice constant 460 nm, from SEM. (b) Zero-order transmission spectra of circular hole array in silver film with film thickness 200 nm, hole diameter 150 nm, and lattice constant 600 nm, for TM-mode normal incident light. (c) Calculated |**E**| at the resonance peak with the substrate removed. The |**E**| is normalized by the amplitude of the incident light [49, 50].

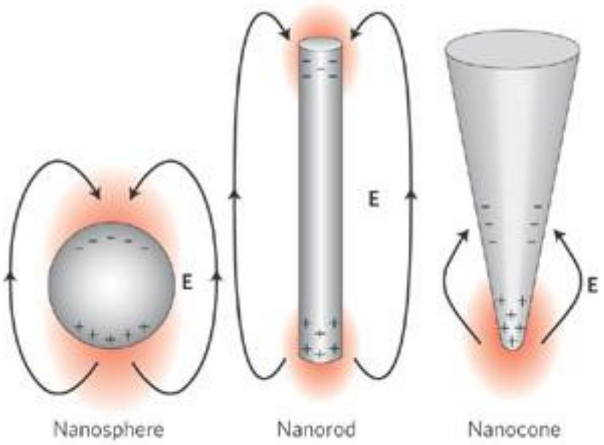

Fig. 1.9. Intuitive pictures of LSPs in nanosphere, nanorod, and nanocone [55].

gives the full solutions of the electromagnetic fields in the spherical nanoparticles which are expressed in terms of the spherical Hankel function of the first kind for the region outside the particle and the spherical Bessel function for the region inside the particle [4,54]. Fig. 1.9 shows intuitive pictures of LSPs in some widely studied nanoparticles [55].

We have seen from this section that new electromagnetic modes emerge if we look at the metallic surface, reduce size of the metal, or sculpt the metal into different shape. This concept is important for THz radiation band in which the incident light is almost completely reflected and the SPs is weakly bound to the metallic surface. In the next section, we will show that by structuring metallic surface with cavities, new electromagnetic modes resembling SPs appear. These electromagnetic modes are named spoof surface plasmons.

1.4.4 Spoof surface plasmons

We explain the spoof surface plasmons or SSPs by considering the metallic surface which is engraved by periodic grooves having the same depth (*h*) as schematically shown in Fig. 1.10 (a). The metal is modelled as perfect electrical conductor (PEC) which means that there is no loss inside the metal. We define groove width *d* to be much smaller than wavelength of the incident light so that only the fundamental waveguide mode inside each groove is taken into account. Then, the dispersion relation obtained by the coupled-mode analysis can be expressed as [50,56]

$$i\frac{d}{p}\sum_{m=-\infty}^{\infty}\frac{(\omega/c)}{\sqrt{(\omega/c)^2-\beta_m^2}}\operatorname{sinc}^2(\beta_m d/2)=\cot(k_0 h), \tag{1.13}$$

where *m* is an integer representing diffraction order, and $\beta_m = k_x + m2\pi/p$ is Bloch wavenumber. The left hand side term converges rapidly by increasing diffraction order due to the sinc function. If $p \ll \lambda$, the *m*=0 order is dominant term and gives good approximation, and then Eq. (1.13) can be reduced to more simpler form [57]

$$i\frac{\omega/c}{\sqrt{(\omega/c)^2-k_x^2}}=\cot(k_0 h). \tag{1.14}$$

Both Equations show signs of SSPs, but we will use Eq. (1.13) to accurately obtain their dispersion relations and field distributions. Frequencies giving zeros to the real part of the left hand side term in Eq. (1.13) for given k_x are plotted as a function of k_x for various groove depths in 1.10 (b). It can be seen that the dispersion relations resemble those of the SPs in optical regime. By increasing the groove depths, the dispersion lines of SSPs deviate from the light line in vacuum which is indicated by the dashed black line. This means that if the grooves become deeper, the larger wavenumbers they can support. These are quasi-particles known as SSPs. The frequencies approach the cavity mode $\omega_c = \pi c/2h$ by increasing wavenumbers as can be from Eq. (1.6) by taking $k_x = \infty$. The reflected |Re(H_z)| normalized by that of the incident magnetic field impinging on the groove interface for *h*=1.0*p* are shown in Fig. 1.11 (a)-(c). At the frequency 0.86552 THz, the SSP wavenumber is only 0.3 π/p which is close to the light line and therefore the field is delocalized above the perforated plane as shown in Fig 1.11 (a). As the frequency increase to 1.06777, the SSP wavenumber also increases to

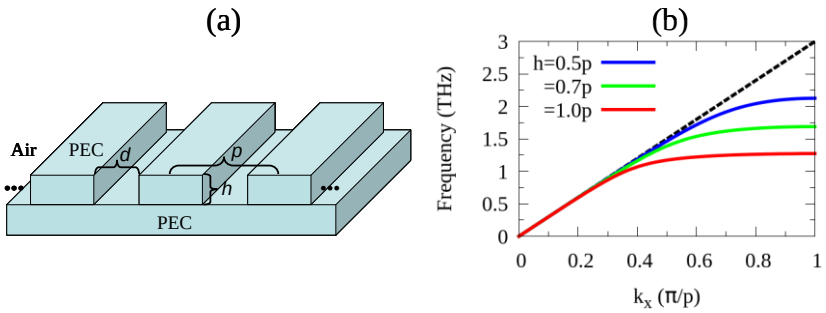

Fig. 1.10. (a) Schematic view of PEC plane perforated by periodic grooves with the same depth. The region above PEC plane and inside the grooves are defined as air. (b) SSPs dispersion relations of for various groove depths. The period is defined as p=50 μm, and the groove width d=0.2p. The black dashed line indicates the light line in air.

0.4 π/p which is about 1.12 times larger than wavenumber of light in vauum and thus the localization of magnetic field from the SSP is seen on the perforated surface as shown in Fig. 1.11 (b).

By increasing frequency more to 1.22092 THz, the SSP wavenumber increases to 0.6 π/p which is about 1.5 times larger than that of the light line and therefore the more strongly localization is seen in Fig. 1.11 (c). This means that we can design SSPs as we want by simply varying the geometry of the structure. The SSPs are not only supported by the perforated plane, but also perforated PEC cylindrical wires [58]. In this case, the wires are perforated by radial grooves which exhibit the same features of SSPs in perforated PEC. For example, the cut-off frequency in this structure is the same as that of the perforated PEC plane.

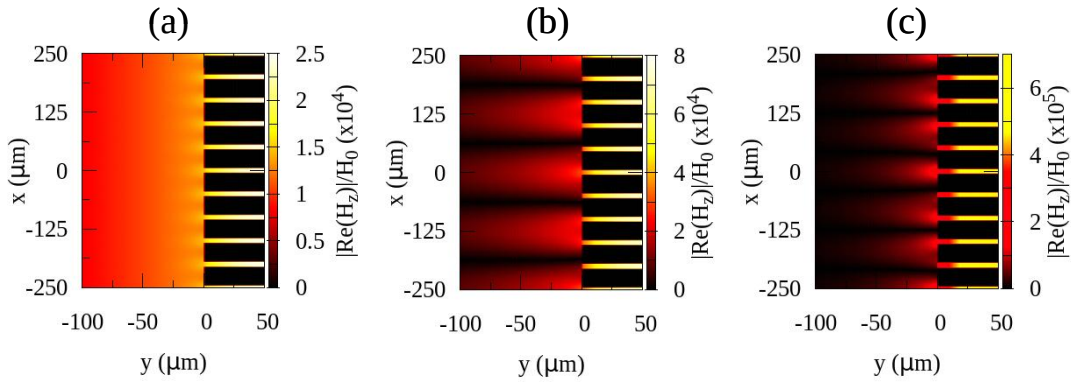

Fig. 1.11. The distribution of $|\mathrm{Re}(H_z)|$ normalized that of the incident light impinging on the groove interface for the groove depth h=1.0p in which p=50 μm at frequencies (a) f=0.86552 THz, k_x=0.3 π/p, (b) f=1.06777 THz, k_x=0.4 π/p, f=1.22092 THz, k_x=0.6 π/p.

A PEC slab which is cut through by periodic array of square holes support SSPs [59]. The effective parameters of this artificial structure are anisotropic which means that electric displacement **D** and magnetic induction **B** feel different electromagnetic forces in different directions. The effective parameters are grouped in 3x3 matrices. The matrices are uniaxial which means that they have non-zero elements only along the diagonal elements. These matrices are written as

$$\varepsilon_{\mathrm{eff}} = \begin{bmatrix} \varepsilon_x & 0 & 0 \\ 0 & \varepsilon_y & 0 \\ 0 & 0 & \varepsilon_z \end{bmatrix}, \quad \mu_{\mathrm{eff}} = \begin{bmatrix} \mu_x & 0 & 0 \\ 0 & \mu_y & 0 \\ 0 & 0 & \mu_z \end{bmatrix}, \tag{1.15}$$

where $\varepsilon_z = \mu_z = \infty$, and

$$\mu_x = \mu_y = \frac{8\mu_h}{\pi^2}\left(\frac{a}{d}\right)^2, \quad \varepsilon_x = \varepsilon_y = \frac{\pi^2\varepsilon_h}{8}\left(\frac{d}{a}\right)^2\left(1-\frac{\omega_p^2}{\omega^2}\right), \quad \omega_p = \frac{\pi c}{a\sqrt{\varepsilon_h\mu_h}}, \tag{1.16}$$

where *a* is size of the square hole, *d* is lattice constant, and ε_h, μ_h are dielectric constant and magnetic permeability of hole filling material. Notice that $\varepsilon_x, \varepsilon_y$ have exactly the same form as the Drude model with the spoof plasma frequency exactly the same as the frequency of the cavity mode. The $\varepsilon_x, \varepsilon_y$ are negatively large below the spoof plasma frequency due to the small filling ratio *a/d.*

The SSPs, like SPs in optical regime, are important in subwavelength sensing and imaging in THz band. In the next section, we will describe subwavelength imaging technique which applies SPs in a metal to make new lens that can support the propagation of evanescent waves with large wavevectors. The new lens is called hyperlens.

1.4.5 Hyperbolic medium and hyperlens

In some materials, energy of light can propagate in perpendicular direction to the propagation direction of light itself. This phenomenon does not occur in isotropic media such as air and glass, but it can occur in anisotropic medium whose equi-frequency contour (EFC) is hyperbolic. The EFC is the plot showing the relation between components of wavevectors at particular frequency. Air and glass are said to have circular EFC because they satisfy the dispersion relations having circular EFC. Hyperbolic medium is said to have hyperbolic EFC because it satisfies the dispersion relation having hyperbolic EFC. The hyperbolic medium dose exist in nature but only in the mid-infrared band. A thin hexagonal boron nitride (h-BN) has been experimentally demonstrated to exhibit low-loss hyperbolic dispersion in frequency range 760-825 cm^{-1} and 1,370-1,610 cm^{-1} due to the coupling of phonons with light [26-28]. At the time of writing this thesis, there is no other naturally occurring hyperbolic medium observed by experiments. Nevertheless, the hyperbolic medium can be artificially fabricated by simply altering negative dielectric constant layers and positive dielectric constant layers. We will explain this artificial hyperbolic material after describing the properties of hyperbolic medium.

Hyperbolic medium (HM) with hyperbolic EFC requires the opposite signs between dielectric constants parallel (ε_z) and transversal (ε_t) to the propagation direction of light. Therefore, it comes with two different types depending on the signs as shown in Fig. 1.12. (a)-(b) that show, respectively, type-I HM in which $\varepsilon_t > 0, \varepsilon_z < 0$, and type-II HM in which the sign is opposite and $\varepsilon_t < 0, \varepsilon_z > 0$. In the type-I HM, k_z is never be zero and therefore the light never reverse its propagation direction by reducing the transversal component of the wavevector as denoted by k_t. However, in the type-II HM, the light can reverse the propagation direction by reducing k_t because k_z is allowed to be zero with the small k_t. Therefore, the type-I HM is required for the magnifying process in which the k_t emitted by the source can decreases as the electromagnetic wave propagate out from the source. Both types can support large wavevectors, the properties that we have seen in surface plasmons. Therefore, the HM can be used to collect large wavevectors scattered from the sub-diffraction objects and send them to the

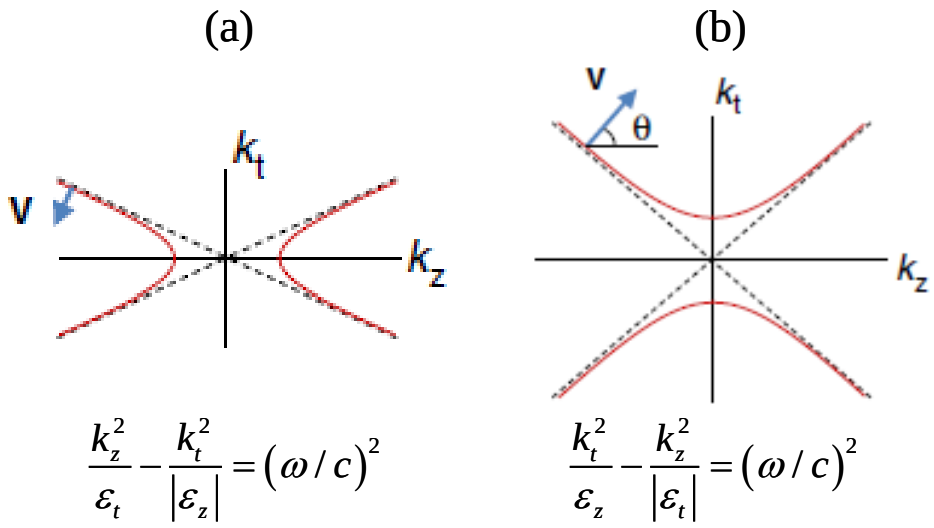

Fig. 1.12. Two types of hyperbolic medium (a) type-I, and (b) type-II [27].

opposite side, and therefore it can beat the diffraction limit as demonstrated in the mid-infrared radiation band [27]. The energy flow of light inside the HM is described by the group velocity $\mathbf{v}_g = \nabla_{\mathbf{k}}\omega$, which is the gradient of the angular frequency with respect to wavevectors. Therefore, the group velocity is perpendicular to the equi-frequency contour and point into other higher frequency contours as also shown in Fig. 1.12 (a) -(b). The group velocity is thus forced to be perpendicular to the phase velocity which always points into the same direction as the corresponding wavevector. It can be immediately seen that this behaviour cannot occur in the circular dispersion of isotropic medium in which group velocity always point into the same direction as phase velocity. The group velocity corresponding to large wavevector also points in the specific direction relative to the optical axis (*z*-axis). The critical angle of the group velocity θ_c determines the largest angle to which the energy can flow which can be explicitly expressed in terms of dielectric constants and the critical angle of large wavevectors α_c as [21]

$$\theta_c = \tan^{-1}\left(\mathrm{Re}\left(\varepsilon_\perp / \varepsilon_z\right)\tan\alpha_c\right). \tag{1.17}$$

The directional propagation inside the HM leads to the subwavelength focusing and it is frequency employed to demonstrate the HM.

As already described above, the hyperbolic medium is hardly found in nature. But we can build hyperbolic metamaterials (HMMs) by simply alternating metal and dielectric layers whose thicknesses are much smaller than the wavelength of incident light. In this subwavelength thickness regime, the effective dielectric constants of the HMMs can be retrieved by the effective medium approximation (EMA)

$$\varepsilon_t = \frac{\delta_m}{\delta_m+\delta_d}\varepsilon_m + \frac{\delta_d}{\delta_m+\delta_d}\varepsilon_d, \quad \frac{1}{\varepsilon_z} = \frac{\delta_m}{\delta_m+\delta_d}\frac{1}{\varepsilon_m} + \frac{\delta_d}{\delta_m+\delta_d}\frac{1}{\varepsilon_d}, \tag{1.18}$$

where ε_m is dielectric constant of the metal, ε_d is dielectric constant of the dielectric, δ_m is thickness of the metal, and δ_d is thickness of the dielectric. These effective dielectric constants emerge naturally

by imposing the Floquet-Bloch wave along the propagation direction and $\delta_m, \delta_d \ll \lambda$ [60]. It can be seen from these equations that the effective dielectric constants can have different signs because $\varepsilon_m < 0$ and $\varepsilon_d > 0$. Therefore, we can build both type-I and type-II HMMs by choosing the proper metals and dielectric with subwavelength thicknesses. This concept has been used by Z. Jacob et al. [19] to design the cylindrical HMMs working in visible band that can capture large wavevectors scattered from the objects placed inside the inner core of the cylindrical HMMs to propagate into the outer region. The large wavevectors will be transformed into the smaller wavevectors as they propagate outward because the orbital angular momentum of light must be conserved, and therefore they can match the low wavevector in air to propagate into the far-field. This is known as the magnification process which occurs only in curve space. The cylindrical HMMs has been experimentally demonstrated by Z. Liu et al at the ultraviolet wavelength 365 nm as shown in Fig. 1.13 [20], and these devices are now known as the cylindrical hyperlens or CHs. The CHs is fabricated by alternating silver and alumina layers each with thickness 35 nm onto a quartz substrate. The sub-diffraction-limited information from the object inscribed into chromium layer deposited directly to the inner core of the CHs are collected by the CHs, being magnified as they propagate outward, and then are collected by the conventional lens placed in the far-field. The spatial resolution of 130 nm is achieved in this experiment. However, the resolution of these devices is strongly limited by losses in silver layer.

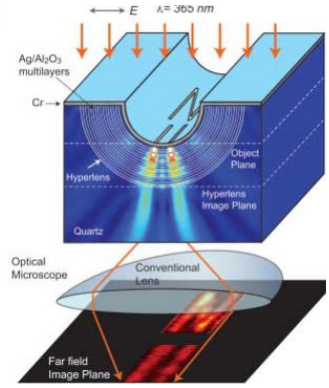

Fig. 1.13. The first experimental demonstration of the cylindrical hyperlens metamaterials working in ultraviolet band [20].

In the THz band, the dielectric constant of the metals explodes, and the metals are required to be structured into the rod arrays. The rod arrays packed inside the tapered fibre as shown in Fig. 1.14 (a) has been experimentally demonstrated to show the subwavelength imaging and focusing [30]. The rod arrays are made from indium rods embedded in low loss Zeonex polymer. These fibres behave as type-I HMMs with $|\varepsilon_z| \ll \varepsilon_t$, and therefore all tangential components of wavevectors are forced to propagate with the same propagation constant $k_z = \sqrt{\varepsilon_t}(\omega/c)$. Then, the EFC of this structure is completely flat and the contours are parallel to the transversal axis, and thus the group velocity is always parallel to the propagation axis. The fibres work at the Faby-Perot resonances to convey light to another side, and their long lengths make them work at low frequency. The experimenters can achieve the focal spot size about 143 μm at the frequency 75 GHz (λ=4000 μm) as shown in Fig. 1.14 (b) in the

region close to the smaller interface of the tapered fibre whose the larger interface is combined with the aperture to create large wavevectors. The focal spot size obtained by this structure is restricted by the ratio between two ends of the fibres, and the even small loss of the Zeonex polymer resulting from the Faby-Perot resonance.

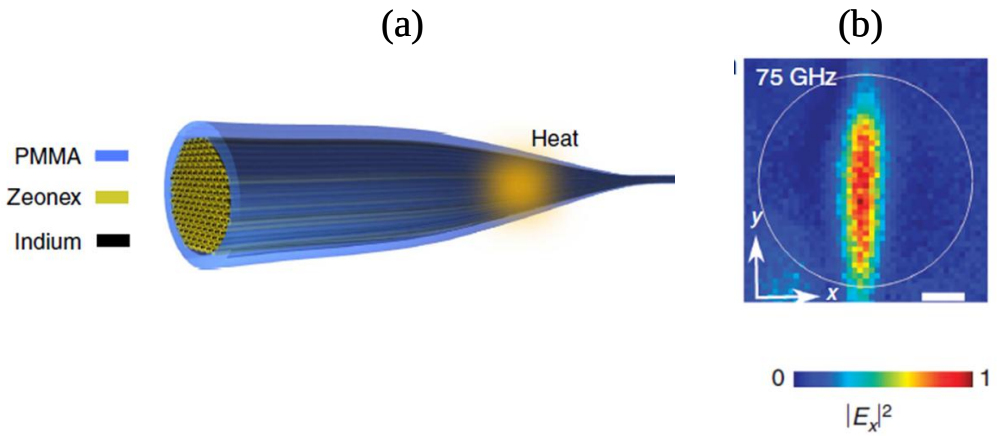

Fig. 1.14. (a) Schematic view of tapered fibre consisting Indium rods embedded in Zeonex polymer. (b) Intensity distribution at the small interface of the tapered fibre with the aperture placed on the large interface [30].

In order to obtain smaller imaging resolution in the scale of a few micron which will be practically important in the biomedical imaging, we need smaller HMMs, and we need to optimize the electromagnetic fields inside those HMMs and in surrounding media by solving the Maxwell's equations. The conventional method which is widely used in academics is the finite difference time domain method (FDTD). We review the Maxwell's equations and FDTD simulation in the next section. The advantage an disadvantage of the FDTD simulation will be also given.

1.4.7 Maxwell's equations and finite difference time domain simulation (FDTD)

The year 2015 is declared by UNESCO to be the international year of light to celebrate some important achievements in optics. One of those achievements is the formulation of the electromagnetic theory of light by J. C. Maxwell 150 years ago. The equations are known today as the Maxwell's equations to honour his name. The Maxwell's equations show that light is composed of electric and magnetic fields which induce each other in space and time so that the light can propagate throughout space with the constant speed. These equations describe the behaviour of the electromagnetic fields of light, and they are expressed compactly as

$$\nabla \cdot \mathbf{D}(\mathbf{r},t) = \rho(\mathbf{r},t), \tag{1.19}$$

$$\nabla \cdot \mathbf{B}(\mathbf{r},t) = 0, \tag{1.20}$$

$$\nabla \times \mathbf{E}(\mathbf{r},t) = -\frac{\partial \mathbf{B}(\mathbf{r},t)}{\partial t}, \tag{1.21}$$

$$\nabla \times \mathbf{H}(\mathbf{r},t) = \frac{\partial \mathbf{D}(\mathbf{r},t)}{\partial t} + \mathbf{J}(\mathbf{r},t), \tag{1.22}$$

where **E** denotes the electric field, **D** the electric displacement, **H** the magnetic field, **B** magnetic induction, **J** current density, and ρ the charge density. These field quantities are related by the constitutive relations

$$\mathbf{D}(\mathbf{r},t)=\varepsilon_0\varepsilon\mathbf{E}(\mathbf{r},t),\quad \mathbf{B}(\mathbf{r},t)=\mu_0\mu\mathbf{H}(\mathbf{r},t), \tag{1.23}$$

where ε_0 and μ_0 are electric permittivity and magnetic permeability in free space, respectively, ε and μ are dielectric constant and magnetic permeability of the medium in which light propagates, respectively. ε and μ are scalar in isotropic medium and tensors in anisotropic medium. In conducting medium, the conduction current density $\mathbf{J}=\tilde{\sigma}\mathbf{E}$ where $\tilde{\sigma}$ is complex optical conductivity. After substituting the conduction current into Eq. (1.22) with the time harmonic $\exp(-i\omega t)$ dependence, the complex dielectric constant $\tilde{\varepsilon}$ of the metal is redefined and become related to $\tilde{\sigma}$ via the relation

$$\tilde{\varepsilon}=\varepsilon_\infty+i\frac{\sigma}{\omega\varepsilon_0}, \tag{1.24}$$

where ε_∞ is the background dielectric constant. The complex dielectric constant of a metal is described by the Drude's model given in Eq. (1.7) and the complex conductivity of the metal can be obtained by applying Eq. (1.7) and (1.24). Therefore, the right hand side of Eq. (1.22) for the metal can be written only in terms of the summation between electric displacement associated with complex dielectric constant of the metal and the free electric current density.

Once the complex electromagnetic fields of light with the time harmonic $\exp(-i\omega t)$ are known by the Maxwell's equations, the energy flow of light is obtained by calculating the time-averaged Poynting vector **S** expressed as

$$\langle\mathbf{S}\rangle=\frac{1}{2}\mathrm{Re}\left(\mathbf{E}\times\mathbf{H}^*\right). \tag{1.25}$$

The real part and imaginary parts of the electromagnetic fields must be taken to calculate the energy flow of light, but only the real parts are taken if one considers the propagation direction of light. As in the case of hyperlens, these two directions can be different. For any time-dependence electromagnetic field, the instantaneous Poynting vector at time *t* is obtained by $\mathbf{S}=\mathbf{E}\times\mathbf{H}$.

In order to solve for the electromagnetic fields, the boundary conditions must be given. In the open system, the electromagnetic fields radiating from a source must be radiating wave at the far-field. In the composite system comprising more than two media, the electromagnetic fields must satisfy the boundary conditions at the interfaces between two media. The boundary conditions at the interface between two media denoted by *i* and *j* are listed as follows

$$E_{\square}^{(i)}-E_{\square}^{(j)}=0, \tag{1.26}$$

$$H_{\square}^{(i)}-H_{\square}^{(j)}=K, \tag{1.27}$$

$$D_{\perp}^{(i)}-D_{\perp}^{(j)}=K_\sigma, \tag{1.28}$$

$$B_{\perp}^{(i)}-B_{\perp}^{(j)}=0, \tag{1.29}$$

where K is surface current and K_σ is surface charge density. In most case, even in the case of the metal, there are no surface currents and surface charge density because the materials are considered as dielectric medium (negative dielectric constant for metal). This is not true if the radiating sources are placed directly at the interface. In the case of $K = K_\sigma = 0$, the tangential components of the electric and magnetic fields are continuous. These two conditions will be applied frequently in the analysis of subsequent chapters. The remaining two boundary conditions for the normal components are automatically satisfied as the normal components of the fields are linked to the tangential components of the fields via the Maxwell's equations.

Although the boundary conditions have already been given, the Maxwell's equations are still hard to solve. The popular method is to solve the Maxwell's equations numerically using the so called finite difference time domain method of FDTD. Consider an isotropic medium with an arbitrary shape which is surrounded by air excited by TM-polarized incident light as schematically shown in Fig. 1.15. The magnetic field is perpendicular to the plane and therefore has only z component $\mathbf{H} = H_z \hat{z}$. The variation of the magnetic field in space is equivalent to the variation of the electric field in time via Eq. (1.22) of the Maxwell's equations, and we have from this equation

$$\varepsilon_0 \varepsilon \frac{\partial \mathbf{E}}{\partial t} = \left(\frac{\partial H_z}{\partial y} - J_x \right) \hat{x} - \left(\frac{\partial H_z}{\partial x} + J_y \right) \hat{y} , \tag{1.30}$$

where J_x and J_y are components of electric current density which generates the incident light. The variation of the electric field in space is also equivalent to the variation of the magnetic field in time according to Eq. (1.21) of the Maxwell's equations, and we have from this equation

$$-\mu_0 \mu \frac{\partial \mathbf{H}}{\partial t} = \left(\frac{\partial E_y}{\partial x} - \frac{\partial E_x}{\partial y} \right) \hat{z} . \tag{1.31}$$

Eq. (1.30) and (1.31) gives 3 coupled-equations for all components of the electromagnetic field

$$\varepsilon_0 \varepsilon \frac{\partial E_x}{\partial t} = \frac{\partial H_z}{\partial y} - J_x , \tag{1.32}$$

$$\varepsilon_0 \varepsilon \frac{\partial E_y}{\partial t} = -\frac{\partial H_z}{\partial x} - J_y , \tag{1.33}$$

$$-\mu_0 \mu \frac{\partial H_z}{\partial t} = \frac{\partial E_y}{\partial x} - \frac{\partial E_x}{\partial y} . \tag{1.34}$$

The FDTD method replaces the partial derivatives with the finite difference, and thus the space and time coordinates become discretized as shown by red dots in Fig. 1.15 for the discretized space. For example, the partial derivative of a function $f(x,y,t)$ with respect to x at the point (x_0,y,t) is approximated by the finite derivative as

$$\left. \frac{\partial f(x,y,t)}{\partial x} \right|_{x=x_0,y,t} \approx \frac{f(x+\Delta x/2, y, t) - f(x-\Delta x/2, y, t)}{\Delta x} , \tag{1.35}$$

where Δx is an interval of the discretized x-coordinate. The similar expressions can be obtained for the partial derivative with respect to other coordinates. By substituting the finite differences for all components of the electromagnetic fields into Eq. (1.19)-(1.22), the solutions of the electromagnetic fields at all discretized points can be obtained by the so called Yee algorithm. The challenge is reduced

to the programming implementation to apply the boundary conditions at the boundary between two media. In this thesis, we employ the freely-distributed FDTD code called MEEP in this thesis [61]. This program is stable and widely used in academics.

The FDTD method allows us to witness the time-evolution of the electromagnetic fields in our structure. But the accuracy of this method dramatically depends on the chosen intervals. The intervals must be varied until the solutions of the electromagnetic fields converge within some degree of accuracy. Otherwise, it will give trivial solutions. Therefore, the disadvantages of FDTD simulation are time consuming and inaccuracy. It can be said that it is not efficient method. Specifically, in the structure whose size much smaller than the working wavelength, FDTD performs very poorly or even impossible in the extreme case. Therefore, one must not completely rely on the FDTD simulation in

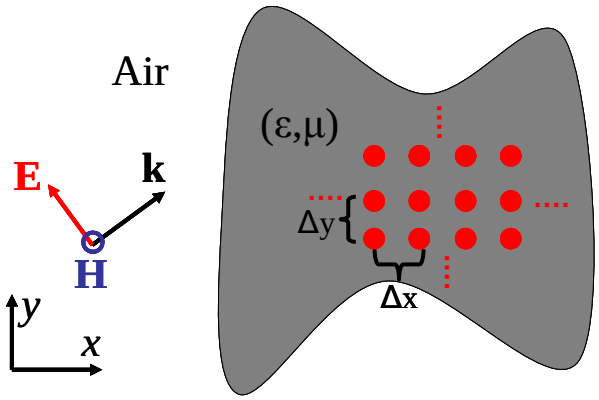

Fig. 1.15. An isotropic object with an arbitrary shape, which is excited by an TM-polarized incident light, is discretized in space and time in FDTD simulation.

the subwavelength regime. Instead, one should look for the analytical solution of the structure of interest and use FDTD simulation as theory-validity checking with simple parameters. After that, we can use the analytical solution to obtain the electromagnetic fields with extreme parameters in the subwavelength scale. Because FDTD simulation is consistent with an experiment, so as the analytical solution. The analytical solution give the very efficient tool to optimize our structure.

Chapter 2

Analytical solutions of electromagnetic fields in focusing and magnifying cylindrical hyperlenses : Green's function approach

The cylindrical hyperlens (CHs) is hyperbolic-dispersion metamaterials supporting the propagation of near fields with high spatial frequencies, which are extremely weak in the far-field region in conventional dielectric materials, thereby allowing the far-field imaging and the image magnification of two-dimensional subwavelength objects beyond the optical diffraction limit (called magnifying CHs) [19,20]. The image magnifying process of subwavelength objects results from the angular momentum conservation of the cylindrical waves, and it was realized in the CHs made by alternating Ag and Al_2O_3 concentric cylindrical layers (CCLs) in ultraviolet band for the first time [20]. The magnifying CHs can be optimized by using the Finite Element simulation (FE) with realizing the effective medium approximation [19,20,62,63]. However, the numerical simulations FE or Finite Difference Time Domain (FDTD) are time consuming and inaccurate in some cases. The reverse process as the magnifying CHs, that is focusing light into the subwavelenth region (focusing CHs), is suffered from the total reflection of the incoming light at the interfaces between air and the CHs due to the large difference of the wavevectors between these two regions [64]. The plasmonic waveguide coupler (PWC) can be used to convert low wavevectors to high wavevectors and vice versa by controlling the phase of light for a metamaterial slab [64]. However, the PWC has sophisticated structure which is difficult to fabricate. Other approaches use the diffraction grating, double slits and a single slit to generate near fields which then can propagate along the cone in specific direction relative to the optical axis, and then the interferences of these waves give rise to the subwavelength fringes inside the hyperlens slabs [65,21,66]. However, this concept of the sub-wavelength focusing has not been demonstrated in the CHs yet. The sub-wavelength slits may be treated as the collections of point sources [21,66]. The analytical solutions of light propagation can be obtained if the single point source is located inside the homogeneous CHs by using the Green's function analysis [67]. These solutions are obtained by completely neglecting the outermost and innermost interfaces, and thus they are useful for investigating the electromagnetic waves in the infinitely large homogeneous anisotropic material. However, the anisotropic material with inherently hyperbolic dispersion is hardly found in nature. Therefore, the optical metamaterial with hyperbolic dispersion made by alternating metallic and insulator layers is more practical in experiment [20]. The solutions in Ref. 67 may be applied to this inhomogeneous structure as well if the structure is much smaller than the wavelength of light to be satisfied by the effective medium approximation. However, it would be difficult to fabricate the fine structure to completely avoid the inhomogeneity in the visible and ultraviolet regions.

In this chapter, the Green's function analysis is revisited and applied to obtain the electromagnetic fields in the metamaterial CHs comprising the CCLs for both focusing and magnifying processes in which the multiple sources are located outside the CHs and inside the core, respectively. These solutions are new efficient tools for the optimizations of the CHs beyond the effective medium approximation.

The chapter is organized as follows. The dispersion relations of light propagation in anisotropic media for two polarizations are clarified in section 2.1. We will see how to obtain the hyperbolic dispersion for each polarization in this section, and why only specific polarization is important if metals are chosen to make the CHs. In section 2.2, the Green's function analysis for point sources embedded in vacuum is revisited. This section shows the main features of this analytical technique which can be applied to solve the inhomogeneous Helmholtz's equation. In section 2.3, the Green's function analysis is applied to the CHs in both focusing and magnifying processes. The analytical solutions for the focusing process are given first, and then followed by the analytical solutions for the magnifying process. In section 2.4, the subwavelength focusing of two point sources in the optical band is demonstrated by using the analytical solutions. The results are compared with the real structure to validate the point source assumption. In section 2.5, we show the enhancement of the magnifying resolution in the UV band by using our analytical solutions. Lastly, the chapter is concluded in the section 2.6.

2.1 The role of polarization in dispersion relation of anisotropic medium

The electromagnetic waves propagating in anisotropic media are contributed by two states of polarizations : transverse magnetic (TM) polarization and transverse electric (TE) polarization. We can consider each of them separately because they are independent to each other. The two polarizations are more well known as TM-mode and TE-mode. We will show in this section that both TE-mode and TM-mode can satisfy hyperbolic dispersion. For the TE-mode, the signs of magnetic permeabilities associated with two orthogonal axes must be different. For the TM-mode, the signs of the dielectric constants associated with two orthogonal axes must be different. This is important to understand why we can consider only the TM-mode in subwavelength imaging with noble metals such as gold and silver, and the TE-mode is always neglected.

2.1.1 Dispersion relation of TE-mode

We consider an uniaxial anisotropic medium whose dielectric constants and magnetic permeabilities are expressed in terms of tensors as follows

$$\overline{\overline{\varepsilon}} = \begin{bmatrix} \varepsilon_x & 0 & 0 \\ 0 & \varepsilon_y & 0 \\ 0 & 0 & \varepsilon_z \end{bmatrix}, \quad \overline{\overline{\mu}} = \begin{bmatrix} \mu_x & 0 & 0 \\ 0 & \mu_y & 0 \\ 0 & 0 & \mu_z \end{bmatrix}. \tag{2.1}$$

For the TE-mode, the wavevector $\mathbf{k}$ and the magnetic field $\mathbf{H}$ lie on the *xy*-plane : $\mathbf{k} = k_x\hat{x} + k_y\hat{y}$, $\mathbf{H} = \left(H_x\hat{x} + H_y\hat{y}\right)\exp\left(ik_x x + ik_y y\right)$, while the electric field is parallel to the *z*-axis : $\mathbf{E} = E_z\hat{z}$. Then, the Maxwell's equations for the TE-mode with time-harmonic $\exp(-i\omega t)$ become

$$\varepsilon_0\varepsilon_z k_z E_z = 0, \tag{2.2}$$

$$\mu_0\mu_x k_x H_x + \mu_0\mu_y k_y H_y = 0, \tag{2.3}$$

$$k_y E_z\hat{x} - k_x E_z\hat{y} = \omega\mu_0\mu_x H_x\hat{x} + \omega\mu_0\mu_y H_y\hat{y}, \tag{2.4}$$

$$\left(k_x H_y - k_y H_x\right)\hat{z} = -\omega\varepsilon_0\varepsilon_z E_z\hat{z}. \tag{2.5}$$

Eq. (2.2) is automatically satisfied because $k_z = 0$. Eq. (2.3) gives the relation between two components of the magnetic field. Eq. (2.4) gives us two equations for each coordinate *x* and *y*, then we can write H_x and H_y in terms of E_z

$$H_x = \frac{k_y}{\omega\mu_0\mu_x}E_z, \quad H_y = -\frac{k_x}{\omega\mu_0\mu_y}E_z. \tag{2.6}$$

The Eq. (2.3) is automatically satisfied by using H_x and H_y from Eq. (2.6). We substitute Eq. (2.6) into Eq. (2.5) to obtain the dispersion relation of the TE-mode, and we have for $E_z \neq 0$, the following condition must be satisfied

$$\frac{k_x^2}{\mu_y} + \frac{k_y^2}{\mu_x} = \varepsilon_z k_0^2 , \tag{2.7}$$

where $k_0 = \omega / c$ is wavenumber in free space. Eq. (2.7) is the dispersion relation of the TE-mode propagating in anisotropic medium. We can immediately see that the medium exhibit the hyperbolic dispersion relation if $\mu_x > 0, \mu_y < 0, \varepsilon_z > 0$ or $\mu_x < 0, \mu_y > 0, \varepsilon_z > 0$. The TE-mode with large wavevectors are allowed to propagate in such a medium. However, if the medium has the same signs of magnetic permeabilities $\left(\mu_x > 0, \mu_y > 0\right)$ but different absolute value, then the medium exhibit the elliptical dispersion which cannot support the TE-mode with large wavevector. In the isotropic medium in which the magnetic permeabilities are the same, the dispersion relation is circular and therefore completely suffers from the diffraction limit. The dispersion relations at a particular frequency which are called the equi-frequency contours for these three cases are schematically drawn in Fig. 2.1.

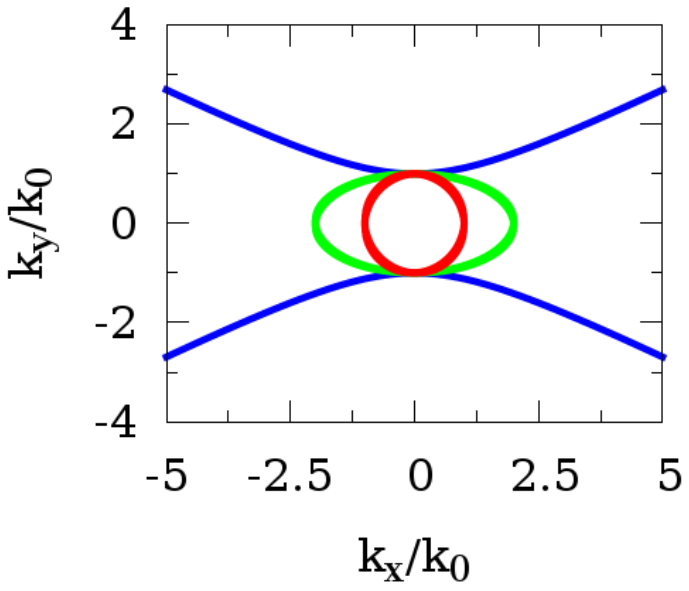

Fig. 2.1. Equi-frequency contours of TE-mode calculated by Eq. (2.7) for hyperbolic medium with $\mu_y = -4, \mu_x = \varepsilon_z = 1$ denoted by the blue line, elliptical medium with $\mu_y = 4, \mu_x = \varepsilon_z = 1$ denoted by the green line, and isotropic medium with $\mu_y = \mu_x = \varepsilon_z = 1$ denoted by the red line.

2.1.2 Dispersion relation of TM-mode

We consider the same anisotropic medium whose dielectric constants and magnetic permeabilities are expressed in Eq. (2.1). But for the TM-mode, the electric fields lie on the same plane as the wavevector : $\mathbf{E} = \left(E_x \hat{x} + E_y \hat{y}\right) \exp\left(ik_x x + ik_y y\right)$, and the magnetic field is parallel to the *z*-axis : $\mathbf{H} = H_z \hat{z}$. We can follow the same procedure as the TE-mode, assume the time-harmonic $\exp\left(-i\omega t\right)$ and list all the Maxwell's equations, which we have

$$\varepsilon_0 \varepsilon_x k_x E_x + \varepsilon_0 \varepsilon_y k_y E_y = 0, \tag{2.8}$$

$$\mu_0 \mu_z k_z H_z = 0, \tag{2.9}$$

$$\left(k_x E_y - k_y E_x\right) \hat{z} = \omega \mu_0 \mu_z H_z \hat{z}\ , \tag{2.10}$$

$$k_y H_z \hat{x} - k_x H_z \hat{y} = -\omega \varepsilon_0 \varepsilon_x E_x \hat{x} - \omega \varepsilon_0 \varepsilon_y E_y \hat{y}\ . \tag{2.11}$$

Eq. (2.9) is automatically satisfied because $k_z = 0$. Eq. (2.11) gives two equations for E_x and E_y written in terms of H_z which are

$$E_x = \frac{-k_y}{\omega \varepsilon_0 \varepsilon_x} H_z, \quad E_y = \frac{k_x}{\omega \varepsilon_0 \varepsilon_y} H_z\ . \tag{2.12}$$

It can be seen that Eq. (2.8) is satisfied by applying E_x and E_y given by Eq. (2.12). We can obtain the dispersion relation of TM-mode by substituting Eq. (2.12) into Eq. (2.10). For $H_z \neq 0$, the following condition must be satisfied

$$\frac{k_x^2}{\varepsilon_y} + \frac{k_y^2}{\varepsilon_x} = \mu_z k_0^2, \tag{2.13}$$

where $k_0 = \omega / c$ is wavenumber in free space. The Eq. (2.13) is the dispersion relation of the TM-mode which is equivalent to that of the TE-mode by swapping the magnetic permeabilities and the dielectric constants. We arrive at the similar conclusion as the TE-mode. The TM-mode can satisfy the hyperbolic dispersion in a medium with parameters $\left(\varepsilon_x > 0, \varepsilon_y < 0, \mu_z > 0\right)$ or $\left(\varepsilon_x < 0, \varepsilon_y > 0, \mu_z > 0\right)$. However, the TM-mode satisfies elliptical dispersion if the signs of dielectric constants are the same but having different values. The TM-mode exhibits the circular dispersion if the signs and absolute value of dielectric constants are the same. These situations are the same as Fig. 2.1 by swapping magnetic permeabilities and dielectric constants.

Noble metals such as gold and silver are non-magnetic and have negative dielectric constant below their plasma frequency, and thus we are particularly interested in the TM-waves. In the focusing process, the TM-waves in hyperbolic medium cannot be directly excited by an external radiation due to the large difference between transverse components of their wavevectors and those of air. The incident light will be completely reflected back by the hyperbolic medium. Therefore, phase-matching structures are required to couple an incident light wave to the TM-waves of the hyperbolic medium. The subwavelength metallic apertures (SMAs) such as holes and slits are simple structures for this purpose as schematically shown in Fig. 2.2. The SMAs act as secondary sources which generate

diffraction waves carrying large wavevectors depending on the aperture size. Then, the diffraction waves can excite high-spatial-frequency TM-waves of the hyperbolic medium, and the coupled-waves propagate through the medium. As the aperture size becomes smaller, the aperture can be treated as a point source. It has been shown by coupled-mode analysis that finite array of slits in perfect electric conductor diffracts the same electromagnetic waves as point sources in the limit of slit width much smaller than the wavelength of light [56]. Therefore, at the subwavelength aperture regime we can model the apertures as point sources. This model allows us to apply the Green's function analysis which is powerful technique for the analysis of the Maxwell's equations with the presence of free sources [68]. The techniques can be also applied to the magnifying process in which an object is treated as a collection of point sources.

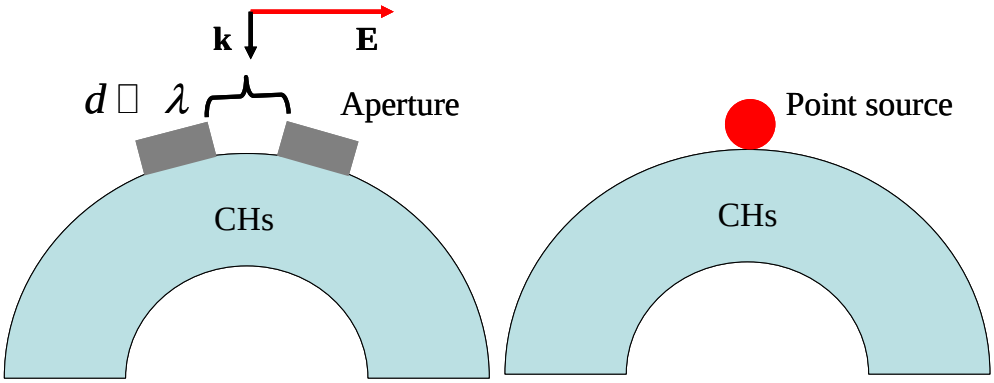

Fig. 2.2. Modelling of subwavelength aperture as a point source.

2.2 Green's function analysis in two-dimensional vacuum

The Green's function analysis can be employed to solve the Maxwell's equations with sources. By including the point sources or line sources, the separation of variables that we are familiar with cannot be directly applied. The Green's function analysis gives us tricks to deal with the boundary conditions at the positions close the sources so that the separation of variable method is still applicable. Perhaps, the best way to illustrate this method is to consider the electromagnetic waves generated by a single source embedded in vacuum.

The analysis starts with the inhomogeneous Helmholtz's equation as the main equation which can be derived from the Maxwell's equations. We work in the two-dimensional cylindrical coordinate whose spatial position is described by radial distance ρ and azimuthal angle ϕ as shown in Fig. 2.3. We assert the presence of the fictitious magnetic line source $\mathbf{J}_M$ pointing in the *z* direction, infinitely long along the *z*-axis, and located at the position (ρ',ϕ') to generate the TM-wave. We can then work in two dimensions, and the line source appears as the point source on two-dimensional plane. The $\mathbf{J}_M$ is assumed to have magnitude $-M_0$, and therefore it can be explicitly expressed in the cylindrical coordinate as

$$\mathbf{J}_M = -\hat{z}M_0\delta(\mathbf{r}-\mathbf{r}') = -\hat{z}M_0\delta(\rho-\rho')\delta(\phi-\phi')/\rho\,, \tag{2.14}$$

where δ is Dirac delta function. The negative sign in source magnitude is used just for the sake of convenience. The Maxwell's equations with the fictitious magnetic point source and the time-harmonic $\exp(-i\omega t)$ read

$$\nabla\cdot\mathbf{D}=0, \tag{2.15}$$

$$\nabla\cdot\mathbf{B}=0, \tag{2.16}$$

$$\nabla\times\mathbf{E}=i\omega\mathbf{B}+\mathbf{J}_M, \tag{2.17}$$

$$\nabla\times\mathbf{H}=-i\omega\mathbf{D}. \tag{2.18}$$

Notice that $\mathbf{J}_M$ is added to the right hand side of Eq. (2.17) to generate the variation of electric field which then triggers the propagation of electromagnetic wave. Then, we can take curl operator to Eq. (2.18) and apply the identity $\nabla\times\nabla\times\mathbf{H}=\nabla\nabla\cdot\mathbf{H}-\nabla^2\mathbf{H}=-\nabla^2\mathbf{H}$, we have

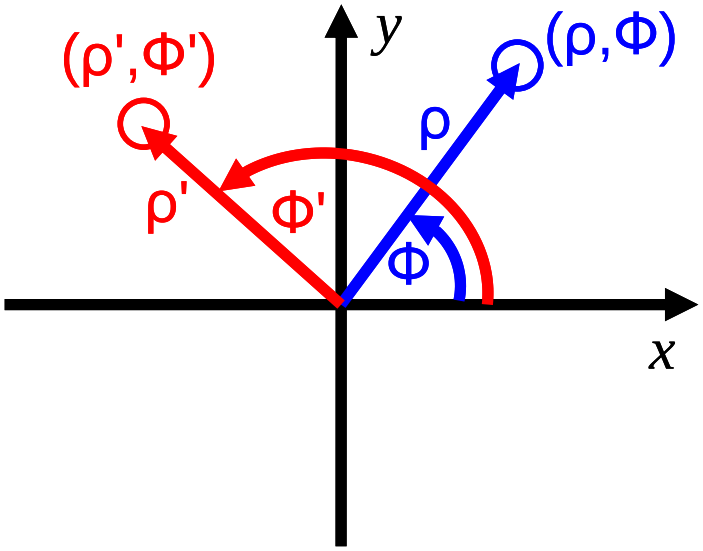

Fig. 2.3. Cylindrical coordinate for Green's function analysis. ρ denotes radial distance, and ϕ denotes azimuthal angle. The location of point source is labelled by prime.

$$-\nabla^2\mathbf{H}=-i\omega\nabla\times\mathbf{D}=-i\omega\varepsilon_0\left(i\omega\mu_0\mathbf{H}+\mathbf{J}_M\right)=k_0^2\mathbf{H}-i\omega\varepsilon_0\mathbf{J}_M, \tag{2.19}$$

where $k_0=\omega/c$ is wavenumber in free space. By considering only the TM-mode : $\mathbf{H}=H_z\hat{z}$ and using the $\mathbf{J}_M$ from Eq. (2.14), we finally have the wave equation for H_z as follows

$$\left(\nabla^2+k_0^2\right)H_z=-i\omega\varepsilon_0M_0\delta\left(\rho-\rho'\right)\delta\left(\phi-\phi'\right)/\rho. \tag{2.20}$$

Eq. (2.20) is the inhomogeneous Helmholtz's equation with the fictitious point source. In the two-dimensional cylindrical coordinate, Eq. (2.20) takes the following form

$$\left(\frac{1}{\rho}\frac{\partial}{\partial\rho}\left(\rho\frac{\partial}{\partial\rho}\right)+\frac{1}{\rho^2}\frac{\partial^2}{\partial\phi^2}+k_0^2\right)H_z=-i\omega\varepsilon_0M_0\delta(\rho-\rho')\delta(\phi-\phi')/\rho. \tag{2.21}$$

Eq. (2.21) is our starting point. The followings are analytical steps for solving the inhomogeneous Helmholtz's equation in cylindrical coordinate.

We expand the azimuthal delta function $\delta(\phi-\phi')$ and the magnetic field in terms of the harmonic function as

$$\delta(\phi-\phi')=\frac{1}{2\pi}\sum_{m=-\infty}^{\infty}\exp\left[im(\phi-\phi')\right], \tag{2.22}$$

and

$$H_z=\frac{1}{2\pi}\sum_{m=-\infty}^{\infty}R_m(\rho,\rho')\exp\left[im(\phi-\phi')\right], \tag{2.23}$$

where m is an integer and $R_m(\rho,\rho')$ is radial function which is yet to be determined. By substituting Eq. (2.22) and (2.23) into Eq. (2.21) and apply the orthogonality of the harmonic function, we obtain the differential equation for the radial function as follows

$$\rho\frac{d}{d\rho}\left(\rho\frac{dR_m}{d\rho}\right)+\left[(k_0\rho)^2-m^2\right]R_m=-i\omega\varepsilon_0 M_0\rho\delta(\rho-\rho'). \tag{2.24}$$

The problem is now reduced to solving Eq. (2.24) for $R_m(\rho,\rho')$, and the solution of the magnetic field is obtained by substituting the $R_m(\rho,\rho')$ back into Eq. (2.23). At the position $\rho\neq\rho'$, the right hand side of Eq. (2.24) becomes zero and the Eq. (2.24) becomes well known as Bessel equation. Because the Bessel equation is second order differential equation, thus the solution is summation of two special functions which are called Bessel functions $J_m(k_0\rho)$ and Neumann functions $Y_m(k_0\rho)$. In the far-field, the combination of these two functions must become the out-going propagating waves. This combination gives rise to the new function called Hankel functions of the first kind (because of time-harmonic $\exp(-i\omega t)$) which are defined as $H_m^{(1)}(k_0\rho)=J_m(k_0\rho)+iY_m(k_0\rho)$. Therefore, we can write the solution in the region $\rho>\rho'$ as

$$R_m(\rho>\rho,\rho')=A_m(\rho')H_m^{(1)}(k_0\rho),\ \rho>\rho', \tag{2.25}$$

where $A_m(\rho')$ are field coefficients which are yet to be determined by applying boundary condition at the source location. In the region $\rho<\rho'$, the field coefficients of the Neumann function $Y_m(k_0\rho)$ must be forced to become zero because the Neumann functions diverge at the origin. The Bessel functions $J_m(k_0\rho)$ are finite at the origin, and thus we can write the solution of $R_m(\rho,\rho')$ in terms of them within this region as

$$R_m(\rho<\rho,\rho')=B_m(\rho')J_m(k_0\rho),\ \rho<\rho'. \tag{2.26}$$

We notice that as the radial distance approach the source location from the origin and from the far-field, the $R_m(\rho,\rho')$ must be continuous at the source. By taking the this symmetry into account, we expect that the solutions of Eq. (2.25) and (2.26) must take the following forms

$$R_m(\rho,\rho')=\begin{cases}C_mJ_m(k_0\rho')H_m^{(1)}(k_0\rho), & \rho>\rho'\\ C_mH_m^{(1)}(k_0\rho')J_m(k_0\rho), & \rho<\rho'\end{cases}. \tag{2.27}$$

The remaining task is to find common constant C_m which appears in Eq. (2.27). This can be done by substituting $R_m(\rho,\rho')$ from Eq. (2.27) into its original equation with sources written in Eq. (2.24), and

then integrate both sides of the equation with respect to ρ from $\rho'-\varepsilon$ to $\rho'+\varepsilon$ where $\varepsilon \to 0$. This will lead to the following equation

$$k_0\rho' C_m \left\{ J_m\left(k\rho'\right) H_m^{(1)\prime}(k\rho') - J_m'\left(k\rho'\right) H_m^{(1)}(k\rho') \right\} = -i\omega\varepsilon_0 M_0 , \tag{2.28}$$

where primes on the Bessel function and the Hankel function of the first kind denote the derivative with respect to their arguments. The term in the curl bracket is called Wronskian of Bessel function and the Hankel function of the first kind which is equal to $2i/\left(\pi k_0\rho'\right)$. Therefore, the coefficient C_m becomes

$$C_m = -\frac{\pi\omega\varepsilon_0 M_0}{2} . \tag{2.29}$$

Therefore, the radial function has been finally determined by substituting C_m from Eq. (2.29) to Eq. (2.27). Therefore, the complete solution of the magnetic field is written as

$$H_z = \begin{cases} -\dfrac{\omega\varepsilon_0 M_0}{4} \displaystyle\sum_{m=-\infty}^{\infty} J_m\left(k_0\rho'\right) H_m^{(1)}\left(k_0\rho\right) \exp\left[im\left(\phi-\phi'\right)\right] \\ -\dfrac{\omega\varepsilon_0 M_0}{4} \displaystyle\sum_{m=-\infty}^{\infty} H_m^{(1)}\left(k_0\rho'\right) J_m\left(k_0\rho\right) \exp\left[im\left(\phi-\phi'\right)\right] \end{cases} . \tag{2.30}$$

The Eq. (2.30) is our general solution of the magnetic field, and the electric field can be obtained from this equation via the Maxwell's equations expressed in the cylindrical coordinate as

$$\mathbf{E} = E_\rho \hat{e}_\rho + E_\phi \hat{e}_\phi = -\frac{1}{i\omega\varepsilon_0}\frac{1}{\rho}\frac{\partial H_z}{\partial\phi}\hat{e}_\rho + \frac{1}{i\omega\varepsilon_0}\frac{\partial H_z}{\partial\rho}\hat{e}_\phi . \tag{2.31}$$

The calculations of the electromagnetic fields are now very easy because we just have to increase number of orders until the fields converge. The calculations are therefore much faster than FDTD simulation. However, in the region close to the source, the number of orders required can be very high. Therefore, the closed analytical form is needed in this region. The closed form means that we include all diffraction orders from minus infinity to plus infinity, packed in one term, without the need of the summation. In this simple case, the closed form can be formulated by recalling the mathematical theorem called addition theorem [69] which states that

$$H_0^{(1)}\left(\sqrt{\upsilon^2+u^2-2\upsilon u\cos\left(\phi-\phi'\right)}\right) = \sum_{m=-\infty}^{\infty} J_m\left(\upsilon\right) H_m^{(1)}\left(u\right) e^{im(\phi-\phi')} . \tag{2.32}$$

Therefore, we have that the solutions in both sides of the source, $\rho<\rho'$ and $\rho>\rho'$, including at $\rho=\rho'$ have exactly the same closed form by applying Eq. (2.32) to Eq. (2.30). The closed form of the magnetic field is written as

$$H_z = -\frac{\omega\varepsilon_0 M_0}{4} H_0^{(1)}\left(k_0\sqrt{\rho^2-\rho'^2-2\rho\rho'\cos\left(\phi-\phi'\right)}\right). \tag{2.33}$$

The Green's function analysis for a single point source can be easily extended in to multiple point sources. More point sources can be included in the equation by adding them to the right hand side of Eq. (2.17) of the Maxwell's equations, and then the summation over all sources will appear on the right hand side of the inhomogeneous Helmholtz's equation. For clarity, we write the inhomogeneous

Helmholtz's equation for N multiple point sources, each located at (ρ_j, ϕ_j) and has magnitude $-M_j$, as follows

$$\left(\frac{1}{\rho}\frac{\partial}{\partial\rho}\left(\rho\frac{\partial}{\partial\rho}\right)+\frac{1}{\rho^2}\frac{\partial^2}{\partial\phi^2}+k_0^2\right)H_z=-i\omega\varepsilon_0\sum_{j=1}^{N}M_j\delta(\rho-\rho_j')\delta(\phi-\phi_j')/\rho\,. \tag{2.34}$$

By following the same procedure as the single point source, the closed form of the magnetic field is expressed as

$$H_z=-\frac{\omega\varepsilon_0}{4}\sum_{j=1}^{N}M_jH_0^{(1)}\left(k_0\sqrt{\rho^2-\rho_j'^2-2\rho_j\rho_j'\cos\left(\phi-\phi_j'\right)}\right). \tag{2.35}$$

We have to check the validity of the arguments of the Green's function analysis given so far by comparing with FDTD simulation [61]. For the Green's function analysis, the Bessel function and the Hankel function of the first kind are calculated by freely-distributed subroutine [70]. First, we compare the case of the single point source. The single point source radiates an continuous wave with wavelength λ=368 nm. We put this point source at the location $(\rho',\phi')=(200\text{ nm},\pi/2)$. The computational cell of the FDTD simulation is surrounded by perfectly matched layer with thickness 4 times larger than the wavelength of light to prevent the reflection at the boundaries so that light is only propagating out from the source. We have to vary the resolutions of the FDTD simulation. In another word, we have to change the spatial intervals along x and y axes : Δx, Δy. The current version of FDTD program defines $\Delta x=\Delta y$, thus it generates only square grids. The time interval is automatically determined by the spatial interval via the Courant factor S which is defined as $S=\Delta t/\Delta x$ where the speed of light $c=1$. In our FDTD simulation, the Courant factor is default value which is equal to 0.5. In stead of saying how small Δx we use, we will say how large the resolution we use. Then, Δx is obtained by the inverse of the resolution. For example, if we define the resolution as 5 pix/nm, then the spatial interval is 1/5=0.2 nm. Therefore, increasing resolution means decreasing both spatial interval and time interval. In Fig. 2.4(a), we plot the intensity distribution of the single point source calculated taking into account the maximum number of orders 110. The intensity distribution obtained by the FDTD simulation gives the same distribution so that we show only from the analytics. Now we compare the intensities from the Green's function analysis and from the FDTD simulation along the specific radial line which approaches the source. That line is $\phi=\pi/2$ or the y-axis. The comparison is shown in Fig. 2.4(b). It can be seen that both number of orders 20 and 110 yield the consistent intensity profiles with the FDTD simulation in the region relatively far from the source. However, as we approach the source (located at $y=200$ nm), there is the great inconsistent between the Green's function analysis and the FDTD simulation. This means that higher orders are required in the region close to the source, the near field region. In fact, the analytical intensity profile with the maximum number of order 110 is consistent with FDTD only in the region whose distance from the source is larger than 5 nm. This result also means that TM waves close to the source have large azimuthal component of wavevectors k_ϕ from the conservation of angular momentum $m=k_\phi\rho$ [19]. Then, we plot the intensity profile calculated by the closed form which includes all orders in the same figure. It can be seen that the intensity profile from the analytical solution is now perfectly consistent with FDTD

simulation. In deed, Eq. (2.33) is the exact solution of the magnetic field that the FDTD simulation must satisfy by increasing more resolutions.

We also plot the field distribution of the two point sources calculated by the Green's function analysis in Fig. 2.4(c). The diffraction-limited focal spot can be noticed near the origin because of the circular dispersion of the vacuum. Fig. 2.4(d) shows the comparison between the analytical intensity profile and the FDTD intensity profile along the curve $\rho = 100$ nm for the two point sources. It clearly shows that the solutions from Green's function analysis are perfectly consistent with those from FDTD simulation in the case of multiple point sources. Therefore, the Green's function analysis is useful for the optimization of the subwavelength focusing from multiple sources.

We are now confident that the Green's function analysis is consistent with the numerical method. We will apply the Green's function analysis to the CHs in the next section.

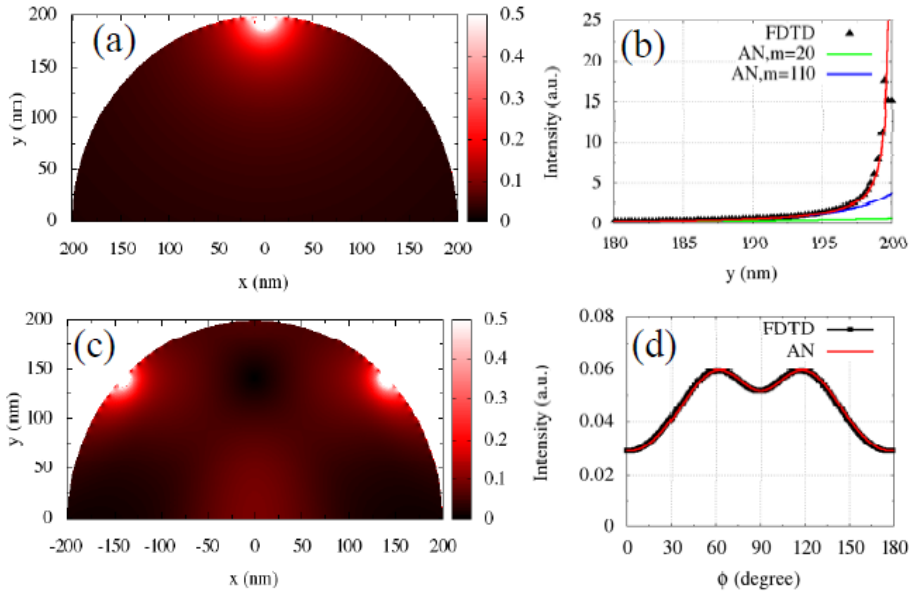

Fig. 2.4. (a) The intensity distribution of the single point source obtained by the Green's function analysis with the number of order 110. (b) The intensity profiles of the single point source along the y-axis obtained by the Green's function analysis with the number of orders 110 and 20 labelled by the blue and green lines, respectively. The intensity profile obtained by the FDTD simulation is indicated by black triangular points. The red line is the intensity profile obtained by the Green's function analysis taking into account all orders. (c) The intensity distribution of the double point sources obtained by the Green's function analysis with the number of order 110. (d) The intensity profiles of the double point sources along the curve $\rho = 100$ nm obtained by the Green's function analysis indicated by red line and FDTD simulation indicated by black circular points. The resolution of FDTD simulation is 4 pix/nm.

2.3 Green's function analysis of two-dimensional cylindrical hyperlens (CHs)

When point sources are located near the CHs, the electromagnetic fields obtained from the previous section are perturbed by the presence of the CHs, and the new field distributions are generated. In the source region where the sources are embedded, the electromagnetic fields are the summation between the free solutions which are given by Eq. (2.30) without the presence of the CHs and the scattered field

caused by the scattering due to the presence of the CHs. The scattered field can be expressed in terms of the Hankel function of the first kind if the source region is the outer region, or the Bessel function if the source region is the inner region (the core). The electromagnetic fields in other regions can be expressed generally as the summation of the Bessel function and the Hankel function of the first kind. Then, all field coefficients are determined by applying the continuities of H_z and E_ϕ. We can compute intensity distributions and compare our results with the FDTD simulation.

2.3.1 Focusing process

The schematic view of the CHs in the focusing process is shown in Fig. 2.5. We imagine that sources which are created by some subwavelength apertures are located in the outer region of the CHs. The CHs collect high-spatial frequency waves from these secondary sources and guide them to the core region. If the sources are set up in proper condition, we can obtain the focusing in the core region. The focusing is said to be "partial focusing" if the critical angle of the Poynting vector with respect to the radial axis is large and the optical energy is split into the light cone. The focusing yields better signal to noise ratio and thus increase the imaging resolution.

We describe the notations of the focusing CHs as follows. The focusing CHs comprises N numbers of non-magnetic concentric cylindrical layers (CCLs) with finite dielectric constant. The dielectric constant of the core region is denoted by ε_{in}, the outer region ε_{out}, and each jth-CCL ε_j where j=1,2,...,N. Notice that all regions are isotropic. The innermost and outermost radii of the CHs are denoted by ρ_c and ρ_N, respectively, while the interfaces between the jth-CCL and (j+1)th-CCL are defined as ρ_j. The magnetic point source is located at (ρ_s', ϕ_s').

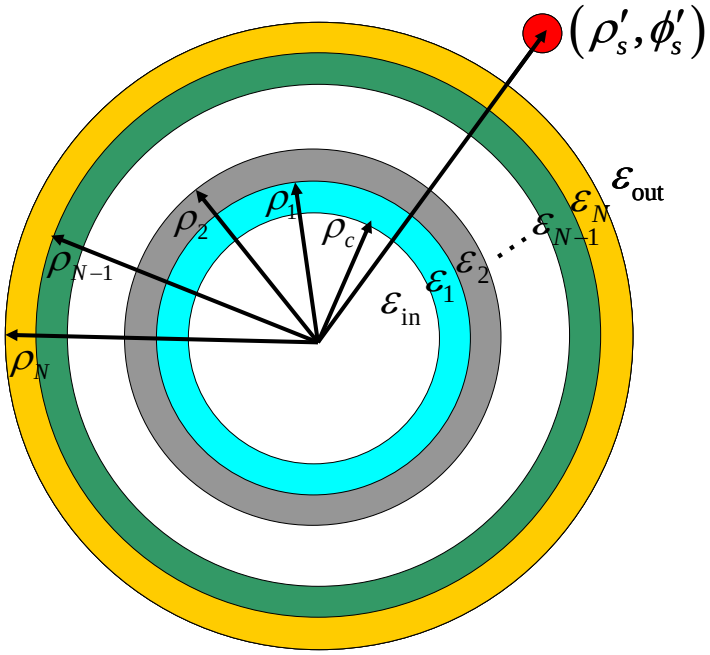

Fig. 2.5. Schematic view of focusing CHs with sources located in the outer region

Next, we give the solutions of the electromagnetic fields in each region. Only the H_z and E_ϕ will be explicitly written because they are sufficient to determine the field coefficients. The E_ρ can be easily obtained from H_z using Eq. (2.31).

Solutions in outer region

In the outer region, which is our source region in the focusing process, the magnetic field $H_z^{(\text{out})}$ is the sum between the free solution $H_z^{(\text{out,f})}$ and the scattering solution $H_z^{(\text{out,s})}$

$$H_z^{(\text{out})} = H_z^{(\text{out,f})} + H_z^{(\text{out,s})} . \tag{2.36}$$

The free solution $H_z^{(\text{out,f})}$ is similar to Eq. (2.30) but now with the dielectric constant ε_{out} and wavenumber $k_{\text{out}} = \sqrt{\varepsilon_{\text{out}}} k_0$. Then, the $H_z^{(\text{out,f})}$ is written as

$$H_z^{(\text{out,f})} = \begin{cases} -\dfrac{\omega\varepsilon_0\varepsilon_{\text{out}} M_0}{4} \displaystyle\sum_{s'} \sum_{m=-\infty}^{\infty} J_m\left(k_{\text{out}}\rho_s'\right) H_m^{(1)}\left(k_{\text{out}}\rho\right) \exp\left[im\left(\phi-\phi_s'\right)\right], & \rho > \rho_s' \\ -\dfrac{\omega\varepsilon_0\varepsilon_{\text{out}} M_0}{4} \displaystyle\sum_{s'} \sum_{m=-\infty}^{\infty} H_m^{(1)}\left(k_{\text{out}}\rho_s'\right) J_m\left(k_{\text{out}}\rho\right) \exp\left[im\left(\phi-\phi_s'\right)\right], & \rho < \rho_s' \end{cases} . \tag{2.37}$$

The summation $\sum_{s'}$ means including only sources which satisfy the condition of radial distance relative to the sources which is $\rho > \rho'$ or $\rho < \rho'$. In usual case, all sources have the same radial distances, and thus this summation means including all the sources available. However, care must be taken if the sources locate in different radial distances because there will be the region between the sources which satisfy the condition $\rho < \rho'$ for some set of sources and $\rho > \rho'$ for another set of sources. In the latter case, we must perform partial sum over the set of sources which satisfy the condition $\rho < \rho'$, and make another partial sum over the set of sources which satisfy the condition $\rho > \rho'$, then two functions are summed up to obtain the final free solution for that region. This situation would be the case for three-dimensional imaging where the height of the objects are taken into account. Hereafter, we define all sources located in the same radial distance but different azimuthal angle.

The scattering solution $H_z^{(\text{out,s})}$ must behave as an outgoing wave in the far-field. Therefore, we write it generally as the linear summation of the *m*th-order Hankel function of the first kind

$$H_z^{(\text{out,s})} = \frac{i\omega\varepsilon_0\varepsilon_{\text{out}} M_0}{2\pi} \sum_{m=-\infty}^{\infty} A_m^{(\text{out})} H_m^{(1)}\left(\rho k_{\text{out}}\right) e^{im\phi} , \tag{2.38}$$

where $A_m^{(\text{out})}$ are field coefficients to be determined by applying the boundary conditions.

The tangential electric field is obtained by Eq. (2.31) and (2.36) and it is written as

$$E_\phi^{(\text{out})} = E_\phi^{(\text{out,f})} + E_\phi^{(\text{out,s})}, \tag{2.39}$$

where

$$E_\phi^{(\text{out,f})} = \begin{cases} \dfrac{iM_0 k_{\text{out}}}{4} \displaystyle\sum_{s'} \sum_{m=-\infty}^{\infty} J_m\left(k_{\text{out}}\rho_s'\right) H_m^{(1)\prime}\left(k_{\text{out}}\rho\right) \exp\left[im\left(\phi-\phi_s'\right)\right], & \rho > \rho_s' \\ \dfrac{iM_0 k_{\text{out}}}{4} \displaystyle\sum_{s'} \sum_{m=-\infty}^{\infty} H_m^{(1)}\left(k_{\text{out}}\rho_s'\right) J_m'\left(k_{\text{out}}\rho\right) \exp\left[im\left(\phi-\phi_s'\right)\right], & \rho < \rho_s' \end{cases} , \tag{2.40}$$

and

$$E_{\phi}^{(\mathrm{out,f})} = \frac{M_0 k_{\mathrm{out}}}{2\pi} \sum_{m=-\infty}^{\infty} A_m^{(\mathrm{out})} H_m^{(1)\prime}\left(\rho k_{\mathrm{out}}\right) e^{im\phi} \,. \tag{2.41}$$

Solutions in *j*th-CCL

In the *j*th-CCL, the electromagnetic fields experience multiple reflections, and thus both Bessel function and Hankel function of the first kind, which are the solutions of the homogeneous Helmholtz's equation in the cylindrical coordinate, must be included. The magnetic fields in these layers are denoted by their indices j : $H_z^{(j)}$, where j=1,2,...,N. Then, $H_z^{(j)}$ can be expressed in the general form as

$$H_z^{(j)} = \frac{i\omega\varepsilon_0\varepsilon_j M_0}{2\pi} \sum_{m=-\infty}^{\infty} \left(A_m^{(j)} H_m^{(1)}\left(\rho k_j\right) + B_m^{(j)} J_m\left(\rho k_j\right)\right) e^{im\phi} \,, \tag{2.42}$$

where $k_j = \sqrt{\varepsilon_j} k_0$ is wavenumber in this layer, $A_m^{(j)}$ and $B_m^{(j)}$ are field coefficients to be determined by the boundary conditions.

The tangential electric field $E_{\phi}^{(j)}$ obtained by Eq. (2.31) and (2.42) is written as

$$E_{\phi}^{(j)} = \frac{M_0 k_j}{2\pi} \sum_{m=-\infty}^{\infty} \left(A_m^{(j)} H_m^{(1)\prime}\left(\rho k_j\right) + B_m^{(j)} J_m'\left(\rho k_j\right)\right) e^{im\phi} \,. \tag{2.43}$$

Solutions in the core region

In the core region or the inner region, the electromagnetic field must be finite at the origin, and thus only the Bessel function, which is the solution of the homogeneous Hemlholtz's equation in cylindrical coordinate, is included. The magnetic field $H_z^{(\mathrm{in})}$ can be written in the general form as

$$H_z^{(\mathrm{in})} = \frac{i\omega\varepsilon_0\varepsilon_{\mathrm{in}} M_0}{2\pi} \sum_{m=-\infty}^{\infty} B_m^{(\mathrm{in})} J_m\left(\rho k_{\mathrm{in}}\right) e^{im\phi} \,, \tag{2.44}$$

where $B_m^{(\mathrm{in})}$ are field coefficients to be determined by the boundary conditions.

The tangential electric field $E_{\phi}^{(\mathrm{in})}$ obtained by Eq. (2.31) and (2.44) is written as

$$E_{\phi}^{(\mathrm{in})} = \frac{M_0 k_{\mathrm{in}}}{2\pi} \sum_{m=-\infty}^{\infty} B_m^{(\mathrm{in})} J_m'\left(\rho k_{\mathrm{in}}\right) e^{im\phi} \,. \tag{2.45}$$

Obtaining field coefficients

All field coefficients are obtained by applying the continuities of H_z and E_{ϕ} at (N+1) number of interfaces. Then, there will be 2(N+1) linear equations which can be solved by building up a single matrix equation $\left[A_m\right]\left\{x_m\right\} = \left\{b_m\right\}$ for each order m , where $[A_m]$ is coefficient matrix, $\left\{x_m\right\}$ is field coefficient vector, and $\left\{b_m\right\}$ is constant vector, and then the LAPACK subroutine [71] can be used to solve the matrix equation [24]. There is another method called the transfer matrix method which is more elegant than the former method. The transfer matrix method is also easy to implement in the program, so we will describe this method as follows.

We apply the boundary conditions by starting at the interface ρ_N which is the closest interface to the sources. The interface ρ_N separates the electromagnetic fields in the *N*th-CCL and the outer region. We will obtain two linear equations, where one equation is from the continuity of H_z and another equation is from the continuity of E_ϕ. Then, the two linear equations can be grouped as the matrix equation which relates the field coefficients in the *N*th-CCL and the outer region as follows

$$\begin{pmatrix} A_m^{(N)} \\ B_m^{(N)} \end{pmatrix} = \mathbf{T}_m^{(\text{out})} \begin{pmatrix} A_m^{(\text{out})} \\ I_m^{(\text{F})} \end{pmatrix}, \tag{2.46}$$

where $I_m^{(\text{F})}$ denotes the excitation from all sources emitting the cylindrical wave with the order *m* which is defined in the focusing process as

$$I_m^{(\text{F})} = \frac{i\pi}{2} \sum_{s=1}^{N} H_m^{(1)}\left(\rho_s' k_{\text{out}}\right) e^{-im\phi_s'}, \tag{2.47}$$

and the $\mathbf{T}_m^{(\text{out})}$ is the outer transfer matrix whose matrix elements are written as

$$T_m^{(\text{out})}(1,1) = \frac{i\pi\left(k_N\rho_N\right)}{2}\left[\frac{\varepsilon_{\text{out}}}{\varepsilon_N} H_m^{(1)}\left(k_{\text{out}}\rho_N\right) J_m'\left(k_N\rho_N\right) - \sqrt{\frac{\varepsilon_{\text{out}}}{\varepsilon_N}} H_m^{(1)\prime}\left(k_{\text{out}}\rho_N\right) J_m\left(k_N\rho_N\right)\right], \tag{2.48}$$

$$T_m^{(\text{out})}(1,2) = \frac{i\pi\left(k_N\rho_N\right)}{2}\left[\frac{\varepsilon_{\text{out}}}{\varepsilon_N} J_m\left(k_{\text{out}}\rho_N\right) J_m'\left(k_N\rho_N\right) - \sqrt{\frac{\varepsilon_{\text{out}}}{\varepsilon_N}} J_m'\left(k_{\text{out}}\rho_N\right) J_m\left(k_N\rho_N\right)\right], \tag{2.49}$$

$$T_m^{(\text{out})}(2,1) = -\frac{i\pi\left(k_N\rho_N\right)}{2}\left[\frac{\varepsilon_{\text{out}}}{\varepsilon_N} H_m^{(1)}\left(k_{\text{out}}\rho_N\right) H_m^{(1)\prime}\left(k_N\rho_N\right) - \sqrt{\frac{\varepsilon_{\text{out}}}{\varepsilon_N}} H_m^{(1)\prime}\left(k_{\text{out}}\rho_N\right) H_m^{(1)}\left(k_N\rho_N\right)\right], \tag{2.50}$$

$$T_m^{(\text{out})}(2,2) = -\frac{i\pi\left(k_N\rho_N\right)}{2}\left[\frac{\varepsilon_{\text{out}}}{\varepsilon_N} J_m\left(k_{\text{out}}\rho_N\right) H_m^{(1)\prime}\left(k_N\rho_N\right) - \sqrt{\frac{\varepsilon_{\text{out}}}{\varepsilon_N}} J_m'\left(k_{\text{out}}\rho_N\right) H_m^{(1)}\left(k_N\rho_N\right)\right]. \tag{2.51}$$

Next, we can move on to another interfaces between *j*th-CCL and (*j*+1)th-CCL where *j*=*N*-1,*N*-2,...,1. By applying the continuities of H_z and E_ϕ at these interfaces, we obtain the matrix equations which relate the field coefficients of the *j*th-CCL and those of the (*j*+1)th-CCL as follows

$$\begin{pmatrix} A_m^{(j)} \\ B_m^{(j)} \end{pmatrix} = \mathbf{T}_m^{(j,j+1)} \begin{pmatrix} A_m^{(j+1)} \\ B_m^{(j+1)} \end{pmatrix}. \tag{2.52}$$

The matrix elements of the inter-layer transfer matrix $\mathbf{T}_m^{(j,j+1)}$ are similar to those of $\mathbf{T}_m^{(\text{out})}$. They can be obtained by Eq. (2.48)-(2.51) with the substitutions $\varepsilon_{\text{out}} \to \varepsilon_{j+1}$, $k_{\text{out}} \to k_{j+1}$, $\varepsilon_N \to \varepsilon_j$, $k_N \to k_j$, and $\rho_N \to \rho_j$.

Lastly, we apply the continuities of H_z and E_ϕ at the interface ρ_c which separates the electromagnetic fields in the 1st-CCL and the inner region. The matrix equation obtained at this interface is written as follows

$$B_m^{(\text{in})} \begin{pmatrix} J_m\left(k_{\text{in}}\rho_c\right) \\ J_m'\left(k_{\text{in}}\rho_c\right) \end{pmatrix} = \mathbf{T}_m^{(\text{in})} \begin{pmatrix} A_m^{(1)} \\ B_m^{(1)} \end{pmatrix}, \tag{2.53}$$

where the matrix elements of the inner transfer matrix $\mathbf{T}_m^{(\text{in})}$ are given as

$$T_m^{(\mathrm{in})}(1,1) = \frac{\varepsilon_1}{\varepsilon_{\mathrm{in}}} H_m^{(1)}(k_1\rho_c), \tag{2.54}$$

$$T_m^{(\mathrm{in})}(1,2) = \frac{\varepsilon_1}{\varepsilon_{\mathrm{in}}} J_m(k_1\rho_c), \tag{2.55}$$

$$T_m^{(\mathrm{in})}(2,1) = \sqrt{\frac{\varepsilon_1}{\varepsilon_{\mathrm{in}}}} H_m^{(1)\prime}(k_1\rho_c), \tag{2.56}$$

$$T_m^{(\mathrm{in})}(2,2) = \sqrt{\frac{\varepsilon_1}{\varepsilon_{\mathrm{in}}}} J_m'(k_1\rho_c). \tag{2.57}$$

By using Eq. (2.46), (2.52), and (2.53), we can write the coefficient $B_m^{(\mathrm{in})}$ in terms of the coefficient $A_m^{(\mathrm{out})}$ and $I_m^{(\mathrm{F})}$ as

$$B_m^{(\mathrm{in})}\begin{pmatrix} J_m(k_{\mathrm{in}}\rho_c) \\ J_m'(k_{\mathrm{in}}\rho_c) \end{pmatrix} = \mathbf{T}_m^{(\mathrm{in})}\mathbf{T}_m^{(1,2)}\mathbf{T}_m^{(2,3)}\cdots\mathbf{T}_m^{(N-1,\mathrm{N})}\mathbf{T}_m^{(\mathrm{out})}\begin{pmatrix} A_m^{(\mathrm{out})} \\ I_m^{(\mathrm{F})} \end{pmatrix} = \mathbf{S}_m\begin{pmatrix} A_m^{(\mathrm{out})} \\ I_m^{(\mathrm{F})} \end{pmatrix}, \tag{2.58}$$

where $\mathbf{S}_m$ is the scattering matrix defined as

$$\mathbf{S}_m = \mathbf{T}_m^{(\mathrm{in})}\mathbf{T}_m^{(1,2)}\mathbf{T}_m^{(2,3)}\cdots\mathbf{T}_m^{(N-1,\mathrm{N})}\mathbf{T}_m^{(\mathrm{out})}. \tag{2.59}$$

Therefore, we can write the field coefficients $B_m^{(\mathrm{in})}$ and $A_m^{(\mathrm{out})}$ in terms of the matrix elements of the scattering matrix and the excitation parameter by solving Eq. (2.58), then we have

$$A_m^{(\mathrm{out})} = \left[\frac{S_m(2,2)J_m(k_{\mathrm{in}}\rho_c) - S_m(1,2)J_m'(k_{\mathrm{in}}\rho_c)}{S_m(1,1)J_m'(k_{\mathrm{in}}\rho_c) - S_m(2,1)J_m(k_{\mathrm{in}}\rho_c)}\right] I_m^{(\mathrm{F})}, \tag{2.60}$$

and

$$B_m^{(\mathrm{in})} = \left[\frac{\det(\mathbf{S}_m)}{S_m(1,1)J_m'(k_{\mathrm{in}}\rho_c) - S_m(2,1)J_m(k_{\mathrm{in}}\rho_c)}\right] I_m^{(\mathrm{F})}. \tag{2.61}$$

The field coefficients in the *N*th-CCL are obtained by $A_m^{(\mathrm{out})}$ by using Eq. (2.46), and then these field coefficients yield the solutions of the remaining field coefficients via Eq. (2.50). Therefore, all field coefficients are completely determined. It is useful to note that the scattering matrix satisfies the relation $\mathbf{S}_{-|m|} = (-1)^{|m|}\mathbf{S}_{|m|}$ which results from the identity $\zeta_{-|m|} = (-1)^{|m|}\zeta_{|m|}$ where ζ denotes the Bessel function or the Hankel function of the first kind. These relations are required when one implements the program because both positive and negative orders must be taken into account.

The intensity distribution

From the analytical solutions of the electromagnetic fields, we can compute the time-averaged intensity from the time-averaged Poynting vector $\mathbf{S} = (1/2)\mathrm{Re}(\mathbf{E}\times\mathbf{H}^*)$. The inner and outer regions of the CHs are defined as vacuum. The innermost radius is defined as 100 nm. The CHs is made by alternating Ag/insulator CCLs in which the innermost layer is the insulator CCL. The thickness of each CCL is 10 nm, the number of CCLs is 10, and thus the outermost radius is 200 nm. Two point sources are located at the outermost radius, one is at $\phi' = \pi/4$ and another is at $\phi' = 3\pi/4$. The two point sources have the same strength and radiate at the wavelength 368 nm. The dielectric constant of Ag at this wavelength from the Drude model with neglecting the size effect is -3.11+0.123*i* [72]. The dielectric constant of the insulator is chosen as 3.2 so that effective dielectric constants from the

effective medium approximation are about $\varepsilon_\rho = -72.949 + 108.444i$ and $\varepsilon_\phi = 0.045 + 0.062i$. The real part of the effective dielectric constants from the hyperbolic dispersion with no caustic (type I) [19].

Fig. 2.6(a) shows the intensity profiles along the innermost curve $\rho = \rho_c$ in the inner region for different number of orders. It can be seen that the intensity converges quickly as the number of order reaches 40. The calculation of the field profile takes less than a minute to compute even in the case of high number of orders. Fig. 2.6(b) shows the comparison between the analytical intensity profile and the FDTD intensity profiles. It can be seen that the FDTD intensity profiles approach the

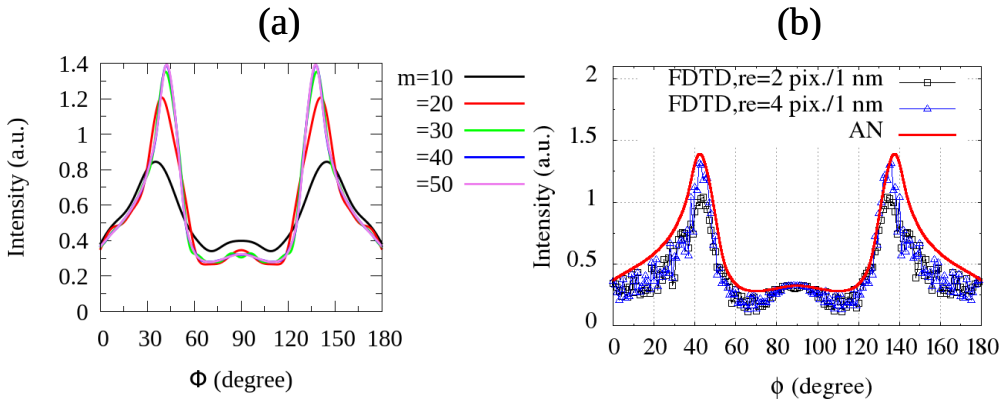

Fig. 2.6. (a) Analytical intensity profiles along the innermost curve of the focusing CHs with increasing the number of orders. The parameters of the CHs can be seen in the main text. (b) Comparison between the analytical intensity profile with the number of order 110 and the FDTD intensity profiles with the resolutions 2 and 4 pix/nm.

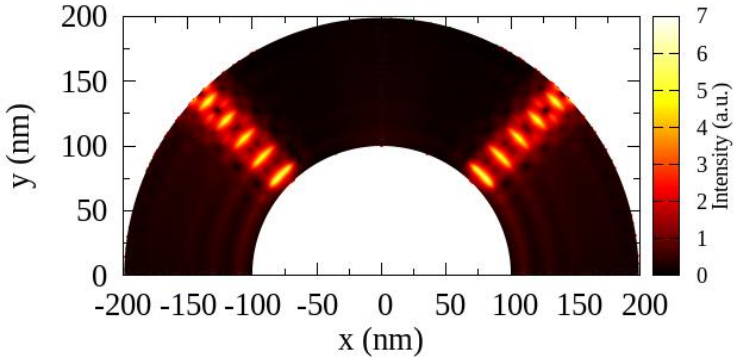

Fig. 2.7. The intensity distribution in focusing CHs. The CHs has the same parameters as Fig. 2.6.

analytical intensity profile by increasing the resolutions from 2 pix/nm to 4 pix/nm. The FDTD simulations are performed on a single PC computer with the Intel(R) Core(M) i7-3970X CPU @ 3.50GHz, and the simulation times for 2 and 4 pix/nm are about 4 hours and more than a day, respectively. Therefore, we obtain the consistent results with FDTD simulation, but our solutions are more efficient than the FDTD simulation.

We also notice that the angular locations of the peaks deviate from the angular locations of the sources by 2.78 degree. This behaviour can be clearly seen in the intensity distribution in the CHs shown in Fig. 2.7. The bright spots between Ag and insulator layers correspond to the surface plasmon excitations. The surface plasmons are found to located only within narrow strip. From the deviation angle 2.78, the angle of the cone with respect to the radial axis passing through the source becomes

2.77 degree according to simple geometrical consideration. However, the effective medium approximation gives the critical angle of the large wavevectors relative to the radial axis denoted as α_c equal to 88.65 degree from the condition $\mathrm{Re}\left(\varepsilon\left(\alpha_c\right)\right)=0$ where $\varepsilon\left(\alpha\right)$ is defined as follows [21]

$$\varepsilon\left(\alpha\right)=\frac{\varepsilon_\rho\varepsilon_\phi}{\varepsilon_\rho\cos^2\alpha+\varepsilon_\phi\sin^2\alpha}. \tag{2.62}$$

The critical angle of the energy flow θ_c (the Poynting vector) relative to the radial axis is obtained by the relation [21]

$$\theta_c=\tan^{-1}\left(\mathrm{Re}\left(\varepsilon_\phi/\varepsilon_\rho\right)\tan\left(\alpha_c\right)\right). \tag{2.63}$$

Then, the θ_c becomes 0.48 degree. Therefore, the analytical solution gives the critical angle of energy flow almost 6 times larger than predicted by the simple effective medium approximation. By reducing thickness of each CCL and keeping the total number of layers, we expect that the critical angle of the energy flow will converge to the value predicted by the effective medium approximation. We reduce the thickness of each CCL to 1 nm, and keep all remaining parameters. The intensity profile along the innermost curve $\rho=\rho_c$ in the inner region taking into account the maximum of orders 100 is shown in Fig. 2.8. According to this figure, the deviation angle from the radial line passing through the source is only 0.12 degree which leads to the critical angle of the energy flow 0.60 degree. The value of the critical angle of energy flow obtained by the analytical solution becomes close to that obtained by the effective medium approximation which is equal to 0.48 degree. Therefore, the analytical solutions are consistent with the FDTD simulation and also yield satisfying results comparing with the effective medium approximation.

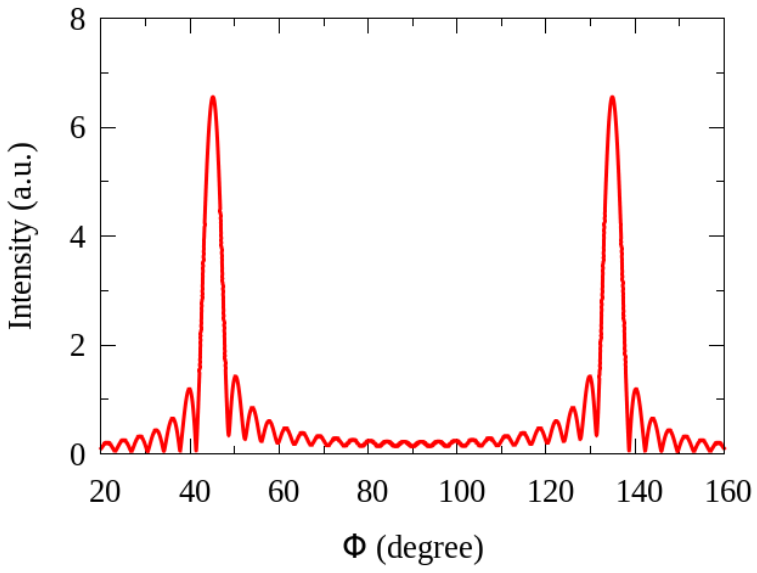

Fig. 2.8. The intensity profile of focusing CHs with ultrathin CCL thickness 1 nm.

2.3.2 Magnifying process

The schematic view of the CHs in the magnifying process is shown in Fig. 2.9. In this case, the sources are located inside the core region. The sources correspond to subwavelength objects that we want to magnify to be larger than the diffraction limit so that the conventional microscope can detect them in the far-field.

In this process, the core region is the source region. The solutions of the electromagnetic fields in this process can be obtained by those in the focusing process. The solutions in the outer region will now have only the scattering solutions. The contributions from the free solutions will appear in the core region, and we write the solutions in this region as the summation between the free and scattering solutions. Finally, the solutions inside the *j*th-CCL, where *j*=1,2,...,*N*, are the same as those in the focusing process, respectively. The field coefficients in all regions, however, will be modified by applying the boundary condition.

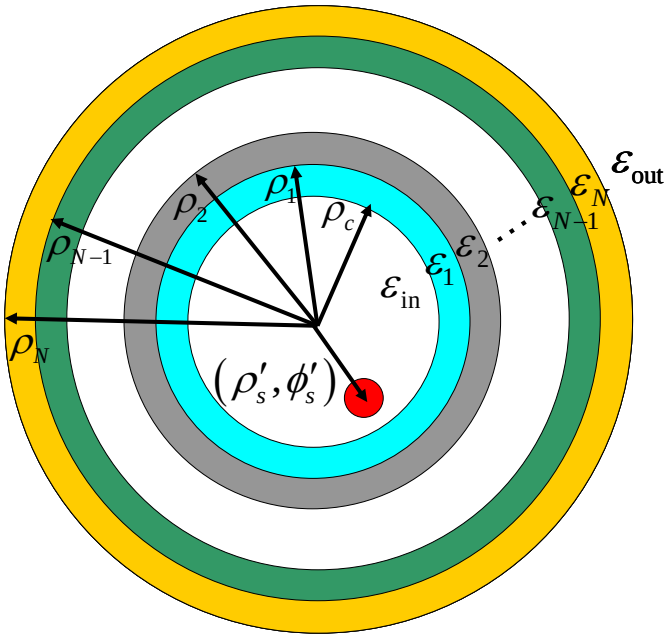

Fig. 2.9. Schematic view of magnifying hyperlens with sources located in the core region.

Obtaining field coefficients

We obtain the field coefficients using the transfer matrix method similar to the focusing process. We start by imposing the continuities of H_z and E_ϕ to the innermost interface ρ_c which is the interface closest to the sources. Then, we can write the matrix equation which relates the field coefficients of the core and the 1st-CCL as

$$\begin{pmatrix} A_m^{(1)} \\ B_m^{(1)} \end{pmatrix} = \mathbf{T}_m^{(\text{in})} \begin{pmatrix} B_m^{(\text{in})} \\ I_m^{(\text{M})} \end{pmatrix}, \tag{2.64}$$

where $\mathbf{T}_m^{(\text{in})}$ is inner transfer matrix for the magnifying process whose matrix elements are defined as

$$T_m^{(\mathrm{in})}(1,1)=\frac{i\pi k_1\rho_c}{2}\left[\frac{\varepsilon_{\mathrm{in}}}{\varepsilon_1}J_m(k_{\mathrm{in}}\rho_c)J_m'(k_1\rho_c)-\sqrt{\frac{\varepsilon_{\mathrm{in}}}{\varepsilon_1}}J_m'(k_{\mathrm{in}}\rho_c)J_m(k_1\rho_c)\right], \tag{2.65}$$

$$T_m^{(\mathrm{in})}(1,2)=\frac{i\pi k_1\rho_c}{2}\left[\frac{\varepsilon_{\mathrm{in}}}{\varepsilon_1}H_m^{(1)}(k_{\mathrm{in}}\rho_c)J_m'(k_1\rho_c)-\sqrt{\frac{\varepsilon_{\mathrm{in}}}{\varepsilon_1}}H_m^{(1)\prime}(k_{\mathrm{in}}\rho_c)J_m(k_1\rho_c)\right], \tag{2.66}$$

$$T_m^{(\mathrm{in})}(2,1)=-\frac{i\pi k_1\rho_c}{2}\left[\frac{\varepsilon_{\mathrm{in}}}{\varepsilon_1}J_m(k_{\mathrm{in}}\rho_c)H_m^{(1)\prime}(k_1\rho_c)-\sqrt{\frac{\varepsilon_{\mathrm{in}}}{\varepsilon_1}}J_m'(k_{\mathrm{in}}\rho_c)H_m^{(1)}(k_1\rho_c)\right], \tag{2.67}$$

$$T_m^{(\mathrm{in})}(2,1)=-\frac{i\pi k_1\rho_c}{2}\left[\frac{\varepsilon_{\mathrm{in}}}{\varepsilon_1}H_m^{(1)}(k_{\mathrm{in}}\rho_c)H_m^{(1)\prime}(k_1\rho_c)-\sqrt{\frac{\varepsilon_{\mathrm{in}}}{\varepsilon_1}}H_m^{(1)\prime}(k_{\mathrm{in}}\rho_c)H_m^{(1)}(k_1\rho_c)\right], \tag{2.68}$$

and the parameter $I_m^{(\mathrm{M})}$ denotes the excitation from all sources emitting the cylindrical wave with the order *m* which is defined in the magnifying process as

$$I_m^{(\mathrm{M})}=\frac{i\pi}{2}\sum_{s=1}^{N}J_m(\rho_s'k_{\mathrm{in}})e^{-im\phi_s'}\ . \tag{2.69}$$

We notice that the excitation parameter in the focusing process is a function of the Hankel function of the first kind, while the excitation parameter in the magnifying process is a function of the Bessel function.

Similarly, the matrix equation obtained by applying the continuities of H_z and E_ϕ at the interface ρ_j is written as

$$\begin{pmatrix}A_m^{(j+1)}\\B_m^{(j+1)}\end{pmatrix}=\mathbf{T}_m^{(j+1,j)}\begin{pmatrix}A_m^{(j)}\\B_m^{(j)}\end{pmatrix}, \tag{2.70}$$

where $\mathbf{T}_m^{(j+1,j)}$ is the inter-layer transfer matrix for the magnifying process whose matrix elements are defined as

$$T_m^{(j+1,j)}(1,1)=\frac{i\pi k_{j+1}\rho_j}{2}\left[\frac{\varepsilon_j}{\varepsilon_{j+1}}H_m^{(1)}(k_j\rho_j)J_m'(k_{j+1}\rho_j)-\sqrt{\frac{\varepsilon_j}{\varepsilon_{j+1}}}H_m^{(1)\prime}(k_j\rho_j)J_m(k_{j+1}\rho_J)\right], \tag{2.71}$$

$$T_m^{(j+1,j)}(1,2)=\frac{i\pi k_{j+1}\rho_j}{2}\left[\frac{\varepsilon_j}{\varepsilon_{j+1}}J_m(k_j\rho_j)J_m'(k_{j+1}\rho_j)-\sqrt{\frac{\varepsilon_j}{\varepsilon_{j+1}}}J_m'(k_j\rho_j)J_m(k_{j+1}\rho_J)\right], \tag{2.72}$$

$$T_m^{(j+1,j)}(2,1)=-\frac{i\pi k_{j+1}\rho_j}{2}\left[\frac{\varepsilon_j}{\varepsilon_{j+1}}H_m^{(1)}(k_j\rho_j)H_m^{(1)\prime}(k_{j+1}\rho_j)-\sqrt{\frac{\varepsilon_j}{\varepsilon_{j+1}}}H_m^{(1)\prime}(k_j\rho_j)H_m^{(1)}(k_{j+1}\rho_J)\right], \tag{2.73}$$

$$T_m^{(j+1,j)}(2,2)=-\frac{i\pi k_{j+1}\rho_j}{2}\left[\frac{\varepsilon_j}{\varepsilon_{j+1}}J_m(k_j\rho_j)H_m^{(1)\prime}(k_{j+1}\rho_j)-\sqrt{\frac{\varepsilon_j}{\varepsilon_{j+1}}}J_m'(k_j\rho_j)H_m^{(1)}(k_{j+1}\rho_J)\right]. \tag{2.74}$$

Lastly, the field coefficients of the outer region are related by the field coefficients of the *N*th-CCL by the following matrix equation

$$A_m^{(\mathrm{out})}\begin{pmatrix}H_m^{(1)}(k_{\mathrm{out}}\rho_N)\\H_m^{(1)\prime}(k_{\mathrm{out}}\rho_N)\end{pmatrix}=\mathbf{T}_m^{(\mathrm{out})}\begin{pmatrix}A_m^{(N)}\\B_m^{(N)}\end{pmatrix}, \tag{2.75}$$

where $\mathbf{T}_m^{(\mathrm{out})}$ is the outer transfer matrix whose matrix elements are defined as follows

$$T_m^{(\mathrm{out})}(1,1)=\frac{\varepsilon_N}{\varepsilon_{\mathrm{out}}}H_m^{(1)}(k_N\rho_N), \tag{2.76}$$

$$T_m^{(\mathrm{out})}(1,2)=\frac{\varepsilon_N}{\varepsilon_{\mathrm{out}}}J_m(k_N\rho_N), \tag{2.77}$$

$$T_m^{(\mathrm{out})}(2,1) = \sqrt{\frac{\varepsilon_N}{\varepsilon_{\mathrm{out}}}} H_m^{(1)\prime}(k_N \rho_N), \tag{2.78}$$

$$T_m^{(\mathrm{out})}(2,2) = \sqrt{\frac{\varepsilon_N}{\varepsilon_{\mathrm{out}}}} J_m'(k_N \rho_N). \tag{2.79}$$

Now, we can multiply all transfer matrices together and define the scattering matrix $\mathbf{S}_m$ as follows

$$\mathbf{S}_m = \mathbf{T}_m^{(\mathrm{out})} \mathbf{T}_m^{(N,N-1)} \cdots \mathbf{T}_m^{(2,1)} \mathbf{T}_m^{(\mathrm{in})}, \tag{2.80}$$

and the analytical solutions of $B_m^{(\mathrm{in})}$ and $A_m^{(\mathrm{out})}$ are written in terms of the matrix elements of $\mathbf{S}_m$ as

$$B_m^{(\mathrm{in})} = \left\{ \frac{S_m(2,2) H_m^{(1)}(k_{\mathrm{out}} \rho_N) - S_m(1,2) H_m^{(1)\prime}(k_{\mathrm{out}} \rho_N)}{S_m(1,1) H_m^{(1)\prime}(k_{\mathrm{out}} \rho_N) - S_m(2,1) H_m^{(1)}(k_{\mathrm{out}} \rho_N)} \right\} I_m^{(\mathrm{M})}, \tag{2.81}$$

$$A_m^{(\mathrm{out})} = \left\{ \frac{\det(\mathbf{S}_m)}{S_m(1,1) H_m^{(1)\prime}(k_{\mathrm{out}} \rho_N) - S_m(2,1) H_m^{(1)}(k_{\mathrm{out}} \rho_N)} \right\} I_m^{(\mathrm{M})}. \tag{2.82}$$

The remaining field coefficients are automatically obtained from $B_m^{(\mathrm{in})}$ and $A_m^{(\mathrm{out})}$ by using the transfer matrices.

The intensity distribution

We use the CHs with the same parameters as those of the focusing process but now with two sources located inside the core region at the innermost interface ρ_c and with angular distance λ/3.2=115 nm between them. That means $(\rho_1', \phi_1') = (\rho_c, 57.05^\circ)$ and $(\rho_2', \phi_2') = (\rho_c, 122.95^\circ)$. The intensity profiles along the curve $\rho = 185$ nm in the outer region obtained by the analytical solutions with increasing number of orders are shown in Fig. 2.10(a). It can be seen that the solutions are converged at the number of order equal to 40. It must be note that the orders needed for the convergence increase as the radial distance of the observational curve approaches that of the sources. The analytical intensity profile is compared with the intensity profile obtained from the FDTD simulation in Fig. 2.10(b). Two dominant peaks due to the excitation of the surface plasmons are consistent between the analytics and FDTD simulation. In the angular region about 90 degree, the FDTD intensity profiles deviate from the analytical profile. However, we notice that the FDTD curves tend to approach analytical curve by increasing the resolution. Therefore, we expect that the FDTD simulation will also be consistent with analytics by increasing more resolution. The simulation time of the FDTD simulation with resolution 4 pix/nm is more than a day. If the resolution will be increased more, it would take several days to obtain accurate solutions. Therefore, the analytical solutions give

highly efficient tool to analyze electromagnetic fields in the magnifying CHs because it takes a few minute to compute the intensity profiles.

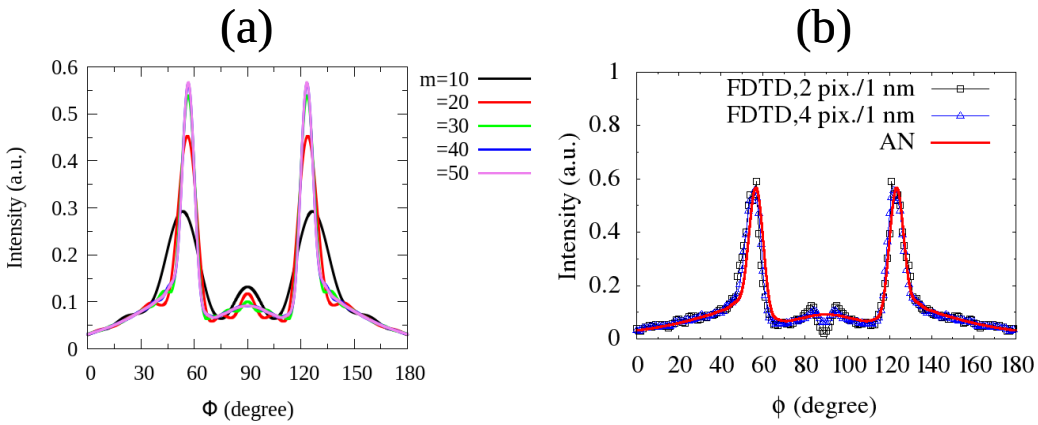

Fig. 2.10. (a) Analytical intensity profiles along the curve $\rho = 185$ nm inside an insulator layer with increasing the number of orders from 10 to 50. (b) Comparison between the analytical intensity profile with the number of orders 110 indicated by the red line and the intensity profiles obtained by FDTD simulation with resolutions 2 and 4 pix/nm which are indicated in the figure along the same curve as Fig. (a).

Next, we plot the analytical intensity distribution within all CCLs of this magnifying CHs in Fig. 2.11(a). The intensity distribution obtained by the FDTD simulation yields the same distribution as that obtained by the analytic, and thus we show only the analytical intensity distribution. According to this figure, the surface plasmons between Ag/Insulator interfaces are weakly excited, and their intensities decrease as they propagate outward. This situation is different from the focusing process as shown in Fig. 2.7. where the surface plasmon excitations are clearly seen and move to the core without decaying. The reason for this difference is the different locations of the sources relative to the first interface of excitation. In the case of focusing process, the sources directly excite surface plasmons at the interface between the unbound air medium and Ag layer. However, in the case of magnifying process, the sources excite the surface plasmons at the interface between insulator and Ag layers which is located 10 nm from the sources. Therefore, the surface plasmon excitations in the latter case are weaker than the former case. We show the evidence for this explanation by swapping the order of Ag and insulator CCLs in the magnifying CHs so that the Ag layer becomes the innermost layer, and then the surface plasmons at the interface between the air core and Ag layer are excited by the sources. The intensity distribution from this swapped-magnifying CHs is shown in Fig. 2.11(b). It can be seen that the intensity envelops appear at the interfaces between Ag and insulator layers which correspond to the surface plasmons. However, the intensity still decreases as the radial distance increases. Is it because of loss? The answer is yes, but the loss is not the dominant contribution to the decay of surface plasmons in the magnifying process. If it was, the surface plasmons in the focusing process would also suffer the same fate, but they don't as we have already seen. The main reason for the decrease of intensity as radial distance increases is the magnifying mechanism. Let's us neglect the loss in Ag, and then draw the intensity distribution in the magnifying CHs with the same parameters as those in Fig. 2.11(b) excepting the dielectric constant of Ag (dielectric constant of Ag becomes -3.11). The analytical

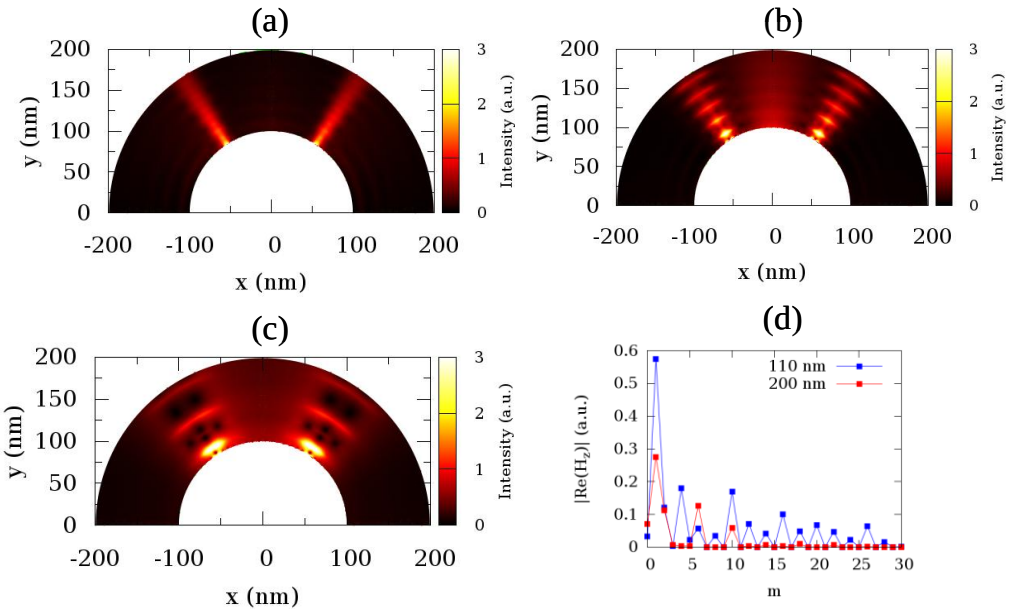

Fig. 2.11. (a) Analytical intensity distribution in magnifying CHs with the same parameters as those in Fig. where the innermost layer is an insulator. The number of order is 80. (b) Analytical intensity distribution in magnifying CHs with the same parameters as Fig. (a) but the order of Ag and insulator layers is swapped so that the innermost layer becomes Ag. (c) Analytical intensity distribution in magnifying CHs with the same structure as Fig. (b) but the loss in Ag is neglected. (d) Amplitude of real part of magnetic field corresponding to each diffraction order *m* determined at the peak positions of surface plasmons localized along the curves $\rho = 110$ nm and $\rho = 200$ nm.

intensity distribution in this loss-free magnifying CHs is shown in Fig. 2.11(c). The bright spots in this figure correspond to the surface plasmons. The intensity of surface plasmons decrease as they propagate outward although there is no loss in the CHs. This behaviour can be explained as follows. The magnifying process requires the conservation of angular momentum corresponding to each order, that is $m = k_\phi \rho$, where k_ϕ is tangential component of wavevector [19]. Therefore, the high order m which contribute to the surface plasmons will have smaller k_ϕ as the radial distance ρ increases. The smaller k_ϕ is then matched with that of the smaller order m. In this way, the energy from high order is transformed into lower order. This results in the decrease of electric field corresponding to the high orders which undergo the transformation, and thus the intensity of surface plasmons appear fainter, and their sizes become larger. The magnified electromagnetic waves can propagate to the far-field if they have k_ϕ smaller than wavenumber in the vacuum, but they will be reflected back, undergo reverse-magnifying process, and interfere with other electromagnetic waves if they have k_ϕ larger than wavenumber in the vacuum. The interferences generate the dark spots which also appear in Fig. 2.11(c). Fig. 2.11(d) shows the contribution of each diffraction order to the magnetic field H_z at the intensity peak positions of surface plasmons along the curved $\rho = 110$ nm and $\rho = 200$ nm in Fig. 2.11(c). At the peak position of the curve $\rho = 110$ nm which is close to the sources, some high diffraction modes and also small diffraction modes are generated. The high diffraction modes are subjected to the magnifying process as the radial distance increase, and thus the magnetic fields corresponding to these modes at the peak position of the curve $\rho = 200$ nm are suppressed. Surprisingly, at *m*=6, the magnetic

field of the curve $\rho = 200\,\text{nm}$ exceeds that of the curve $\rho = 110$ nm. This means that some part of energies from high diffraction modes are transformed into this lower order mode. The fundamental diffraction mode of the curve $\rho = 200\,\text{nm}$ is also found to be slightly larger than that of the curve $\rho = 110$ nm which also indicates the transformation of energy into the lower mode.

2.4 Subwavelength focusing in optical band

We apply the analytical solutions of the focusing CHs to optimize the subwavelength focusing of two point sources generated by subwavelength double slits. The focusing CHs comprise alternating SiO_2/Ag CCLs with the SiO_2 layer being the innermost layer. The working wavelength is 465 nm, and the dielectric constants of Ag and SiO_2 at this wavelength are -7.82+0.247i and 2.1, respectively [8,18]. According to the effective medium approximation, the effective dielectric constants become $\varepsilon_\rho = 5.74 + 0.0665i$ and $\varepsilon_\phi = -2.86 + 0.124i$. The real part of the effective dielectric constants form hyperbolic dispersion with caustic which means that the radial component of wavevectors can change sign (type II). The critical angle of the wavevector α_c obtained by Eq. (2.62) is 54.76 degree, and the critical angle of energy flow obtained by applying Eq. (2.63) becomes 35.18 degree. The geometrical parameters of the CHs are defined as : inner radius $\rho_c = 500\,\text{nm}$, and thickness of each CCL 2 nm.

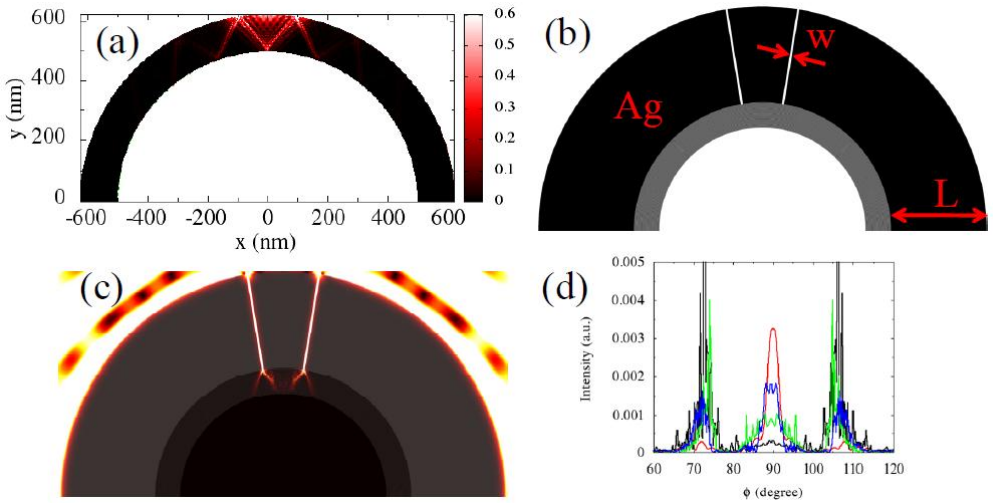

Fig. 2.12. (a) The analytical intensity distribution in the focusing CHs with the number of order 220. The angular distance between two point sources which are located at the outermost interface is 200 nm. The remaining parameters of the CHs can be seen in the main text. (b) The realistic structure comprising subwavelength double slits with slit width 10 nm perforated in Ag screen with thickness 465 nm and the same CHs as Fig. (a) without the point sources. The double slits are equivalent to the two point sources in Fig. (a). (c) FDTD intensity distribution with the resolution 1.5 pix/nm in the structure of Fig. (b). The external radiation is p-polarized light and wavelength 465 nm. (d) The intensity profiles along the innermost curve ($\rho_c = 500\,\text{nm}$) obtained by the analytical solutions (red line) for the structure shown in Fig. (a) and the FDTD simulation for the structure shown in Fig. (b) and (c) with the resolutions 0.5, 1.0, and 1.5 pix/nm, indicated by the black, green, and blue lines, respectively.

The core and outer regions are vacuum. Now, we don't fix the number of CCLs, but we will optimize it instead. We will optimize the number of CCLs so that the constructive interference is obtained at the

location $(\rho_c, \pi/2)$ in the core region. The angular distance between two point sources is kept as $d = 200$ nm, and they are always located at the outermost interface. This means that their radial distances are changed by varying the number of CCLs, and their azimuthal angles are also changed according to the radial distance and the angular separation distance $(\phi_1' = \pi/2 - d/(2\rho_N), \phi_2' = \pi - \phi_1')$. We find that the number of CCLs must be equal to 61 in order to obtain the focal spot at $(\rho_c, \pi/2)$. This condition is also obtained by varying the number of orders. If the number of order is too small, the width of the focal spot is wide and the intensity is weak. However, the width of the focal spot is narrower and the intensity increases by increasing the number of orders. The number of orders 160 leads to the convergence of the intensity profile along the innermost curve, and this analytical intensity profile is shown by the red line in Fig. 2.12(d). The intensity distribution with the number of orders 220 is shown in Fig. 2.12(a) where the directional propagation can be seen. According to Fig. 2.12(d), the full width at half maximum (FWHM) of the analytical intensity profile is about 28.6 nm or λ/16.26 which is much smaller than the wavelength of light. The Poynting vector at the peak position directly points to the origin. The intensity peak however suffers the loss in the CHs, and therefore the FWHM is limited [21]. The intensity peak is split by changing the number of CCLs because the positions of the point sources are shifted simultaneously resulting in the change in direction of energy flow. Therefore, we can optimize the parameters such as the innermost radius, the thickness of each CCL, the number of CCLs, and the separation distance between two point sources to obtain the focal spot at desired location. The structure comprising the thick Ag screen perforated by double slits and the same CHs as Fig. 2.12(a) is simulated by FDTD simulation to confirm that our analytical solutions can be realized in real structure. The structure is shown schematically in Fig. 2.12(b) where the slit width and the Ag screen thickness are defined as 10 nm and 465 nm, respectively. The output side of the slits perfectly touch the outermost interface of the CHs with the same angular distance as that between the point sources in Fig. 2.12(a). The far-field excitation with p-polarization and wavelength 465 nm impinges on the whole structure so that the slits become secondary sources which behave like point sources able to excite high diffraction modes in the CHs to propagate directionally in the CHs as shown in Fig. 2.12(c). The intensity profiles along the innermost curve from FDTD simulation with the resolution 0.5, 1.0, and 1.5 pix/nm are shown by the black, green, and blue lines, respectively, in Fig. 2.12(d). The FDTD simulation times are about 30 minutes, 6 hours, and 13 hours for the FDTD resolutions 0.5, 1.0, and 1.5 pix/nm, respectively, while the calculation time of the analytical intensity profile is in a few minutes using the angular interval 0.01 degree. According to Fig. 2.12(d), the FDTD intensity profiles approach the analytical intensity profile by increasing the resolutions. This means that our analytical solutions yield the most accurate intensity profiles and they are also very efficient because it takes relatively short period of time to obtain the results using the analytical solutions.

2.5 Enhancement of the magnifying resolution in UV band

After the first experimental demonstration of the CHs made by alternating Ag and Al_2O_3 at the wavelength 365 nm by Z. Liu et al (2007) [20], the magnifying resolution of the CHs working at this wavelength is still restricted to 130 nm (λ/2.8) since then [90]. This implies the lack of the efficient methods to optimize the magnifying CHs even though the fabrication technology is already available. Therefore, it is always said that the magnifying CHs can magnify the "small object" into the far-field image, without knowing how really small the object can be. With the advent of our analytical solutions, we show in this section that the magnifying resolutions of these CHs can be enhanced by (i) reducing the thickness of each CCL and the inner radius of the CHs, and (ii) increasing the number of CCL. The CHs can possibly magnify the object with size 20 nm (λ/18) into the far-field. However, this CHs requires 1 nm thickness of the CCL and 2000 numbers of the CCL due to the intrinsic loss in the Ag. Therefore, another negative dielectric constant material with smaller loss than that of Ag is required if we want to magnify the object with size smaller than 20 nm at this wavelength.

Here, we describe the optimization method. The testing objects are two point sources separated by the subwavelength distance (the distance smaller than λ). In air, the two point sources cannot be resolved in the far-field because of the decay of the large wavevector waves which contain the information about the subwavelength distance. However, by putting the two point sources inside the core of the CHs and sit on the innermost radius of the CHs, the distance between the two point sources, which we call the image, can be enlarged to be larger than λ, and then the image can propagate to the far-field. We observe the image on the far-field plane at the radial distance 2λ from the outermost interface of the CHs. We vary the inner radius denoted as ρ_c, the thickness of each CCL denoted as d and the number of CCL denoted as N until we obtain the resolved image on the far-field observing plane. The inner core is defined as air, and the outer region is defined as the quartz with the dielectric constant 2.174. The CHs is made by alternating Ag and Al_2O_3 CCLs. The dielectric constants of these materials at λ=365 nm are -2.4012+0.2488i and 3.217, respectively [20]. They form the type-I hyperbolic metamaterials because the tangential component of the dielectric constant is positive that is $\varepsilon_\phi = 0.4079 + 0.1244i$, and the normal component of the dielectric constant is negative that is $\varepsilon_\rho = -16.7786 + 7.0793i$ according to the conventional effective medium approximation. Therefore, these medium support the propagation of large wavevetor waves. As the large wavevecor waves propagate outward, their tangential component wavevectors shrink due to the conservation of the angular momentum $m = k_\phi \rho$. Therefore, the near-field image can be transformed into the far-field image if the CHs is properly designed.

The results of the intensity distributions and the far-field intensity profiles are shown in Fig. 2.13. We start from the relatively large separation distance (along the x-axis) of the two point sources defined as 150 nm (λ/2.43) whose intensity distribution is shown in Fig. 2.13 (a). The white colour indicates the large intensity and the black colour indicates the small intensity. The geometry of this CHs is optimized as ρ_c=475 nm, d=30 nm, and N=50. It can be seen that the image is magnified as it propagates outward. Fig. 2.13 (b) shows the intensity profile in the far-field plane from this CHs. The two point sources are clearly resolved in the far-field.

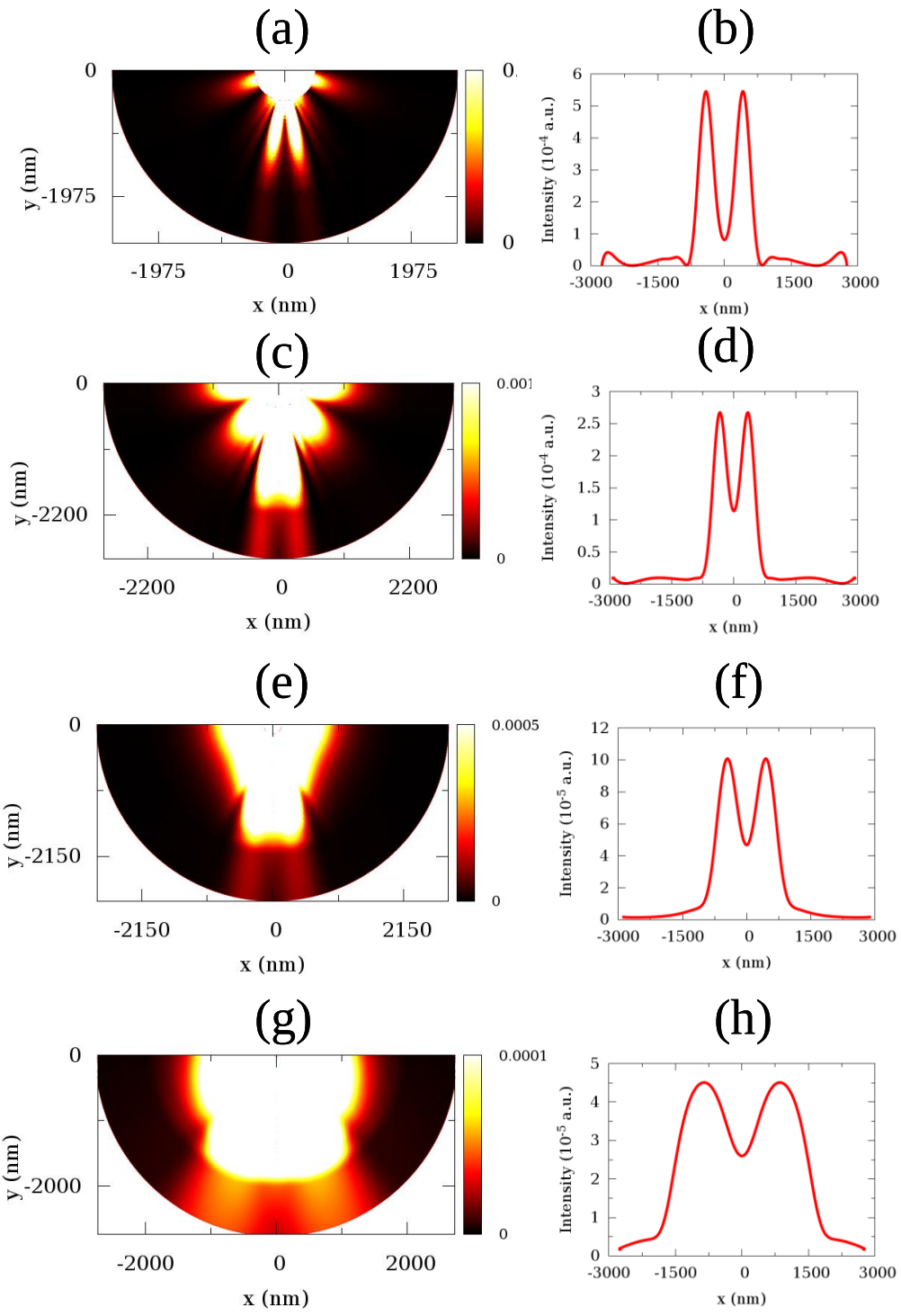

Fig. 2.13. Intensity distribution in the magnifying hyperlens with two point sources separated by the distance (a) 150 nm, (c) 100 nm, (e) 50 nm, and (g) 20 nm, along the *x*-axis. The parameters of the hyperlens are optimized as (a) : ρ_c=475 nm, *d*=30 nm, *N*=50; (c) : ρ_c=400 nm, *d*=20 nm, *N*=90 ; (e) : ρ_c=150 nm, *d*=5 nm, *N*=400; (g) : ρ_c=30 nm, *d*=1 nm, *N*=2000. The intensity profiles at the radial distance 2λ from the outermost interface ρ_N of the hyperlens (a), (c), (e), and (g), are shown in Fig. (b), (d), (f), and (h), respectively. $x=(\rho_N+2\lambda)\cos\phi$ where $\pi \le \phi \le 2\pi$. The wavelength λ is 365 nm.

The size of the image is 843 nm which is larger than the wavelength and about 5.62 times larger than the separation distance between the two point sources. Next, we reduce the separation distance between the point sources to 100 nm (λ/3.65). We need to reduce the inner radius to ρ_c=400 nm and the thickness of each CCL to d=20 nm because the point sources generate larger wavevectors or shorter effective wavelengths. Moreover, we also need to increase the number of CCL to N=90 in order to increase the magnification of the CHs. Fig. 2.13 (c) shows the intensity distribution for the separation distance between the point sources 100 nm (λ/3.65). The image can be magnified into the far-field but the intensity outside the CHs becomes smaller than the intensity inside the CHs because of higher loss in the CHs. Fig. 2.13 (d) shows the intensity profile along the far-field plane from the intensity distribution in Fig. 2.13 (c). The two point sources are clearly resolved. The size of the image is 674 nm which is larger than the wavelength of light and about 6.74 times larger than the distance between the two point sources. We can reduce the separation distance between the point sources further to 50 nm (λ/7.3), and the geometry of the CHs required to resolve these point sources in the far-field is ρ_c=150 nm, d=5 nm, and N=400. The intensity distribution of the 50 nm separation distance (λ/7.3) is shown in Fig. 2.13 (e). The image can be magnified into the far-field but the transmitted intensity becomes much smaller than the intensity inside the CHs. Fig. 2.13 (f) shows the intensity profile along the far-field plane from the intensity distribution in Fig. 2.13 (e). The two point sources are clearly resolved in the far-field. The size of the image is 900 nm which is larger than the wavelength of light and about 18 times larger than the separation distance between the point sources. Lastly, we reduce the separation distance between the point sources to just 20 nm (λ/18.25). We need to reduce the inner radius to ρ_c=30 nm and also the thickness of each CCL to d=1 nm. Moreover, the number of CCL is required to be N=2000. The intensity distribution for this case is shown in Fig. 2.13 (g). The image can still be magnified into the far-field, but the transmitted intensity is very small comparing to the intensity inside the CHs. Fig. 2.13 (h) shows the intensity profile along the far-field plane from the intensity distribution in Fig. 2.13 (g). The two point sources are still resolved. The contrast between the image signal and the background signal (intensity between two peaks) is poorer than those of the larger distances between the point sources. The size of the image is 1706 nm which is larger than the wavelength of light and about the 85.3 times larger than the separation distance between the point sources. Therefore, we obtain the magnifying resolution λ/18.25. It is obvious that the automatic fabrication technique is required to achieve the better magnifying resolution by depositing high number of CCL with small thickness. Note that we assume the size-independent dielectric constants of the Ag. However, the free electrons can scatter with the interfaces of the structure and thus the additional loss is introduced into the dielectric constant [91]. The additional loss may deteriorate the magnifying resolution. Therefore, the magnifying resolution of around 20 nm (λ/18.25) may be the highest magnifying resolution that can be achieved by using the Ag at this wavelength because we cannot reduce the thickness further and the presence of the additional loss due to the size-effect on the dielectric constant of the Ag hampers the propagation of the image signal.

2.6 Conclusion

We have successfully formulated the analytical solutions of electromagnetic fields in focusing and magnifying cylindrical hyperlens (CHs) comprising concentric cylindrical layers (CCLs) by applying the Green's function analysis. The analytical solutions are consistent with FDTD simulations, but they give more accurate results and more efficient than the FDTD simulation. The optimization of the CHs that would take several days by using the FDTD simulation becomes only a few minutes by using the new analytical theory of the CHs. We have applied the analytical solutions to obtain the subwavelength focusing in the optical band and to enhance the magnifying resolution in the UV band. The subwavelength focal spot for the visible light about 28 nm ($\lambda/16$) is demonstrated by focusing two point sources using the focusing CHs comprising alternating SiO_2/Ag CCLs. The point sources can be realized in the experiment with the subwavelength apertures perforated in thick Ag screen. We have obtained the magnifying resolution for the UV light about 20 nm ($\lambda/18$) by using the magnifying CHs comprising the Al_2O_3/Ag CCLs. The analytical solutions are general and applicable to any radiation band at which the finite negative dielectric constants of the metals are found.

Chapter 3

Analytical solutions of dielectrics/grating/dielectrics as hyperbolic metamaterials for terahertz radiation

We cannot continue the discussion in the cylindrical hyperlens for terahertz (THz) radiation because the metals have positively large imaginary part of the dielectric constant and they become the perfect electric conductor or PEC in this radiation band. Then, our analytical solutions which deal with the finite dielectric constant of the metals as developed in the previous chapter cannot be applied. The real part of the dielectric constant of the metals should not be so negatively large , and the imaginary part of the dielectric constant must be vanishingly small. Their negative response should be also tunable over wide frequency range by some external stimuli. However, noble metals are the PEC in the THz band because they have very high electrical conductivity which make them reflect almost all incident light without heat being generated inside them. Thanks to many pioneers who had shown that PEC could support the artificial surface plasmons like the natural surface plasmons in visible band just by perforating the metals with grooves [73]. These quasi-particles are called spoof surface plasmons (SSPs). The discovery opened up the possibility of making good hyperbolic medium for THz radiation by structuring metals as rod arrays [30]. We naively expect that by combining such layers of metallic rods with dielectric layers, the hyperbolic dispersion would be achieved. We focus on layers of rectangular metallic rods which are closely spaced and form a metallic grating with subwavelength slit width. In the previous chapter, we have used the slits to couple the incident light to the surface plasmons in the cylindrical hyperlens, but we will use the slits as the optical components to create the SSPs in this chapter. This model allows us to apply the coupled-mode analysis which is successfully applied to study the extraordinary transmission effects (PEC) in the bare PEC grating and the bare hole-array [50]. We generalize the structure by attaching dielectric layers on both sides of the grating and formulate new analytical solutions for this structure. The analytical solutions are the bases for the optimization scheme of the subwavelength imaging with the stacked grating/dielectric layers as the hyperbolic metamaterials which will be given in the next chapter. The analytical solutions of these structures also lead to the realization of the novel devices for the thin-film sensing application which we will describe in this chapter.

The ability of controlling light in subwavelength scale with the hole array had allowed researchers to sense the presences of thin films whose thicknesses are much smaller than the wavelength of light [51,52]. However, there is still no limit of how small thickness we can achieve using the SSPs generated in the grating. The analytical solutions of the dielectrics/grating/dielectrics structurs may lead to the answer of this problem. Here, we apply the analytical solutions to make perfect absorbers (PAs) with ultrahigh Q-factors for thin film subwavelength sensing, and we optimize their sensing performances. The physical origins of the ultrahigh Q-factors and the tunability of these PAs are explained by Wood's anomalies and excitations of the SSPs. The sensing perfornances can be optimized by monitoring the frequency shifts of the resonance peaks and the drops of the absorbance. It is found that 2 nm-thick transparent film (n=1.6) can be detected with the PAs which have Q-factor equal to 30,267 and grating period 100 μm. The analytical solutions close the gaps between the small

thickness of thin film and long wavelength of THz radiation, and provide time-effective tools to investigate these structures.

The chapter is organized as follows. We express the analytical solutions and compare the results with FDTD simulation in section 3.1. In the section 3.2, we explain the properties of SSPs in a bare grating. We will understand in this section how to go into deep-subwavelength regime at the THz band. The remaining sections devote to the subwavelength sensing application, and the discussion in subwavelength imaging will be recovered in the chapter 4 and 5, when we extend the analytical solutions to the stacked dielectrics/grating/dielectrics structure. In section 3.3, we introduce the perfect absorbers for the purpose of subwavelength sensing. Section 3.4 will give the sensitivities of the perfect absorbers as refractive index sensors. The chapter is summarized in the section 3.5.

3.1 Analytical solutions of dielectrics/grating/dielectrics metamaterials

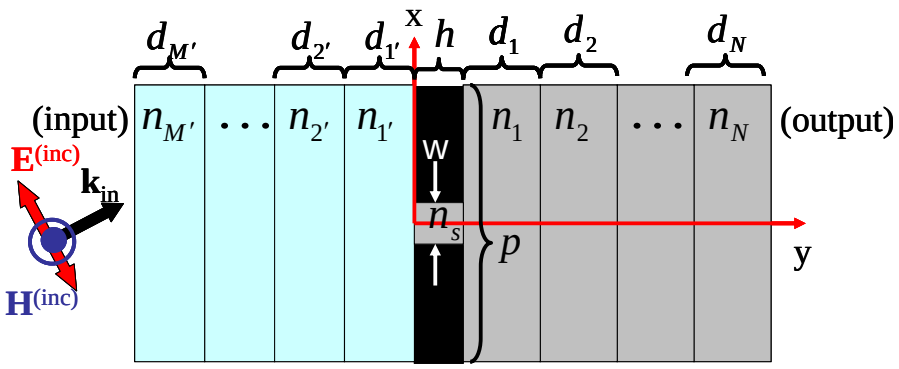

Fig. 3.1. Schematic view of the dielectrics/grating/dielectrics structure. The grating is made by perforating subwavelength slits on PEC layer. Dielectric layers are attached on both sides of the grating. A whole structure is excited by TM-polarized incident light with the amplitude of the incident magnetic field H_0 from the input region. The relevant parameters are indicated in the figure. The apostrophe on the subscript is used to distinguish the parameters of the dielectric layers of the input side from those of the output side.

The schematic view of the dielectrics/grating/dielectrics is drawn in Fig. 3.1. The external excitation is continuous TM-polarized light with the incident magnetic field polarized along the *z*-axis : $\mathbf{H}^{(\mathrm{inc})} = \hat{z}H_0 \exp\left(ik_y y + ik_x x - i\omega t\right)/\sqrt{p}$, where p is period of the grating and H_0 is amplitude of the magnetic field. The incident light impinges on the whole structure form the input region, and light transmits out from the structure in the output region. The M and N number of dielectric layers are attached in front of and behind the grating, respectively, and the apostrophes distinguish the dielectric layers of the input side from those of the output side. The grating is modelled as PEC cut through by subwavelength slits ($w \ll \lambda$). The solutions of the electromagnetic fields in each region are given following sections (3.1.1-3.15).

3.1.1. Electromagnetic fields in the input region

The reflected magnetic field which results from the diffraction by the grating can be expanded in terms of the Bloch's basis functions written in real space as $\langle x|\beta_m\rangle = \exp(i\beta_m x)/\sqrt{p}$, where $\beta_m = k_x + m2\pi/p$, and $m = 0, \pm1, \pm2, \ldots$. The total magnetic field is then the summation of the incident magnetic field and the reflected magnetic field which is expressed in Dirac's ket notation as

$$\left|H_z^{(\mathrm{in})}(y)\right\rangle = H_0 \exp\left(iq_0^{(\mathrm{in})} y\right)|\beta_0\rangle + \sum_m B_m^{(\mathrm{in})} \exp\left(-iq_m^{(\mathrm{in})}\left(y + D_{\mathrm{in}}\right)\right)|\beta_m\rangle, \tag{3.1}$$

where $B_m^{(\mathrm{in})}$ are *m*h-order reflection coefficients, $q_m^{(\mathrm{in})} = \sqrt{k_{\mathrm{in}}^2 - \beta_m^2}$, and $D_{\mathrm{in}} = \sum_{j=1}^{M} d_{j'}$ is thickness of all dielectric layers in front of the grating. The tangential component of the electric field obtained by the Maxwell's equations is written as

$$\left|E_x^{(\mathrm{in})}(y)\right\rangle = \frac{-H_0 q_0^{(\mathrm{in})}}{\omega\varepsilon_0\varepsilon_{\mathrm{in}}} \exp\left(iq_0^{(\mathrm{in})} y\right)|\beta_0\rangle + \frac{1}{\omega\varepsilon_0\varepsilon_{\mathrm{in}}} \sum_m q_m^{(\mathrm{in})} B_m^{(\mathrm{in})} \exp\left(-iq_m^{(\mathrm{in})}\left(y + D_{\mathrm{in}}\right)\right)|\beta_m\rangle, \tag{3.2}$$

where $\varepsilon_{\mathrm{in}}$ is dielectric constant of the input region.

3.1.2. Electromagnetic fields in dielectric layers in front of the grating

The magnetic field in the dielectric layer j' in front of the grating can be written as the summation between the left (-*y*) and right (+*y*) travelling waves with the Bloch's basis functions as follows

$$\left|H_z^{(j')}(y)\right\rangle = \sum_m \left\{\left(A_m^{(j')} \exp\left[iq_m^{(j')}\left(y + D_{(j-1)'}\right)\right] + B_m^{(j')} \exp\left[-iq_m^{(j')}\left(y + D_{(j-1)'}\right)\right]\right)\right\}|\beta_m\rangle, \tag{3.3}$$

where $A_m^{(j')}$ and $B_m^{(j')}$ are *m*th-order field coefficients of right and left travelling waves, respectively, $q_m^{(j')} = \sqrt{k_{j'}^2 - \beta_m^2}$, and $D_{j'} = \sum_{r'=1}^{j'} d_{r'}$. The tangential component of the electric field obtained by the Maxwell's equations are expressed as

$$\left|E_x^{(j')}(y)\right\rangle = -\frac{1}{\omega\varepsilon_0\varepsilon_{j'}} \sum_m q_m^{(j')} \left\{\left(A_m^{(j')} \exp\left[iq_m^{(j')}\left(y + D_{(j-1)'}\right)\right] - B_m^{(j')} \exp\left[-iq_m^{(j')}\left(y + D_{(j-1)'}\right)\right]\right)\right\}|\beta_m\rangle, \tag{3.4}$$

where $\varepsilon_{j'}$ is dielectric constant of the dielectric layer j'.

3.1.3. Electromagnetic fields in the grating

The grating has non-zero magnetic field only inside the slits. The magnetic field in each slit can be written in terms of the infinite summation of the waveguide modes. In our assumption, the slit width is much smaller than the wavelength of the incident light, and therefore only the fundamental waveguide mode, written in real space as $\langle x|0\rangle = 1/\sqrt{w}$, is taken into account. The remaining modes are evanescent waves transferring no energy inside the slit. In this circumstance, the magnetic field is homogeneous along the *x*-axis, and it can be written as

$$\left|H_z^{(\mathrm{s})}\right\rangle = -\left(A_0 \exp(ik_{\mathrm{s}} y) - B_0 \exp(-ik_{\mathrm{s}} y)\right)|0\rangle, \tag{3.5}$$

where A_0 and B_0 are slit's field coefficients for right and left travelling waves, respectively, and k_s is wavenumber of the material filling the slit. The tangential component of the electric field obtained by the Maxwell's equations is written as

$$\left|E_x^{(s)}(y)\right\rangle = \frac{k_s}{\omega\varepsilon_0\varepsilon_s}\left(A_0\exp(ik_s y)+B_0\exp(-ik_s y)\right)|0\rangle, \tag{3.6}$$

where ε_s is dielectric constant of material filling the slit. The normal component of the electric field of the fundamental mode inside the slit is completely zero. For the reference to the next chapter, we also give the magnetic and electric fields including all waveguide modes inside the slit which is located at the position x_s as follows

$$\left|H_z^{(s)}(y)\right\rangle = -\sum_\alpha\left[A_\alpha\exp\left(ig_y^{(\alpha)}y\right)-B_\alpha\exp\left(-ig_y^{(\alpha)}y\right)\right]|\alpha\rangle, \tag{3.7}$$

$$\left|E_x^{(s)}(y)\right\rangle = \frac{1}{\omega\varepsilon_0\varepsilon_s}\sum_\alpha g_y^{(\alpha)}\left[A_\alpha\exp\left(ig_y^{(\alpha)}y\right)+B_\alpha\exp\left(-ig_y^{(\alpha)}y\right)\right]|\alpha\rangle, \tag{3.8}$$

where $\alpha = 0,1,2,...$ are waveguide mode numbers, $g_y^{(\alpha)} = \sqrt{k_s^2 - g_x^{(\alpha)2}}$, $g_x^{(\alpha)} = \alpha\pi/w$, A_α and B_α are field coefficients for +*y* and -*y* travelling waves, respectively, and the waveguide mode in real space is expressed as

$$\langle x|\alpha\rangle = \sqrt{\frac{C_\alpha}{w}}\cos\left[g_x^{(\alpha)}\left(x-x_s+w/2\right)\right]\Theta\left(w/2-|x-x_s|\right), \tag{3.9}$$

where $C_0 = 1$ and $C_{\alpha\neq 0} = 2$, and Θ is the Heaviside step function defined as $\Theta(x) = 0, x<0$ and $\Theta(x) = 1, x\geq 0$. The Heaviside step function is included just to make sure that the electromagnetic fields are zero outside the slits.

3.1.4. Electromagnetic fields in dielectric layers behind the grating

The magnetic field in the dielectric layer j behind the grating can be written as the summation between the left (-*y*) and right (+*y*) travelling waves with the Bloch's basis functions as follows

$$\left|H_z^{(j)}(y)\right\rangle = \sum_m\left\{\left(A_m^{(j)}\exp\left[iq_m^{(j)}\left(y-D_{j-1}\right)\right]+B_m^{(j)}\exp\left[-iq_m^{(j)}\left(y-D_{j-1}\right)\right]\right)\right\}|\beta_m\rangle, \tag{3.10}$$

where $A_m^{(j)}$ and $B_m^{(j)}$ are *m*th-order field coefficients of right and left travelling waves, respectively, $q_m^{(j)} = \sqrt{k_j^2-\beta_m^2}$, k_j is wavenumber in the dielectric layer *j*, and $D_j = h+\sum_{r=1}^{j} d_r$. The tangential component of the electric field obtained by the Maxwell's equations is expressed as follows

$$\left|E_x^{(j)}(y)\right\rangle = -\frac{1}{\omega\varepsilon_0\varepsilon_j}\sum_m q_m^{(j)}\left\{\left(A_m^{(j)}\exp\left[iq_m^{(j)}\left(y+D_{j-1}\right)\right]-B_m^{(j)}\exp\left[-iq_m^{(j)}\left(y+D_{j-1}\right)\right]\right)\right\}|\beta_m\rangle, \tag{3.11}$$

where ε_j is dielectric constant of the dielectric layer j.

3.1.5. Electromagnetic fields in the output region

Similar to the input medium and dielectric layers, the transmitted magnetic field is expanded in terms of the Bloch's basis functions. The transmitted has only the right travelling wave, and thus it can be written as

$$\left|H_z^{(\mathrm{out})}(y)\right\rangle = \sum_m A_m^{(\mathrm{out})} \exp\left(iq_m^{(\mathrm{out})}\left(y - D_{\mathrm{out}}\right)\right)\left|\beta_m\right\rangle, \tag{3.12}$$

where $A_m^{(\mathrm{out})}$ are mth-order reflection coefficients, $q_m^{(\mathrm{out})} = \sqrt{k_{\mathrm{out}}^2 - \beta_m^2}$, k_{out} is wavenumber in the output region, and $D_{\mathrm{out}} = D_N$. The tangential component of electric field obtained by the Maxwell's equations is written as

$$\left|E_x^{(\mathrm{out})}(y)\right\rangle = -\frac{1}{\omega\varepsilon_0\varepsilon_{\mathrm{out}}}\sum_m q_m^{(\mathrm{out})} A_m^{(\mathrm{out})} \exp\left(iq_m^{(\mathrm{out})}\left(y - D_{\mathrm{out}}\right)\right)\left|\beta_m\right\rangle, \tag{3.13}$$

where $\varepsilon_{\mathrm{out}}$ is dielectric constant of he output medium.

3.1.6 Determination of field coefficients in all regions

The idea of obtaining the field coefficients is simple. We can apply the transfer matrix on both sides of the grating to transfer the field coefficients of the slits A_0 and B_0 into the input and output regions via diffraction waves. This process, according to the language of the coupled-mode analysis, is the re-radiation of the diffraction waves emitted by slits [56]. After that, the field coefficients will be transferred back to the grating again which are then received by the slits. The latter process may be regarded as the re-absorption of the diffraction waves by the slits. These two processes keep going on due to the multiple reflections inside the structure. Finally, we can obtain the linear equations connecting A_0 and B_0 from two sides of the grating, and therefore, the all field coefficients are automatically determined by the solutions of field coefficients.

According to the coupled-mode analysis, it's easier to define new field coefficients of the slits : $E_0^{(\mathrm{in})}$ and $E_0^{(\mathrm{out})}$ which are defined as the complex amplitude of $E_x^{(\mathrm{s})}$ at the slit input (y=0) and the negative complex amplitude of $E_x^{(\mathrm{s})}$ at the slit output (y=h). Then, A_0 and B_0 are related to $E_0^{(\mathrm{in})}$ and $E_0^{(\mathrm{out})}$ via the following relations

$$A_0 = -\frac{\omega\varepsilon_0\varepsilon_{\mathrm{s}}}{k_{\mathrm{s}}}\left[\frac{E_0^{(\mathrm{in})}\exp\left(-ik_{\mathrm{s}}h\right) + E_0^{(\mathrm{out})}}{2i\sin\left(k_{\mathrm{s}}h\right)}\right], \quad B_0 = \frac{\omega\varepsilon_0\varepsilon_{\mathrm{s}}}{k_{\mathrm{s}}}\left[\frac{E_0^{(\mathrm{in})}\exp\left(ik_{\mathrm{s}}h\right) + E_0^{(\mathrm{out})}}{2i\sin\left(k_{\mathrm{s}}h\right)}\right]. \tag{3.14}$$

By using the magnetic field and electric fields given in Eq. (3.1)-(3.13) and following the procedures given above, the linear equation of the slit's field coefficients $E_0^{(\mathrm{in})}$ and $E_0^{(\mathrm{out})}$ obtained at the output side can be written as

$$G_{\mathrm{V}}E_0^{(\mathrm{in})} - \left(G_{\infty\mathrm{s}}^{(\mathrm{out})} - \gamma\right)E_0^{(\mathrm{out})} = 0, \tag{3.15}$$

where $G_{\mathrm{V}} = \csc\left(k_{\mathrm{s}}h\right)$ couples two sides of the grating, $\gamma = \cot\left(k_{\mathrm{s}}h\right)$ accounts for the multiple reflections inside the slits, and $G_{\infty\mathrm{s}}^{(\mathrm{out})}$ takes into account the re-radiation and the re-absorption of the diffractions waves by the slits in the output side which is defined as

$$G_{\infty\mathrm{s}}^{(\mathrm{out})} = i\frac{n_{\mathrm{s}}\varepsilon_1}{n_1\varepsilon_{\mathrm{s}}}\sum_m W_m^{(\mathrm{out})}Y_m^{(1)}\left(w/p\right)\mathrm{sinc}^2\left(\beta_m w/2\right), \tag{3.16}$$

where $Y_m^{(1)} = k_1 / q_m^{(1)}$ is called the admittance, and the $W_m^{(\mathrm{out})}$ takes into account the multiple reflection of *m*th-diffraction wave in the output side which is defined as

$$W_m^{(\mathrm{out})} = \frac{S_{22}^{(m)} - S_{21}^{(m)}}{S_{22}^{(m)} + S_{21}^{(m)}}, \tag{3.17}$$

where $S_{ij}^{(m)}$ is the matrix element of the output scattering matrix defined as

$$\mathbf{S}^{(m)} = \mathbf{T}_{\mathrm{out}}^{(m)} \mathbf{T}_{N,N-1}^{(m)} \cdots \mathbf{T}_{2,1}^{(m)}, \tag{3.18}$$

where $\mathbf{T}_{i,j}^{(m)}$ and $\mathbf{T}_{\mathrm{out}}^{(m)}$ are transfer matrices in the output side defined as

$$\mathbf{T}_{i,j}^{(m)} = \begin{bmatrix} \exp\left(i\phi_m^{(j)}\right) & r_{i,j}^{(m)} \exp\left(-i\phi_m^{(j)}\right) \\ r_{i,j}^{(m)} \exp\left(i\phi_m^{(j)}\right) & \exp\left(-i\phi_m^{(j)}\right) \end{bmatrix}, \tag{3.19}$$

$$\mathbf{T}_{\mathrm{out}}^{(m)} = \begin{bmatrix} t_{N,\mathrm{out}}^{(m)} \exp\left(i\phi_m^{(N)}\right) & 0 \\ -r_{N,\mathrm{out}}^{(m)} \exp\left(i\phi_m^{(N)}\right) & \exp\left(-i\phi_m^{(N)}\right) \end{bmatrix}, \tag{3.20}$$

where $\phi_m^{(j)} = q_m^{(j)} d_j$, $r_{i,j}^{(m)}$ and $t_{i,j}^{(m)}$ are the *m*th-order reflection and transmission coefficients from the medium *i* to the medium *j* which are defined for the TM wave as

$$r_{i,j}^{(m)} = \frac{\varepsilon_j q_m^{(i)} - \varepsilon_i q_m^{(j)}}{\varepsilon_j q_m^{(i)} + \varepsilon_i q_m^{(j)}}, \quad t_{i,j}^{(m)} = \frac{2\varepsilon_j q_m^{(i)}}{\varepsilon_j q_m^{(i)} + \varepsilon_i q_m^{(j)}}. \tag{3.21}$$

If thickness of dielectric layer is zero, the transfer matrix must be reduced to the identity matrix. In the output side, we also can write the *m*th-order transmission coefficient in terms of $E_0^{(\mathrm{out})}$ as

$$\frac{A_m^{(\mathrm{out})}}{H_0} = \frac{\omega \varepsilon_0 \varepsilon_1}{k_0 n_1} \frac{1}{t_{N,N-1}^{(m)} \cdots t_{2,1}^{(m)}} \left[\frac{\det\left(\mathbf{S}^{(m)}\right)}{S_{22}^{(m)} + S_{21}^{(m)}} \right] Y_m^{(1)} \frac{E_0^{(\mathrm{out})}}{H_0} \sqrt{\frac{w}{p}} \operatorname{sinc}\left(\frac{\beta_m w}{2}\right). \tag{3.22}$$

The field coefficients of the *j* dielectric layer are connected to the *j*-1 dielectric layer via the relation $\left(A_m^{(j)} \quad B_m^{(j)}\right)^T = \left(1/t_{j,j-1}^{(m)}\right) \mathbf{T}_{j,j-1}^{(m)} \left(A_m^{(j-1)} \quad B_m^{(j-1)}\right)^T$, therefore all field coefficients of the dielectric layer $j > 1$ are obtained if the field coefficients of the *j*=1 are known. The $A_m^{(1)}$ and $B_m^{(1)}$ are connected to the $E_0^{(\mathrm{out})}$ via the following equation

$$A_m^{(1)} = n_1 \left[\frac{S_{22}^{(m)}}{S_{22}^{(m)} + S_{21}^{(m)}} \right] i Y_m^{(1)} \sqrt{w/p} \operatorname{sinc}\left(\beta_m w/2\right) E_0^{(\mathrm{out})}, \tag{3.23}$$

$$B_m^{(1)} = -n_1 \left[\frac{S_{21}^{(m)}}{S_{22}^{(m)} + S_{21}^{(m)}} \right] i Y_m^{(1)} \sqrt{w/p} \operatorname{sinc}\left(\beta_m w/2\right) E_0^{(\mathrm{out})}. \tag{3.24}$$

Therefore, all field coefficients will be known if the $E_0^{(\mathrm{out})}$ is determined. That means another linear equation relating $E_0^{(\mathrm{in})}$ and $E_0^{(\mathrm{out})}$ must be obtained at the input side.

The linear equation connecting $E_0^{(\mathrm{in})}$ and $E_0^{(\mathrm{out})}$ at the input side is written as

$$\left(G_{\infty \mathrm{s}}^{(\mathrm{in})} - \gamma\right) E_0^{(\mathrm{in})} - G_{\mathrm{V}} E_0^{(\mathrm{out})} = H_0 I_0 \exp\left(-i\phi_0^{(\mathrm{in})}\right) \left(\frac{2ik_0 n_{\mathrm{s}}}{\omega \varepsilon_0 \varepsilon_{\mathrm{s}}} \right) \frac{t_{\mathrm{in},M'}^{(0)} \cdots t_{2',1'}^{(0)}}{\bar{S}_{12}^{(0)} + \bar{S}_{11}^{(0)}}, \tag{3.25}$$

where $\phi_0^{(\mathrm{in})} = q_0^{(\mathrm{in})} D_{\mathrm{in}}$, $I_0 = -\sqrt{w/p}\,\mathrm{sinc}\left(k_x w/2\right)$ is direct excitation, $G_{\infty\mathrm{s}}^{(\mathrm{in})}$ takes into account the re-radiation and the re-absorption of the diffractions waves by the slits in the input side which is defined as

$$G_{\infty\mathrm{s}}^{(\mathrm{in})} = i\frac{n_{\mathrm{s}}\varepsilon_{1'}}{n_{1'}\varepsilon_{\mathrm{s}}}\sum_m W_m^{(\mathrm{in})} Y_m^{(1')}\left(w/p\right)\mathrm{sinc}^2\left(\beta_m w/2\right), \tag{3.26}$$

$W_m^{(\mathrm{in})}$ takes into account the multiple reflection of *m*th-diffraction wave in the input side which is defined as

$$W_m^{(\mathrm{in})} = \frac{\bar{S}_{11}^{(m)} - \bar{S}_{12}^{(m)}}{\bar{S}_{11}^{(m)} + \bar{S}_{12}^{(m)}}. \tag{3.27}$$

The *m*th-order input transfer matrix is defined as

$$\bar{\mathbf{S}}^{(m)} = \bar{\mathbf{T}}_{\mathrm{in},M'}^{(m)} \cdots \bar{\mathbf{T}}_{2',1'}^{(m)}. \tag{3.28}$$

The $\bar{\mathbf{T}}_{i,j}^{(m)}$ denotes the *m*th-order input transfer matrix from the medium *i* to the medium *j*, which is defined as

$$\bar{\mathbf{T}}_{i',j'}^{(m)} = \begin{bmatrix} \exp\left(-i\phi_m^{(j')}\right) & r_{i',j'}^{(m)} \exp\left(i\phi_m^{(j')}\right) \\ r_{i',j'}^{(m)} \exp\left(-i\phi_m^{(j)}\right) & \exp\left(i\phi_m^{(j')}\right) \end{bmatrix}, \tag{3.29}$$

where $\phi_m^{(j')} = q_m^{(j')} d_{j'}$, and the reflection coefficient is given in Eq. (3.21). The *m*th-order reflection coefficient is expressed in terms of the $E_0^{(\mathrm{in})}$ as

$$B_m^{(\mathrm{in})}/H_0 = \exp\left(-i\phi_0^{(\mathrm{in})}\right)\left[\frac{\bar{S}_{22}^{(0)} + \bar{S}_{21}^{(0)}}{\bar{S}_{12}^{(0)} + \bar{S}_{11}^{(0)}}\right]\delta_{m0} + \left(\frac{\omega\varepsilon_0\varepsilon_{1'}}{k_{1'}}\right)\frac{1}{t_{\mathrm{in},M'}^{(m)} \cdots t_{2',1'}^{(m)}}\left[\frac{\det\left(\bar{\mathbf{S}}^{(m)}\right)}{\bar{S}_{12}^{(m)} + \bar{S}_{11}^{(m)}}\right] Y_m^{(1')}\sqrt{\frac{w}{p}}\,\mathrm{sinc}\left(\frac{\beta_m w}{2}\right)\frac{E_0^{(\mathrm{in})}}{H_0}, \tag{3.30}$$

where δ_{m0} is Dirac delta function. The field coefficients of the j' dielectric layer are connected to those of the $j'-1'$ dielectric layer via the relation $\left(A_m^{(j')} \quad B_m^{(j')}\right)^T = \left(1/t_{j',j'-1'}^{(m)}\right)\mathbf{T}_{j',j'-1}^{(m)}\left(A_m^{(j'-1')} \quad B_m^{(j'-1')}\right)^T$, therefore all field coefficients of the dielectric layer $j' > 1'$ are obtained if the field coefficients of the $j' = 1'$ are known. The $A_m^{(1')}$ and $B_m^{(1')}$ are connected to the $E_0^{(\mathrm{in})}$ via the following equation

$$A_m^{(1')} = H_0 \exp\left(-i\phi_0^{(\mathrm{in})}\right)\left[\frac{t_{\mathrm{in},M'}^{(0)} \cdots t_{2',1'}^{(0)}}{\bar{S}_{12}^{(0)} + \bar{S}_{11}^{(0)}}\right]\delta_{m0} - \left(\frac{\omega\varepsilon_0\varepsilon_{1'}}{k_{1'}}\right)\left[\frac{\bar{S}_{12}^{(m)}}{\bar{S}_{12}^{(m)} + \bar{S}_{11}^{(m)}}\right] Y_m^{(1')}\sqrt{\frac{w}{p}}\,\mathrm{sinc}\left(\frac{\beta_m w}{2}\right)E_0^{(\mathrm{in})}, \tag{3.31}$$

$$B_m^{(1')} = H_0 \exp\left(-i\phi_0^{(\mathrm{in})}\right)\left[\frac{t_{\mathrm{in},M'}^{(0)} \cdots t_{2',1'}^{(0)}}{\bar{S}_{12}^{(0)} + \bar{S}_{11}^{(0)}}\right]\delta_{m0} + \left(\frac{\omega\varepsilon_0\varepsilon_{1'}}{k_{1'}}\right)\left[\frac{\bar{S}_{11}^{(m)}}{\bar{S}_{12}^{(m)} + \bar{S}_{11}^{(m)}}\right] Y_m^{(1')}\sqrt{\frac{w}{p}}\,\mathrm{sinc}\left(\frac{\beta_m w}{2}\right)E_0^{(\mathrm{in})}. \tag{3.32}$$

Finally, the slit's field coefficients are obtained by solving the Eq. (3.15) and (3.25), then we have

$$E_0^{(\mathrm{in})} = H_0 I_0 \exp\left(-i\phi_0^{(\mathrm{in})}\right)\frac{2ik_{\mathrm{s}}}{\omega\varepsilon_0\varepsilon_{\mathrm{s}}}\left[\frac{t_{\mathrm{in},M'}^{(0)} \cdots t_{2',1'}^{(0)}}{\bar{S}_{12}^{(0)} + \bar{S}_{11}^{(0)}}\right]\left(\frac{G_{\infty\mathrm{s}}^{(\mathrm{out})} - \gamma}{\Omega}\right), \tag{3.33}$$

$$E_0^{(\mathrm{out})} = H_0 I_0 \exp\left(-i\phi_0^{(\mathrm{in})}\right)\frac{2ik_{\mathrm{s}}}{\omega\varepsilon_0\varepsilon_{\mathrm{s}}}\left[\frac{t_{\mathrm{in},M'}^{(0)} \cdots t_{2',1'}^{(0)}}{\bar{S}_{12}^{(0)} + \bar{S}_{11}^{(0)}}\right]\left(\frac{G_{\mathrm{V}}}{\Omega}\right), \tag{3.34}$$

where Ω is the dispersion function which determines the resonances of the structure. The dispersion is defined as

$$\Omega = \left(G_{\infty \mathrm{S}}^{(\mathrm{in})} - \gamma\right)\left(G_{\infty \mathrm{S}}^{(\mathrm{out})} - \gamma\right) - G_{\mathrm{V}}^2 . \tag{3.35}$$

By substitution $E_0^{(\mathrm{in})}$ from Eq. (3.33) into Eq. (3.30), the analytical expression of the *m*th-order reflection coefficient can be explicitly written as follows

$$\frac{B_m^{(\mathrm{in})}}{H_0} = e^{-i\phi_0^{(\mathrm{in})}} \left(\frac{\bar{S}_{22}^{(0)} + \bar{S}_{21}^{(0)}}{\bar{S}_{12}^{(0)} + \bar{S}_{11}^{(0)}} \right) \left\{ \delta_{m0} + I_0 \left(\frac{t_{\mathrm{in},M'}^{(0)} \cdots t_{2',1'}^{(0)}}{\bar{S}_{22}^{(0)} + \bar{S}_{21}^{(0)}} \right) \left(\frac{n_s \varepsilon_{1'}}{n_{1'} \varepsilon_s} \right) i Y_m^{(1')} \left(\frac{2 \det\left(\bar{\mathbf{S}}^{(m)}\right)}{t_{\mathrm{in},M'}^{(m)} \cdots t_{2',1'}^{(m)} \left(\bar{S}_{12}^{(m)} + \bar{S}_{11}^{(m)} \right)} \right) \sqrt{\frac{w}{p}} \operatorname{sinc}\left(\beta_m w / 2\right) \frac{G_{\infty \mathrm{S}}^{(\mathrm{out})} - \gamma}{\Omega} \right\}. \tag{3.36}$$

The first term in the curl bracket, the Dirac delta function, is referred to the non-diffraction term because it dose not depend on the slit's parameters. The second term in the curl bracket is referred to the diffraction term because it does depend on the slit's parameters. By substituting $E_0^{(\mathrm{out})}$ from Eq. (3.34) into Eq. (3.22), the *m*th-order transmission coefficient can be explicitly written as follows

$$\frac{A_m^{(\mathrm{out})}}{H_0} = e^{-i\phi_0^{(\mathrm{in})}} \left(\frac{t_{\mathrm{in},M'}^{(0)} \cdots t_{2',1'}^{(0)}}{\bar{S}_{12}^{(0)} + \bar{S}_{11}^{(0)}} \right) \frac{1}{t_{N,N-1}^{(m)} \cdots t_{2,1}^{(m)}} \left(\frac{2 \det\left(\mathbf{S}^{(m)}\right)}{S_{22}^{(m)} + S_{21}^{(m)}} \right) I_0 \left(\frac{n_s \varepsilon_1}{n_1 \varepsilon_s} \right) i Y_m^{(1)} \sqrt{\frac{w}{p}} \operatorname{sinc}\left(\beta_m w / 2\right) \frac{G_V}{\Omega} . \tag{3.37}$$

The transmittance and reflectance are calculated by computing the time-averaged Poynting vector parallel to the propagation axis (*y*-axis) in the far-field and integrate all energy over the unit cell of the grating, then the transmittance and reflectance are written as

$$T = \frac{\varepsilon_{\mathrm{in}}}{\varepsilon_{\mathrm{out}}} \mathrm{P}\left\{ \sum_m \frac{q_m^{(\mathrm{out})}}{q_0^{(\mathrm{in})}} \left| \frac{A_m^{(\mathrm{out})}}{H_0} \right|^2 \right\}, \quad R = \mathrm{P}\left\{ \sum_m \frac{q_m^{(\mathrm{in})}}{q_0^{(\mathrm{in})}} \left| \frac{B_m^{(\mathrm{in})}}{H_0} \right|^2 \right\}, \tag{3.38}$$

where the function P includes only the propagating diffraction waves.

3.1.7 Comparison with FDTD simulation

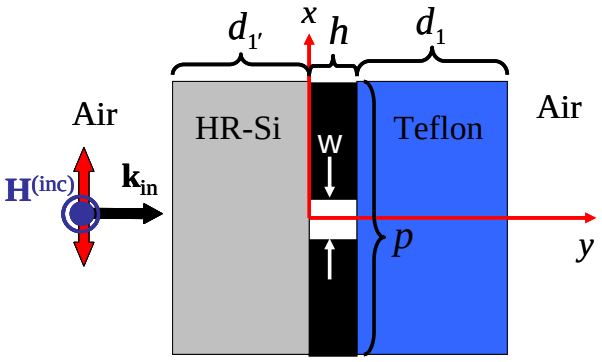

Fig. 3.2. Schematic view of dielectric/grating/dielectric structure for comparing with FDTD simulation. The dielectric layer in front of the grating is high-resistivity silicon (HR-Si), and the dielectric layer behind the grating is Teflon. The dielectric constants of HR-Si and Teflon are 11.7 [74], and 2.088 [75], respectively, with the imaginary part neglected. The thickness of both layers is defined as 10 μm. The grating has period 100 μm, slit width 1 μm, and slit height 1 μm. The slit's filling material is air. The structure is excited by TM-polarized normal incident light.

We check the validity of the analytical solutions by computing the optical spectra of a single dielectric/grating/dielectric structure with *M*=*N*=1 as schematically shown in Fig. 3.2, and we compare the analytical spectra with the spectra obtained by the FDTD simulation. The imaginary part of the

dielectric constant of HR-Si is negligible [74]. We also neglect the imaginary part of the dielectric constant of Teflon because the complex dielectric constant has to be defined as a function of frequency in the FDTD simulation which slow down the calculation. Therefore, we will give the effect of losses using the analytical solutions once they are shown to be consistent with the FDTD in the case of no losses. Fig. 3.3(a) shows that the FDTD transmission spectra approach the analytical transmission spectra by increasing the resolutions. This means that analytical solutions are consistent with the FDTD simulation with high resolution. The consistency could be improved by increasing more resolution in the FDTD simulation, but this scheme is very time-consuming. The simulation time of FDTD simulation with the resolution 10 pix/μm takes 59 hours on a single PC computer with Intel(R) Core(M) i7-3970X CPU @3.50 GHz, while the analytical spectra takes only one minute to compute. This means that the analytical solutions are 3,540 times faster than the FDTD simulation. Next, let's us try to understand the origin of the resonant peaks seen in Fig. 3.3(a) by using the analytical solution. The resonant frequencies obtained by the analytical solutions are 2.1325 THz, 2.7676 THz, and 2.8860 THz, which can be precisely obtained by the resonant condition $\mathrm{Re}(\Omega)=0$. The imaginary part of the dispersion function determine the amplitude of the spectra. The maximum of diffraction orders leading to the converged $G_{\infty s}^{(\mathrm{in})}$ and $G_{\infty s}^{(\mathrm{out})}$ are 97 and 94, respectively, at these resonances. Therefore, the accurate positions of the resonances require high diffraction modes.

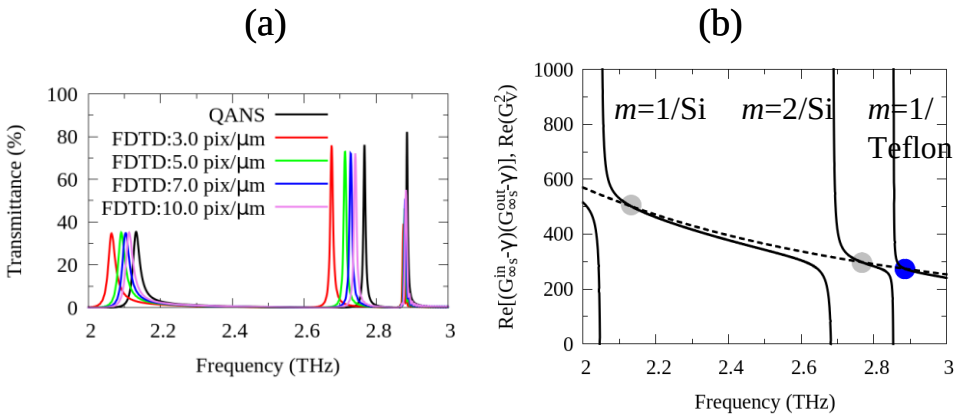

Fig. 3.3. (a) Analytical and FDTD with resolution 3-10 pix/μm transmission spectra of the structure shown in Fig. 3.2. The black line is the analytical spectra and the colour lines are the FDTD spectra. (b) Real parts of the components of the dispersion function. The black solid line denotes $\mathrm{Re}\left[\left(G_{\infty s}^{(\mathrm{in})}-\gamma\right)\left(G_{\infty s}^{(\mathrm{out})}-\gamma\right)\right]$ and the black dashed line denotes $\mathrm{Re}\left[G_V^2\right]$. The grey and blue circles indicate the resonant positions which are induced by the *m*th-order Wood's anomalies in HR-Si and Teflon layers, respectively, which are also indicated by texts.

The two components of the dispersion function are plotted in Fig. 3.3(b). In the case of a bare grating (no dielectric layers), $G_{\infty s}^{(\mathrm{in})}=G_{\infty s}^{(\mathrm{out})}$ and the two components do not cross each other within this frequency band. By introducing the dielectric layers, the symmetry between $G_{\infty s}^{(\mathrm{in})}$ and $G_{\infty s}^{(\mathrm{out})}$ is broken. In the latter case, the diffraction waves can interfere with the incident light and generate the divergences in the $G_{\infty s}^{(\mathrm{in})}$ and $G_{\infty s}^{(\mathrm{out})}$. These divergence are called the Wood's anomaly [89]. At the

Wood's anomaly, the transmittance is exactly zero because $1/|\Omega| \approx 0$ due to the divergences of the coupling parameters $G_{\infty S}^{(\mathrm{in})}$ and $G_{\infty S}^{(\mathrm{out})}$. This means that the Wood's anomalies may be regarded as the results of the strong coupling between the waveguide modes in the slits via the diffraction modes generating the shot-circuit so that the transmittance is zero. The divergences of $G_{\infty S}^{(\mathrm{in})}$ and $G_{\infty S}^{(\mathrm{out})}$ occur due to the interferences between the zeroth-order diffraction mode (non-diffracted wave) and the ±*m* diffraction modes where *m* is not equal to zero. The Wood's anomalies induce the crossing points between the two components of the dispersion function at the frequency higher than their frequencies, and thus generate the resonances at which the reflected light becomes out of phase with the incident light allowing the light energy to transmit to the far-field. For convenience, we will call the Wood's anomaly corresponding to the interference between the zeroth-order diffraction mode and ±*m* diffraction modes that lead to the divergence of $G_{\infty S}^{(\mathrm{in})}$ or $G_{\infty S}^{(\mathrm{out})}$ as *m*th-order Wood's anomaly. The frequency position of the *m*th-order Wood's anomaly can be obtained by considering the spectrum of the amplitude of $G_{\infty S}^{(\mathrm{in})}$ or $G_{\infty S}^{(\mathrm{out})}$. The amplitude of each of these coupling parameters is typically smaller than one. The Wood's anomaly will appear as the sharp peak within this spectrum with the amplitude of the $G_{\infty S}^{(\mathrm{in})}$ or $G_{\infty S}^{(\mathrm{out})}$ greater than one. Therefore, we can have one condition of the Wood's anomaly that the amplitude of $G_{\infty S}^{(\mathrm{in})}$ or $G_{\infty S}^{(\mathrm{out})}$ must be greater than one. We need this condition because finding where the amplitude of $G_{\infty S}^{(\mathrm{in})}$ or $G_{\infty S}^{(\mathrm{out})}$ is maximum in the spectrum is difficult to implement in the program. Another condition of the Wood's anomaly is that the real part of the coupling parameter $G_{\infty S}^{(\mathrm{in})}$ or $G_{\infty S}^{(\mathrm{out})}$ suddenly changes its sign from positively large value to the negatively large value (and vice versa) when the frequency crosses the Wood's anomaly. Therefore, we have two conditions to obtain the frequency position of the Wood's anomaly : $\mathrm{Re}\left(G_{\infty S}^{(\mathrm{in})}\right) = 0$ and $\left|G_{\infty S}^{(\mathrm{in})}\right| > 1$ (the same conditions applied to $G_{\infty S}^{(\mathrm{out})}$). Lastly, we take only three diffraction modes to calculate $G_{\infty S}^{(\mathrm{in})}$ or $G_{\infty S}^{(\mathrm{out})}$ that are the zeroth-order mode and the ±*m* modes when we look for the frequency position of the *m*th-order Wood's anomaly. The resonant frequencies 2.1325 THz and 2.7676 THz are induced by the 1st-order and 2nd-order Wood's anomalies in the HR-Si, respectively, as indicated in the Fig. 3.3(b). The resonant frequency 2.8860 THz is induced by the 1st-order Wood's anomaly in the Teflon layer as indicated in Fig. 3.3(b). We can compute the Q-factor defined as $\mathrm{Q} = \Delta f / f$ for each resonant peak. The Q-factors for the resonances at frequencies 2.1325 THz, 2.7676 THz, and 2.8860 THz are 105, 419, and 627, respectively. The origin of the high Q-factor can be seen in Fig. 3.3 (b). The Q-factor is determined by the respective position between the resonant peak and the Wood's anomaly, i.e., the closer to the Wood's anomaly, the stronger variation in the amplitude of the dispersion function and the higher Q-factor. Therefore, the Q-factor is tunable by varying thickness of dielectric layer because the Wood's anomaly makes blue shift toward the Rayleigh's anomaly at which $k = m2\pi / p$ ($k_x = 0$) by decreasing the thickness of the dielectric layer. For example, by decreasing the thickness of Teflon layer from 10 μm to 4 μm, the 1st-order Wood's anomaly in Teflon layer which is contained only in the function $\mathrm{Re}\left[\left(G_{\infty S}^{(\mathrm{in})} - \gamma\right)\left(G_{\infty S}^{(\mathrm{out})} - \gamma\right)\right]$ makes the blue shift while the function $\mathrm{Re}\left[G_V^2\right]$ remains

unchanged. Then, the crossing point between these two components indicated by the blue dot in Fig. 3.3(b) is pushed toward the divergence position of the 1st-order Wood's anomaly. Therefore, the spectra is more rapidly change resulting in smaller frequency width and higher Q-factor about 3,985 at the new resonant frequency 2.98134 THz for the Teflon layer with the thickness 4 μm.

The divergences of $G_{\infty S}^{(\mathrm{in})}$ and $G_{\infty S}^{(\mathrm{out})}$ are caused by the zeros of their denominators. Therefore, the physical pictures of the Wood's anomalies can be illuminated by simplifying these denominators. Consider the dielectric layer with finite dielectric constant ε_1, the corresponding wavenumber k_1, and finite size with thickness d_1 which is located behind the grating. The *m*th-order Wood's anomaly is found by including only the zero and ±*m* diffraction modes in the $G_{\infty S}^{(\mathrm{out})}$, and then the zeros of the denominator of the $G_{\infty S}^{(\mathrm{out})}$ lead to the following condition

$$q_0^{(1)} q_m^{(1)} q_{-m}^{(1)} \left(1 - r_{1,\mathrm{out}}^{(0)} e^{2i\phi_0^{(1)}}\right)\left(1 - r_{1,\mathrm{out}}^{(m)} e^{2i\phi_m^{(1)}}\right)\left(1 - r_{1,\mathrm{out}}^{(-m)} e^{2i\phi_{-m}^{(1)}}\right) = 0 \,. \tag{3.39}$$

Equation (3.39) is satisfied if $q_0^{(1)} = 0$, $q_m^{(1)} = 0$, or $q_{-m}^{(1)} = 0$. These diffraction waves propagate exactly parallel to the tangential axis (*x*-axis) and they are referred to the *n*th-order Rayleigh's anomalies, where *n*=0,*m*,-*m*. Equation (3.39) is also satisfied if $1 - r_{1,\mathrm{out}}^{(n)} e^{2i\phi_n^{(1)}} = 0$, where *n*=0,*m*,-*m*, and not confuse this *n* with the refractive index. This is the condition for the Wood's anomalies, and we apparently have three Wood's anomalies : 0th-order Wood's anomaly, *m*th-order Wood's anomaly, and -*m*th-order Wood's anomaly. The condition of the Wood's anomaly can be satisfied if $k_1 > |\beta_n|$ and $k_{\mathrm{out}} < |\beta_n|$, that is the *n*th-order diffraction mode is propagating wave in the dielectric layer but it is evanescent wave in the output medium. Notice that the electromagnetic waves at the Wood's anomalies are not propagating perfectly parallel to the *x*-axis unlike those at the Raleigh's anomalies. By imposing these conditions, we finally obtain the simplified condition of the *n*th-order Wood's anomaly as follows

$$\mathrm{WD}_n = \tan\left(d_1 \sqrt{k_1^2 - \beta_n^2}\right) - \left(\varepsilon_1 / \varepsilon_{\mathrm{out}}\right) \sqrt{\left(\beta_n^2 - k_{\mathrm{out}}^2\right) / \left(k_1^2 - \beta_n^2\right)} = 0 \,, \tag{3.40}$$

where "WD" stands for "Wood". By giving *n* as zero, *m*, or -*m*, and imposing the conditions $k_1 > |\beta_n|$ and $k_{\mathrm{out}} < |\beta_n|$, the frequencies of the *n*th-order Wood's anomalies for all incidence angles obtained by Eq. (3.40) are the same as those obtained directly by checking the divergences of $G_{\infty S}^{(\mathrm{out})}$ using the aforementioned method. For the dielectric layer located in front of the grating, the WD_n derived by the $G_{\infty S}^{(\mathrm{in})}$ is the same as Eq. (3.40) if the input and the output regions are the same. However, if these two regions are different, the WD_n of the dielectric layer located in front of the grating can be obtained from Eq. (3.40) by replacing $\varepsilon_{\mathrm{out}} \to \varepsilon_{\mathrm{in}}$ and $k_{\mathrm{out}} \to k_{\mathrm{in}}$.

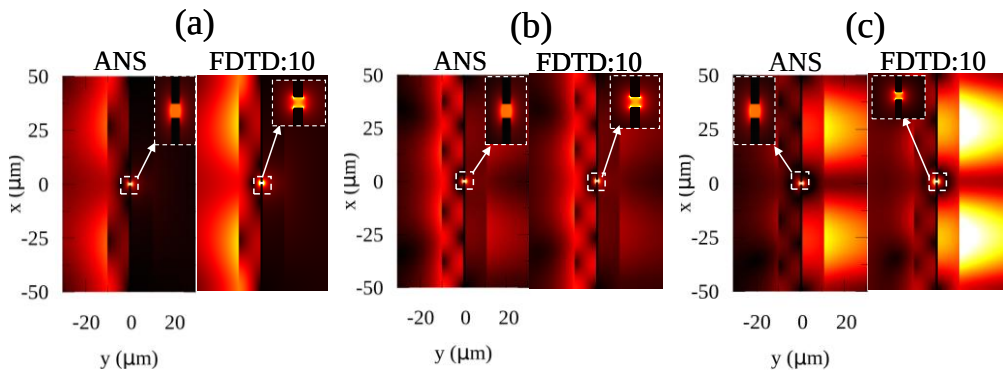

Fig. 3.4. |E|-distributions of dielectric/grating/dielectric structure. (a) At the frequency 2.1325 THz for the analytical solutions (ANS) and 2.1130 THz for the FDTD simulation with resolution 10 pix/μm (FDTD:10) . (b) At the frequency 2.7676 THz for ANS and 2.7420 THz for FDTD:10. (c) At the frequency 2.8860 THz for ANS and 2.883 THz for FDTD:10. The insets show the regions close to the slit.

We also compare the |**E**|-distributions at the resonant frequencies obtained by the analytical solutions and FDTD simulation as shown in Fig. 3.4. The maximum of order used to calculate the |**E**|-distribution in the input region and inside HR-Si layer is the same as that leading to the converged $G_{\infty S}^{(\mathrm{in})}$, and the maximum of order used to calculate the |**E**|-distribution in the output region and inside Teflon layer is the same as that leading to the converged $G_{\infty S}^{(\mathrm{out})}$. The |**E**|-distributions at 2.1325 THz, 2.7676 THz are normalized by the maxima of $|\mathbf{E}|/E_0$ at the origin $(x,y)=(0,0)$ inside the HR-Si layer which are 63 and 85, respectively, while the |**E**|-distribution at 2.8860 THz is normalized by the $|\mathbf{E}|/E_0$ at $(x,y)=(0,h)$ inside the Teflon layer which is 88.5. The higher electric field at the centre of the slit openings is associated with the larger transmittance. The maximum of $|\mathbf{E}|/E_0$ on the surface of the HR-Si at 2.1325 THz is 17.7 at $x=\pm 28.10$ μm, and that at 2.7676 THz is 22.0 at $x=\pm 14.15$ μm. The maximum of $|\mathbf{E}|/E_0$ on the surface of Teflon at 2.886 THz is 36.8 at $x=\pm 25.62$ μm. We obtain the consistent field distributions as those from the FDTD simulation. We observe that the electric field is localized on the surface of HR-Si layer in the case of the resonances at the frequencies 2.1325 THz and 2.7676 THz, but the field becomes localized on the surface of the Teflon layer in the case of the resonance at the frequency 2.8860 THz. The localization of the electric field is the characteristic of the SSPs. Therefore, these electromagnetic modes correspond to the excitations of the SSPs. We may be confused by the appearances of the nodes on the surface of the grating which lead us to think that these modes are quasi-waveguide resonances (QWRs) which occur in the dielectric layer sandwiched in between the grating and the metallic plane [77]. The best way to characterize the electromagnetic modes in any optical structure is to draw or measure the dispersion relation of that structure. That is we increase the tangential component of the wavevector and obtain the frequency corresponding to those wavevectors. We expect that the light energy will move along the tangential axis by increasing the tangential wavevector, and the dispersion will have non-zero slope and thus non-zero group velocity. However, if the band is completely flat, it means that the electromagnetic modes are QWRs. They are the standing waves formed inside the structure. For our structure, the electromagnetic modes are not the QWRs but they are the higher-order SSPs.

To clarify this, we replace the Teflon layer by the HR-Si layer, and obtain the dispersion relation of the resonant modes of this structure as shown in Fig. 3.5 (a). The red line corresponds to the SSPs on the surface of the bare grating whose cut-off frequency is the FP resonance of the slit cavity which is about 150 THz for the slit height 1 μm. Therefore, these SSPs are close to the light line within this frequency range. The next four colour lines are evidently not flat, and they are the excitations of the higher-order SSPs. The dashed colour lines have sharp resonant peaks because they locate very close to the Wood's anomalies. The dispersion relation of the Wood's anomalies is shown in Fig. 3.5 (b). By increasing k_x, the *m*th-order Wood's anomaly is split into the negative dispersion (negative slope) and the positive dispersion (positive slope). Therefore, the resonant frequency is also split into the negative and positive branches according to the Wood's anomaly. That means the energy is split into two part propagating in the different direction on the surface of the HR-Si. Interestingly, the 0th-order Wood's anomaly also appear just above the frequencies of the SSPs on the surface of the bare grating. Therefore, the SSPs on the surface of the bare grating can be designated as the 0th-order SSPs. Then, the electromagnetic modes in the green line are designated as the negative 1st-order SSPs on the HR-Si surface. This name is too long. It is more convenient to define the shorthand for these modes as $\mathrm{SSPs}\left(1^{(-)}/\mathrm{HR\text{-}Si}\right)$ where $1^{(-)}$ denotes the first-order with the negative dispersion. Similarly, the electromagnetic modes in the blue line can be designated as the positive 1st-order SSPs on the HR-Si surface with the shorthand $\mathrm{SSPs}\left(1^{(+)}/\mathrm{HR\text{-}Si}\right)$ where $1^{(+)}$ denotes the first-order with the positive dispersion. The electromagnetic modes in the cyan and the violet lines can be also designated with the shorthand $\mathrm{SSPs}\left(2^{(-)}/\mathrm{HR\text{-}Si}\right)$ and $\mathrm{SSPs}\left(2^{(+)}/\mathrm{HR\text{-}Si}\right)$, respectively. At the $k_x = 0$, the green and blue lines are merged into one mode which we call $\mathrm{SSPs}\left(1/\mathrm{HR\text{-}Si}\right)$ without the sign, and the cyan and violet lines are also merged into one mode which we call $\mathrm{SSPs}\left(2/\mathrm{HR\text{-}Si}\right)$. Therefore, with this notation, the resonant frequencies 2.1325 THz, 2.7676 THz in Fig. 3.3 (a) are the $\mathrm{SSPs}\left(1/\mathrm{HR\text{-}Si}\right)$ and $\mathrm{SSPs}\left(2/\mathrm{HR\text{-}Si}\right)$, respectively, With the same consideration, the resonant frequency 2.8860 THz is the excitation of the 1st-order SSPs on the surface of the Teflon layer denoted as $\mathrm{SSPs}\left(1/\mathrm{Teflon}\right)$. Next, we discuss more about the meaning of "higher-order" SSPs. There are two points related to the higher-order SSPs. The first point is that the higher-order SSPs can have k_x larger than that of the light in air only in the higher-order Brillouin zone of k_x corresponding to their orders. For example, within the first Brillouin zone, only the 0th-order SSPs of the bare grating lie outside the line cone, and thus only the 0th-order SSPs have k_x larger than that of light in air. In the second Brillouin zone in which we add $\pm 2\pi / p$ to the k_x within the first Brllouin zone, the 1st-order SSPs can lie outside the light cone and thus they can have k_x larger than that of the light in air. The second point is about the localization of the electromagnetic fields. The higher-order SSPs can localize the electromagnetic fields on the surface of the structure because the diffraction modes corresponding to their orders decay in air, but they propagate inside the structure. For example, the 1st-order SSPs use the decay of the diffraction modes $m = \pm 1$ in air, and the 2nd-order SSPs use the decay of the diffraction modes $m = \pm 2$ in air. Therefore,

the localization length of the electromagnetic field from the surface of the structure due to the higher-order SSPs depends on the mode order *m*. The more higher *m*, the more rapid decay of the electromagnetic field.

We can now understand why the first two peaks have larger frequency differences between the analytical solutions and FDTD simulation than the last peak as shown in Fig. 3.3(a). The resonant frequency of the last peak obtained by FDTD simulation with resolution 10 pix/μm is only 3 GHz smaller than that from the analytical solutions. The larger discrepancies of the first and second peaks from the FDTD simulation which are 20 GHz and 26 GHz, respectively, are attributed to the low resolution of the FDTD simulation in the high dielectric constant HR-Si. The contribution of higher diffraction modes in HR-Si is more significant than that in the Teflon layer with lower dielectric

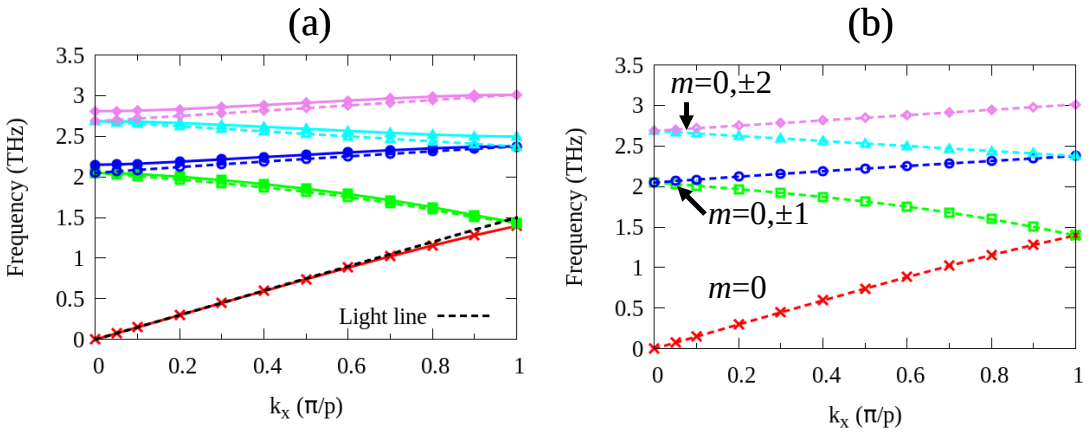

Fig 3.5. (a) The dispersion relation of the resonant modes in the HR-Si/grating/HR-Si structure. (b) The dispersion relation of the Wood's anomaly in the HR-Si/grating/HR-Si structure. The parameters of the HR-Si layer and the grating are the same as those in Fig 3.2.

constant, and therefore the FDTD simulation gives different accuracy for the resonant peak of each layer. The |**E**|-distributions from the analytical solutions are greatly consistent with those from FDTD simulation except in the regions near the slit's edges as shown in the insets where the analytical |**E**|-distributions are homogeneous inside the slit's cavities but the FDTD |**E**|-distributions are maximum at the slit's edges. According to the FDTD simulation, the |**E**| at the slit's edges is about two times larger than |**E**| at the centre of the slit's openings. This field enhancement results from the localized surface plasmons (LSPs) [53]. There effects can be accounted for by increasing the higher waveguide modes in the slit cavity. The higher waveguide modes are evanescent waves within this frequency range [78]. We notice that the LSPs also contribute to the relatively larger |**E**| above the dielectric layer especially at the $\mathrm{SSPs}(1/\mathrm{Teflon})$ shown in Fig. 3.4 (c) which is also affirmed by the relatively large difference of the transmittance obtained by the analytical solutions and the FDTD simulation at this frequency as shown in Fig. 3.3 (a). This means that the higher waveguide modes are required to have more accurate transmittance and field distribution when the wavelength is about 104 times larger than the width of the slit width.

It is important to note that there is no absorption in the system unless the imaginary part of dielectric constant (loss) is introduced into the system. The imaginary part of the dielectric constant of

Teflon is about 0.01-0.02 in the frequency range 0.5-3.0 THz [75]. According to the analytical solutions, the absorbance $A = 1 - R - T$ arising at the resonance frequencies of the $\mathrm{SSPs}(1/\mathrm{HR\text{-}Si})$, $\mathrm{SSPs}(2/\mathrm{HR\text{-}Si})$, and $\mathrm{SSPs}(1/\mathrm{Teflon})$ due to the presence of the imaginary part of the dielectric constant of Teflon 0.02 (no loss in HR-Si) are 4.0%, 38.8%, and 70.5%, respectively, as shown in Fig 3.6 (a). It can be seen that even the small loss of Teflon generates high absorbance in $\mathrm{SSPs}(1/\mathrm{Teflon})$. Note that the inclusion of higher-order waveguide modes in the slit cavity could decrease the transmittance of the $\mathrm{SSPs}(1/\mathrm{Teflon})$ as discussed in the previous section. Therefore, the absorbance at this frequency may also decrease by including higher-order waveguide modes within the slit cavity. Interestingly, the heat is also generated in the $\mathrm{SSPs}(1/\mathrm{HR\text{-}Si})$ and the $\mathrm{SSPs}(2/\mathrm{HR\text{-}Si})$, and the

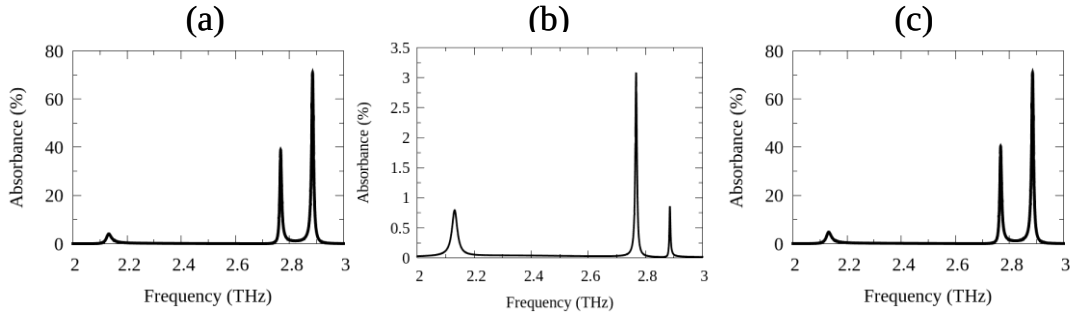

Fig. 3.6. Absorption spectra of dielectric/grating/dielectric structure. (a) The absorption spectra the due to the presence of loss only in Teflon layer where the imaginary part of the dielectric constant of the Teflon is 0.02. (b) The absorption spectra due to the presence of loss only in HR-Si where the imaginary part of the dielectric constant of the HR-Si is 0.0004. (c) The absorption spectra due to the presence of loss in both Teflon and HR-Si with the imaginary part of the dielectric constants from (a) and (b). All spectra are obtained by the analytical solutions.

and the $\mathrm{SSPs}(2/\mathrm{HR\text{-}Si})$ has higher absorbance than that in the $\mathrm{SSPs}(1/\mathrm{HR\text{-}Si})$ because the former resonance is closer to the $\mathrm{SSPs}(1/\mathrm{Teflon})$ and thus more strongly interacts with the $\mathrm{SSPs}(1/\mathrm{Teflon})$ that the latter. The imaginary part of the dielectric constant of the HR-Si is about 0.0004 in the frequency range 1-2 THz [74]. The presence of this loss in HR-Si (and no loss in Teflon) slightly heat the structure. In this case, the absorbance in the $\mathrm{SSPs}(1/\mathrm{HR\text{-}Si})$, $\mathrm{SSPs}(2/\mathrm{HR\text{-}Si})$, and $\mathrm{SSPs}(1/\mathrm{Teflon})$ are 0.8%, 3.1%, and 0.9%, respectively, as shown in Fig. 3.6 (b). The absorbance in the $\mathrm{SSPs}(1/\mathrm{HR\text{-}Si})$, $\mathrm{SSPs}(2/\mathrm{HR\text{-}Si})$, and $\mathrm{SSPs}(1/\mathrm{Teflon})$ due to the presences of losses in both HR-Si and Teflon layers are 4.8%, 40.4%, and 70.5%, respectively, as shown in Fig. 3.6 (c). This means that the inclusion of loss in HR-Si layer slightly change the optical property of the whole structure.

3.2 Properties of the spoof surface plasmons (SSPs) in a bare grating

It had been known that the PEC grating has strange effective anisotropic property. Its effective propagation constant (normal component of the wavevector) is always equal to the wavenumber of the material filling the slit k_s, and the effective dielectric constant along the *x*-axis denoted as $\varepsilon_x^{(\mathrm{eff})}$ is determined just by the dielectric constant of the material filling the slit and the geometry of the grating via the relation $\varepsilon_x^{(\mathrm{eff})} = \varepsilon_s p / w$ [79]. Whatever k_x presences in the grating, these two conditions must be satisfied. The same property was also pointed out before in the perforated PEC plane [57]. These conditions are sufficient to determine the zeroth-order reflection and transmission coefficients quite accurately in the subwavlength regime $p \ll \lambda$, and therefore there are no need to consider the remaining parameters $\varepsilon_y^{(\mathrm{eff})}$ and $\mu_z^{(\mathrm{eff})}$. The previous work on the perforated PEC suggested that $\varepsilon_y^{(\mathrm{eff})} \to \infty$ (or $\varepsilon_y^{(\mathrm{eff})} \to -\infty$) to eliminate k_x from the effective propagation constant, and gives $\mu_z^{(\mathrm{eff})} = w / p$ so that the effective propagation constant is the same as k_s [57]. This means that the perforated PEC and the PEC grating behave as type-I hyperbolic metamaterial (HMMs) with completely flat equi-frequency contour (EFC). The grating behaves like PEC along the propagation axis, and it behave like an insulator along the tangential axis. However, this model gives up the free-electron model due to the presence of the SSPs whose dispersion deviates from the light line, just like natural surface plasmons in the optical band, and lie below the Fabry-Perot (FP) resonance of the slit ($\lambda_c = n_s 2h$) which acts as their artificial plasma frequency. The free-electron model dictates that the $\varepsilon_x^{(\mathrm{eff})}$ has to be negative below the FP because the SSPs propagate along the grating interfaces below this frequency, but the conventional model as described above always gives the positive $\varepsilon_x^{(\mathrm{eff})}$. We revisit the effective model of the gratings stacked into multilayers in the chapter 5. We show in the chapter 5 that the stacked gratings can have the negative $\varepsilon_x^{(\mathrm{eff})}$ in favour to the free-electron model, and the $\varepsilon_y^{(\mathrm{eff})}$ is finite and always positive. There was the theoretical work suggesting to use the grating as endoscope at the FP resonance [80]. However, this work didn't employ the SSPs which lie a little bit below the FP. Instead, the authors theoretically excited the grating with structured Gaussian beam having closely-spaced two peaks at the FP of the finite size grating, and then the two peaks could propagate to the another side of the grating without suffering from the diffraction limit. In our case, we will employ the SSPs for the deep-subwavelength imaging instead of the FP resonance. Therefore, we discuss the properties of SSPs in this section. The message of this section is that we can use the SSPs in a bare grating for deep-subwavelength imaging in THz radiation band if we properly design the grating.

We give the definite parameters of the grating for THz radiation, and the reason for this choice will become clear shortly. The period of the slit is defined as 1 μm, slit width 0.2 μm, and the slit height 150 μm. The material filling the slit is defined as air. The input and output media are also air. In this case, the parameters $G_{\infty s}^{(\mathrm{in})} = G_{\infty s}^{(\mathrm{out})}$ and the analytical dispersion relation is obtained by the zeros of the dispersion function given in Eq. (3.35). Only the real part of the dispersion function is sufficient, and the imaginary part determines the amplitude of the spectra. In the case of the homogenized grating

using the conventional effective model [79], the dispersion relation is obtained by the zeros of the common denominator of zeroth-order reflection and transmission coefficients obtained by simple transfer matrix method. Therefore, the difference between the analytical dispersion relation and the effective dispersion relation is that the analytical solutions take into account all diffraction modes until the parameter $G_{\infty s}^{(\mathrm{in})}$ converged, while the effective dispersion relation takes only m=0 diffraction mode for the parameter $G_{\infty s}^{(\mathrm{in})}$ and all modes are neglected. Fig. 3.7 (a) and (b) show the transmission spectra and dispersion relations, respectively, comparing between the analytical solution (AN) and the conventional effective medium model (EFM). It can be seen that the EFM gives unprecedented consistent results with analytical spectra. For example, the analytical transmittance at 1 THz is 99.98%, and the effective transmittance at the same frequency is 100.00%, thus only 0.02% difference in transmittance. The dispersion relations obtained by two methods are also the same. In both case, the SSP dispersion relations are nearly flat. The cut-off frequency is approximately determined by the FP that is $\lambda_c = 2h$. Therefore, we choose the slit height as 150 so that the SSP frequency is close to 1 THz. In this case, we obtain the deep-subwavelength condition $k_x \gg k_0$. For example, at the edge of the Brillouin zone $k_x = \pi / p$, where p is 1 μm, we have k_x about 150 times larger than wavenumber in air for $f \approx 1$ THz. Therefore, if we are able to employ the SPPs in this structure, we could go down in the scale deep below the wavelength of light.

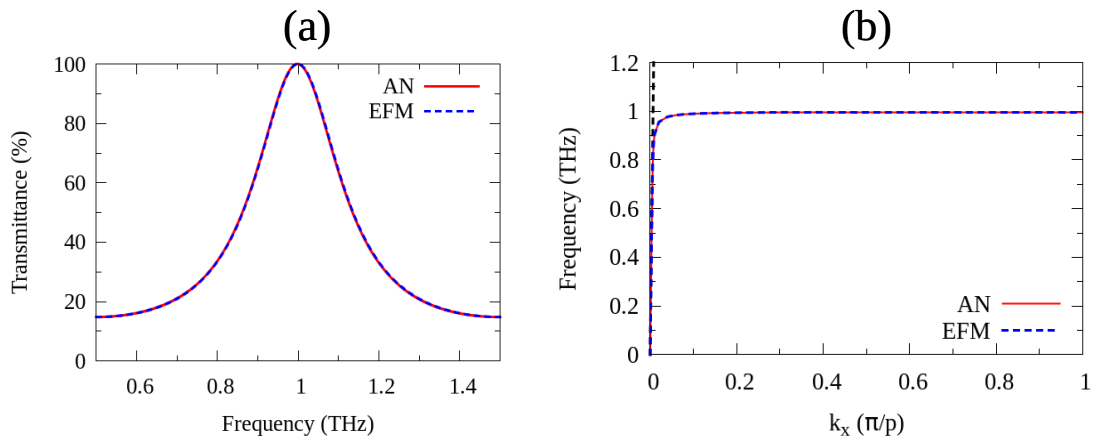

Fig. 3.7. (a) Transmission spectra of a bare grating comparing between analytical solutions and effective medium approximation. (b) Dispersion relation of the SSPs in a bare grating. Black dashed line indicates the light line. The parameters of the geometry are given in the main text.

Next, we give typical values of the localization length and the field enhancement of the SSPs in the bare grating. Such parameters are important to understand the interaction between the SSPs and the objects. We consider the SSP with the largest wavenumber at the edge of the first Brillouin zone $k_x = \pi / p$ which occurs at the frequency 0.99706 THz according to Fig. 3.7 (b). The $|H_z|$-distributions normalized with the amplitude of the incident evanescent light at y=0 in front of the grating, inside the grating, and behind the grating obtained by the analytical solutions are drawn over 7 unit cells as shown in Fig. 3.8 (a)-(c), respectively. The localizations of the magnetic fields on both sides of the grating due

to the SSPs are clearly seen in this figure. The decay length of the magnetic field, which is defined as the distance at which the amplitude of the magnetic field decrease by 1/*e*, is 225 nm in both interfaces of the grating. The magnetic field enhancement is in the second order which is relatively small. This is because the magnetic field forms the standing wave inside the slits in the grating with the maximum magnetic field reaches the fifth order at the centre of the grating. This leads to the smaller magnetic field enhancement at two faces of the gratings. Fig. 3.8 (d)-(e) show the |**E**|-distributions normalized with the amplitude of the incident evanescent light at *y*=0 in front of the grating, inside the grating, and behind the grating, respectively. The electric field is more strongly localized to the interfaces of the grating than the magnetic field. The decay length of the electric field is only 144 nm for two interfaces of the gratings. The amplitude of the electric field at the interfaces of the grating is in the fifth order which is much larger than the magnetic field along these interfaces. The reason for this can be seen in the |**E**|-distribution inside the grating. The electric field forms the standing wave inside the grating but with the minimum at the centre of the grating. It shows the maxima on two faces of the grating which lead to the higher field enhancement. This means that the electric field is more important than the magnetic field. It is necessary to bring the subwavelength objects within the decay length of the electric field in order to excite the SSPs in the grating. Therefore, the THz radiation at this frequency can reach the nano-scale by using the SSPs in the grating with the aforementioned parameters.

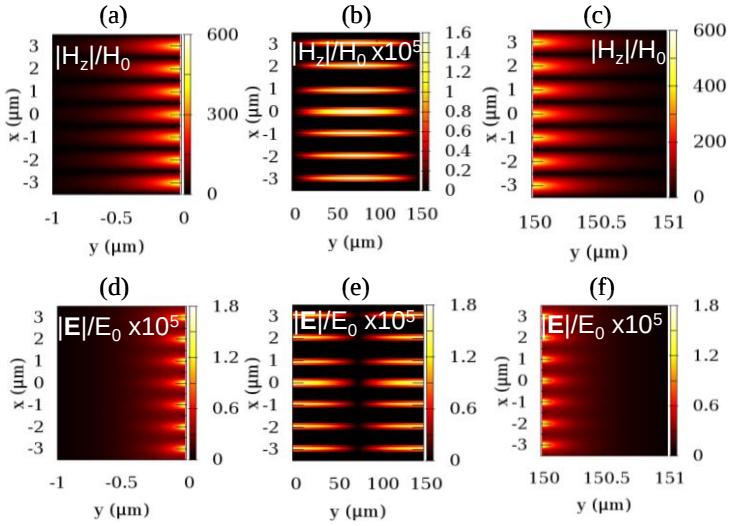

Fig. 3.8. SSPs in a bare grating. The $|H_z|$-distributions normalized by the amplitude of the incident magnetic field in (a) input region, (b) inside the grating, and (c) behind the grating of the SSP with wavenumber π / p at the frequency 0.99706 . The geometry of the grating is the same as Fig. 3.6. The |**E**|-distributions normalized by the amplitude of the incident electric field in (d) input region, (e) grating region, and (f) output region, of the SSP with the same wavenumber and frequency are also plotted.

3.3 Perfect absorbers for subwavelength sensing

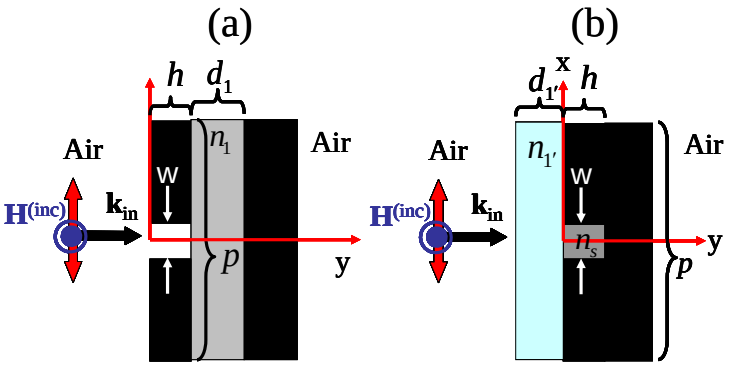

Fig. 3.9. Two types of perfect absorbers (PAs). (a) Back-PAs : the dielectric layer 2 is defined as PEC, and the dielectric layer 1 is defined as absorbing spacer, and the slit is filled with air. (b) Front-PAs: the dielectric layer 1 is defined as PEC, the slit is filled with absorbing material, and the dielectric layer $1'$ flats the surface of grating.

We first consider the perfect absorbers (PAs) proposed by A. P. Hibbins and J.R. Samples [77] as schematically shown in Fig. 3.9 (a). We will call these PAs as back-PAs since the heat is generated in the spacer behind the grating. Although the back-PAs have been widely investigated since then, there is no report of the exact formula of the absorbance to the best of our knowledge. The dielectrics/grating/dielectrics structure equivalent to the back-PAs is grating/spacer/PEC (M=0,N=2). In our case, the slit is filled with air. The thickness of PEC layer becomes irrelevant, and the transmittance is always zero. Therefore, the absorbance is only determined by the reflectance by A=1-R. The functions $W_m^{(\mathrm{in})}$ and $W_m^{(\mathrm{out})}$ become one and $i\cot\left(q_m^{(1)}d_1\right)$, respectively. Notice that if $d_1 = 0$, we obtain the SSPs on the perforated PEC surface. For $d_1 \neq 0$, the QWRs are induced inside the spacer (their dispersions are completely flat) by the Wood's anomaly whose frequency is determined by the condition $\sin\left(q_m^{(1)}d_1\right) = 0$

$$f_{m,j}^{(\mathrm{W})} = \frac{c}{n_1}\sqrt{\left(\frac{k_x}{2\pi}+\frac{m}{p}\right)^2+\frac{1}{4}\left(\frac{j}{d_1}\right)^2}\,, \tag{3.41}$$

where m,j=0,±1,±2,.... For j=0, the Wood's anomaly is identical to the Rayleigh's anomaly. The spacer must have small but non-zero imaginary part, otherwise light will be totally reflected. We choose the low-loss Zeonex polymer previously used in the metamaterial fibre as the spacer [30]. By assuming that the dielectric constant of Zeonex is non-dispersive and equal to 2.3104+0.002i, the frequency can be scaled by the period of the grating which is chosen as the length scale. The unit of frequency in this scalable is c/p. The slit height is defined as 0.01p so that the dispersion of the SSPs of a bare grating (no dielectric layers) is close to the light line which means that the electromagnetic field is delocalized in front of and behind the bare grating. However, the electromagnetic field can be localized inside the spacer due to the QWRs. Fig. 3.10 (a) shows that the nearly 100% absorbance of the 1st-QWR and 3rd-QWR can be achieved by optimizing the spacer thickness as $5\times10^{-4}\,p$ and $1.4\times10^{-3}\,p$, respectively. The 1st-QWR and 3rd-QWR are the standing waves which have one node and three nodes of the amplitude of the electric field on the metallic part of the grating, respectively. Fig. 3.10 (b) shows the

amplitude of the electric field inside the spacer normalized by the amplitude of the incident electric field for the 1st-QWR in the back-PA with $d_1 = 5\times10^{-4}\,p$. The amplitude of the electric field is three orders larger than the amplitude of the incident electric field, and one node is clearly seen between the two slits. The large amplitude of the electric field is due to the strong excitation of the surface charges on the metallic part of the grating surface which give the strong net dipole moment that can be coupled with the normal incident light [81]. Fig. 3.10 (c) also shows the amplitude of the electric field inside the spacer normalized by the amplitude of the incident electric field for the 3rd-QWR in the back-PA with $d_1 = 1.4\times10^{-3}\,p$. The electric field is weaker than the former case, and three nodes are clearly seen between the two slits. The even-order QWRs have zero net dipole moments on the metallic part of the grating surface at the normal incidence, and thus they can be excited only by the oblique incidence where $k_x \neq 0$ [81]. The Q-factors (f/Δf) for the 1st-QWR and the 3rd-QWR with the optimized thickness are 573 and 738, respectively. By further increasing the spacer thickness to $d_1 = 8.0\times10^{-3}\,p$, both resonant peaks make red shift, the corresponding absorbance and Q-factors drop, as shown in Fig. 3.10 (a). In this sense, the back-PA is mechanically tunable.

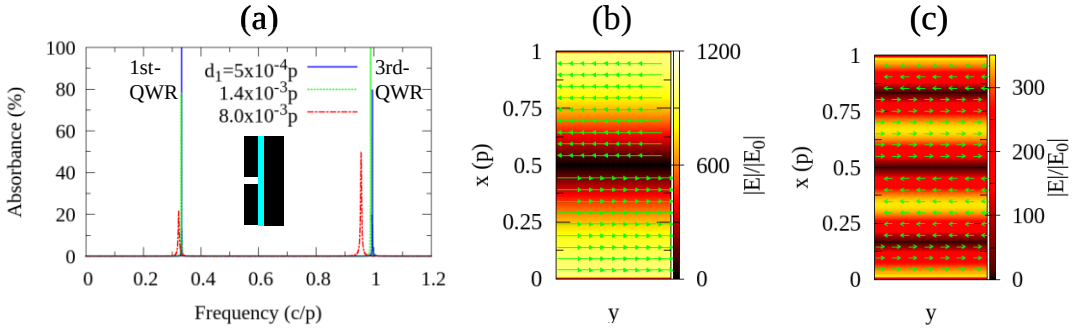

Fig. 3.10. Analytical absorption spectra and |E|-distributions of back-PAs. (a) Absorption spectra of three back-PAs with different spacer thickness indicated in the figure. The resonant frequencies of the 1st-QWR of the $d_1 = 5\times10^{-4}\,p$ and the 3rd-QWR of the $d_1 = 1.4\times10^{-3}\,p$ are 0.33278 c/*p* and 0.98970 c/*p*, respectively. (b) Normalized |**E**|-distribution inside the spacer at the 1st-QWR of the $d_1 = 5\times10^{-4}\,p$. (c) Normalized |**E**|-distribution inside the spacer at the 3rd-QWR of the $d_1 = 1.4\times10^{-3}\,p$. The green arrows indicate the directions of electric fields which also imply the distribution of surface charges on the metallic part of the grating. The |**E**|-distribution is between the centre of two slits and covers only one unit cell. The slit height and slit width are 0.0*2*p.

For sensing application we are interested in changes of the resonant peak, e.g., frequency shift due to the presence of a thin film. Therefore, it is important to consider the |**E**|-distribution in the input region at the resonant frequency. Fig. 3.11 shows the |**E**|-distribution normalized by the amplitude of the incident electric field at the 3rd-QWR in front of the grating of the back-PAs with the optimized thickness $d_1 = 1.4\times10^{-3}$. It is found the normalized |**E**| is strongly localized to the slit's opening at x(p)=-1, 0 1 with the full width at half maximum (FWHM) along the *y*-axis equal to 0.008*p* and the maximum of the normalized |**E**| is 5.8 times weaker than that inside the spacer. However, the |**E**| between two slits is delocalized with the FWHM along the *y*-axis equal to 0.881*p* and the maximum of the normalized |**E**| only 13. This makes the back-PAs insensitive to the presence of the thin film located

just next to the grating. Furthermore, the back-PA is not really flat sensor, and thus it is not convenient to serve as the platform for characterizing subwavelength films.

In order to bring the large field enhancement to the front side of the grating, we introduce a flat front-PAs as schematically shown in Fig. 3.9 (b). The dielectrics/grating/dielectrics structure in Fig. 3.1 equivalent to the front-PAs is dielectric/grating/PEC (*M*=1,*N*=1). The grating/PEC now becomes the perforated PEC plane. The slit is filled with absorbing material which we define as Zeonex polymer. The dielectric layer in front of the grating is defined as HR-Si with no loss. Therefore, heat is generated only inside the slit. The dispersion relation of the front-PAs is identical to that of the SSPs : $G_{\infty s}^{(\mathrm{in})} - \gamma = 0$. The cut-off frequency of the SSPs excited on the surface of the perforated PEC plane with the approximation $p \ll \lambda$ and $w \ll \lambda$ is determined by the condition $\cos(k_s h) = 0$ which leads to the cut-off frequency $f_c = c(2j-1)/4n_s h$ where *j*=1,2,3,... [57]. These SSPs may be considered as the odd-order SSPs because of the odd integer 2*j*-1 in the numerator of the cut-off frequency. The Fabry-Perot (FP) inside the slit cavity also leads to the excitation of the SSPs below its frequency, and the cut-off frequency due to the FP is determined by the condition $\sin(k_s h) = 0$ which leads to another cut-off frequency $f_c = c2j/4n_s h$ where *j*=1,2,3,... . These SSPs may be considered as the even-order SSPs because of the even integer 2*j* in the numerator of the cut-off frequency. Therefore, we can tune the frequency of SSPs by changing the slit height. In our case, we store the heat at the frequency below the Fabry-Perot resonance (FP) inside the slit cavity which is the cut-off frequency of the second-order SSPs on the grating surface. That means the heat is stored in some part of the SSPs on the surface of the perforated PEC plane. Then, these SSPs are excited by the first-order SSPs on the surface of the finite size HR-Si layer as denoted by $\mathrm{SSPs}(1/\mathrm{HR\text{-}Si})$. Therefore, we have two types of SSPs play role in the front-PAs, different from the back-PAs which have only the QWRs.

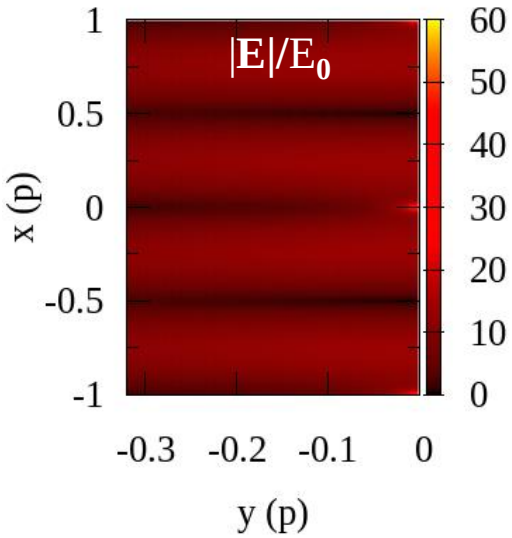

Fig. 3.11. Analytical normalized |E|-distribution in font of the grating of the back-PAs. The back-PAs has $d_1 = 1.4\times10^{-3}$ and the resonant frequency is at the 3rd-QWR as shown in Fig. 3.10 (a). The normalized |**E**|-distribution covers two unit cells along the *x*-axis.

Fig. 3.12 (a) shows sharp and nearly perfect absorption peaks of front-PAs with HR-Si thicknesses $d_{1'} = 0.03p, 0.056p, 0.10p$ and optimized slit heights $h = 0.300p, 0.342p, 0.465p$, respectively. The smaller absorption peaks correspond to the excitations of higher-order SSPs on the surface of the HR-Si. The Q-factors of the $d_{1'} = 0.03p, 0.056p, 0.10p$ front-PAs are 30,267, 10,115, and 3,505, respectively. The ultrahigh Q-factors of the front-PAs are induced by two divergences in the dispersion function that are the divergences of the Wood's anomaly and the divergences of the Fabry-Perot (FP) in the slit' cavity. For example, Fig. 3.12 (b) shows the components of the dispersion function of the $d_{1'} = 0.10p$ front-PA. The divergence of $G_{\infty S}^{(\mathrm{in})}$ as indicated by red solid line corresponds to the *m*th-order Wood's anomaly as also indicated in the figure, the divergence of γ as indicated by the red dashed line corresponds to the Faby-Perot resonance, and the crossing point as indicated by solid circle marks the resonant frequency. The Q-factors of the front-PAs are higher than those of the previous back-PAs because of the more rapidly changes of dispersion function as a function of frequency around the resonant frequency. The ultrahigh Q-factor leads to the large electric field enhancement at the air/HR-Si interface. Fig. 3.12 (c) shows the |**E**|-distribution normalized by the amplitude of the incident electric field at the resonant frequency of the optimized $d_{1'} = 0.10p$ front-PA in front of the grating. The bright spots at the air/HR-Si interface has the electric field enhancement about 88.8 with the FWHM of the electric field along the *y*-axis about 0.151*p*. The decay of |**E**| results from the decay of E_y of the *m*=±1 diffraction modes in air as shown in Fig. 3.12 (d). The blobs seen inside the HR-Si in Fig. 3.12 (c) are due to the localization of the E_x of the *m*=±1 diffraction modes from the air/HR-Si interface as shown in Fig. 3.12 (e). These electromagnetic fields are evanescent waves which do not propagate to the far-field. Fig. 3.13 also shows the |**E**|-distributions at the resonant frequencies for the other two front-PAs. It can be seen that, by reducing the HR-Si thickness, the electric field enhancement is larger, but the FWHM of the electric field along the *y*-axis is longer. Therefore, by reducing the thickness of the HR-Si, the maximum of |**E**| is larger along with higher Q-factor, but the electric field becomes more delocalized along the *y*-axis. This behaviour suggests the optimized thickness of the HR-Si layer which yields the largest sensitivity to the resonant peak due to the presence of a thin layer next to the HR-Si layer. The sensitivities of the front-PAs as the subwavelength film sensor is given in the next section.

3.4 Sensitivities of perfect absorbers as subwavelength film sensors

The presence of a thin layer 2′ with thickness $d_{2'}$=0.01*p* causes red shifts of the resonant peaks of the front-PAs as shown in Fig. 3.14 (b) for $d_{1'}$=0.056*p*, *h*=0.342*p* front-PA. The frequency shifts from the front-PAs are apparently larger than those from the back-PA which is also shown in Fig. 3.14 (a). The sensitivity is usually defined as the slope of the frequency shift curve as a function of sample refractive index $n_{2'}$. We then numerically compute the sensitivities of three front-PAs as a function of $n_{2'}$ with fixed thickness $d_{2'}$=0.01*p*, and the results are shown in Fig. 3.14 (c). We find that the sensitivities of all front-PAs are not constant but behave like upturned curves having the maximum values at $n_{2'}$ close to 1 and making broad dips over small ranges of $n_{2'}$. For small $n_{2'}$ close to 1, the $d_{1'}$=0.056*p* front-PA yields the highest sensitivity although its field enhancement is smaller than that of $d_{1'}$=0.03*p* front-PA. The

sensitivity of $d_{1'}$=0.056p front-PA at $n_{2'}$=1.6 (photoresist) is about 0.0167 (c/p)/RIU (RIU: refractive index unit). Therefore, if p=100 μm, the sample's thickness becomes $d_{2'}$=1 μm, and the sensitivity of $d_{1'}$=0.056p=5.6 μm front-PA is equal to 50 GHz/RIU which is 5 times larger than that obtained by the Fano resonance in non-flat asymmetric split ring metamaterial [82].

Although the behaviours seen in Fig. 3.14 (c) can be expected to be described in terms of |**E**| and FWHM along the y-axis as mentioned in the previous section, but we find that it is much more easier to describe these results by using the first-order Wood's anomaly whose frequency is determined for the case of no sample. Indeed, the red shift due to the presence of the thin film 2′ results from the red shift of the first-order Wood's anomaly due to the change of the denominator of $W_{m=1}^{(\mathrm{in})}$. We find similar behaviours as Fig. 3.14 (c) by monitoring the m=1 Wood's anomaly frequency which means that the first-order Wood's anomaly can be used to optimize the HR-Si layer thickness $d_{1'}$ giving the highest sensitivity in terms of the frequency shift. This scheme is much more convenient than the direct use of the resonant frequency which takes into account all diffraction modes.

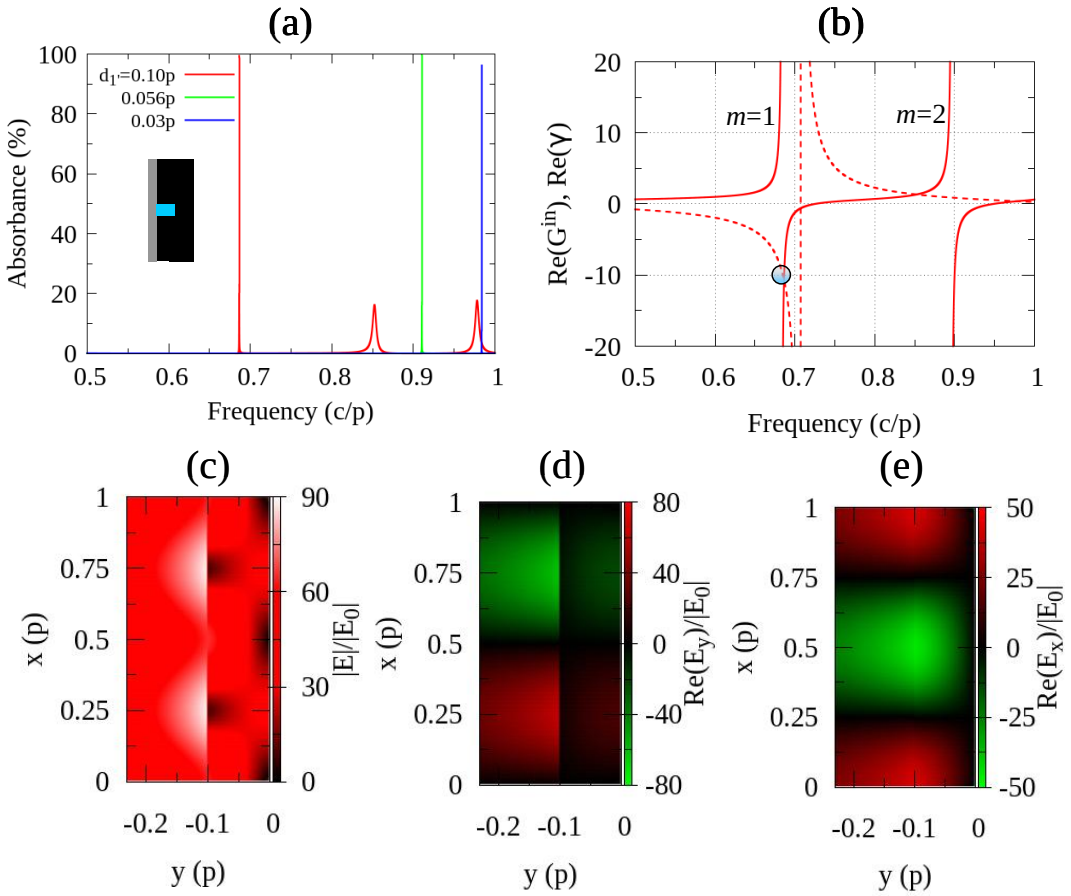

Fig. 3.12. Analytical absorption spectra and normalized |E|-distribution of front-PAs. (a) Absorption spectra of three front-PAs with different thicknesses of HR-Si layer as indicated in the figure. The slit heights are optimized as h=0.465p, 0.342p, and 0.300p, for the HR-Si thickness $d_{1'}$=0.10p, 0.056p, and 0.03p, respectively. The slit width is fixed as w=0.02p. The nearly perfect absorption peaks for the optimized $d_{1'}$=0.10p, 0.056p, and 0.03p front-PAs are at the frequencies 0.686445 c/p, 0.910399 c/p, and 0.983693 c/p, respectively. (b) Components of the dispersion function for the optimized $d_{1'}$=0.10p front-PA. The $\mathrm{Re}\left(G_{\infty s}^{(\mathrm{in})}\right)$ is indicated by red solid line, and $\mathrm{Re}(\gamma)$ is indicated by red dashed line. The solid circle at the crossing point between the two components marks

the resonant peak of this front-PA. (c) Normalized |**E**|-distributions, (d) Normalized real part of E_y , and (e) Normalized real part of E_x, in front of the grating at the nearly perfect absorption peaks of (c) the optimized $d_{1'}$ =0.10p front-PA, (d) the optimized $d_{1'}$ =0.056p front-PA, and (e) the optimized $d_{1'}$ =0.03p front-PA.

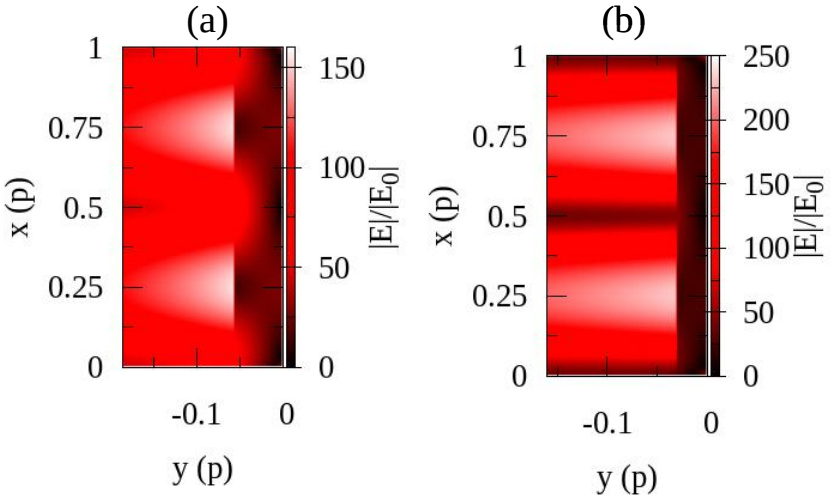

Fig. 3.13. Analytical normalized |E|-distributions of front-PAs. (a) The optimized $d_{1'} = 0.056p$ front-PA at its resonant frequency. (b) The optimized $d_{1'} = 0.03p$ front-PA at its resonant frequency.

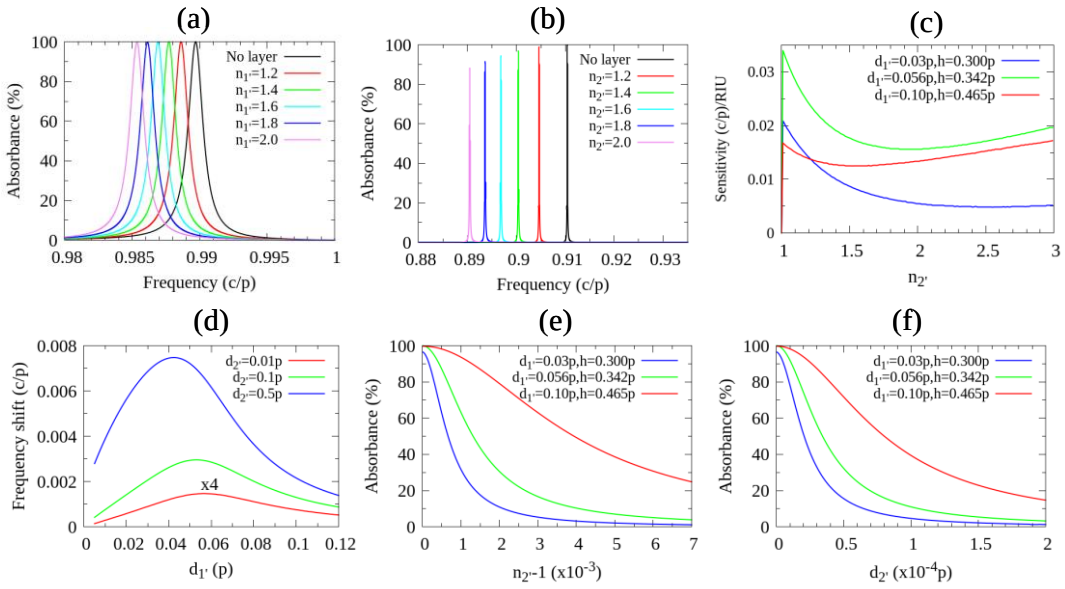

Fig. 3.14. Sensitivities of front-PAs as subwavelength film sensor. (a) Absorption spectra of the $d_1 = 1.4\times10^{-3}\,p$ back-PA near its 3rd-QWR when the sample layer 1' with thickness $d_{1'} = 0.01p$ and various refractive indices $n_{1'}$ are placed in front of the grating. (b) Absorption spectra of the $d_{1'} = 0.056p, h = 0.342p$ front-PA near its resonant frequency when sample layer 2' with thickness $d_{2'} = 0.01p$ and various refractive indices $n_{2'}$ are placed in front of the HR-Si layer. (c) Sensitivities of three front-PAs indicated in the figure as a function of sample refractive index $n_{2'}$. The thickness of the sample is fixed as $d_{2'} = 0.01p$. (d) Frequency shifts as a function of HR-Si thickness obtained by monitoring the spectral position of the Wood's anomaly for the sample with fixed refractive index $n_{2'} = 1.01$ and three values of the sample thicknesses as indicated in the figure. The frequency shifts for the sample thickness $d_{2'} = 0.01p$ are multiplied by the factor 4. (e.f) Absorbance at the original resonant

frequency of three front-PAs indicated in the figure as a function of small variations (e) in sample refractive index with fixed sample thickness $d_{2'} = 0.01p$, and (d) in sample thickness with fixed refractive index $n_{2'} = 1.6$.

Fig. 3.14 (d) shows the frequency shifts of the m=1 Wood's anomaly as a function of $d_{1'}$ for three sample thicknesses with fixed sample refractive index $n_{2'}$=1.01. The HR-Si layer thickness which yields the maximum frequency shifts for sample thicknesses 0.01p, 0.1p, and 0.5p are equal to 0.056p, 0.053p, and 0.042p, respectively. Therefore, the thicker the sample, the thinner HR-Si layer is needed to provide the largest frequency shift because the field enhancement becomes larger and delocalized by increasing the HR-Si thickness. Note that this approach doesn't include the effect of γ. But it can be seen from Fig. 3.14 (b) that the frequency shifts also depend on the slope of γ. Therefore, the frequency shifts obtained by monitoring the first-order Wood's anomaly slightly decrease by including the non-zero slope of γ parameter. The frequency shifts shown in Fig. 3.14 (d) are sufficient for thin film detections if we monitor the absorbance at the original resonant peak and harness its ultrahigh Q-factor and the perfect absorption. Fig. 3.14 (e) shows the absorbance as a function of small variations in refractive indices of the sample with the same thickness $d_{2'}$=0.01p at the original resonant peak of three front-PAs. The absorbance of $d_{1'}$=0.03p, 0.056p, and 0.1p front-PAs decrease 50% by increasing refractive indices with an amount $0.69\text{x}10^{-3}$, $1.31\text{x}10^{-3}$, and $5.62\text{x}10^{-3}$ RIU respectively. Although the $d_{1'}$=0.056p front-PA gives the largest frequency shift, but the highest Q-factor of $d_{1'}$=0.03p front-PA is more sensitive by monitoring the absorbance at the original resonant frequency. The change of refractive index by $0.69\text{x}10^{-3}$ in this $d_{2'}$=0.01p film can be detected by observing 50% decrease in the absorbance. Fig. 3.14 (f) also shows the absorbance as a function of small variations in sample thicknesses with fixed refractive index $n_{2'}$=1.6 at the original resonant peak. The absorption curves in this figure follow the same trends as those in Fig. 3.14 (e). The absorbance of $d_{1'}$=0.03p, 0.056p, and 0.1p front-PA decrease 50% by increasing sample thickness by $0.213\text{x}10^{-4}p$, $0.342\text{x}10^{-4}p$, and $1.137\text{x}10^{-4}p$, respectively. Therefore, the presence of deep-subwavelength film can be detected by the front-PA. For example, if p=100 μm, then $d_{1'}$=0.03p front-PA can detect nanofilm with thickness 2.13 nm by observing 50% decrease of the absorbance at the original resonant peak of this front-PA which is at f=2.94904 THz or λ=101.658 μm.

Lastly, we note that the analytical solutions may be applied to the higher frequency region by including the surface impedance boundary condition to the surface of the metallic grating [50]. The analytical solutions of the dielectrics/grating/dielectrics structure lead to the development of the new hyperbolic metamaterials with the stacked grating/dielectric layers as will be described in the chapter 4 and 5. The analytical solutions developed in this chapter takes into account only the fundamental waveguide mode of the slit cavity, and the more rigorous analysis taking into account all waveguides are given in the chapter 4 which can be applied to this chapter. The analytical solutions are valid only for the one-dimensional grating, but they can be easily extended into two-dimensional structures such as the rectangular hole array [52], and the spherical hole array [49], by changing the waveguide modes and modify the coupling parameters. The finite number of slits and holes can be also realized by replacing the summation of the discrete diffraction waves with the integration of the continuous diffraction waves [56].

3.5 Conclusion

In this chapter, we have developed the analytical solutions of the dielectrics/grating/dielectrics metamaterials to make new hyperbolic metamaterials for the THz radiation. The analytical solutions are consistent with the FDTD simulation, but yield more accurate results and more efficient. The resonant peaks in the transmission spectra are studied analytically by the analytical solutions. We have found and explained that the Wood's anomalies are the origins of the ultrahigh Q-factors found in the resonant peaks corresponding to the excitations of the high-order SSPs on the surface of the dielectric layer attached to the grating. This leads us to realize another applications of these structures in the THz subwavelength sensing with the ultrahigh-Q factor. We have applied the first-order SSPs in the HR-Si/grating/PEC structure to make the new perfect absorbers with ultrahigh Q-factors for the subwavelength-films sensing. The new scheme for the optimization of the largest frequency shift due to the presence of the subwavelength film by using the first-order Wood’s anomaly is introduced. The results suggest the target-dependent sensing in which the highest frequency shifts depend on sizes and refractive indices of the samples. The sensitivity of our new structure is 5 times larger than the sensitivity of the asymmetric split ring metamaterial. We also demonstrated another scheme of subwavelength-films sensing by monitoring the drop of the absorbance at the resonant peak of the structure. We showed that the presence of nanofilms with size down to a few nanometre can be detected by observing the 50% drop of the absorbance at the resonant peak. The analytical solutions close the gap of the difficulties in the optimizations of subwavelength dielectrics/gratings/dielectrics metamaterials with FDTD simulation and open the new route to the efficient designs of the novel devices for both subwavelength imaging and sensing for THz.

Chapter 4

Analytical solutions of stacked grating/dielectric metamaterials for THz subwavelength imaging

This chapter extends the analytical solutions of the dielectrics/grating/dielectrics structures developed in the previous chapter to the case of stacked grating/dielectric structures in which grating and dielectric layers are alternated along the propagation axis. The stacked grating/dielectric structures form the effective hyperbolic metamaterials which can be applied to image subwavelength objects in THz frequency band. The similar structure to our structure is two layers of hole arrays separated by the dielectric layer which is known as the fishnet structure [83]. The fishnet structure has been theoretically investigated as an isotropic medium having the same refractive index in all directions. By stacking the fishnet structure into multilayered fishnet, the effective refractive index of this metamaterial can be negative in the infrared band due to the excitation of magnetic resonance between two layers of hole arrays [84]. However, the single fishnet and multilayered fishnet structures have not yet been applied in subwavelength imaging, and only its optical spectra have been investigated [85]. In this chapter, we analytically demonstrate the deep-subwavelength imaging of the array of the slits as the object with size down to 1 μm for the THz radiation at the wavelength 300 μm by using (i) a bare grating, and (ii) stacked grating/dielectric structure. The imaging properties, i.e., imaging resolution, image intensity, and optical spectra are given. Unlike the fishnet structures which are considered as the isotropic medium, the stacked grating/dielectric structures are regarded as hyperbolic metamaterials, the properties hinted by the anisotropic property of the grating. The effective parameters of the stacked grating/dielectric hyperbolic metamaterials will be given in the next chapter.

The chapter is organized as follows. The analytical solutions of the electromagnetic fields in the stacked grating/dielectric structures are given in the section 4.1. We will learn from this section how to calculate the electromagnetic fields and optical spectra of the stacked grating/dielectric structures. The section 4.2 compares the analytical solutions with the FDTD simulation. The analytical demonstration of the deep-subwavelength imaging over a short distance with a bare grating is given in the section 4.3, and the deep-subwavelength imaging over the long distance by using the stacked grating/dielectric layers is analytically demonstrated in the section 4.4. The chapter is summarized in the section 4.5.

4.1 Analytical solutions of electromagnetic fields in stacked grating/dielectric structures.

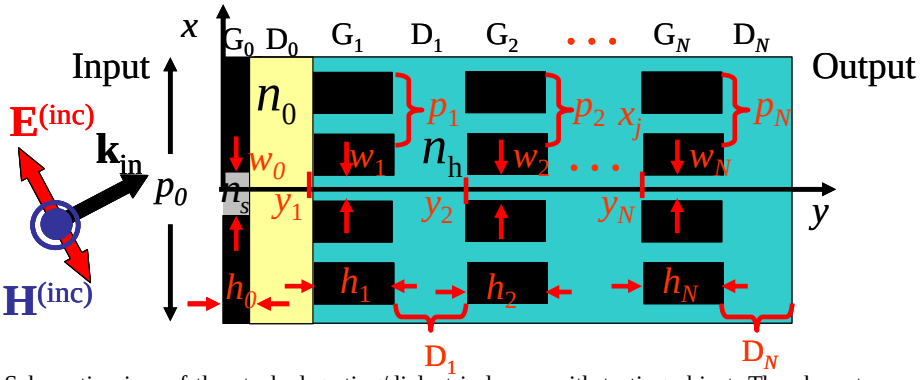

Fig. 4.1 Schematic view of the stacked grating/dielectric layers with testing object. The characters on top of the structure indicate the regions beneath them. The thickness of dielectric layer is denoted by the same character which indicates the dielectric region. Location of the grating D_j along the *y*-axis is denoted by y_i , and the location of the slit along the *x*-axis in each grating is denoted by x_j. The grating G_0 represents the testing object whose unit cell is called the superlattice.

The schematic view of the stacked grating/dielectric layers metamaterials is shown in Fig. 4.1. There are two main parts in this figure. The first part is an subwavelength object to be imaged to the far-field. This object is infinite array of slits in the front grating denoted by G_0. The width of the slit w_0 is the size of the object, and the grating period is the distance between the two objects. The second part is the lens as indicated by the blue region in this figure. The lens is the metamaterial made by stacked grating/dielectric layers. The slit width, slit height and period of the gratings in this lens can be different from another grating. The number of slits (or waveguides) within the period p_0 of the object can be varied. Lastly, the number of stacked grating/dielectric layers is denoted by *N*. These two parts are separated from each other by the dielectric layer with refractive index n_0 (zero indicates the object and does not indicate air) and with thickness D_0. The distance D_0 plays important role in subwavelength imaging, and one should not assume that the object perfectly touches the lens and D_0 is zero in the first place. Next, we have to solve for the electromagnetic fields in each region similar to the previous chapter. It is useful to review the solution in each region again for convenience.

4.1.1 Electromagnetic fields in all regions

We will explain the solutions of the electromagnetic fields in all regions from the input region (left) to the output region (right). The solutions of $H_z^{(\text{in})}$ and $E_x^{(\text{in})}$ in the input region of the stacked grating/dielectric structure are the same as Eq. (3.1) and (3.2), respectively, with $D_{\text{in}} = 0$. The field coefficients for the reflected light is also denoted by the same variable $B_m^{(\text{in})}$. For the grating G_0 whose slits are considered as subwavelength objects, only the fundamental waveguide mode is excited within the slits, and thus the magnetic field in the slit denoted as $H_z^{(\text{G0})}$ and the electric field in the slit denoted as $E_x^{(\text{G0})}$ are the same as Eq. (3.5) and (3.6), respectively. We move quickly to the dielectric layer D_0. The solutions of magnetic field denoted as $H_z^{(\text{D0})}$ and the electric field denoted as $E_x^{(\text{D0})}$ in this region

are expanded in terms of the Bloch's basis functions, and thus they are expressed in the same forms as Eq. (3.10), and (3.11), respectively, with the substitutions $\varepsilon_j \to \varepsilon_0$ and $q_m^{(j)}\left(y - D_{j-1}\right) \to q_m^{(\mathrm{h})}\left(y - D_0\right)$, where $q_m^{(\mathrm{h})}$ denotes the normal component of the Bloch wavevectors in the host medium. The field coefficients for right and left travelling waves are denoted by $A_m^{(\mathrm{D0})}$ and $B_m^{(\mathrm{D0})}$, respectively.

Next, we enter the lens region. The grating G_1 is the closest grating to the subwavelength objects. We will relax the assumption about the width of the slit to make the solution more general. We will take into account all waveguide modes of the slit as given in Eq. (3.9). But please note that if the slit width is comparable to the wavelength of light, the high number of waveguide modes are required to determine the electromagnetic fields in all regions accurately, and then this analytical solutions become poor choices. The analytical solutions are best applied to the case of the slit with subwavelength width because then only the fundamental waveguide mode is used in the calculation which makes the method very fast. Anyway, we would not know all of these if we didn't include all waveguide modes and try out how slow they are for the case of wide slits. Therefore, let's us include them all. We will denote the waveguide mode by the symbol α, and also we define the location of waveguide (slit) in the *x*-direction within the superlattice of the grating G_0 by x_j. Then, the waveguide mode α in the slit located at the location x_j (called *j*-slit hereafter) of the grating G_1 is labelled by $\left|\mathrm{G1},j,\alpha\right\rangle$. By using these waveguide modes as the basis functions, the magnetic and electric fields in the *j*-slit of the grating G_1 are expressed as

$$\left|H_z^{(\mathrm{G1})}\left(y\right)\right\rangle = -\sum_j \sum_\alpha \left\{C_{G1,j,\alpha} \exp\left[ig_y^{(j,\alpha)}\left(y - y_1\right)\right] - D_{G1,j,\alpha} \exp\left[-ig_y^{(j,\alpha)}\left(y - y_1\right)\right]\right\} \left|\mathrm{G1},j,\alpha\right\rangle, \quad (4.1)$$

$$\left|E_x^{(\mathrm{G1})}\left(y\right)\right\rangle = \frac{1}{\omega\varepsilon_0\varepsilon_{\mathrm{h}}} \sum_j \sum_\alpha g_y^{(j,\alpha)} \left\{C_{G1,j,\alpha} \exp\left[ig_y^{(j,\alpha)}\left(y - y_1\right)\right] + D_{G1,j,\alpha} \exp\left[-ig_y^{(j,\alpha)}\left(y - y_1\right)\right]\right\} \left|\mathrm{G1},j,\alpha\right\rangle, \quad (4.2)$$

where $\alpha = 0,1,2,\ldots$, $g_x^{(j,\alpha)}$, $g_y^{(j,\alpha)} = \sqrt{k_h^2 - g_x^{(j,\alpha)2}}$. For $\alpha \neq 0$, the normal component of the electric field is not-zero an can be obtained by the magnetic field. The field coefficients of the slits are re-defined by $E_{G1,j,\alpha}^{(\mathrm{in})}$ and $E_{G1,j,\alpha}^{(\mathrm{out})}$ via the relations given in Eq. (3.14) with the substitutions $k_{\mathrm{s}} \to g_y^{(\alpha)}$ and $\varepsilon_{\mathrm{s}} \to \varepsilon_{\mathrm{h}}$. Then, we will solve for the $E_{G1,j,\alpha}^{(\mathrm{in})}$ and $E_{G1,j,\alpha}^{(\mathrm{out})}$ instead by applying the coupled-mode analysis.

We move to the dielectric layer D_1 separating the gratings G_1 and G_2. The magnetic field denoted as $H_z^{(\mathrm{G1})}$ and electric field denoted as $E_x^{(\mathrm{D1})}$ in this region are also expressed in terms of the Bloch's basis functions. Therefore, they have the same form as Eq. (3.10) and (3.11) for the magnetic field and electric field, respectively, with the substitutions $\varepsilon_j \to \varepsilon_{\mathrm{h}}$ and $q_m^{(j)}\left(y - D_{j-1}\right) \to q_m^{(\mathrm{h})}\left(y - \left(y_1 + h_1\right)\right)$. The field coefficients for the right and left travelling waves in this region are denoted by $A_m^{(\mathrm{D1})}$ and $B_m^{(\mathrm{D1})}$, respectively. The magnetic field $H_z^{(\mathrm{Di})}$ and electric field $E_x^{(\mathrm{D}i)}$ in the remaining dielectric layers $\mathrm{D}_{i\neq 1}$ of the lens also have the same form as those in the dielectric layer D_1 except the phase factor and the field coefficients. The phase factor for right and left

travelling wave becomes $q_m^{(\mathrm{h})}\left(y-\left(y_i+h_i\right)\right)$, and the field coefficients for the right and left travelling waves are defined as $A_m^{(\mathrm{D}i)}$ and $B_m^{(\mathrm{D}i)}$, respectively.

The remaining gratings $\mathrm{G}_{i\neq 1}$ of the lens have the magnetic field denoted as $H_z^{(\mathrm{G}i)}$ and electric field denoted as $E_x^{(\mathrm{G}i)}$ with the same form as Eq. (4.1) and (4.2), respectively, except the phase factor and the field coefficients. The phase factor of the grating $\mathrm{G}_{i\neq 1}$ becomes $g_y^{(\alpha)}\left(y-y_i\right)$ which is defined from its location along the *y*-axis, and the field coefficient for the input and output sides of the grating are defined as $E_{Gi,j,\alpha}^{(\mathrm{in})}$ and $E_{Gi,j,\alpha}^{(\mathrm{out})}$, respectively.

The last region is the output region. We have only the transmitted light in this region. The magnetic field $H_z^{(\mathrm{out})}$ and the electric field $E_x^{(\mathrm{out})}$ have the same form as Eq. (3.12) and (3.13), respectively. The parameter $\mathrm{D}_{\mathrm{out}}$ refers to the total length of the structure from the grating G_0 to the last dielectric layer D_{N}.

4.1.2 Coupling of electromagnetic fields between two gratings

At the first glance, the problem of solving for all field coefficients seems to be very easy. Those who know the transfer matrix method may try to homogenize the grating as an effective medium and apply the transfer matrix method to the stacked homogenized-grating/dielectric structure. The solutions may look simple, but they will be surprised that the results are not consistent with FDTD simulation as shown by black dashed line in Fig. 4.3 (a). Then, we are led to think that there is near-field interaction between the gratings where high diffraction modes play important role. The homogenized grating discards those modes and retain only $m=0$, thus it misses this interaction. This section will explain the coupling between two gratings. Once we know this, it becomes easy to connect the field coefficients in all regions. We consider two cases. The first case is the dielectric region between the grating G_0 and the grating G_1 which is the region between the object and the lens. The second case is the dielectric region between two gratings of the lens.

In the first case, we start from the interface $y=h_0$. The field coefficients of the dielectric layer D_0 are related to the field coefficients of the grating G_0 via the continuties of H_z and E_x at the output interface of the slit in the grating G_0. This relation can be written in the matrix notation as

$$\begin{pmatrix} A_m^{(\mathrm{D}0)} \\ B_m^{(\mathrm{D}0)} \end{pmatrix} = \frac{n_{\mathrm{s}}}{2}\begin{bmatrix} G_{\mathrm{V}}^{(\mathrm{G}0)} & n_{0\mathrm{s}}iY_m^{(0)}+\gamma^{(\mathrm{G}0)} \\ G_{\mathrm{V}}^{(\mathrm{G}0)} & -\left(n_{0\mathrm{s}}iY_m^{(0)}+\gamma^{(\mathrm{G}0)}\right) \end{bmatrix}\begin{pmatrix} \bar{E}_0^{(\mathrm{in})} \\ \bar{E}_0^{(\mathrm{out})} \end{pmatrix}\left\langle \beta_m \middle| 0 \right\rangle, \tag{4.3}$$

where $G_{\mathrm{V}}^{(\mathrm{G}0)}=\csc\left(k_{\mathrm{s}}h_0\right)$, $\gamma^{(\mathrm{G}0)}=\cot\left(k_{\mathrm{s}}h_0\right)$, $n_{0\mathrm{s}}=n_0/n_{\mathrm{s}}$, $Y_m^{(0)}=k_{\mathrm{h}}/q_m^{(0)}$ is the admittance, and bar on the field coefficients of the grating G_0 denotes the normalization of the original field coefficients by the factor $\left(\omega\varepsilon_0/ik_0\right)/H_0$ where H_0 is the amplitude of the incident magnetic field. The field coefficients of the dielectric layer D_0 are also related to the field coefficients of the grating G_1 by the continuties of H_z and E_x at the input interface of the *j*-slit in this grating. This relation can be expressed in the matrix form as follows

$$\begin{bmatrix} \exp\left(i\phi_m^{(\mathrm{D0})}\right) & \exp\left(-i\phi_m^{(\mathrm{D0})}\right) \\ \exp\left(i\phi_m^{(\mathrm{D0})}\right) & -\exp\left(-i\phi_m^{(\mathrm{D0})}\right) \end{bmatrix} \begin{pmatrix} A_m^{(\mathrm{D0})} \\ B_m^{(\mathrm{D0})} \end{pmatrix} = n_0 \sum_j \sum_\alpha \begin{bmatrix} \gamma_{j,\alpha}^{(\mathrm{G1})} & G_{\mathrm{V},j,\alpha}^{(\mathrm{G1})} \\ -iY_m^{(0)} & 0 \end{bmatrix} \begin{pmatrix} \bar{E}_{G1,j,\alpha}^{(\mathrm{in})} \\ \bar{E}_{G1,j,\alpha}^{(\mathrm{out})} \end{pmatrix} \langle \beta_m | G1, j, \alpha \rangle, \quad (4.4)$$

where $\phi_m^{(\mathrm{D0})} = q_m^{(\mathrm{D0})} D_0$, $G_{\mathrm{V},j,\alpha}^{(\mathrm{G1})} = \left(k_\mathrm{s} / \mathrm{g}_y^{(j,\alpha)}\right) \csc\left(\mathrm{g}_y^{(j,\alpha)} h_1\right)$, and $\gamma_\alpha^{(\mathrm{G1})} = \left(k_\mathrm{s} / g_y^{(j,\alpha)}\right) \cot\left(g_y^{(j,\alpha)} h_1\right)$. Then, by substituting Eq. (4.3) into (4.4), we obtain two linear equations which relate the fields coefficients between the gratings G_0 and G_1 which are written as

$$\begin{aligned} & G_\mathrm{V}^{(\mathrm{G0})} \sin\left(\phi_m^{(\mathrm{D0})}\right) \bar{E}_0^{(\mathrm{in})} \langle \beta_m | 0 \rangle + \left\{ n_{0\mathrm{s}} Y_m^{(0)} \cos\left(\phi_m^{(\mathrm{D0})}\right) + \gamma^{(\mathrm{G0})} \sin\left(\phi_m^{(\mathrm{D0})}\right) \right\} \bar{E}_0^{(\mathrm{out})} \langle \beta_m | 0 \rangle \\ & = -n_{0\mathrm{s}} Y_m^{(0)} \sum_j \sum_\alpha \bar{E}_{G1,j,\alpha}^{(\mathrm{in})} \langle \beta_m | G1, j, \alpha \rangle, \end{aligned} \quad (4.5)$$

and

$$\begin{aligned} & G_\mathrm{V}^{(\mathrm{G0})} \cos\left(\phi_m^{(\mathrm{D0})}\right) \bar{E}_0^{(\mathrm{in})} \langle \beta_m | 0 \rangle + \left\{ -n_{0\mathrm{s}} Y_m^{(0)} \sin\left(\phi_m^{(\mathrm{D0})}\right) + \gamma^{(\mathrm{G0})} \cos\left(\phi_m^{(\mathrm{D0})}\right) \right\} \bar{E}_0^{(\mathrm{out})} \langle \beta_m | 0 \rangle \\ & = n_{0\mathrm{s}} \sum_j \sum_\alpha \left\{ \gamma_{j,\alpha}^{(\mathrm{G1})} \bar{E}_{G1,j,\alpha}^{(\mathrm{in})} \langle \beta_m | G1, j, \alpha \rangle + G_{\mathrm{V},j,\alpha}^{(\mathrm{G1})} \bar{E}_{G1,j,\alpha}^{(\mathrm{out})} \langle \beta_m | G1, j, \alpha \rangle \right\}. \end{aligned} \quad (4.6)$$

Let's consider in the case of finite thickness $D_0 \neq 0$. In this case, we can divide both sides of the Eq. (4.5) by the function $\sin\left(\phi_m^{(\mathrm{D0})}\right)$, then it can be seen that the information about the phase of the diffraction wave appears only with the admittance $Y_m^{(0)}$. According to the coupled-mode analysis, these terms represent the re-radiation and the re-absorption of the diffraction modes by the waveguide modes in the slits [50,56]. The equation is valid for any non-zero diffraction wave, and by multiplying both sides of the resulting equation by the fundamental waveguide mode of the slit in grating G_0, Eq. (4.5) is transformed into the following equation

$$G_\mathrm{V}^{(\mathrm{G0})} \bar{E}_0^{(\mathrm{in})} + \left\{ G_{0|0}^{(\mathrm{M})} + \gamma^{(\mathrm{G0})} \right\} \bar{E}_0^{(\mathrm{out})} = -\sum_j \sum_\alpha G_{0|G1,j,\alpha}^{(\mathrm{F})} \bar{E}_{G1,j,\alpha}^{(\mathrm{in})}, \quad (4.7)$$

where the new parameters $G_{0|0}^{(\mathrm{M})}$ and $G_{0|G1,j,\alpha}^{(\mathrm{F})}$ are defined as

$$G_{0|0}^{(\mathrm{M})} = n_{0\mathrm{s}} \sum_m Y_m^{(0)} \cot\left(\phi_m^{(\mathrm{D0})}\right) \langle 0 | \beta_m \rangle \langle \beta_m | 0 \rangle, \quad (4.8)$$

$$G_{0|G1,j,\alpha}^{(\mathrm{F})} = n_{0\mathrm{s}} \sum_m Y_m^{(0)} \csc\left(\phi_m^{(\mathrm{D0})}\right) \langle 0 | \beta_m \rangle \langle \beta_m | G1, j, \alpha \rangle. \quad (4.9)$$

The parameter $G_{0|0}^{(\mathrm{M})}$ describes the multiple reflections of the diffraction modes $|\beta_m\rangle$ emitted by the waveguide mode $|0\rangle$ between the metallic part of the gratings G_0 and G_1. The reflected diffraction mode is then re-absorbed by the fundamental waveguide mode $|0\rangle$ of another slits. The superscript "M" stands for the "metal" because this parameter arises inside the spacer when we combine the grating with the metallic plane which is the case for the back-perfect absorber shown in the previous chapter. The parameter $G_{0|G1,j,\alpha}^{(\mathrm{F})}$ gives the connection between two gratings. The diffraction modes $|\beta_m\rangle$ are emitted by the waveguide modes $|G1, j, \alpha\rangle$ of the slit in the grating G_1, and then they are re-absorbed by the fundamental waveguide mode $|0\rangle$ of the slit in the grating G_0. The superscript "F" stands for the Fabry-Perot because it diverges at the FP resonance determined by the condition $\sin\left(\phi_m^{(\mathrm{D0})}\right) = 0$.

Notice that Eq. (4.7) gives only one linear equation. We can obtain more linear equations by considering the Eq. (4.6). First we divide both sides of Eq. (4.6) by $\cos\left(\phi_m^{(\mathrm{D0})}\right)$ to bring the information about the phase of the diffraction wave to the admittance of the field coefficient $\bar{E}_0^{(\mathrm{out})}$. Then, we can subtract the resulting equation from Eq. (4.5) which is divided by the function $\sin\left(\phi_m^{(\mathrm{D0})}\right)$. By multiplying both sides of the resulting equation by $\cos\left(\phi_m^{(\mathrm{D0})}\right)$, taking into account non-zero diffraction modes, and multiplying both sides of the resulting equation by the waveguide modes $|G1, j, \alpha\rangle$ of the grating G_1, then we can obtain another equations which connect two gratings as follows

$$-G^{(\mathrm{F})}_{G1,j,\alpha|0}\bar{E}_0^{(\mathrm{out})} = \left(G^{(\mathrm{M})}_{G1,j,\alpha|G1,j,\alpha} + n_{0\mathrm{s}}\gamma^{(\mathrm{G1})}_{j,\alpha}\right)\bar{E}^{(\mathrm{in})}_{G1,j,\alpha} + n_{0\mathrm{s}}G^{(\mathrm{G1})}_{\mathrm{V},j,\alpha}\bar{E}^{(\mathrm{out})}_{G1,j,\alpha} + \sum_{j'\neq j} G^{(\mathrm{M})}_{G1,j,\alpha|G1,j',\alpha}\bar{E}^{(\mathrm{in})}_{G1,j',\alpha} + \sum_{\alpha'\neq\alpha} G^{(\mathrm{M})}_{G1,j,\alpha|G1,j,\alpha'}\bar{E}^{(\mathrm{in})}_{G1,j,\alpha'} + \sum_{j'\neq j}\sum_{\alpha'\neq\alpha} G^{(M)}_{G1,j,\alpha|G1,j',\alpha'}\bar{E}^{(\mathrm{in})}_{G1,j',\alpha'} \quad (4.10)$$

The parameters $G^{(\mathrm{M})}$ and $G^{(\mathrm{F})}$ are define in Eq. (4.8) and (4.9), respectively. Eq. (4.10) must be satisfied by all waveguide modes of the grating G_1 in the superlattice (one period of the grating G_0). Therefore, this equation yield (number of slit) × (number of waveguide modes in each slit) linear equations. In this equation, we also include the re-radiation and re-absorption among different location of slits and different waveguide modes. If we use only the fundamental waveguide mode, that is $|G1, j, 0\rangle$, then the last two terms in the right hand side of Eq. (4.10) are zero. If there is only one slit in the superlattice located at the position labelled by j=0, and only the fundamental waveguide mode is taken, then the last three terms in the right hand side of Eq. (4.10) are zero. It can be seen that this equation looks complicated only because we include all waveguide modes, and have many slits inside the supperlattice.

Eq. (4.7) and (4.10) show us how to connect the two gratings. But care must be taken applying these equations. We consider so far the case of finite thickness of the dielectric layer D_0 which allows us to manipulate the equations by dividing the equations with $\sin\left(\phi_m^{(\mathrm{D0})}\right)$. However, we cannot do that in the case zero of thickness (the object perfectly touches the lens) because now $\sin\left(\phi_m^{(\mathrm{D0})}\right) = 0$ and $\cos\left(\phi_m^{(\mathrm{D0})}\right) = 1$ for all diffraction waves. In the latter case, the fundamental waveguide mode $|0\rangle$ of the slit in the grating G_0 directly excite the waveguide modes $|G1, j, \alpha\rangle$ of slits in the grating G_1 which are "in contact" with it. This behaviour can be seen by inserting $\phi_m^{(\mathrm{D0})} = 0$ into Eq. (4.5), and then we have the following equation

$$\bar{E}_0^{(\mathrm{out})} = -\sum_j\sum_\alpha \bar{E}^{(\mathrm{in})}_{G1,j,1}\langle 0|G1, j, \alpha\rangle. \quad (4.11)$$

The scalar product in Eq. (4.11) clearly shows the direct excitation between two waveguide modes. The same consideration is applied to Eq. (4.6). By inserting the condition $\phi_m^{(\mathrm{D0})} = 0$ into the Eq. (4.6), the admittance function disappear, that means there are no the re-radiation and re-absorption processes anymore, and the resulting equation reads

$$G^{(\mathrm{G0})}_{\mathrm{V}}\bar{E}_0^{(\mathrm{in})} + \gamma^{(\mathrm{G0})}\bar{E}_0^{(\mathrm{out})} = n_{0\mathrm{s}}\sum_j\sum_\alpha\left\{\gamma^{(\mathrm{G1})}_{j,\alpha}\bar{E}^{(\mathrm{in})}_{G1,j,\alpha} + G^{(\mathrm{G1})}_{\mathrm{V},j,\alpha}\bar{E}^{(\mathrm{out})}_{G1,j,\alpha}\right\}\langle 0|G1, j, \alpha\rangle. \quad (4.12)$$

In the second case, we consider the dielectric layer D_i which separates the grating G_i and G_{i+1} of the lens. Note that we preserve the subscript "*j*" for the location of the slit along the *x*-axis, and we use the subscript "*i*" to indicate the location of the slit along the *y*-axis. By applying similar arguments as the previous case, we obtain two equations which connect the two gratings.

$$\begin{aligned} & G_{\mathrm{V},j,\alpha}^{(\mathrm{Gi})}\bar{E}_{Gi,j,\alpha}^{(\mathrm{in})}+\left(\frac{G_{Gi,j,\alpha|Gi,j,\alpha}^{(\mathrm{M})}}{n_{0\mathrm{s}}}+\gamma_{j,\alpha}^{(Gi)}\right)\bar{E}_{Gi,j,\alpha}^{(\mathrm{out})}+\sum_{j'\neq j}\frac{G_{Gi,j,\alpha|Gi,j',\alpha}^{(\mathrm{M})}}{n_{0\mathrm{s}}}\bar{E}_{Gi,j',\alpha}^{(\mathrm{out})}+\sum_{\alpha'\neq\alpha}\frac{G_{Gi,j,\alpha|Gi,j,\alpha'}^{(\mathrm{M})}}{n_{0\mathrm{s}}}\bar{E}_{Gi,j,\alpha'}^{(\mathrm{out})} \\ & +\sum_{j'\neq j}\sum_{\alpha'\neq\alpha}\frac{G_{Gi,j,\alpha|Gi,j',\alpha'}^{(\mathrm{M})}}{n_{0\mathrm{s}}}\bar{E}_{Gi,j',\alpha'}^{(\mathrm{out})}=-\sum_{j_2}\sum_{\alpha_2}\frac{G_{Gi,j,\alpha|G(i+1),j_2,\alpha_2}^{(\mathrm{F})}}{n_{0\mathrm{s}}}\bar{E}_{G(i+1),j_2,\alpha_2}^{(\mathrm{in})} \end{aligned}, \quad (4.13)$$

and

$$\begin{aligned} -\sum_{j}\sum_{\alpha}\frac{G_{G(i+1),jj,\alpha\alpha|Gi,j,\alpha}^{(\mathrm{F})}}{n_{0\mathrm{s}}}\bar{E}_{Gi,j,\alpha}^{(\mathrm{out})} &= \left(\frac{G_{G(i+1),j_2,\alpha_2|G(i+1),j_2,\alpha_2}^{(\mathrm{M})}}{n_{0\mathrm{s}}}+\gamma_{j_2,\alpha_2}^{(\mathrm{D}(i+1))}\right)\bar{E}_{G(i+1),j_2,\alpha_2}^{(\mathrm{in})}+G_{\mathrm{V},j_2,\alpha_2}^{(\mathrm{D}(i+1))}\bar{E}_{G(i+1),j_2,\alpha_2}^{(\mathrm{out})} \\ &+\sum_{j_2'\neq j_2}\frac{G_{G(i+1),j_2,\alpha_2|G(i+1),j_2',\alpha_2}^{(\mathrm{M})}}{n_{0\mathrm{s}}}\bar{E}_{G(i+1),j_2',\alpha_2}^{(\mathrm{in})} \\ &+\sum_{\alpha_2'\neq\alpha_2}\frac{G_{G(i+1),j_2,\alpha_2|G(i+1),j_2,\alpha_2'}^{(\mathrm{M})}}{n_{0\mathrm{s}}}\bar{E}_{G(i+1),j_2,\alpha_2'}^{(\mathrm{in})} \\ &+\sum_{j_2'\neq j_2}\sum_{\alpha_2'\neq\alpha_2}\frac{G_{G(i+1),j_2,\alpha_2|G(i+1),j_2',\alpha_2'}^{(\mathrm{M})}}{n_{0\mathrm{s}}}\bar{E}_{G(i+1),j_2',\alpha_2'}^{(\mathrm{in})} \end{aligned}, \quad (4.14)$$

where the indices j_2 denotes the location of the slit along the *x*-axis in the grating G_{i+1}, and the α_2 denotes the waveguide mode of the slit in the grating G_{i+1}. As we have already said, the equations look complicated because we take into account all waveguide modes, and put many slits inside the superlattice to image the subwavelength objects. If we use only the fundamental waveguide mode for the grating G_i, and this grating has only one slit, then Eq. (4.13) and (4.14) are just similar to the Eq. (4.7) and (4.10), respectively. These equations look more simple if only the fundamental waveguide mode for both gratings G_i and G_{i+1} are taken. In the latter case, the closed form of the total reflection and transmission spectra for the stacked grating/dielectric structure can be obtained.

We have shown in this section how to connect the field coefficients between two gratings. Our remaining task, as usual, is to find the solutions for these field coefficients. We will illustrate the technique for computing all field coefficients of gratings which are then used to determine the reflectance and transmittance.

4.1.3 Determination of all grating field coefficients

We show how to obtain all grating field coefficients with simple *N*=2 stacked grating/dielectric structure. The grating G_1 and G_2 have two slits in the superlattice demoted by *j*=1,2. For simplicity, we take into account only the fundamental waveguide mode in all slits. Therefore, there are 10 unknown grating field coefficients. We can group all grating field coefficients into a vector as follows

$$\bar{\mathbf{E}}=\left(\bar{E}_0^{(\mathrm{in})}\quad \bar{E}_0^{(\mathrm{out})}\quad \bar{E}_{G1,1,0}^{(\mathrm{in})}\quad \bar{E}_{G1,1,0}^{(\mathrm{out})}\quad \bar{E}_{G2,1,0}^{(\mathrm{in})}\quad \bar{E}_{G2,1,0}^{(\mathrm{out})}\quad \bar{E}_{G1,2,0}^{(\mathrm{in})}\quad \bar{E}_{G1,2,0}^{(\mathrm{out})}\quad \bar{E}_{G2,2,0}^{(\mathrm{in})}\quad \bar{E}_{G2,2,0}^{(\mathrm{out})}\right)^{\mathrm{T}}. \quad (4.15)$$

The first two columns are the field coefficients of the grating G_0. The next four columns are the field coefficients of the j_1 slits in the grating G_1 followed by the those in the grating G_2. The last four columns are the field coefficients of the j_2 slits in the the grating G_1 followed by the those in the grating G_2. We solve the vector $\bar{\mathbf{E}}$ by formulating a single matrix equation $\mathbf{A}\bar{\mathbf{E}}=\mathbf{B}$ where $\mathbf{A}$ is the coefficient matrix and $\mathbf{B}$ is the constant vector, and then perform the partial pivoting.

In order the formulate the coefficient matrix $\mathbf{A}$ and the constant vector $\mathbf{B}$, it is useful to list all equations that we know. We need 10 equations for 10 variables. We use the indices to list all equations in the compact form.

In the input region, we obtain one linear equation that relates the field coefficients $\bar{E}_0^{(\mathrm{in})}$ and $\bar{E}_0^{(\mathrm{out})}$ as

$$-\left(G_{\infty s}^{(\mathrm{in})}-\gamma^{(\mathrm{G0})}\right)\bar{E}_0^{(\mathrm{in})}+G^{(\mathrm{G0})}\bar{E}_0^{(\mathrm{out})}=-2n_{\mathrm{s}}I_0\,, \tag{4.16}$$

where $I_0=-\sqrt{w/p}\,\mathrm{sinc}\left(k_x w/2\right)$ is the excitation function, and $G_{\infty s}^{(\mathrm{in})}$ is obtained by Eq. (3.26) and can be written as follows (the subscript ∞s is replaced by $0|0$)

$$G_{0|0}^{\mathrm{in}}=i\frac{n_{\mathrm{in}}}{n_s}\sum_m Y_m^{(\mathrm{in})}\left(w/p\right)\mathrm{sinc}^2\left(\beta_m w/2\right). \tag{4.17}$$

We still have 9 more equations to go. In the region between the gratings G_0 and G_1, 1 equation is obtained by Eq. (4.7), and 2 equations are obtained by Eq. (4.10), written as follows

$$G_{\mathrm{V}}^{(\mathrm{G0})}\bar{E}_0^{(\mathrm{in})}+\left\{G_{0|0}^{(\mathrm{M})}+\gamma^{(\mathrm{G0})}\right\}\bar{E}_0^{(\mathrm{out})}=-\sum_{j=1}^{2}G_{0|G1,j,0}^{(\mathrm{F})}\bar{E}_{G1,j,0}^{(\mathrm{in})}\,, \tag{4.18}$$

$$\begin{aligned}-G_{G1,j,0|0}^{(\mathrm{F})}\bar{E}_0^{(\mathrm{out})}&=\left(G_{G1,j,0|G1,j,0}^{(\mathrm{M})}+n_{0\mathrm{s}}\gamma_{j,0}^{(\mathrm{G1})}\right)\bar{E}_{G1,j,0}^{(\mathrm{in})}+n_{0\mathrm{s}}G_{j,0}^{(\mathrm{G1})}\bar{E}_{G1,j,0}^{(\mathrm{out})}\\&\quad+\sum_{j'\neq j}G_{G1,j,0|G1,j',0}^{(\mathrm{M})}\bar{E}_{G1,j',0}^{(\mathrm{in})}\quad\left(j=1,2\right)\end{aligned}\,. \tag{4.19}$$

In the region between the gratings G_1 and G_2, 4 equations can be acquired by Eq. (4.13) and (4.14) which are expressed as follows

$$G_{\mathrm{V},j,0}^{(\mathrm{G1})}\bar{E}_{G1,j,0}^{(\mathrm{in})}+\left(\frac{G_{G1,j,0|G1,j,0}^{(\mathrm{M})}}{n_{0\mathrm{s}}}+\gamma_{j,0}^{(\mathrm{G1})}\right)\bar{E}_{G1,j,0}^{(\mathrm{out})}+\sum_{j'\neq j}\frac{G_{G1,j,0|G1,j',0}^{(\mathrm{M})}}{n_{0\mathrm{s}}}\bar{E}_{G1,j',0}^{(\mathrm{out})}=-\sum_{j_2=1}^{2}\frac{G_{G1,j,0|G2,j_2,0}^{(\mathrm{F})}}{n_{0\mathrm{s}}}\bar{E}_{G2,j_2,0}^{(\mathrm{in})}\,, \tag{4.20}$$

where j=1,2, and

$$-\sum_{j=1}^{2}\frac{G_{G2,j_2,0|G1,j,0}^{(\mathrm{F})}}{n_{0\mathrm{s}}}\bar{E}_{G1,j,0}^{(\mathrm{out})}=\left(\frac{G_{G2,j_2,0|G1,j_2,0}^{(\mathrm{M})}}{n_{0\mathrm{s}}}+\gamma_{j_2,0}^{(\mathrm{G2})}\right)\bar{E}_{G2,j_2,0}^{(\mathrm{in})}+G_{\mathrm{V},j_2,0}^{(\mathrm{G2})}\bar{E}_{G2,j_2,0}^{(\mathrm{out})}+\sum_{j_2'\neq j_2}\frac{G_{G2,j_2,0|G2,j_2',0}^{(\mathrm{M})}}{n_{0\mathrm{s}}}\bar{E}_{G2,j_2',0}^{(\mathrm{in})}\,, \tag{4.21}$$

where j_2=1,2. In the output region, we can obtain 2 equations from Eq. (3.16). But we also need to add the re-radiation and re-absorption of the diffraction modes by two slits in the grating G_2. These equations are written as

$$G_{\mathrm{V},0}^{(\mathrm{G2})}\bar{E}_{G2,j,0}^{(\mathrm{in})}-\left(G_{G2,j,0|G2,j,0}^{(\mathrm{out})}-\gamma_{j,0}^{(\mathrm{G2})}\right)\bar{E}_{G2,j,0}^{(\mathrm{out})}-\sum_{j'\neq j}G_{G2,j,0|G2,j',0}^{(\mathrm{out})}\bar{E}_{G2,j',0}^{(\mathrm{out})}=0\,, \tag{4.22}$$

where j=1,2, and the parameter $G_{G2,j,0|G2,j,0}^{(\mathrm{out})}$ is generalized from Eq. (3.16) to any waveguide mode located at any location in the supper lattice and it is defined as

$$G_{G2,j,0|G2,j,0}^{(\mathrm{out})}=i\frac{n_h}{n_s}\sum_m\left\{\frac{1+r_{\mathrm{h,out}}^{(m)}\exp\left(2i\phi_m^{(\mathrm{D2})}\right)}{1-r_{\mathrm{h,out}}^{(m)}\exp\left(2i\phi_m^{(\mathrm{D2})}\right)}\right\}Y_m^{(\mathrm{h})}\left\langle G2,j,0\middle|\beta_m\right\rangle\left\langle\beta_m\middle|G2,j,0\right\rangle\,, \tag{4.23}$$

where the Fresnel reflection coefficient $r_{\mathrm{h,out}}^{(m)}$ is given in Eq. (3.21), and $\phi_m^{(\mathrm{D2})} = q_m^{(\mathrm{D2})} D_2$. In the case of $D_2 = 0$, the dielectric layer D2 can be virtually considered as the output medium, the term in the curl bracket becomes one, the admittance becomes the admittance of the output medium, and the ratio $n_h / n_s = n_{\mathrm{out}} / n_s$.

Now, we have 10 equations needed to formulate the coefficient matrix $\mathbf{A}$. The 10×10 matrix $\mathbf{A}$ can be decomposed into sub-matrices as follows

$$\mathbf{A} = \begin{bmatrix} [\mathbf{A}_{11}]_{2\times2} & [\mathbf{A}_{12}]_{2\times4} & [\mathbf{A}_{13}]_{2\times4} \\ [\mathbf{A}_{21}]_{4\times2} & [\mathbf{A}_{22}]_{4\times4} & [\mathbf{A}_{23}]_{4\times4} \\ [\mathbf{A}_{31}]_{4\times2} & [\mathbf{A}_{32}]_{4\times4} & [\mathbf{A}_{33}]_{4\times4} \end{bmatrix}. \tag{4.23}$$

Each sub-matrix of the matrix $\mathbf{A}$ is given as follows

$$\mathbf{A}_{11} = \begin{bmatrix} -\left(G_{0|0}^{\mathrm{in}} - \gamma^{(\mathrm{G0})}\right) & G_V^{(\mathrm{G0})} \\ G_{\mathrm{V}}^{(\mathrm{G0})} & G_{0|0}^{(\mathrm{M})} + \gamma^{(\mathrm{G0})} \end{bmatrix},\ \mathbf{A}_{1j} = \begin{bmatrix} 0 & 0 & 0 & 0 \\ G_{0|G1,j-1,0}^{(\mathrm{F})} & 0 & 0 & 0 \end{bmatrix}\ \ (j = 2,3). \tag{4.24}$$

The sub-matrix $\mathbf{A}_{j1}$ $(j = 2,3)$ are the matrix transpose of $\mathbf{A}_{1j}$, and the parameter $G_{0|G1,j-1,0}^{(\mathrm{F})}$ of the $\mathbf{A}_{1j}$ is changed to $G_{G1,j-1,0|0}^{(\mathrm{F})}$ for the $\mathbf{A}_{j1}$ (Hermitian operation). Notice that these matrices depend only on the properties of the gratings G_0 and G_1 because they are obtained by Eq. (4.16)-(4.19). The sub-matrices $\mathbf{A}_{jj}$ $(j = 2,3)$ along the diagonal line of the matrix $\mathbf{A}$ are given as follows

$$\mathbf{A}_{jj} = \begin{bmatrix} G_{G1,j-1,0|G1,j-1,0}^{(\mathrm{M})} + n_{0\mathrm{s}}\gamma_{j-1,0}^{(\mathrm{G1})} & n_{0\mathrm{s}} G_{\mathrm{V},j-1,0}^{(\mathrm{G1})} & 0 & 0 \\ G_{\mathrm{V},j-1,0}^{(\mathrm{G1})} & \dfrac{G_{G1,j-1,0|G1,j-1,0}^{(\mathrm{M})}}{n_{0\mathrm{s}}} + \gamma_{j-1,0}^{(\mathrm{G1})} & \dfrac{G_{G1,j-1,0|G1,j-1,0}^{(\mathrm{M})}}{n_{0\mathrm{s}}} & 0 \\ 0 & \dfrac{G_{G1,j-1,0|G1,j-1,0}^{(\mathrm{M})}}{n_{0s}} & \dfrac{G_{G2\,j-1,0|G2,j-1,0}^{(\mathrm{M})}}{n_{0\mathrm{s}}} + \gamma_{j-1,0}^{(\mathrm{G2})} & G_{\mathrm{V},j-1,0}^{(\mathrm{G2})} \\ 0 & 0 & G_{\mathrm{V}j-1,0}^{(\mathrm{G2})} & -\left(G_{G2,j-1,0|G2,j-1,0}^{(\mathrm{out})} - \gamma_{j-1,0}^{(\mathrm{G2})}\right) \end{bmatrix}, \tag{4.25}$$

where j=2,3. The sub-matrices $\mathbf{A}_{jj}$ $(j = 2,3)$ are symmetric if the filling material of the gratings G_0 is the same as the material of the dielectric constant D_0 : $n_s = n_0 \to n_{0s} = 1$. Finally, the off-diagonal sub-matrices of the matrix $\mathbf{A}$ are given as follows

$$\mathbf{A}_{23} = \begin{bmatrix} G_{G1,1,0|G1,2,0}^{(\mathrm{M})} & 0 & 0 & 0 \\ 0 & \dfrac{G_{G1,1,0|G1,2,0}^{(\mathrm{M})}}{n_{0h}} & \dfrac{G_{G1,1,0|G2,2,0}^{(\mathrm{F})}}{n_{0h}} & 0 \\ 0 & \dfrac{G_{G2,1,0|G1,2,0}^{(\mathrm{F})}}{n_{0h}} & \dfrac{G_{G2,1,0|G2,2,0}^{(\mathrm{M})}}{n_{0h}} & 0 \\ 0 & 0 & 0 & -G_{G2,1,0|G2,2,0}^{(\mathrm{out})} \end{bmatrix}, \tag{4.26}$$

and the sub-matrix $\mathbf{A}_{32}$ is obtained from $\mathbf{A}_{23}$ by swapping the orders of re-radiation and re-absorption of the waveguide mode.

Finally, the constant vector $\mathbf{B}$ has non-zero element only in the first row. This element is just $-2n_s I_0$ which is the right hand side of Eq. (4.16) representing the excitation by the external radiation. Therefore, we can solve for the grating field coefficient vector $\bar{\mathbf{E}}$ by simple partial pivoting. This can be done by hand in the simple case, or by using the LAPACK subroutine [71]. In the special case that

there is only one slit in the superlattice of the grating of the *N*-stacked grating/dielectric structure, the closed form of $\bar{E}_{GN,1,0}^{(\mathrm{out})}$ and $\bar{E}_0^{(\mathrm{in})}$ can be obtained which lead to the analytically closed solutions of the dispersion relation, total reflection coefficient, and the total transmission coefficient, as will be given in the section 4.1.6. This technique can be extended to any number of grating/dielectric layer, and any number of slits in each grating of the lens. We give the general code in the CD.

4.1.4 Reflection and transmission coefficients

The *m*th-order transmission coefficient $A_m^{(\mathrm{out})}$ is determined by the output field coefficient of the grating G_N. The relation is written as follows

$$A_m^{(\mathrm{out})} = n_{\mathrm{h}} \frac{t_{\mathrm{h,out}}^{(m)} \exp\left(i\phi_m^{(\mathrm{DN})}\right)}{1 - r_{\mathrm{h,out}}^{(m)} \exp\left(2i\phi_m^{(\mathrm{DN})}\right)} iY_m^{(\mathrm{h})} \sum_j \sum_\alpha \bar{E}_{GN,j,\alpha}^{(\mathrm{out})} \left\langle \beta_m \middle| GN, j, \alpha \right\rangle, \tag{4.27}$$

where the scalar product between the waveguide mode $\left|GN, j, \alpha\right\rangle$ and the diffraction mode $\left|\beta_m\right\rangle$ is given by

$$\left\langle \beta_m \middle| GN, j, \alpha \right\rangle = \frac{1}{2}\sqrt{\frac{w_j C_\alpha}{p_{GN}}} \exp\left(-i\beta_m x_j\right) \left\{ \exp\left(ig_x^{(j,\alpha)} w_j / 2\right) \mathrm{sinc}\left[\left(\beta_m - g_x^{(j,\alpha)}\right) w_j / 2\right] + \exp\left(-ig_x^{(j,\alpha)} w_j / 2\right) \mathrm{sinc}\left[\left(\beta_m + g_x^{(j,\alpha)}\right) w_j / 2\right] \right\}, \tag{4.28}$$

where p_{GN} is period of the grating G_N, $C_0 = 1$, $C_{\alpha\neq 0} = 2$, and $g_x^{(j,\alpha)} = \alpha\pi / w_j$.

The *m*th-order total reflection coefficient $B_m^{(\mathrm{in})}$ is determined by the input field coefficient of the grating G_0 which is written as

$$B_m^{(\mathrm{in})} = \delta_{m0} + n_{\mathrm{in}} iY_m^{(\mathrm{in})} \bar{E}_0^{(\mathrm{in})} \sqrt{w_0 / p}\, \mathrm{sinc}\left(\beta_m w_0 / 2\right), \tag{4.29}$$

where the δ_{m0} denotes Dirac delta function. The reflectance and transmittance are then obtained by applying Eq. (3.36). We can also know the field distribution and thus the intensity of the image from the $A_m^{(\mathrm{out})}$. However, the electromagnetic fields of the image are affected by the interaction between the objects and the lens, and also between the gratings of the lens. Therefore, it is important to investigate the electromagnetic fields between two gratings. This calculation is explained in the next section

4.1.5 Electromagnetic fields between two gratings

One will obtain the wrong electromagnetic fields in the dielectric layer between two gratings if he calculates the field coefficients in this layer using the field coefficients only from one grating. The electromagnetic fields are the interferences of diffraction waves emitted by the slits from both gratings. Therefore, it is necessary to take into account the field coefficients from the two gratings. Let's us consider the electromagnetic fields in the dielectric layer D_0 between the gratings G_0 and G_1. At the output interface of the slit in the grating D_0 that is at y=h_0, the continuity of the E_x leads to the following relation

$$\frac{A_m^{(\mathrm{D0})}}{H_0} - \frac{B_m^{(\mathrm{D0})}}{H_0} = n_0 iY_m^{(0)} \bar{E}_0^{(\mathrm{out})} \left\langle \beta_m \middle| 0 \right\rangle, \tag{4.30}$$

where the scalar product between the fundamental waveguide mode and the diffraction mode is determined by Eq. (4.28) with $x_j = 0, \alpha = 0, w_j = w_0, p_{GN} = p$. At the input interface of the slits in the grating G1 that is at $y=y_1$, the continuity of E_x leads to the following relation

$$\frac{A_m^{(\mathrm{D}0)}}{H_0}\exp\left(i\phi_m^{(\mathrm{D}0)}\right)-\frac{B_m^{(\mathrm{D}0)}}{H_0}\exp\left(-i\phi_m^{(\mathrm{D}0)}\right)=-n_0 iY_m^{(0)}\sum_{\alpha}\sum_{j}\bar{E}_{G1,j,\alpha}^{(\mathrm{in})}\left\langle\beta_m\middle|G1,j,\alpha\right\rangle, \tag{4.31}$$

where the scalar product between the waveguide mode and the diffraction mode is obtained by Eq. (4.28). Then, the normalized field coefficients $A_m^{(0)}/H_0$ and $B_m^{(0)}/H_0$ are easily obtained from Eq. (4.30) and (4.31) as follows

$$\frac{A_m^{(\mathrm{D}0)}}{H_0}=-\frac{n_0}{2}\frac{Y_m^{(0)}}{\sin\left(\phi_m^{(\mathrm{D}0)}\right)}\left\{\exp\left(-i\phi_m^{(\mathrm{D}0)}\right)\bar{E}_0^{(\mathrm{out})}\left\langle\beta_m\middle|0\right\rangle+\sum_{\alpha}\sum_{j}\bar{E}_{G1,j,\alpha}^{(\mathrm{in})}\left\langle\beta_m\middle|G1,j,\alpha\right\rangle\right\}, \tag{4.32}$$

$$\frac{B_m^{(\mathrm{D}0)}}{H_0}=-\frac{n_0}{2}\frac{Y_m^{(0)}}{\sin\left(\phi_m^{(\mathrm{D}0)}\right)}\left\{\exp\left(i\phi_m^{(\mathrm{D}0)}\right)\bar{E}_0^{(\mathrm{out})}\left\langle\beta_m\middle|0\right\rangle+\sum_{\alpha}\sum_{j}\bar{E}_{G1,j,\alpha}^{(\mathrm{in})}\left\langle\beta_m\middle|G1,j,\alpha\right\rangle\right\}. \tag{4.33}$$

Therefore, the field coefficients in the dielectric layer D_0 are different from each other only in the phase factor for $\bar{E}_0^{(\mathrm{out})}$. This concept is easily extended into the dielectric layer between two gratings of the lens. For completeness, we also give the expressions of the field coefficients $A_m^{(\mathrm{D}i)}/H_0$ and $B_m^{(\mathrm{D}i)}/H_0$ between the gratings G_i and G_{i+1} as follows

$$\frac{A_m^{(\mathrm{D}i)}}{H_0}=-\frac{n_{\mathrm{h}}}{2}\frac{Y_m^{(\mathrm{h})}}{\sin\left(\phi_m^{(\mathrm{D}i)}\right)}\left\{\exp\left(-i\phi_m^{(\mathrm{D}i)}\right)\sum_{\alpha}\sum_{j}\bar{E}_{Gi,j,\alpha}^{(\mathrm{out})}\left\langle\beta_m\middle|Gi,j,\alpha\right\rangle+\sum_{\alpha_2}\sum_{j_2}\bar{E}_{G(i+1),j_2,\alpha_2}^{(\mathrm{in})}\left\langle\beta_m\middle|G(i+1),j_2,\alpha_2\right\rangle\right\}, \tag{4.34}$$

$$\frac{A_m^{(\mathrm{D}i)}}{H_0}=-\frac{n_{\mathrm{h}}}{2}\frac{Y_m^{(\mathrm{h})}}{\sin\left(\phi_m^{(\mathrm{D}i)}\right)}\left\{\exp\left(i\phi_m^{(\mathrm{D}i)}\right)\sum_{\alpha}\sum_{j}\bar{E}_{Gi,j,\alpha}^{(\mathrm{out})}\left\langle\beta_m\middle|Gi,j,\alpha\right\rangle+\sum_{\alpha_2}\sum_{j_2}\bar{E}_{G(i+1),j_2,\alpha_2}^{(\mathrm{in})}\left\langle\beta_m\middle|G(i+1),j_2,\alpha_2\right\rangle\right\}. \tag{4.35}$$

4.1.6 Closed form of dispersion relation, *m*th-order reflection coefficient, and *m*th-order transmission coefficient

We consider the stacked grating/dielectric structures only the lens part without the object. That is we neglect the grating G_0 and the dielectric layer D_0 (see Fig. 4.1). We assume that all gratings has the same height equal to *h*, the same width equal to *w*, the same period equal to *p*. Because there is only one slit in the superlattice, then the subscript *j* will be neglected. All slits are located at *x*=0. The slit width is assumed to be much smaller than the wavelength of light, and thus only the fundamental waveguide mode $\alpha=0$ is taken. Because all slits have only the fundamental waveguide mode, we also neglect the subscript α, and thus the waveguide mode of each grating is denoted as $\left|Gi\right\rangle$ where i=1,2,...,N. The dielectric layer has the same thickness *D*, and the phase constant for the diffraction mode *m* is denoted by $\phi_m=q_mD$. By using simple partial pivoting and mathematical induction, we can write the output field coefficient of the grating G_N which is denoted as $\bar{E}_{GN}^{(\mathrm{out})}$, as follows

$$\bar{E}_{GN}^{(\mathrm{out})}=\frac{2I_0}{n_h}\left(G_{\mathrm{V}}\right)^N\left(G^{(\mathrm{F})}\right)^{(N-1)}\frac{1}{\Omega_{\mathrm{disp}}}, \tag{4.36}$$

where $G_{\mathrm{V}}=\csc\left(k_{\mathrm{h}}h\right)$, $G^{(\mathrm{F})}=\sum_m Y_m^{(\mathrm{h})}\csc\left(\phi_m\right)\left(w/p\right)\mathrm{sinc}^2\left(\beta_m w/2\right)$, and Ω_{disp} is the dispersion function which determines the resonance frequency. The closed form of the dispersion function for the case of N=2 is written as

$$\Omega_{\mathrm{disp}}=\left[\left(\Omega_{\mathrm{in}}\Omega_{\mathrm{g}}-G_{\mathrm{V}}^2\right)\Omega_{\mathrm{g}}-\Omega_{\mathrm{in}}G^{(\mathrm{F})2}\right]\Omega_{\mathrm{out}}-\left(\Omega_{\mathrm{in}}\Omega_{\mathrm{g}}-G_{\mathrm{V}}^2\right)G_{\mathrm{V}}^2, \tag{4.37}$$

where $\Omega_{\mathrm{in}}=-\left(G^{(\mathrm{in})}-\gamma\right)$, $\Omega_{\mathrm{out}}=-\left(G^{(\mathrm{out})}-\gamma\right)$, $\Omega_{\mathrm{g}}=G^{(\mathrm{M})}+\gamma$, $\gamma=\cot\left(k_{\mathrm{h}}h\right)$,

$G^{(\mathrm{M})} = \sum_m Y_m^{(\mathrm{h})} \cot(\phi_m)(w/p)\mathrm{sinc}^2(\beta_m w/2)$. In the case of $N > 2$, the closed form of the dispersion function is written in terms of the recurrence relation as follows

$$\Omega_{\mathrm{disp}} = \Omega_{2(N-1)-1}\Omega_{\mathrm{out}} - \Omega_{2(N-1)-2}G_{\mathrm{V}}^2, \tag{4.38}$$

where Ω_j for $j = 0,1,...,2(N-1)-1$ are defined as follows

$$\Omega_j = \begin{cases} \Omega_{\mathrm{in}}\Omega_{\mathrm{g}} - G_{\mathrm{V}}^2 & (j=0) \\ \Omega_0\Omega_g - \Omega_{\mathrm{in}}G^{(\mathrm{F})2} & (j=1) \\ \Omega_{j-1}\Omega_{\mathrm{g}} - \Omega_{j-2}G_{\mathrm{V}}^2 & (\text{even } j,\ j \geq 2) \\ \Omega_{j-1}\Omega_{\mathrm{g}} - \Omega_{j-2}\mathrm{G}^{(\mathrm{F})2} & (\text{odd } j,\ j \geq 3) \end{cases}. \tag{4.39}$$

The closed form of the *m*th-order transmission coefficient is obtained by substituting $\bar{E}_{GN}^{(\mathrm{out})}$ from Eq. (4.36) into Eq. (4.27).

For the *m*th-order reflection coefficient, we can also write the closed form of the input field coefficient of the grating G_1 which is denoted by $\bar{E}_{G1}^{(\mathrm{in})}$, as follows

$$\bar{E}_{G1}^{(\mathrm{in})} = -\frac{2I_0}{n_{\mathrm{h}}}\Omega'_{2(N-1)-1}\frac{1}{\Omega_{\mathrm{disp}}}, \tag{4.40}$$

where the parameter Ω'_j is defined in terms of the recurrence relation as

$$\Omega'_j = \begin{cases} \Omega_{\mathrm{out}}\Omega_{\mathrm{g}} - G_{\mathrm{V}}^2 & (j=0) \\ \Omega'_0\Omega_{\mathrm{g}} - \Omega_{\mathrm{out}}G^{(\mathrm{F})2} & (j=1) \\ \Omega'_{j-1}\Omega_{\mathrm{g}} - \Omega'_{j-2}G_{\mathrm{V}}^2 & (\text{even } j,\ j \geq 2) \\ \Omega'_{j-1}\Omega_{\mathrm{g}} - \Omega'_{j-2}G^{(\mathrm{F})2} & (\text{odd } j,\ j \geq 3) \end{cases}. \tag{4.50}$$

The *m*th-order total reflection coefficient given in Eq. 4.29 is obtained by substituting $\bar{E}_0^{(\mathrm{in})} \to \bar{E}_{G1}^{(\mathrm{in})}$ with the $\bar{E}_{G1}^{(\mathrm{in})}$ given in Eq. (4.40).

These closed forms not only give very fast calculations of the optical spectra, they are also useful to study the electromagnetic modes and therefore the effective parameters of the lens.

4.2 Comparison between the analytical solutions and FDTD simulation

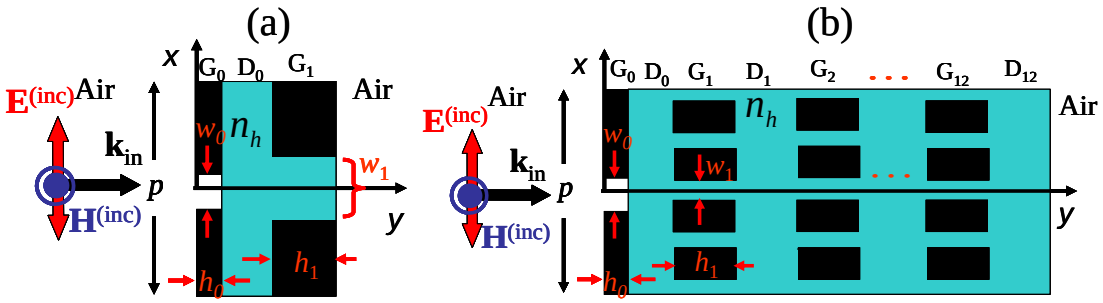

Fig. 4.2 Stacked grating/dielectric structures for comparing with FDTD simulation. (a) Only one grating/dielectric behind the grating G_0. The dielectric layer D_1 is neglected. The dielectric layer D_0 is the same material as the material filling the slit in the grating G_1 defined as Zeonex polymer with neglected loss ($\varepsilon_h = 2.3104$) [30]. The slit in the grating G_0 is filled with air. (b) 12 number of stacked grating/dielectrics behind the grating G_0. The slit height and slit width for the grating G_1 to G_{12} are the same, and the thickness of all dielectric layers is also the same. The parameters of the geometries in two cases are given in the main text.

We compare our analytical solutions with the FTD simulations in two cases. One case is simple structure and another case is more complicated structure. The schematic view of the simple structure is schematically shown in Fig. 4.2 (a). In this case, there is only one grating/dielectric behind the grating G_0 and also the dielectric layer D_1 is neglected. Furthermore, the grating G_1 contains only one slit in the superlattice. The input and output media are defined as air. The grating G_0 has period 100 μm, slit height 1 μm, slit width 1 μm, and the slit is filled with air. The dielectric layer D_0 is defined as Zeonex polymer with neglected loss which is the same material as that filling the grating G_1. We neglect loss because the FDTD simulation is time-consuming with the introduction of complex dielectric constant. The thickness of the dielectric layer D_0 is 10 μm which is the same as the slit height in the grating G_1. The width of the slit in the grating G_1 is defined as 7 μm which is smaller than its height. The whole structure is excited by normal incident light with the incident electric field polarized along the *x*-axis, and the incident magnetic field polarized along the *z*-axis. In the FDTD simulation, the periodic boundary condition is applied along the x-axis, and the perfectly matched layers parallel to the x-axis are defined in the input and output regions to prevent the back-scattering of light at the far-field coming to the structure. The whole structure is excited by broad THz Gaussian pulse, and then the transmittance and reflectance are measured on the far-field planes after all light transmitted through the transmission plane. Fig. 4.3(a) shows that the analytical transmission spectra as indicated by the blue line is almost identical to the that from the FDTD simulation with the resolution 4.5 pix/μm as indicated by the red line. However, the transmission spectra of the homogenized-gratings model show only one peak due to the excitation of the Fabry-Perot. The reason of a little larger discrepancy at higher resonant frequency will become clear shortly. Fig. 4.3(b) gives the |**E**|-distribution at the lower resonant frequency. The analytical field distribution clearly shows the same field distribution from the FDTD. The analytical solutions can capture the main features found in the FDTD simulation. The first feature is the dark circle between two gratings. This circle arises due to the π phase difference of electric dipoles induced on the output interface of the slit G_0 and the input interface of the slit G_1. In

another word, the dipole rotates by 180 degree from the grating G_0 to the grating G_1. Another feature is one dim node on the metallic part of the two gratings. This indicates that the 1st-order quasi-waveguide resonance (QWR) is formed between two grating. The resonant frequency is determined by the period of the supperlattice, the dielectric constant of the dielectric layer, and also the distance between two gratings. Fig. 4.3(c) shows the |**E**|-distribution at higher resonant frequency. The analytical field distribution closely resembles that from the FDTD simulation. In this case, three nodes are formed on the metallic part of two gratings. This indicates the excitation of the 3rd-order QWR. The excitation of the 3rd-order QWR requires higher diffraction modes and thus the higher FDTD simulation is required to capture thses high-k waves. This is the reason why the higher resonant frequency has a little larger discrepancy between the analytical spectra and FDTD spectra than the lower resonant frequency. The 2nd-order QWR cannot be excited by the normal incident light due to the zero net dipole moments of the metallic part of the grating. But they can be excited by the oblique incident light which introduces the normal component of the electric field and thus break the symmetry [81].

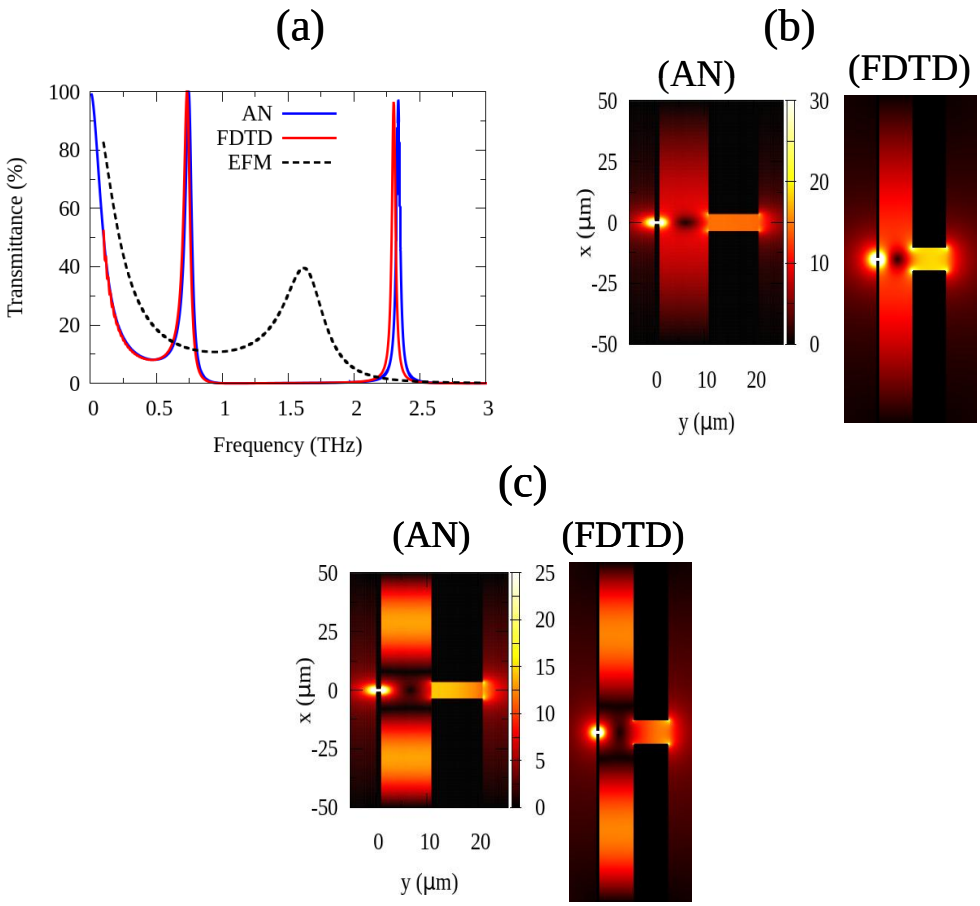

Fig. 4.3 Comparison with FDTD simulation with simple structure (a) Transmission spectra . The analytical resonant peaks are at the frequency 0.7461 THz and 2.3368 THz. Black dashed line is obtained by homogenized the grating G_0 as $k_y^{(G1,\mathrm{eff})} = k_s, \varepsilon_x^{(G1,\mathrm{eff})} = \varepsilon_s\left(p/w_0\right)$ and the grating G_1 as $k_y^{(G2,\mathrm{eff})} = k_h, \varepsilon_x^{(G2,\mathrm{eff})} = \varepsilon_h\left(p/w_1\right)$ and (b) The |**E**|-distribution at the resonant frequency 0.7461 THz. (c) |**E**|-distribution at the resonant frequency 2.3368 THz.

Next, we compare our analytical solutions with more complicated structure as shown in Fig. 4.2 (b). In this case, N=12 and each grating G_1 to G_{12} has 4 slits in the superlattice. The slit width and slit heights of these slits are the same which are defined as 10 μm. The period of the gratings G_1 to G_{12} is defined as 20 μm. The thickness of the dielectric layers D_0 to D_{12} is the same and equal to 10 μm. They are also the same material which is defined as the Zeonex polymer with neglected loss. The period of the grating G_0 is changed to 80 μm so that it can contain 4 slits in the gratings D_0 to D_{12}. The slit width and height of the only one slit in the grating G_0 are the same as the previous case. The whole structure is excited by the normal incident light which is the same excitation configuration as the previous case. In

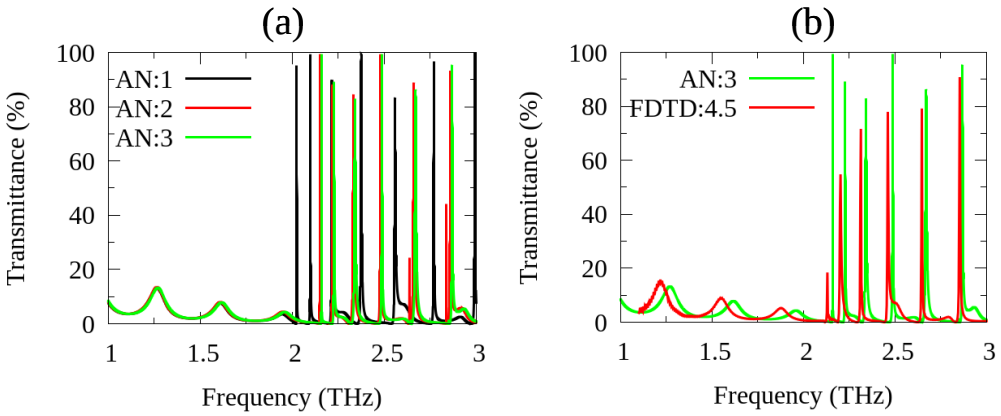

Fig. 4.3 Comparison with FDTD simulation with complicated structure. (a) Transmission spectra of the complicated structure obtained by the analytical solutions with increasing the number of waveguide modes from 1 to 3. The number of waveguide mode 1 means only the fundamental mode is used. (b) Comparison between the analytical and FDTD transmission spectra of the complicated structure.

this structure, the slit width of the lens is only a half of the period of the lens. Therefore, it is necessary to increase the number of waveguide modes until the analytical spectra converges. Fig. 4.4 (a) shows the dependence of the analytical transmission spectra on the number of waveguide modes as indicated in the figure. It can be seen that the analytical spectra converges as the number of waveguide modes equal to 3. Fig. 4.3 (b) shows the comparison between the analytical transmission spectra with the number of waveguide mode equal to 3 and the FDTD simulation with resolution 4.5 pix/μm. Both methods consistently give various peaks. However, all peaks calculated by the FDTD simulation lie in the lower frequencies than those obtained by the analytical solution. We expect that the FDTD spectra will approach our analytical spectra by increasing more resolution because it will be able to capture high-k waves which contribute to the QWR between the gratings, and thus the resonant energy should increase a little more. Note that the FDTD simulation time with this resolution takes 580 min. to compute. It means that you have to wait for it for 10 hours, and hope that it will gives you the correct spectra. By using the analytical solutions, even with this number of waveguide modes equal to 3, it takes only 10 min. to obtain the spectra. Therefore, the analytical solutions given in this chapter yield the efficient tools to investigate this structure with various parameters. More importantly, they can be applied to the structure working in the deep-subwavelength regime. In the next section, we will apply the analytical solutions to demonstrate the deep-subwavelength λ/300 at 1 THz.

4.3 Subwavelength imaging with one grating/dielectric metamaterial

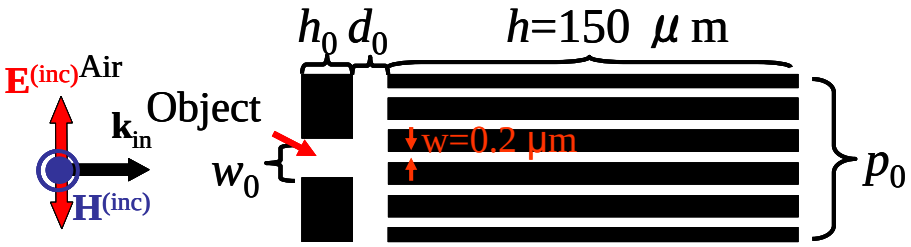

Fig. 4.4 Schematic view of deep-subwavelength imaging at 1 THz with grating/dielectric structure. All dielectric layers are defined as air. The objects to be imaged are the slits in the front grating indicated by the red arrow. The size of the object w_0 is 1 μm. The distance between two objects p_0 is 5 μm, and the thickness of the object h_0 is 1 μm. The lens has length h and the slit width w indicated in the figure. The period of the lens is 1 μm.

In this section, the subwavelength imaging of the object with size 1 μm is demonstrated at the frequency close to 1 THz by spoof surface plasmons (SSPs) in one grating/dielectric structure. We have shown in the previous chapter that the SSPs can be designed by varying the height of the grating because the cut-off frequency of the SSPs is determined by the Fabry-Perot (FP) of the grating. By defining the slit height as 150 μm, the FP occurs at 1 THz. By choosing the period of the grating as 1 μm, the SSPs can have much larger wavenumber comparing to the wavenumber of light in vacuum, and thus the condition of deep-subwavelength is achieved. And by defining the slit width as 200 nm, this grating can be applied to image subwavelength objects via the SSPs.

The schematic view of the subwavelength imaging system is shown in Fig. 4.4. The frequency of the SSPs with wavenumber $k_x = \pi / p$, where p=1 μm is the period of the lens, is 0.997 THz. The objects are the infinite array of subwavelength slits. The size of the object corresponds to the slit width which is equal to 1 μm, and the distance between two objects corresponds to the period p_0 which is defined as 5 μm. The object also has the finite size along the y-axis which corresponds to the slit height h_0. Our aim is to carry the fine information of the objects which are encoded in the large wavenumber s along the x-axis to the detector placed far from the objects. To do this, the lens is brought close to the objects, not touch but with some distance apart denoted by the distance d_0 , in order to carry the large wavenumbers from one side of the lens to another side. The another side of the lens is assumed to have a good detector which can visualize the image intensity brought there by the lens.

Fig. 4.5 (a) shows the |**E**| behind the lens for the separation distance between the object and the lens is 100 nm. This distance is chosen because it is smaller than the decay length of the amplitude of the electric field of the SSPs which is 144 nm for this lens. The |**E**| is normalized by the amplitude of the incident light, and the numerical values on the colour bar indicate how large the amplitude of the electric field on the image compared with the amplitude of the incident light. The image of the object is clearly seen in this figure. The maximum of the electric field amplitude reaches 30.6 times larger than the amplitude of the incident electric field! However, the electric field of the image quickly decays along the y-axis with the decay length δy, defined as the distance at which the |**E**| decreases by 1/*e*, just

122 nm. The resolution of the image is determined by the full width at half maximum (FWHM) of the |**E**| along the output interface of the lens. We found that the resolution is Δx=314 nm, which is even sharper than the size of the object. In order to confirm that this is the unique imaging property of this lens, we substitute the lens with Si slab with the same thickness as the lens. The Si slab is brought in contact with the objects, and the electric field distribution inside the Si slab and behind the Si slab is obtained at a single Fabry-Perot resonance of the Si slab 1.1474 THz. The result is shown in Fig. 4.5 (b). The standing wave is generated inside the Si slab as expected. Behind the Si interface, the amplitude of the electric field becomes constant, and there is no sign of the object. In this case, the large wavenumbers from the object suffer diffraction limit inside Si slab, and thus they quickly decay and unable to reach the image plane. Therefore, the SSPs in the grating can carry the large wavenumber waves of the objects to the image plane without suffering the diffraction limit.

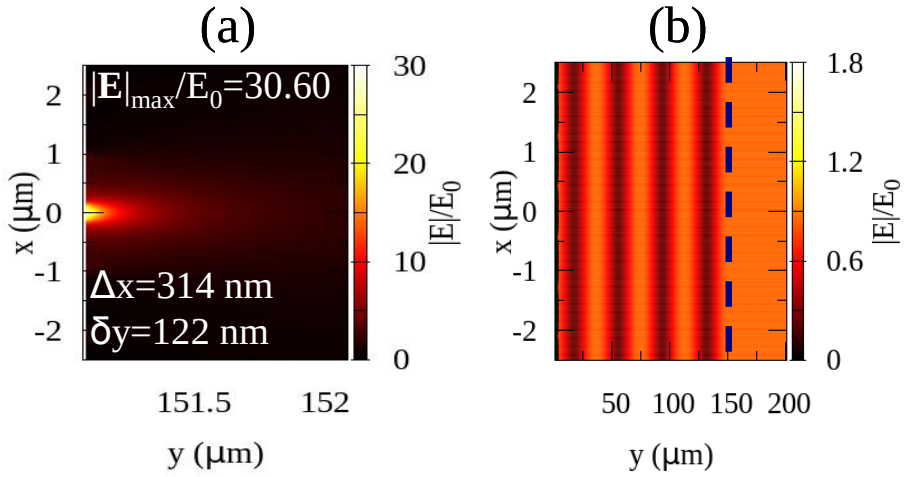

Fig. 4.5 Analytical demonstration of deep-subwavelength imaging. (a) The |**E**|-distribution behind the grating acting as subwavelength imaging lens. (b) The |**E**|-distribution inside Si slab and behind Si slab which is in directly contact with the objects. The Si slab has the same thickness as the grating. The blue dashed line indicates the Si interface.

Next, we consider the effect of the separation distance between the objects and the lens on the imaging properties. The |**E**| distributions for three cases are shown in Fig. 4.6. By increasing the separation distance to 1 μm, two more images appear around the central image. We interpret this result as not-resolved because we cannot distinguish these images, and thus the information about the object is not known. This can be understood by considering the decay length of the SSPs. The separation distance is almost 7 times larger than the decay length of the amplitude of the electric field of the SSPs. Therefore, the SSPs are weakly excited and unable to carry large wavenumber of the objects to the image plane. By reducing the separation distance, we expect that the image intensity ($|\mathbf{E}|^2$) should be larger because the objects are closer to the lens. Surprisingly, the opposite result is obtained as shown in Fig. 4.6 for the 1 nm separation distance. The amplitude of the electric field for the 1 nm separation distance is smaller than the 100 nm separation distance, while the resolution and the decay length do not dramatically changes.

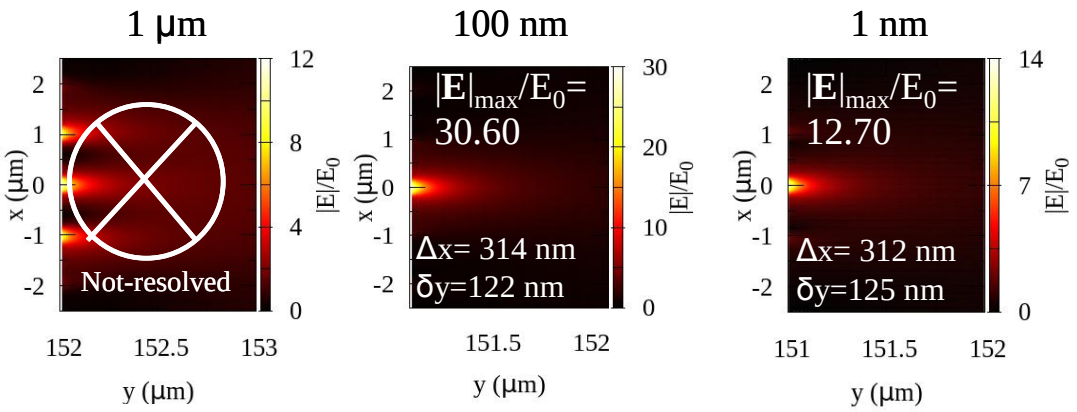

Fig. 4.6 |**E**|-distributions behind the lens for the separation distances (from left to right) 1 μm, 100 nm, and 1 nm.

We can understand this behaviour by considering the development of the transmission spectra as the separation distance decreases.

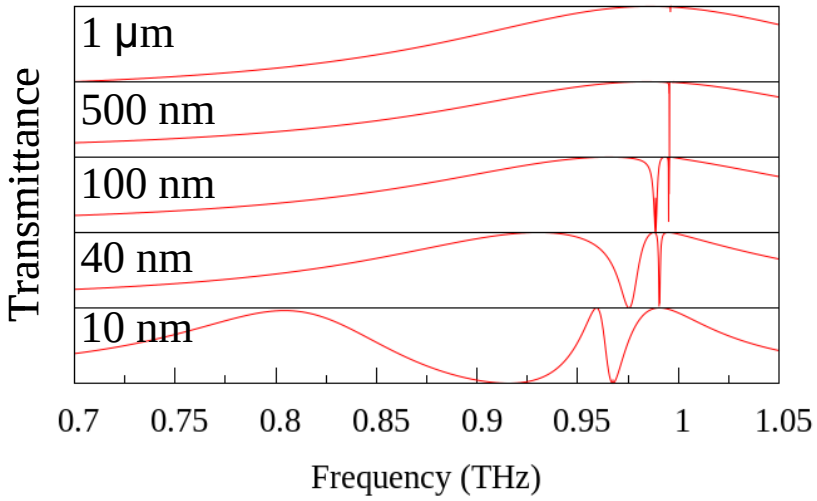

Fig. 4.7 The development of transmission spectra as a separation distance between objects and lens decrease from 1 μm to 10 nm.

Fig. 4.7 shows the transformation of the transmission spectra as the separation distance between objects and lens decrease form 1 μm to 10 nm. At the separation distance 1 μm, only the original FP of the lens is seen due to the weak interaction between the object and the lens. As the separation distance decreases to 500 nm, the sharp dip is observed and the FP starts to split. As the separation distance is smaller to 100 nm, we observe new peak between the two split peaks. This peak occurs at the frequency 0.993 THz which is 4.0 GHz smaller than the original SSPs. This peak corresponds to the QWR between the objects and the lens which will become clear shortly. This position is preferable because the original SSPs accept the energy from the QWR, and thus the amplitude of the electric field of the image increases. By reducing the separation distance further, all peaks shift to lower frequency. The transmittance at the original SSP drastically drop from 99.8% of the 100 nm separation distance to 28.8% of the 1 nm separation distance. The transmission spectra for the 1 nm separation distance is shown in Fig. 4.8 (a).

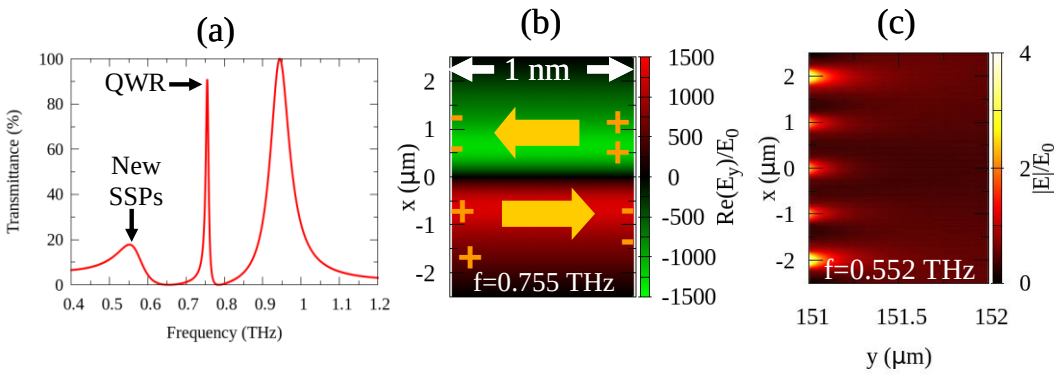

Fig. 4.8. Resonances at 1 nm separation distance. (a) Transmission spectra showing the resonant peaks at 0.552 THz, 0.755 THz, and 0.944 THz. (b) Normal component of the electric field in the region between the objects and the lens at 0.755 THz. The arrows indicate direction of electric field. (c) |**E**|-distribution behind the lens at the frequency 0.552 THz.

The QWR of the 1 nm separation distance is at 0.755 THz which is 0.238 THz lower than the QWR of the 100 nm separation distance. The normal component of the electric field E_y at the QWR of the 1 nm separation distance is shown in Fig. 4.8(b). The maximum of the E_x is only 5 times larger than the amplitude of the incident electric field, while the maximum of E_y reaches 1500. The red colour in the figure 4.8 (b) indicates the electric field pointing to the right, while the green colour indicates the field pointing to the left. The large E_y induces the surface charges on the metallic part of the grating, which then introduce the surface current flowing over the surface of the grating. The current can complete the loop by the normal component of the electric field displacement. This current loop is the characteristic of the QWR [77,]. At the frequency lower than the QWR, the new mode appears due to the splitting of the FP. This mode is the excitation of the new SSPs on the output interface of the lens. The |**E**|-distribution behind the lens at this mode is shown in Fig. 4.8 (c). The SSPs is clearly seen to localize on the output interface of the lens. The SSPs is close to its cut-off frequency determined by the cavity resonance condition $\cos(k_c h) = 0$, and thus $\lambda_c = 4h = 600\ \mu$m or 0.5 THz.

4.4 Subwavelength imaging over long-distance with stacked grating/dielectric layers

The straightforward way of conveying the subwavelength image over longer distance is by simply increasing the length of the bare grating. However, the rods are required to be electrically connected over the long distance, the condition difficult to achieve for the subwavelength rods. As mentioned in the Ref. 30, the rods break up when their diameter is about one micron. Therefore, the bare long-length grating cannot work in the scale down to a single cell. It is required to be able to break up the bare long-length grating into smaller gratings separated by the dielectric layer. This is the stacked grating/dielectric layers as schematically shown in Fig. 4.1 with the testing object. The analytical solutions allow us to efficiently optimize the structure such as the separation distance between the gratings of the lens so that the images appear behind the lens with large number of gratings *N*. The gratings comprising the lens have the same geometry that is grating height h=150 μm, slit width w=0.2 μm, and the period p=1 μm as the previous section. The dielectric host medium is defined as air that is

$n_h = 1$, and thus all slits are filled with air. The thickness of the dielectric layer or the separation distance between the gratings of the lens is defined as *D*. The lens is separated from the object by the air gap with the separation distance defined as D_0=0.1 μm. The object which is the array of slits has the size 1 μm to 4 μm, height 1 μm, and the period 5 μm. Therefore, there are five slits of the lens within the superlattice of the object.

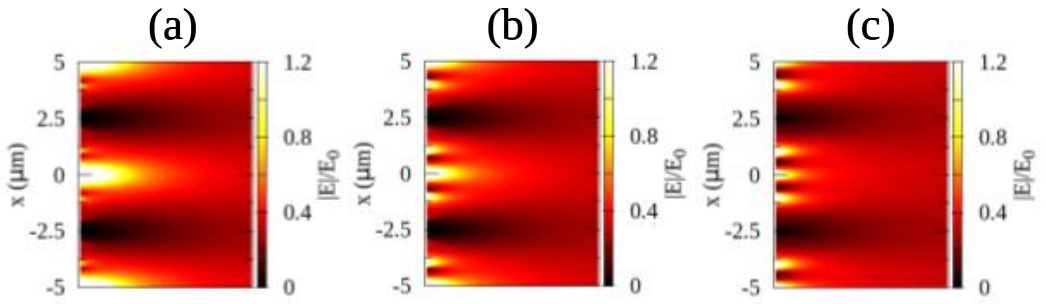

Fig. 4.9. $|\mathbf{E}|/E_0$ behind the stacked grating/dielectric layers with *N*=220 and the optimized separation distance between gratings 80 nm over the distance 2 μm from the end interface of the lens for the object with size (a) 1 μm, (b) 2 μm, and (c) 3 μm. The working frequency is 0.997 THz. Each figure includes two unit cells along the *x*-axis.

Fig. 4.9 (a) shows the normalized amplitude of the electric field behind the lens for the object with size 1 μm. We obtain the sharp subwavelength image, and the object can be resolved. To confirm that this signal really comes from the object, we increase the size of the object to 2 μm and 3 μm while keeping the height and the period, and then check the normalized amplitude of the electric field behind the lens for each case. Fig. 4.9 (b) and (c) show the results for the objects with sizes 2 μm and 3 μm, respectively. The distribution of the normalized amplitude of the electric field changes by increasing the size of the object, and thus confirms that the signal is the energy propagating from the objects. One may expect that the central image located around *x*=0 μm comes directly from the object located around *x*=0. But that is not what happens inside this structure. The object dominantly re-emits the Bloch waves with the tangential component $k_x^{(\mathrm{eff})} = \pm 0.2\pi / p$ where *p*=1 μm (about 30 times larger than wavenumber of light in air), and the effective parameters as discussed in the next chapter leads to the critical angle of the Poynting vector $\theta_c = \pm(0.1229 \pm 0.00002)^\circ$ corresponding to these specific wavevectors. This means that the energy does not propagate perfectly parallel to the *y*-axis, but it rather deviates from the *y*-axis with the small angle θ_c. This critical angle θ_c may look small, but it can affect the image formation in the long length structure such as in our current case. In this case, the total length of the lens is $L = Nh + (N-1)D = 33{,}017.52\ \mu\mathrm{m}$, and therefore the images will be formed at the distance $\delta x = \pm L \tan\theta_c \approx \pm 70\ \mu\mathrm{m}$ from the *y*-axis according to the effective medium model. This means that the energy of the central image at around x=0 really comes from the two objects located at $x = 70\ \mu\mathrm{m}$ and at $x = -70\ \mu\mathrm{m}$. The separation distance between these two objects is 140 μm. Therefore, we can also expect that the energy of the image at around $x = 5\ \mu\mathrm{m}$ comes from the objects

located at $x = 75\ \mu$m and $x = -65\ \mu$m. And also the energy of the image at around $x = -5\ \mu$m comes from the objects located at $x = 65\ \mu$m and $x = -75\ \mu$m.

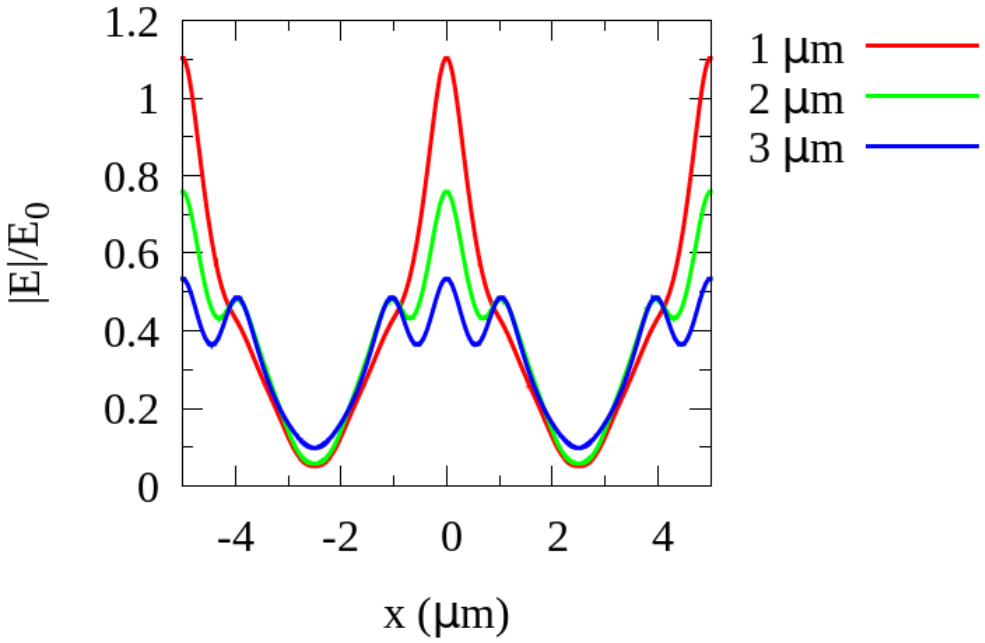

Fig. 4.10. $|\mathbf{E}|/E_0$ along the line parallel to the *x*-axis at the distance 0.398 μm from the end interface of the stacked grating/dielectric layers with *N*=220 and the optimized separation distance between gratings 80 nm for the object with size 1-3 μm as indicated in the figure. The working frequency is 0.997 THz.

Next, we discuss about the resolution of the images. The focal point in our current structure is at the end interface of the structure between the structure and air. However, the amplitude of the electric field is not homogeneous at the end interface due to high electric field in the slits. Therefore, the detection at longer distance from the end interface is required to obtain the smooth image. Unfortunately, the large wavevectors do not propagate in air medium due to the circular equi-frequency contour (EFC) of the air. Therefore, the focal length is poorly defined behind the structure. We may consider the decay length of the intensity δ_I instead. The intensity decay length can be obtained from the tangential component of the wavevector as $\delta_I = 1/2\sqrt{k_x^{(\mathrm{eff})2} - k_0^2}$ which is 0.796 nm for $k_x^{(\mathrm{eff})} = \pm 0.2\pi / p$. The resolution as defined by the full-width-at-half-maximum (FWHM) of the field profile along the line parallel to the *x*-axis at the distance $\delta_I = 0.796\ \mu$m from the end interface is however still poor. We find that at the distance $\delta_I / 2 = 0.398\ \mu$m gives better resolution, and the field profiles at this distance along the line parallel to the *x*-axis are given in Fig. 4.10. The FWHMs for the objects with size 1 μm, 2 μm, and 3 μm are 1.346 μm, 2.778 μm, and 3.260 μm. Therefore, the lens can also distinguish the objects with different sizes from 1-3 μm. The object with size 4 μm can be also distinguished from the objects with smaller size. However, the nearby objects with the same size as 4 μm are barely resolved due to the close separation distance between the objects. We can certainly resolve the objects with smaller separation distance (and smaller size) by reducing the period and the slit width of the lens. The experiment is however would be very challenge.

4.5 Conclusion

We have developed the analytical solutions of the stacked grating/dielectric structures which are the extension of the analytical solutions of the bare grating to make new hyperbolic metamaterials for subwavelength imaging with THz radiation. The analytical solutions are consistent with the FDTD simulation with simple structure and performs beyond the FDTD simulation in the complicated structure. This allows us to apply the analytical solutions to study the imaging of deep-subwavelength object at the frequency close to 1 THz (λ=300 μm). We have found that the spoof surface plasmons (SSPs) in a bare grating at the frequency around 1 THz can carry the subwavelength image with spatial resolution about 314 nm over the distance 150 μm with high electric field enhancement if the objects are located at the preferable distance from the grating. At this preferable distance, the electric field of the subwavelength image can be much larger than the amplitude of the incident light due to the excitation of the quasi-wavegide resonances (QWRs) between the objects and the grating at the frequency close to the SSPs. This new information leads to the realization of the analytical demonstration of the deep-subwavelength imaging over a long distance about 33 mm by using the stacked grating/dielectric layers with the optimized separation distance between the gratings. The imaging signals are confirmed by varying sizes of the objects.

Chapter 5
Effective parameters of stacked grating/dielectric metamaterials

The stacked grating/dielectric layers obviously have the property of the hyperbolic metamaterials (HMMs) because the large wavevectors from the objects can propagate through this structure over the long distance without decaying. But only this argument is not sufficient to confirm that this metamaterial is really the HMMs. The only way to convince the others that it is the HMMs is by (i) drawing the equi-frequency contour (EFC) of electromagnetic waves propagating inside this structure and discuss the type of HMMs, and (ii) obtain the effective parameters of the structure so that we can know the critical angle of the Poynting vector. The critical angle of the Poynting vector can be used to compare the effective model with the analytical solutions. If we obtain the consistent results, it means that the stacked gratings/dielectric structures are really the HMMs. If we don't obtain the consistent results, we have to stick with the analytical solutions (because they are consistent with FDTD) and seek for the new method of retrieving the EFC and the effective parameters of this structure. Here, we can obtain the consistent results and we can firmly state that the stacked gratings/dielectric metamaterials are the HMMs. The type of HMMs depend on frequency and the geometry of the structure. Therefore, the metallic grating can be considered as the new metal for making the HMMs in the THz band. The analytical solutions of the cylindrical hyperlens developed in the chapter 2 may be extended to the THz band by replacing the metallic layer with the grating layer.

In this chapter, we describe the technique of retrieving the effective parameters of the stacked grating/dielectric structures in the section 5.1. By using this technique, we can draw the hyperbolic EFC for any number of the stacked grating/dielectric layers and obtain their effective parameters. We show the EFC and the effective parameters of N=10 numbers of stacked grating/dielectric layers in the section 5.2. In the section 5.3, we compare the image's field distributions obtained by the analytical solutions with the effective model. In the section 5.4, we show how the hyperbolic EFC and the effective parameters change as the number of the unit cells increases. Finally, the chapter is summarized in the section 5.5.

5.1 Method of retrieving effective parameters

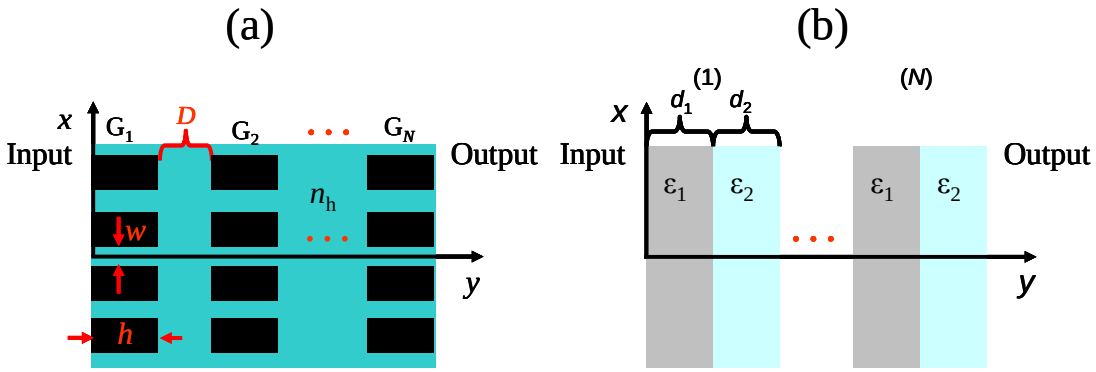

Fig. 5.1. (a) Schematic of the stacked grating/dielectric layers as the THz hyperbolic metamaterials (THz-HMMs) drawn over 4 unit cells along the *x*-axis. The refractive index of the dielectric layer is labelled by n_h, and all slits are filled with this material. All gratings have the same height *h* and slit width *w*. The number of gratings is defined by *N*. (b) Schematic of the alternating metal/dielectric layers. The number of the unit cell is defined by *N* .

We retrieve the effective parameters of the stacked grating/dielectric layers as schematically shown in Fig. 5.1 by comparing their reflection and transmission coefficients with those of the anisotropic medium whose dispersion relation satisfies Eq. (2.13). But now the optical constants become the effective parameters which are denoted by $\varepsilon_x^{(\mathrm{eff})}$, $\varepsilon_y^{(\mathrm{eff})}$, and $\mu_z^{(\mathrm{eff})}$. The components of the wavevectors are also considered as the effective parameters $k_x^{(\mathrm{eff})}$ and $k_y^{(\mathrm{eff})}$. Notice that we also include the magnetic effect on these structures by allowing $\mu_z^{(\mathrm{eff})} \neq 1$. Our tasks are (i) drawing the contour between the $k_x^{(\mathrm{eff})}$ and $k_y^{(\mathrm{eff})}$ at the given frequency called the EFC, and (ii) retrieve the effective parameters $\varepsilon_x^{(\mathrm{eff})}$, $\varepsilon_y^{(\mathrm{eff})}$, and $\mu_z^{(\mathrm{eff})}$. There were some papers which outlined the method of effective parameters retrieval for the anisotropic media [86,87]. We attempted to use the expressions of the refractive index along the *y*-axis *n* and the impedance ξ given in Eq. (12) of Ref. 86, but the reflectance and transmittance of the stacked grating/dielectric layers from the analytical solutions cannot be reproduced even in the case of the normal incidence. The Ref. 87 gives satisfying results for the EFC between the $k_x^{(\mathrm{eff})}$ and $k_y^{(\mathrm{eff})}$. However, the $\varepsilon_x^{(\mathrm{eff})}$ strongly depends on the incident angle in this model, and thus we are forced to fit the EFC for the new $\varepsilon_x^{(\mathrm{eff})}$ which then affects the effective reflection and transmission coefficients. Therefore, the spectra obtained by this model are different from the spectra obtained by the analytical solutions. Here, we describe our simple model which gives the unique $\varepsilon_x^{(\mathrm{eff})}$ and also the same EFC as that obtained by the Ref. 87. From these information, the remaining parameters can be obtained.

We start by comparing the 0th-order transmission coefficient of the stacked grating/dielectric layer from the analytical solutions and that from the effective medium model. From Eq. (4.36) and (4.27), the 0th-order transmission coefficient $A_0^{(\mathrm{out})}$ of the stacked grating/dielectric layers shown in Fig. 5.1 can be written as

$$A_0^{(\mathrm{out})} = \frac{1}{\Omega_{\mathrm{disp}} / \left(i Y_0 s_0 N_{\mathrm{T}} \right)}, \tag{5.1}$$

where $Y_0 = k_0 / k_y$, $s_0 = \sqrt{w/p}\,\mathrm{sinc}\left(k_x w/2\right)$, $N_\mathrm{T} = -\left(2s_0 / n_\mathrm{h}\right)\left(G_\mathrm{V}\right)^N \left(G^{(\mathrm{F})}\right)^{(N-1)}$, and the dispersion function Ω_{disp} is given by Eq. (4.38). The 0th-order transmission coefficient t_0 of the effective medium obtained by applying the boundary conditions of H_z and E_x is written as

$$t_0 = \frac{1}{\left(\dfrac{k_y^{(\mathrm{eff})2} + \left(\varepsilon_x^{(\mathrm{eff})} k_y\right)^2}{2ik_y \varepsilon_x^{(\mathrm{eff})} k_y^{(\mathrm{eff})}}\right)\sin\left(k_y^{(\mathrm{eff})} L\right) + \cos\left(k_y^{(\mathrm{eff})} L\right)}, \tag{5.2}$$

where $L = Nh + \left(N-1\right)D$ is the total length of the structure. By comparing Eq. (5.1) and (5.2), we obtain the first equation of the effective medium model written as follows

$$\left(\frac{k_y^{(\mathrm{eff})2} + \left(\varepsilon_x^{(\mathrm{eff})} k_y\right)^2}{2ik_y \varepsilon_x^{(\mathrm{eff})} k_y^{(\mathrm{eff})}}\right)\sin\left(k_y^{(\mathrm{eff})} L\right) + \cos\left(k_y^{(\mathrm{eff})} L\right) = \Omega_{\mathrm{disp}} / \left(iY_0 s_0 N_\mathrm{T}\right). \tag{5.3}$$

The solutions obtained solely by Eq. (5.3) are not unique, and we need to accompany it with another equation from the 0th-order reflection coefficient. From Eq. (4.29) and (4.40), the 0th-order reflection coefficient $B_0^{(\mathrm{in})}$ of the stacked grating/dielectric layers can be written as

$$B_0^{(\mathrm{in})} = \frac{\Omega_{\mathrm{disp}} / \left(iY_0 s_0 N_\mathrm{R}\right) + 1}{\Omega_{\mathrm{disp}} / \left(iY_0 s_0 N_\mathrm{R}\right)}, \tag{5.4}$$

where $N_\mathrm{R} = \left(2s_0 / n_\mathrm{h}\right)\Omega'_{2(N-1)-1}$ and $\Omega'_{2(N-1)-1}$ is given by Eq. (4.50). The 0th-order reflection coefficient r_0 of the effective medium obtained by applying the boundary conditions of H_z and E_x is written as

$$r_0 = \frac{-\left(\dfrac{k_y^{(\mathrm{eff})2} - \left(\varepsilon_x^{(\mathrm{eff})} k_y\right)^2}{2ik_y \varepsilon_x^{(\mathrm{eff})} k_y^{(\mathrm{eff})}}\right)\sin\left(k_y^{(\mathrm{eff})} L\right)}{\left(\dfrac{k_y^{(\mathrm{eff})2} + \left(\varepsilon_x^{(\mathrm{eff})} k_y\right)^2}{2ik_y \varepsilon_x^{(\mathrm{eff})} k_y^{(\mathrm{eff})}}\right)\sin\left(k_y^{(\mathrm{eff})} L\right) + \cos\left(k_y^{(\mathrm{eff})} L\right)}. \tag{5.5}$$

By comparing Eq. (5.4) and (5.5), their denominators give the same condition as Eq. (5.3), and their numerators lead to the new condition of the effective medium written as follows

$$-\left(\frac{k_y^{(\mathrm{eff})2} - \left(\varepsilon_x^{(\mathrm{eff})} k_y\right)^2}{2ik_y \varepsilon_x^{(\mathrm{eff})} k_y^{(\mathrm{eff})}}\right)\sin\left(k_y^{(\mathrm{eff})} L\right) = \Omega_{\mathrm{disp}} / \left(iY_0 s_0 N_\mathrm{R}\right) + 1. \tag{5.6}$$

By solving Eq. (5.3) and (5.6), the EFC can be obtained by solving the following equation for $k_y^{(\mathrm{eff})}$

$$\cos\left(k_y^{(\mathrm{eff})} L\right) = \frac{1 + \Delta_1 \Delta_2}{\Delta_1 + \Delta_2}, \tag{5.7}$$

where the parameter Δ_1 and Δ_2 are defined as follows

$$\Delta_1 = -N_\mathrm{R} / N_\mathrm{T} = -\left(B_0^{(\mathrm{in})} - 1\right) / A_0^{(\mathrm{out})},\ \Delta_2 = \left(2\Omega_{\mathrm{disp}} + iY_0 s_0 N_\mathrm{R}\right) / \left(iY_0 s_0 N_\mathrm{T}\right) = \left(B_0^{(\mathrm{in})} + 1\right) / A_0^{(\mathrm{out})}. \tag{5.8}$$

By substituting Eq. (5.8) into Eq. (5.7), the condition of $k_y^{(\mathrm{eff})}$ can be re-written in terms of the reflection and transmission coefficients as follows

$$\cos\left(k_y^{(\mathrm{eff})}L\right)=\frac{A_0^{(\mathrm{out})2}-B_0^{(\mathrm{in})2}+1}{2A_0^{(\mathrm{out})}}. \tag{5.8}$$

This equation gives the condition of $k_y^{(\mathrm{eff})}$ for given frequency and k_x. We may then call k_x which leads to the physical $k_y^{(\mathrm{eff})}$ as $k_x^{(\mathrm{eff})}$. By drawing the contour between the $k_x^{(\mathrm{eff})}$ and $k_y^{(\mathrm{eff})}$ at the given frequency, we obtain the EFC of the structure. The EFC may contain the band gaps at which the $k_y^{(\mathrm{eff})}$ are forbidden to propagate if the amplitude of the right hand side (RHS) of Eq. (5.8) exceeds one. Moreover, the EFC may also contain the resonance if the reflection and transmission coefficients are infinite which occur when $\mathrm{Re}\left(\Omega_{\mathrm{disp}}\right)=0$. Lastly, for those who write the programming code to solve Eq. (5.8), care must be taken to the "very small" imaginary part of the RHS of this equation. In our case, if the imaginary part of the RHS of Eq. (5.8) is smaller than 10^{-4}, it is lowered to exactly zero and thus the RHS becomes just real number.

It is useful to check this model by comparing it with the well known effective medium approximation (EMA) for the alternating metal/dielectric layers as schematically shown in Fig. 5.1 (b). If the thickness of each layer is the same (d_1=d_2) and small enough comparing to the wavelength of light, then the EMA predicts that the effective parameters are independent on the thickness and simply given by $\varepsilon_x^{(\mathrm{eff})}=\left(\varepsilon_1+\varepsilon_2\right)/2$ and $\varepsilon_y^{(\mathrm{eff})}=2\varepsilon_1\varepsilon_2/\left(\varepsilon_1+\varepsilon_2\right)$. By using these effective parameters, the EFC from the EMA can be drawn. In our model, the steps are reversed. We don't know the effective parameters, but we can draw the EFC by using the condition of the $k_y^{(\mathrm{eff})}$ in Eq. (5.8) with the reflection and transmission coefficients given as follows

$$B_0^{(\mathrm{in})}=-\frac{S_{21}}{S_{22}},\ A_0^{(\mathrm{out})}=\frac{\det(\mathbf{S})}{S_{22}}, \tag{5.9}$$

where S_{ij} is matrix element of the scattering matrix $\mathbf{S}$ which is obtained from the transfer matrices as follows

$$\mathbf{S}=\mathbf{T}_{\mathrm{out}}\left(\mathbf{T}_{2,1}\mathbf{T}_{1,2}\right)^{N-1}\mathbf{T}_{2,1}\mathbf{T}_{\mathrm{in}}, \tag{5.10}$$

where N is the number of the unit cell, and the transfer matrices which are obtained by applying the boundary conditions are defined as follows

$$\mathbf{T}_{\mathrm{in}}=\frac{1}{t_{1,\mathrm{in}}}\begin{pmatrix}1 & r_{1,\mathrm{in}}\\ r_{1,\mathrm{in}} & 1\end{pmatrix},\ \mathbf{T}_{\mathrm{out}}=\begin{pmatrix}t_{2,\mathrm{out}}\exp\left(i\phi_2\right) & 0\\ -r_{2,\mathrm{out}}\exp\left(i\phi_2\right) & \exp\left(-i\phi_2\right)\end{pmatrix},\mathbf{T}_{\alpha,\beta}=\frac{1}{t_{\alpha,\beta}}\begin{pmatrix}\exp\left(i\phi_\beta\right) & r_{\alpha,\beta}\exp\left(-i\phi_\beta\right)\\ r_{\alpha,\beta}\exp\left(i\phi_\beta\right) & \exp\left(-i\phi_\beta\right)\end{pmatrix}, \tag{5.11}$$

where $r_{\alpha,\beta}$ and $t_{\alpha,\beta}$ are 0th-order reflection and transmission coefficients, respectively, from the medium α to the medium β which are defined in Eq. (3.21) for the TM wave. From the EFC, we then retrieve the effective parameters which will be described shortly. To compare our new model with the old EMA, we assume the fictitious dielectric constants as $\varepsilon_1=-3$ and $\varepsilon_2=4$ at the working frequency 0.1 THz (3 mm). According to the EMA, this medium is HMMs-I where $\varepsilon_x^{(\mathrm{eff})}=0.5$ and $\varepsilon_y^{(\mathrm{eff})}=-24$. Fig. 5.2 (a) shows the EFCs for the layer thickness 20 nm. Our model gives almost identical EFC as that from the EMA because the thickness is 150,000 times smaller than the working

wavelength. The EFC shows the type-I hyperbolic dispersion as expected. Our model also takes into account both layer thickness and finite size of the whole structure. By increasing the thickness to 1 μm, the EFC obtained from our model deviates from that obtained from the EMA as shown in Fig. 5.2 (b). The angle of the wavevectors with respect to the *y*-axis becomes larger resulting in smaller angle of the Poynting vector with respect to the *y*-axis.

After retrieving the EFC of the structure, the next step is retrieving the $\varepsilon_x^{(\text{eff})}$. From Eq. (5.3) and (5.6), the $\varepsilon_x^{(\text{eff})}$ can be written in terms of $k_y^{(\text{eff})}$ as follows

$$\varepsilon_x^{(\text{eff})} = -i\frac{k_y^{(\text{eff})}}{k_y}\left(\frac{\cos\left(k_y^{(\text{eff})}L\right)-\Delta_2}{\sin\left(k_y^{(\text{eff})}L\right)}\right). \tag{5.12}$$

The $\varepsilon_x^{(\text{eff})}$ is independent on the sign of $k_y^{(\text{eff})}$, and its uniqueness can be checked by varying the incident angle. We take into account the causality in order to obtain the $\varepsilon_x^{(\text{eff})}$. That is we choose only the wavevectors which give the energy flowing out from the front interface (*y*=0) to the end interface (*y*=*L*). In another word, only the electromagnetic waves giving the Poynting vector propagating in the +*y* axis direction is taken to retrieve the $\varepsilon_x^{(\text{eff})}$. Therefore, it is required to draw at least two EFCs in order to check the directions of the Poynting vectors. Let's us try to convert the EFC in Fig. 5.2 (a) to the $\varepsilon_x^{(\text{eff})}$. We draw three EFCs in Fig. 5.3 for the alternating metal/dielectric layers with parameters the same as those in Fig. 5.2 (a). Notice that the components of wavevectors are not normalized by k_0 because we want to compare the EFCs at different frequencies. The anomalies found in each EFC occur when $\left|k_x^{(\text{eff})}\right| = k_0$. The Poynting vector (**S**) is parallel to the group velocity which is perpendicular to the EFC and points to

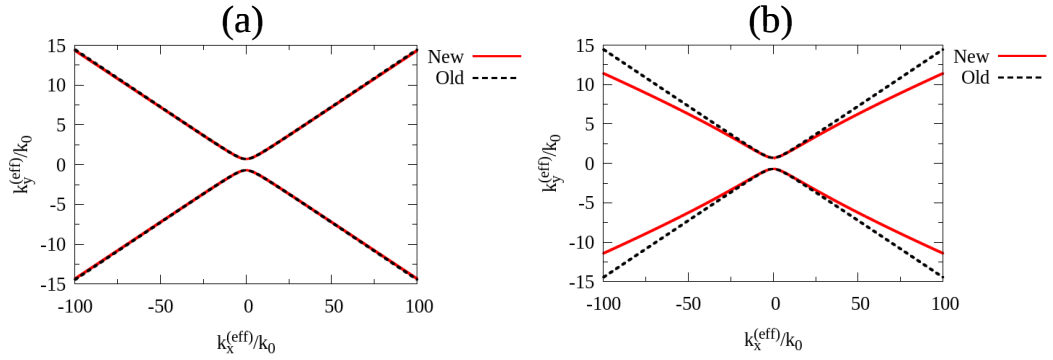

Fig. 5.2. EFC of alternating metal/dielectric layers for layer thickness 20 nm (a), and 1 μm (b). The red line is obtained by the new model and the black dashed line is obtained by EMA. The number of unit cell is defined as 10 (total number of layers is 20). The working frequency is 0.1 THz. The dielectric constants of the metal and dielectric are fictitious and assumed to be $\varepsilon_2 = -3$ and $\varepsilon_1 = 4$, respectively, to form HMMs-I.

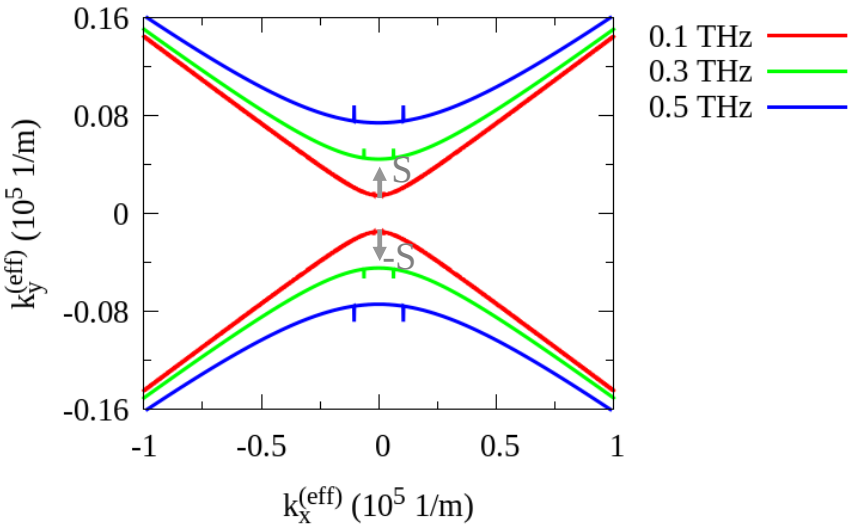

Fig. 5.3. EFCs of alternating metal/dielectric layers at three increasing frequency. The parameters of the structure are the same as those in Fig. 5.2 (a).

higher frequency EFC. The direction of the Poynting vector is also indicated in the Fig. 5.3. According to this figure, the Poynting vector propagates in +*y* direction (flowing out from the front interface) for positive $k_y^{(\text{eff})}$, but it propagates in the -*y* direction (flowing in to the front interface) for the negative $k_y^{(\text{eff})}$. Therefore, we choose the former case to retrieve $\varepsilon_x^{(\text{eff})}$ (and other effective parameters). By applying Eq. (5.12) to retrieve $\varepsilon_x^{(\text{eff})}$ from $k_y^{(\text{eff})}$ given in the EFC in Fig. 5.2 (a), we have $\varepsilon_x^{(\text{eff})} = 0.5000000 - 0.0000734i$. The negative imaginary part must be considered as the accuracy of this retrieval model. Therefore, this model is accurate to the fourth decimal position. The accuracy does not come from the restriction imposed on the imaginary part of the RHS in Eq. (5.8) because the accuracy is the same by relaxing this restriction. This means that the accuracy is intrinsic to this model. The model is not limited only to the lossless material. We introduce the imaginary part to the metal $\varepsilon_1 = -3 + 0.1i$ so that the energy of the electromagnetic waves decay from the front interface as it flows forward. At the normal incidence, the EFC of this structure can be converted to $\varepsilon_x^{(\text{eff})} = 0.5000 + 0.0499i$.

Next, we explain how to obtain the remaining effective parameters. For both types of HMMs, the parameter $\mu_z^{(\text{eff})}$ can be obtained from $k_y^{(\text{eff})}$ and $\varepsilon_x^{(\text{eff})}$ by using the relation $k_y^{(\text{eff})} / k_0 = \pm\sqrt{\varepsilon_x^{(\text{eff})}\mu_z^{(\text{eff})}}$ at the normal incidence. The sign of the $\mu_z^{(\text{eff})}$ is dictated by the $k_y^{(\text{eff})}$, $\varepsilon_x^{(\text{eff})}$ and type of HMMs. The $\mu_z^{(\text{eff})}$ is positive if both $k_y^{(\text{eff})}$ and $\varepsilon_x^{(\text{eff})}$ are positive, but it becomes negative if both $k_y^{(\text{eff})}$ and $\varepsilon_x^{(\text{eff})}$ are negative. The latter case is referred to the backward travelling wave. The $\mu_z^{(\text{eff})}$ is also positive in type-II HMMs with negative $\varepsilon_x^{(\text{eff})}$ because the real part and the imaginary part of $k_y^{(\text{eff})}$ must be zero and positive, respectively, so that the electromagnetic waves are not-propagating at

the normal incidence. The last parameter, the $\varepsilon_y^{(\mathrm{eff})}$, is however not independent variable, because it is completely determined by the EFC, $\varepsilon_x^{(\mathrm{eff})}$, and $\mu_z^{(\mathrm{eff})}$. We obtain this parameter by fitting the EFC with known $\varepsilon_x^{(\mathrm{eff})}$ and $\mu_z^{(\mathrm{eff})}$. By fitting $\varepsilon_y^{(\mathrm{eff})}$, we don't change the reflection and transmission coefficients because the $\varepsilon_x^{(\mathrm{eff})}$ and $k_y^{(\mathrm{eff})}$ are the same. From the EFC and these effective parameters, the critical angle of the Poynting vector can be obtained by Eq. (2.63). Finally, we compare the reflection and transmission spectra of N=10 stacked grating/dielectric layers obtained by the analytical solutions and the effective medium model for the normal incidence light in Fig. 5.4 (a)-(b), respectively. This effective model gives the perfectly identical spectra to those from the analytical solutions. We not only map the amplitude of the reflection and transmission coefficients, but their phases are also correctly mapped to those of the effective parameters as shown by the real and imaginary parts of these coefficients in Fig. 5.4 (c)-(f).

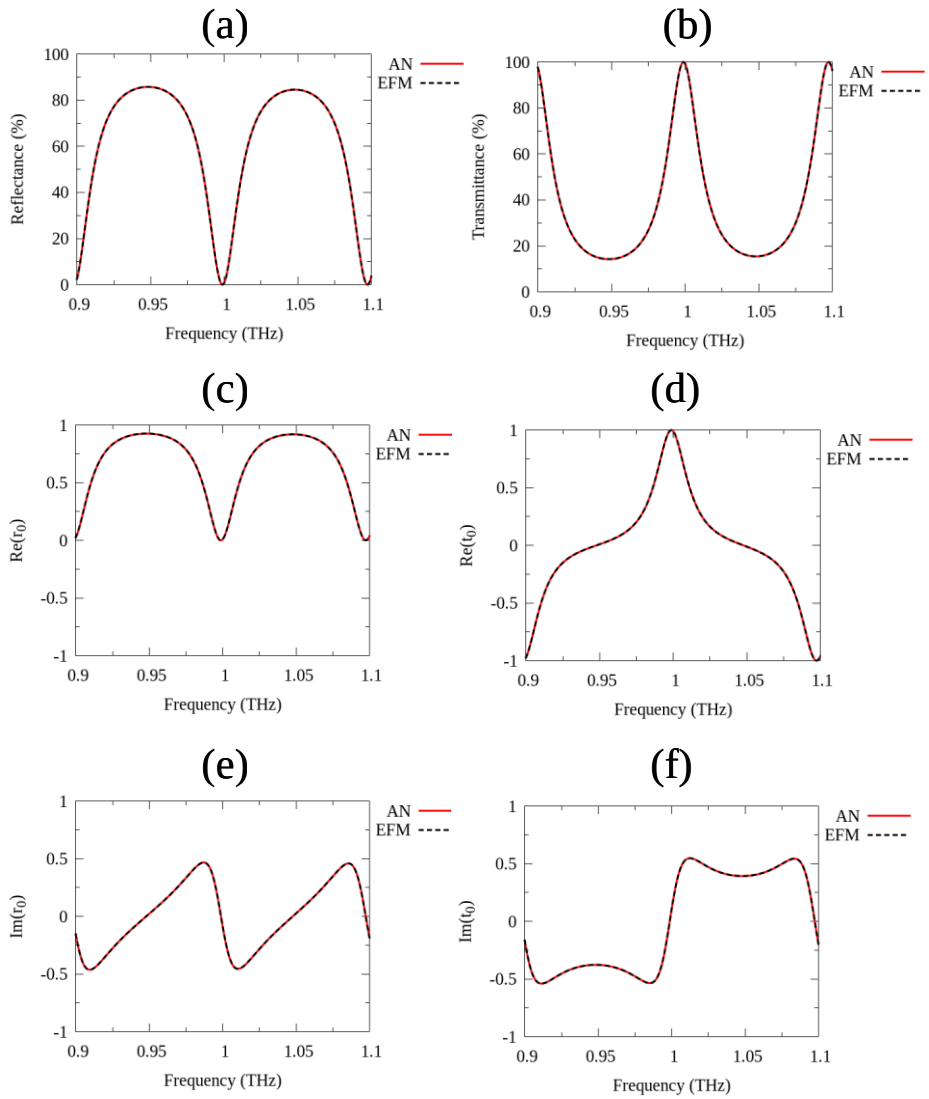

Fig. 5.4. (a) Reflection spectra, and (b) transmission spectra of the N=10 stacked grating/dielectric layers comparing between the analytical solutions (AN) and the effective medium model (EFM). The dielectric is defined as air. The separation distance between grating is 80 nm. The geometrical parameters of the grating are defined as p=1 μm, h=150 μm, and w=1 μm. (c) Real part, and (e) imaginary part of the reflection coefficients of the reflection spectra in Fig. 5.4 (a). (d) Real part, and (f) imaginary part of the transmission coefficients of the transmission spectra in Fig. 5.4(b).

5.2 Equi-frequency contour (EFC) and effective parameters of *N*=10

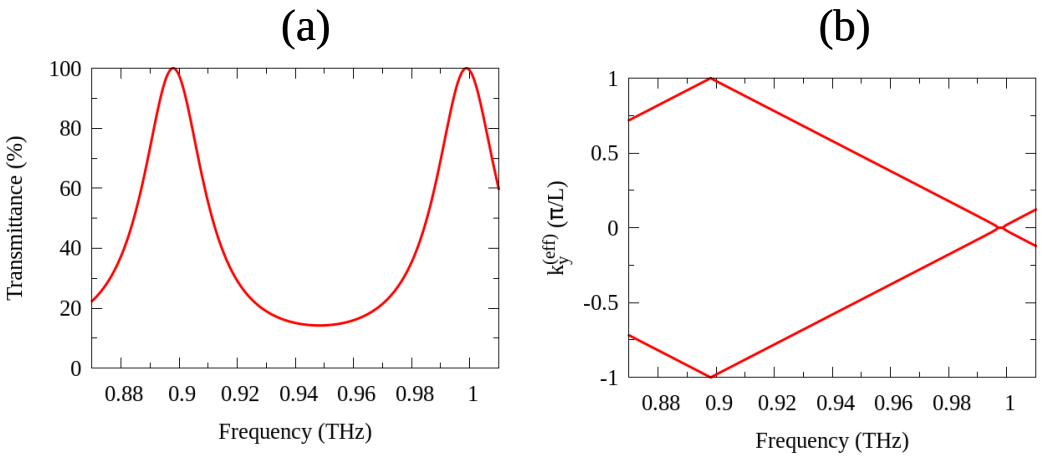

Fig. 5.5. (a) Transmission spectrum, and (b) dispersion relation at the normal incidence (k_x=0) of the *N*=10 stacked grating/dielectric layers where dielectric medium is defined as air and all slits are filled with air. The distance between the gratings is 80 nm. The parameters of the grating is defined as $p=1\ \mu$m, $w=0.2\ \mu$m, $h=150\ \mu$m.

In this section, we use the *N*=10 stacked grating/dielectric layers, where dielectric medium is defined as air and all slits are filled with air, to show the features found in the EFC and the retrieved effective parameters of this structure. The critical angle of the Poynting vector in the stacked grating/dielectric structure is small and therefore we need the structure with long length in order to observe this behaviour and compare this with the analytical solution. The *N*=10 stacked grating/dielectric layers allow us to check the validity of the effective model by comparing the positions of peaks of the amplitude of the electric field behind the structure with those obtained by the analytical solutions.

5.2.1 EFC and type of HMMs

Fig. 5.5 (a) shows the 0th-order transmission spectrum at the normal incidence of the *N*=10 stacked grating/dielectric layers obtained by the analytical solutions compared with that from the effective medium model in the frequency region 0.87-1.01 THz. Two resonant peaks at the frequencies 0.8979 THz and 0.9989 THz correspond to the 9th-order and 10th-order Fabry-Perot (FP) resonances, respectively, of the all-connected gratings with height $10\times150=1{,}500\ \mu$m. The 1st-order FP is at 0.0988 THz ($f_1=c/2\times1{,}500$ Hz) and the frequency difference between two FP resonances is about 0.1 THz. Just below the 10th-FP resonance, the small band gap is created as shown by the dispersion relation in Fig. 5.5 (b) because the $\mathrm{Re}\left(\cos\left(k_y^{(\mathrm{eff})}L\right)\right)>1$. This band gap has the width only 1.7 GHz and the central position of the gap is at about 0.99785 THz. Just above the 9th-FP, the even smaller band gap is created. This band gap has the width only 0.2 GHz with the central frequency of the band gap at 0.8981 THz a little bit higher than the 9th-FP resonance. The width of the band gap can be enlarged by increasing the distance between the gratings as shown in Fig. 5.8. Outside this gap, the $k_y^{(\mathrm{eff})}$ are allowed and become propagating waves. We are reminded that we need to track the history of the phase $k_y^{(\mathrm{eff})}L$ from the lower frequency to the higher frequency to correct the phase within the specific frequency region. There is the confusion again to where in the band gap we should start adding up the

new phase. Technically, we use the centre of the band gap at which the RHS of Eq. (5.8) reaches the maximum or the minimum. The dispersion below the 10th-FP and above the 9th-FP is negative for the forward travelling wave ($k_y^{(\mathrm{eff})} > 0$) that is the frequency decreases by increasing $k_y^{(\mathrm{eff})}$, but the dispersion is positive for the backward travelling wave ($k_y^{(\mathrm{eff})} < 0$) that is the frequency increases by increasing $k_y^{(\mathrm{eff})}$. Therefore, the phase velocity and the group velocity of this structure have opposite signs along the *y*-axis. We need to choose the backward travelling wave when we retrieve the effective parameters due to the causality which will be described shortly. In the frequency below the 9th-FP and above the 8th-FP, the signs of the phase and group velocities become the same. Therefore, we need to choose the forward travelling wave when we retrieve the effective parameters of this structure in the latter case.

Next, we discuss about the type of the HMMs. At the frequencies inside the band gap and below the resonant frequency 0.9989 THz , this structure behaves as type-II HMMs where the major axis is parallel to the tangential component of the wavevector (see Fig. 1.12 (b) for comparison), which are the case for 0.997 THz and 0.998 THz as shown in Fig. 5.6. Outside the band gap, the $k_y^{(\mathrm{eff})}$ are non-zero at $k_x^{(\mathrm{eff})} = 0$, and thus this structure becomes the type-I HMMs where the major axis is parallel to the normal component of the wavevector (see Fig. 1.12 (a) for comparison). The Ponyting vectors (which are parallel to the group velocities) have opposite signs as the phase velocities in both types. The negative phase velocities with respect to the group velocities have been directly measured in the hexagonal boron nitride (h-BN) which shows the hyperbolic dispersion in the mid-infrared band by using s-SNOM combined with time-domain interferometry [26]. We need to choose the backward travelling waves in order to retrieve the effective parameters of this structure because their energy propagate out from the front interface of the structure (*y*=0). Fig. 5.6 shows only the small portion of the EFC within the first Brillouin zone in order to explain the type of each EFC. We extend the EFC at the frequency 0.997 THz

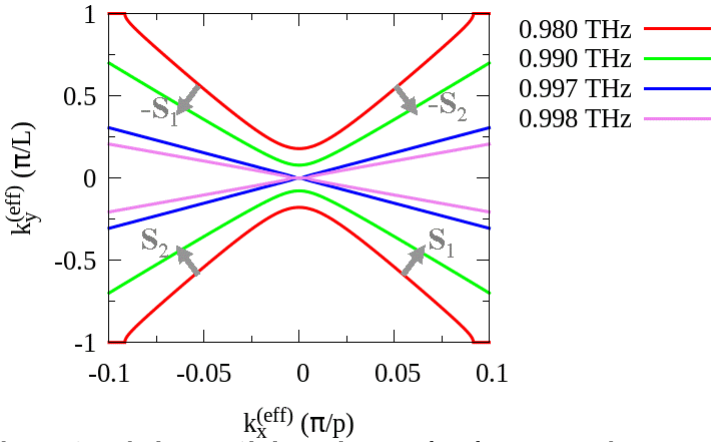

Fig. 5.6. EFCs of the *N*=10 stacked grating/dielectric layers at four frequencies. The parameters of the structure are the same as those in Fig. 5.5. The length of the structure is defined by *L* which is 1500.72 μm for this structure. The arrows schematically indicate the directions of the Poynting vectors which are perpendicular to the EFCs pointing to the higher frequency.

to the edges of the first Brillouin zone of $k_x^{(\text{eff})}$, and the result is shown in Fig. 5.7 (a). We observe the band gap formations when $k_y^{(\text{eff})}$ approach $\pm 1\ (\pi / L)$ and zero. This occurs when the amplitude of the $\cos\left(k_y^{(\text{eff})} L\right)$, as determined by the RHS of Eq. (5.8), exceeds one as shown in Fig. 5.7 (b). The centres of the first band gaps are at about $k_x^{(\text{eff})} = \pm 0.336\ (\pi / p)$. At these positions, the $k_y^{(\text{eff})}$ complete one period from the positive to negative $k_x^{(\text{eff})}$. This region is referred to the zeroth-order $k_y^{(\text{eff})}$. Beyond this region, the $k_y^{(\text{eff})}$ become the first-order that is we need to sum the number $\pm 2\pi / L$ to the $k_y^{(\text{eff})}$ which lie beyond the first band gaps and below the second band gaps at which $k_y^{(\text{eff})}$ complete another period at $k_y^{(\text{eff})} = \pm 1\ (\pi / L)$. The sign of $k_y^{(\text{eff})}$ is chosen according to the slope of $k_y^{(\text{eff})}$ with respect to $k_x^{(\text{eff})}$ in the EFC. If the slope is positive, we add the $-2\pi / L$. If the slope is negative, we add the $+2\pi / L$. The order-corrected EFC is shown in Fig. 5.7 (c) where the flat regions are referred to the band gaps. This structure contain up to the first order $k_y^{(\text{eff})}$. The higher orders will appear in the longer structure because higher order FP resonances are excited. If the interested wavevectors lie only within the region of the zeroth-order $k_y^{(\text{eff})}$, it's sufficient to use only the zeroth-order wavevectors to fit for the $\varepsilon_y^{(\text{eff})}$. However, if the interested wavevectors lie outside the zeroth-order region, it is required to take higher order wavevectors to fit for the $\varepsilon_y^{(\text{eff})}$. Then, the order-correction is needed in the latter case.

We also discuss the effect of the separation distance between the gratings on the EFCs of this structure. Fig. 5.8 (a) shows the effect of the separation distance between the gratings on the transmission spectra. The 9th-FP resonances strongly shift to the lower frequency by increasing the separation distance while the 10th-FP resonances make slightly redshift from the original position. This implies that the 9th-FP is sensitive to the interaction between the gratings while the 10th-FP depends only on the property of the grating. Indeed, the 10th-FP is the 1st-FP of the bare grating with *h*=150 μm comprising the structure. Moreover, we also observe the drop of the transmittance between the two resonant peaks as the separation distance increases. This implies the transformation of $k_y^{(\text{eff})}$ from the propagating waves to the non-propagating wave at the normal incidence. The flat band of the low transmittance is wider by increasing the separation distance. Fig. 5.8 (b) shows the effect of the separation distance between the gratings on the dispersion relation. The band gaps between the 9th-FP and 10th-FP are obviously wider by increasing the separation distances which is the result of the drop of the transmittance and also the wider band of the low transmittance. Fig. 5.8 (b) indicates that the EFC can transform from type-I HMMS to type II-HMMs as a result of the wider band gap. For example, at the frequency 0.95 THz, this structure behaves as type-I HMMs for the separation distances 0.08 μm and 1.00 μm because it lies outside the band gap. As the separation distance increase to 2.00 μm and 3.00 μm , this frequency becomes appear inside the band gap, and thus the structure transforms to the type-II HMMs. These transformations of the EFCs are clearly shown in Fig. 5.8 (d) at the frequency 0.95 THz. For the separation distances 0.08 μm and 1.00 μm, $k_y^{(\text{eff})}$ are propagating

waves at $k_x^{(\mathrm{eff})}=0$, and the major axis is parallel to the $k_y^{(\mathrm{eff})}$. Therefore, the structure is type-I HMMs for these separation distances.

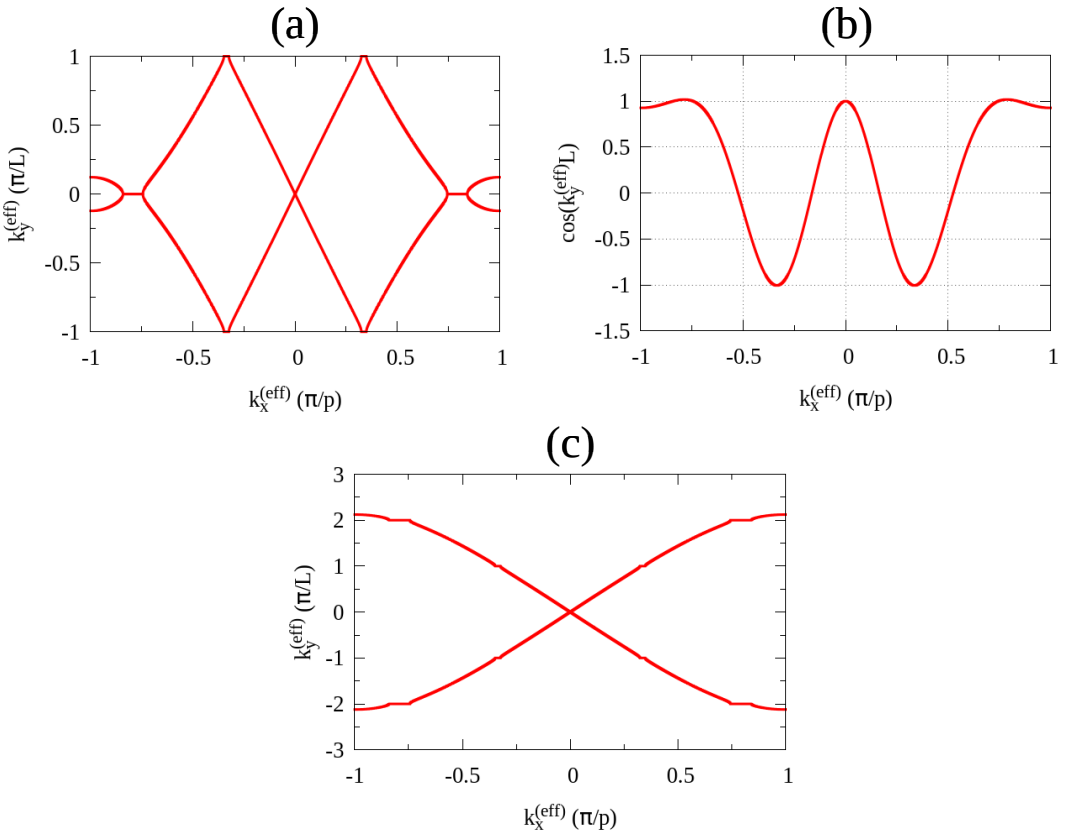

Fig. 5.7. (a) EFC over the first Brillouin zone of the $k_x^{(\mathrm{eff})}$, (b) the RHS of Eq. (5.8) as a function of $k_x^{(\mathrm{eff})}$, and (c) the order-corrected EFC over the first Brillouin zone of the $k_x^{(\mathrm{eff})}$, for the *N*=10 stacked grating/dielectric layers at frequency 0.997 THz. The parameters of the structure are the same as those in Fig. 5.5.

However, for the separation distances 2.00 μm and 3.00 μm, $k_y^{(\mathrm{eff})}=0$ at $k_x^{(\mathrm{eff})}=0$ which means that they are not-propagating, and the major axis is parallel to the $k_x^{(\mathrm{eff})}$. Therefore, the structure is type-II HMMs with these separation distances. The band gap plays important role in the transformation from one type of the HMMs to another type of HMMs, and thus we discuss it in more detail. The band gap is not neither originated by an individual coupling parameter nor the dispersion function alone, but it occurs when the amplitude of the RHS of Eq. (5.8) exceeds one, that is when $\left|\mathrm{Re}\left[\left(A_0^{(\mathrm{out})2}-B_0^{(\mathrm{in})2}+1\right)/2A_0^{(\mathrm{out})}\right]\right|>1$. Therefore, the band gap is originated by the effective model itself. We impose the condition that the $k_y^{(\mathrm{eff})}$ exist, and it must satisfy the condition in Eq. (5.8). However, when the amplitude of $\cos\left(k_y^{(\mathrm{eff})}L\right)$ exceeds one as shown in Fig. 5.8 (c), the real part of the $k_y^{(\mathrm{eff})}$ becomes zero and the imaginary part is positive (we select the positive due to the causality). That means the electromagnetic waves decay inside the structure, they are not the propagating waves. Fig. 5.8 (c) clearly shows that the frequency region where the amplitude of $\cos\left(k_y^{(\mathrm{eff})}L\right)$ exceeds one is

wider by increasing the separation distance. The centre of the band gap is determined by the peak of the amplitude of $\cos\left(k_y^{(\mathrm{eff})}L\right)$, and it shifts to lower frequency by increasing the separation distance.

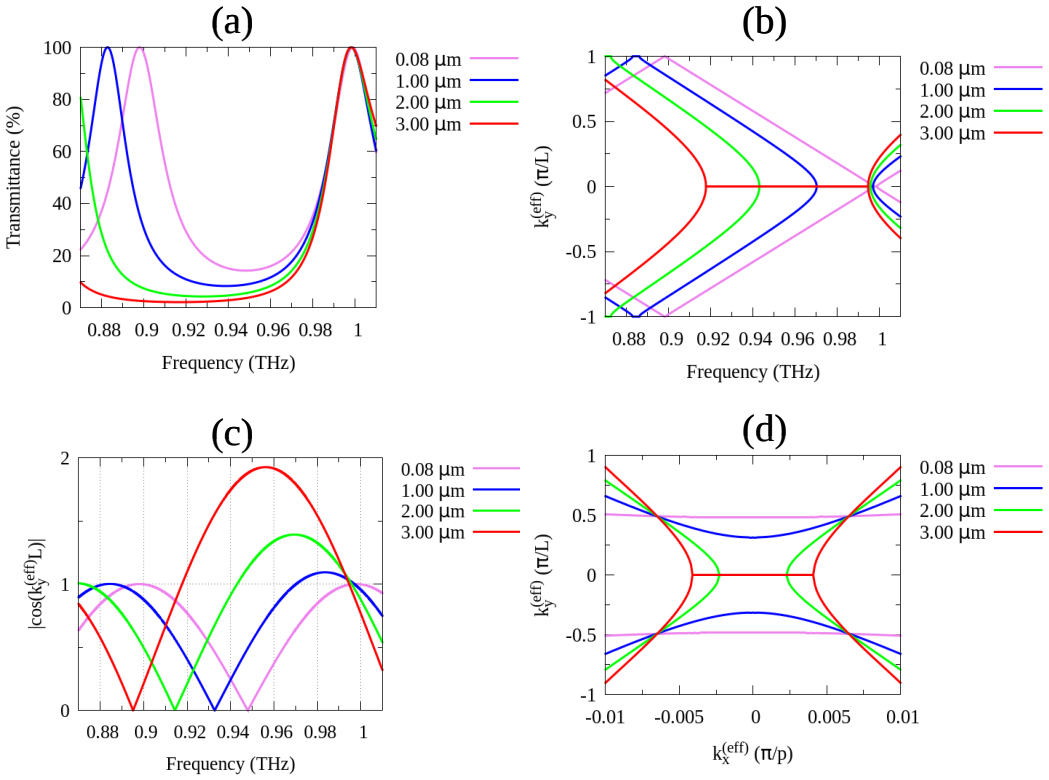

Fig. 5.8. (a) Transmission spectra, (b) dispersion relation, (c) $\left|\cos\left(k_y^{(\mathrm{eff})}L\right)\right|$ as a function of frequency, and (d) EFCs at the frequency 0.95 THz, of the *N*=10 stacked grating/dielectric layers for four separation distances between the gratings as indicated in the figures. The structure is excited by the TM incident light with the normal incidence. The parameters of the structure are the same as those in Fig. 5.5.

5.2.2 The causality

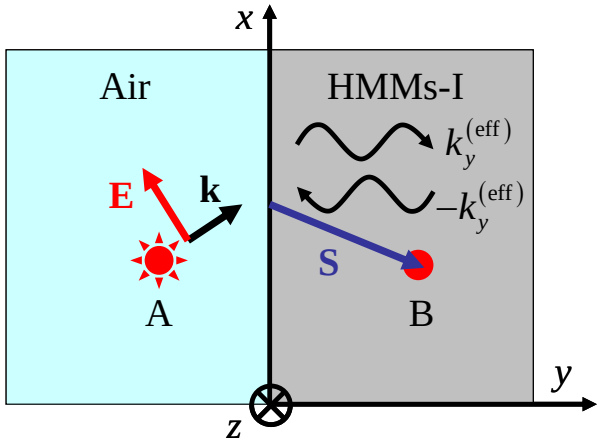

Fig. 5.9. The schematic for the discussion of the causality. Description of the figure is given in the main text.

The causality is the principle of cause and effect. In optics, it means that we cannot have light energy if we don't create light. We discuss this principle in more detail in this section to apply it to retrieve the effective parameters. Consider two semi-infinite media whose interfaces are met at the y=0 plane (xz-plane) as shown in Fig. 5.9. The medium in the region $y<0$ is defined as air while the medium in the region $y>0$ is defined as the HMMs-I. We generate the transverse-magnetic (TM) light at the point A, where the magnetic field is parallel to the z-axis and electric fields are parallel to the xy-plane, close to the interface y=0, and then beam the light onto this interface. The incident light is evanescent wave with $k_x > k_0$. Therefore, it can couple to large wavevector of the HMMs-I and then propagate through the HMMs-I. The Maxwell's equations allow the propagation of the forward travelling wave in which $k_y^{(\mathrm{eff})} > 0$ and the backward travelling wave in which $k_y^{(\mathrm{eff})} < 0$ simultaneously. They can exist only if the causality is satisfied. Suppose we can place the detector inside the HMM-I and detect light at the position B. The light energy that we receive at this position must come from the interface y=0 as indicated by the blue arrow. Therefore, the component of the Poynting vector along the y-axis must be positive, that is the group velocity must be positive. The y-component of the time-averaged Poynting vector in the HMM-I (and also HMM-II) can be expressed as

$$\langle \mathbf{S} \rangle_y = \frac{k_y^{(\mathrm{eff})}}{2\omega\varepsilon_0\varepsilon_x^{(\mathrm{eff})}} \left| H_z^{(\mathrm{T})} \right|^2, \tag{5.13}$$

where $H_z^{(\mathrm{T})}$ denotes the amplitude of the forward or backward travelling wave (T stands for transmitted). Therefore, the forward travelling wave requires the positive $\varepsilon_x^{(\mathrm{eff})}$ while the backward travelling wave requires the negative $\varepsilon_x^{(\mathrm{eff})}$ so that the energy is propagating out from the interface. This is what we mean by the causality here. If we chose the positive $\varepsilon_x^{(\mathrm{eff})}$ for the backward travelling wave, we would obtain the energy propagating into the interface. The same fate would occur if we chose the negative $\varepsilon_x^{(\mathrm{eff})}$ for the forward travelling wave. In both latter cases, the light is fast-light or superluminal [88], which is non-physical in our structure.

5.2.3 The effective parameters

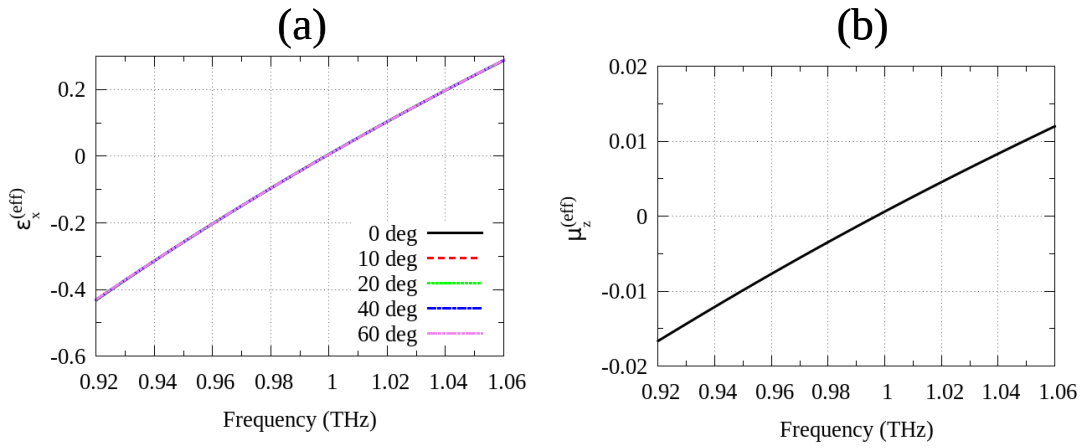

Fig. 5.10. (a) $\varepsilon_x^{(\mathrm{eff})}$ of the N=10 stacked grating/air layers at different incident angles indicated in the figure. (b) $\mu_z^{(\mathrm{eff})}$ of the N=10 stacked grating/air layers at the normal incident angle. The parameters of the structure are the same as those in Fig. 5.5.

Fig. 5.10 (a) shows the $\varepsilon_x^{(\mathrm{eff})}$ as a function of frequency for different incident angles. The $\varepsilon_x^{(\mathrm{eff})}$ does not change by varying the incident angles which means that they are uniquely determined. Moreover, the $\varepsilon_x^{(\mathrm{eff})}$ is independent on the sign of the $k_y^{(\mathrm{eff})}$ according to Eq. (5.12). The $\varepsilon_x^{(\mathrm{eff})}$ is zero at the frequency within the narrow frequency band [0.9987,0.9988] where its sign is changed. This position is very close to the FP which is at 0.9989 THz. Therefore, the $\varepsilon_x^{(\mathrm{eff})}$ is negative below the FP, but it become positive above the FP. This means that the FP is the artificial plasma frequency of this structure in the view of the free electron model (Drude's model). The negative response along the x-axis is due to the excitation of the spoof surface plasmons (SSPs) propagating slowly along the interface of the grating with height h=150 μm. Above the FP, the large wavevectors are no loner supported, and thus there are no neither type-I nor type-II HMMs because there are no more SSPs within this frequency band. Fig. 5.10 (b) shows the $\mu_z^{(\mathrm{eff})}$ as a function of frequency obtained from the $k_y^{(\mathrm{eff})}$ and $\varepsilon_x^{(\mathrm{eff})}$ at the normal incidence. We are reminded that we restrict the condition of the sign on $\mu_z^{(\mathrm{eff})}$ in such a way that it satisfies the EFC and the causality at each frequency. The $\mu_z^{(\mathrm{eff})}$ has similar behaviour as the $\varepsilon_x^{(\mathrm{eff})}$, but the zero position is different. The zero of $\mu_z^{(\mathrm{eff})}$ lies in the narrow frequency band [0.9969,0.9970] where $\mu_z^{(\mathrm{eff})}$ changes its sign. This position is not the same as FP, but it locates very close to the low-energy-side edge of the band gap below the FP. Therefore, it is determined by the frequency position where the HMMs change type or the $k_y^{(\mathrm{eff})}$ at the normal incidence transforms from the propagating wave to non-propagating wave and vice versa.

Because we will compare the analytical solutions working at the frequency f=0.997 THz with our effective medium model, we also fit the EFC at the frequency f=0.997 THz as shown in Fig. 5.7 (a) for the $\varepsilon_y^{(\mathrm{eff})}$. We take into account only the zeroth-order $k_y^{(\mathrm{eff})}$ which are below the first band gap at

$k_x^{(\text{eff})} = \pm 0.336\ (\pi / p)$. At the frequency f=0.997 THz, we know from Fig. 5.10 (a) and (b), respectively, that $\varepsilon_x^{(\text{eff})} = -8.6786 \times 10^{-3}$ and $\mu_z^{(\text{eff})} = 2.9027 \times 10^{-5}$. Then, by applying the non-linear least square method, we obtain the fitted $\varepsilon_y^{(\text{eff})} = 2.1384 \times 10^{3}$. Therefore, the retrieved $\varepsilon_y^{(\text{eff})}$ is positively large number and we obtain the HMMs-II in which the major axis is along the $k_x^{(\text{eff})}$. The fitted EFC at f=0.997 THz is shown by the black dashed line in Fig. 5.11 using this fitted $\varepsilon_y^{(\text{eff})}$. We obtain the identical result as the original EFC within the zeroth-order EFC.

Lastly, we can obtain the critical angle of the Poynting vector with respect to the *y*-axis which is denoted by θ_c. The concept of the critical angle in the HMMs comes from the EMA as it predicts that the infinitely large wavevectors can be supported by the HMMs. Then, all infinitely large wavevectors can propagate only in specific direction with respect to the *y*-axis because of the hyperbolic dispersion. Therefore, they propagate with the critical angle with respect to the *y*-axis which is given by Eq. (2.62). This behaviour forces the Ponyting vector to also propagate with the critical angle θ_c with respect to the *y*-axis. The two directions are different in the hyperbolic medium. In our structure, however, the large wavevectors are limited, and thus the angles of the large wavevectors with respect to the *y*-axis are not constant. Note that even the small difference in the propagation directions of the wavevectors can give the large difference in the positions of the images if the structure has long length comparing to the working wavelength. Therefore, the critical angle loose its meaning here. However, the term critical angle is already familiar to us. Then, we may still use this term with caution that it strictly refers to the "specific" large wavevector. We are reminded that the "large" is much larger than the wavenumber of light in air. We explain more about the trem "specific". Our testing object in the previous chapter is the slit array with the period 5 μm which is five times longer than the period of the slit of the lens. The object then emits many diffraction waves, but the most dominant terms with large wavevectors are the $m = \pm 1$ diffraction modes. Therefore, the "specific" large wavevectors are $k_x^{(\text{eff})} = \pm 0.2\pi / p$ where $p = 1\ \mu$m is the period of the slit of the lens. From Fig. 5.7 (a), the critical angle of this wavevector is ±89.8843°. Then, by applying Eq. (2.63) with ε_ϕ and ε_ρ replaced by $\varepsilon_x^{(\text{eff})}$ and $\varepsilon_y^{(\text{eff})}$, respectively, we obtain the critical of the Poynting vector as $\theta_c = \pm 0.1152^\circ$. In the next section, we will show that this critical angle predict the position of the image only 5 nm difference from the image position obtained by the analytical solutions. Therefore, this model gives the correct EFC and effective parameters. We will also show the dependence of the length of the lens on the image position. All results obtained by the analytical solutions can be explained by the effective model.

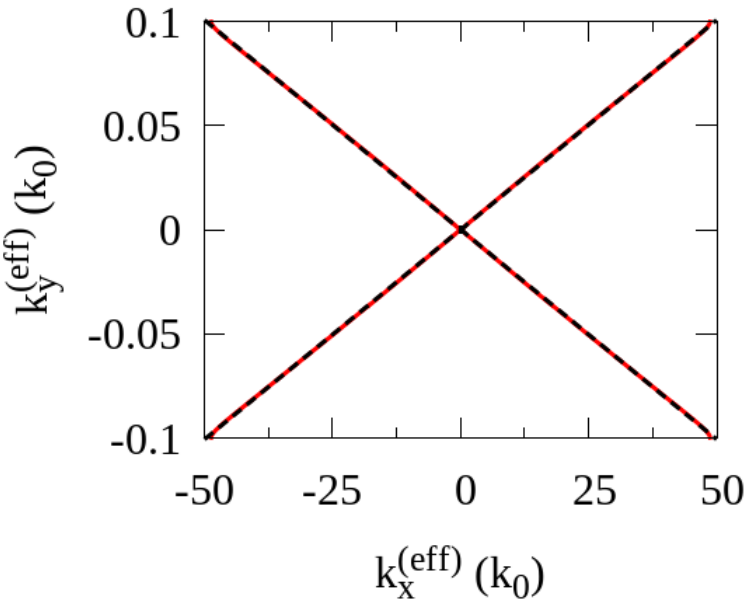

Fig. 5.11. The back dashed line shows the fitted EFC at f=0.997 THz using the effective parameters $\varepsilon_x^{(\mathrm{eff})} = -8.6786\times10^{-3}$, $\mu_z^{(\mathrm{eff})} = 2.9027\times10^{-5}$, and fitted $\varepsilon_y^{(\mathrm{eff})} = 2.1384\times10^{3}$. The red solid line is the original EFC within the first-order.

5.3 Comparison with analytical solutions

In Fig. 5.12 (a), we show the schematic of the subwavelength imaging over the long distance by using the stacked grating/air layers as the lens. The number of the gratings is defined by *N*. We will change *N*, and then check the normalized amplitude of the electric filed $|\mathbf{E}|/E_0$ behind the end interface of the lens. The subwavelength object is the array of the slits which is the same as the previous chapter. Fig. 5.6 (b) shows the $|\mathbf{E}|/E_0$ for *N*=10 drawn over two unit cells along the *x*-axis. We observe two images labelled by i1 and i2 in each unit cells. The positions of the i1 and i2 images along the end interface of the lens and in the positive unit cell (*x*>0) are at *x*=1.988 μm and 3.012 μm, respectively. The origins of these peaks can be understood by the critical angle of the Poynting vector θ_c obtained in the previous section. The effective medium model gives that $\theta_c = \pm 0.1152^\circ$. Therefore, the energy from the object located at the origin (*x*=0) will form the image at the distance $\delta x = L\tan\theta_c$ from the *y*-axis, where *L* is total length of the lens. For *N*=10, *L*=1500.72 μm, and therefore $\delta x = 3.017\ \mu$m. This distance is only 5 nm larger than the position of the i2 image. Therefore, the i2 image in the positive unit cell (*x*>0) must come from the object at the origin and so as the i1 image in the negative unit cell (*x*<0). The i1 image in the positive unit cell (*x*>0) must come from the nearby objects and so as the i2 image in the negative unit cell (*x*<0). As the number of grating increase to *N*=14, the positions of the images shift to new positions as shown in Fig. 5.6(c). Now, the positions of the i1 and i2 in the positive unit cell (*x*>0) are at *x*=1.013 μm and 3.987 μm, respectively. The total length of the lens for *N*=16 is 2101.04 μm, and therefore the effective medium model predicts that the image of the object at the origin (*x*=0) will form the image at the new distance $\delta x = 4.224$ μm from the *y*-axis by using the same critical angle. This

distance is close to the position of the i2 image in the positive unit cell (x>0) . Therefore, the i2 image in the positive unit cell (x>0) must come from the object at the origin and so as the i1 image in the negative unit cell (x<0). This situation is just the same as the previous case. The difference between the image position predicted by the effective model and that obtained by the analytical solution is larger than the previous case due to the interference of the pulses of two images which is not accounted for by the effective medium model.

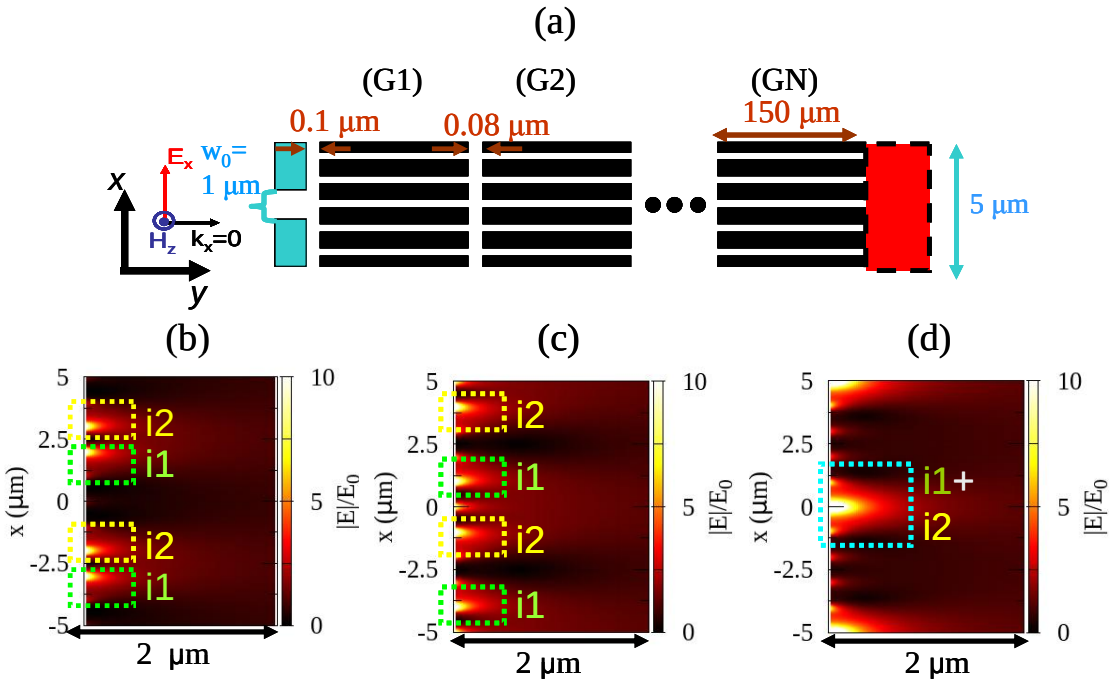

Fig. 5.12. (a) Schematic view of the subwavelength imaging with the stacked grating/air layers. The number of grating is defined by N. All white regions are referred to air. The object as indicated by blue colour has size w_0=1 μm and the separation distance 5 μm. The red region indicates the observational region of the images formed behind the lens. (b)-(d) Normalized |**E**| for N=10 (b), N=14 (c), and N=16 (d), over the distance 2 μm from the end interface of the lens. The figures are drawn over two unit cells along the x-axis. The frequency is at f=0.997 THz.

In the last case, the N=16 and L=2401.2 μm, the positions of the peaks are at 0 and 5 μm. The effective medium model with the same critical angle predicts that the image of the object at the origin will form at the distance 4.891 μm from the y-axis which is close to the distance between the object. Therefore, the image at the center must be formed by the focusing of the energy from the nearby objects ($x=\pm 5$ μm) of the object at the origin. The images in the rim are formed by the objects at the origin and the objects at the positions $x=\pm 10$ μm. Therefore, the analytical solutions are well agreed with the effective medium.

5.4 Equi-frequency contour (EFC) and effective parameters of different *N*

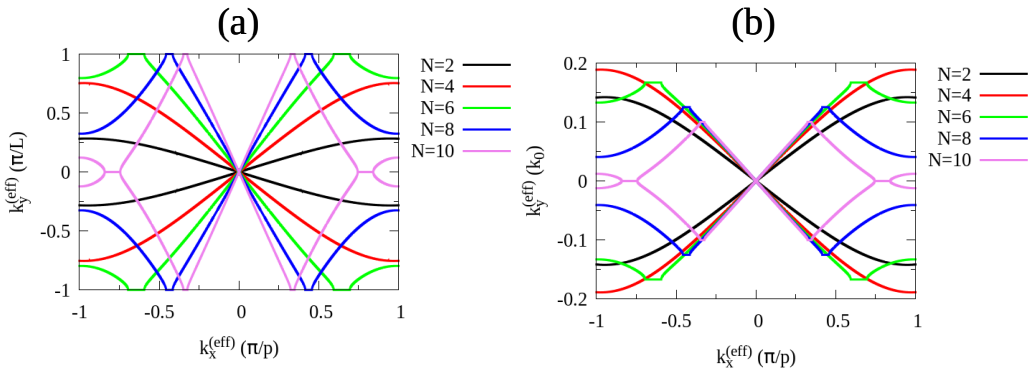

Fig. 5.13. (a) EFCs at the working frequency f=0.997 THz for different number of gratings *N*. (b) The same EFCs as Fig. 5.13 (a) but the *y*-axis is in the unit of the wavenumber of light in air k_0.

This section explains the effect of the number of grating layers *N* on the EFCs and the effective parameters. We start from the EFCs and then the effective parameters. Note that we show only in the case of the separation distance between the grating is 80 nm (the same separation distance as the section 5.3) and also only at the frequency 0.997 THz. The result is valid for any frequency which show the hyperbolic dispersion.

Fig. 5.13 (a) shows the EFCs of the stacked grating/dielectric layers from *N*=2 to *N*=10 number of gratings. The unit of the $k_x^{(\text{eff})}$ is π/p where $p=1\,\mu$m. It is about 150 times larger than the wavenumber of light in air k_0 at this frequency. Therefore, the EFC of light in air is just a tiny circle from $k_x^{(\text{eff})}=-1/150\ \pi/p$ to $k_x^{(\text{eff})}=+1/150\ \pi/p$. The unit of $k_y^{(\text{eff})}$ is π/L where L is length of the lens which is varied according to N as $L=150N+0.08(N-1)\ \mu$m where 150 μm is the height of the grating and 0.08 μm is the separation distance between the gratings. To be able to compare the EFCs of different *N*, we also plot the same EFCs with $k_y^{(\text{eff})}$ in the unit of k_0 in Fig. 5.13 (b). For *N*=2, there are no band gaps within the first Brillouin zone of the $k_x^{(\text{eff})}$. According to Fig. 5.13 (b), the $k_y^{(\text{eff})}$ are relatively small comparing to those in another *N*. We also observe that the $k_y^{(\text{eff})}$ are constant near the edges of the first Brillouin zone of the $k_x^{(\text{eff})}$. Therefore, the large wavevectors in this structure send the energy parallel to the *y*-axis. As *N* increase to 4, we see similar EFC as that of the *N*=2, but the $k_y^{(\text{eff})}$ positively and negatively increase as shown in Fig. 5.13 (b). This means that direction of the energy propagation deviates from the *y*-axis by increasing the length of the lens. The $k_y^{(\text{eff})}$ approach $\pm\pi/L$ by increasing more grating layers, and we see the first band gaps appear when *N*=6. The $k_x^{(\text{eff})}$ centres of the band gaps positively and negatively decrease by increasing *N*. Interestingly the critical angle of the specifically large wavevectors with respect to the *y*-axis within the first order of $k_y^{(\text{eff})}$ converges as the number of *N* increases. Therefore, the critical angle of the Poynting vector also converges as *N* increases. By further increasing *N*, the number of narrow band gaps within the first Brillouin zone of

$k_x^{(\mathrm{eff})}$ increases because higher order FP resonances are excited, and thus higher order $k_y^{(\mathrm{eff})}$ appear within the first Brillouin zone of $k_x^{(\mathrm{eff})}$ as shown for *N*=40 in Fig. 5.14 (a) as an example. There are up to five orders of $k_y^{(\mathrm{eff})}$ in this EFC. The order-corrected EFC of this figure is shown in Fig. 5.14 (b). The EFC shows the smooth curves because of narrow band gaps. We need to be aware that there are electromagnetic waves in Fig. 5.14 (b) which are not allowed to propagate inside the structure, and these electromagnetic waves can be seen in Fig. 5.14(a). Note that $k_x^{(\mathrm{eff})} = \pm 0.2\pi / p$ are propagating waves with the first-order $k_y^{(\mathrm{eff})} = \pm 0.5545\pi / L$. The critical angle of the propagation direction of these waves is ±89.8780˚ which is slightly smaller than that of the *N*=10.

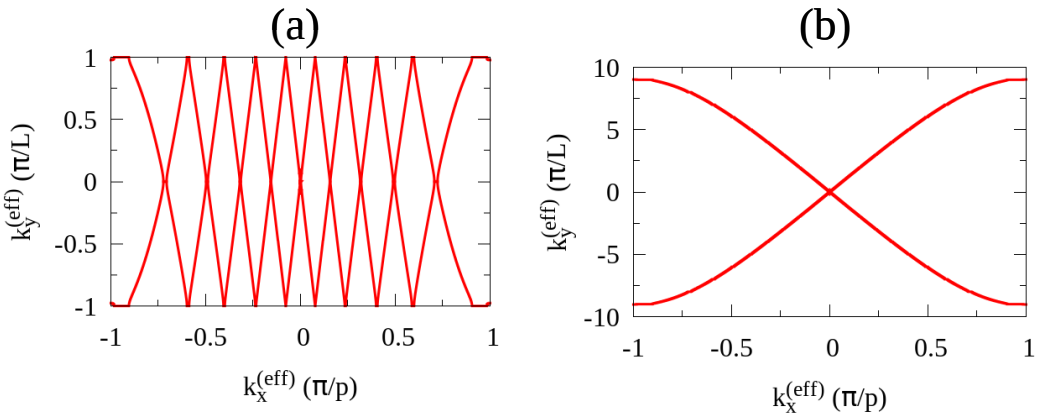

Fig. 5.14. (a) EFCs at the working frequency f=0.997 THz for *N*=40 without the order correction. (b) The same EFCs as Fig. 5.14 (a) but with the order correction.

Next, we show the results of the effect of *N* on $\varepsilon_x^{(\mathrm{eff})}$. Before discussing those results, it is helpful to understand the negative and positive $\varepsilon_x^{(\mathrm{eff})}$ which are found in the spectrum first. This understanding will aid the discussion of the effect of *N* on $\varepsilon_x^{(\mathrm{eff})}$. In Fig. 5.15 (a), we show the $\varepsilon_x^{(\mathrm{eff})}$ of the *N*=2 stacked grating/dielectric layer from 0.1-2.8 THz. It covers five FP resonances of the all-connected gratings as indicated in the figure. The frequency difference is determined by $\Delta f = c / 2L'$ where L' is length of the all-connected gratings, and thus the frequency difference of this structure is about 0.5 THz because $L' = 300\ \mu\mathrm{m}$. We have either positive $\varepsilon_x^{(\mathrm{eff})}$ or negative $\varepsilon_x^{(\mathrm{eff})}$ depending on the FP resonance. The negative $\varepsilon_x^{(\mathrm{eff})}$ occur only below the even-order FP resonances, while the positive $\varepsilon_x^{(\mathrm{eff})}$ occur only below the odd-order FP resonances. Moreover, the negative $\varepsilon_x^{(\mathrm{eff})}$ diverge close to the odd-order FP resonances. These behaviours can be understood from Eq. (5.12) which is used to compute the $\varepsilon_x^{(\mathrm{eff})}$. Fig. 5.15 (b) shows the numerator and denominator of the $\varepsilon_x^{(\mathrm{eff})}$ as a function of frequency taking into account only the backward travelling waves $\left(k_y^{(\mathrm{eff})} < 0\right)$ due to the causality. This figure clearly shows that the negative and positive $\varepsilon_x^{(\mathrm{eff})}$ are originated by the $\pi/2$ out of phase between the numerator as indicated by the red line and the denominator as indicated by the

blue. They have different signs only in the second and fourth quadrants which lie below the even-order FP resonances, and thus the negative $\varepsilon_x^{(\mathrm{eff})}$ occur only below the even-order FP resonances. However, they have the same signs in the first and third quadrants which lie below the odd-order FP resonances, and thus the $\varepsilon_x^{(\mathrm{eff})}$ are positive below the odd-order FP resonances. The divergences of $\varepsilon_x^{(\mathrm{eff})}$, however, are not clearly seen in this figure. The divergence occurs when the denominator of $\varepsilon_x^{(\mathrm{eff})}$ is zero (or close to zero) which is at the FP resonance satisfying the condition $\sin\left(k_y^{(\mathrm{eff})}L\right)=0$, that is $k_y^{(\mathrm{eff})}L = j\pi$ where j is an integer. However, we see the divergences of $\varepsilon_x^{(\mathrm{eff})}$ only near the odd-order FP resonances, not the even-order FP resonances. This is because the frequency at the even-order FP resonance coincides with the zero of the numerator that is $\mathrm{Re}\left(-i\left(k_y^{(\mathrm{eff})}/k_y\right)\left(\cos\left(k_y^{(\mathrm{eff})}L\right)-\Delta_2\right)\right)=0$, and thus $\varepsilon_x^{(\mathrm{eff})}$ does not diverge and becomes zero at this frequency. This condition occurs when $k_y^{(\mathrm{eff})}=0$ at the even-order FP resonance. At the odd-order FP resonance, the $k_y^{(\mathrm{eff})}=\pm\pi/p$ and the numerator of the $\varepsilon_x^{(\mathrm{eff})}$ is not zero, and the $\varepsilon_x^{(\mathrm{eff})}$ diverges.

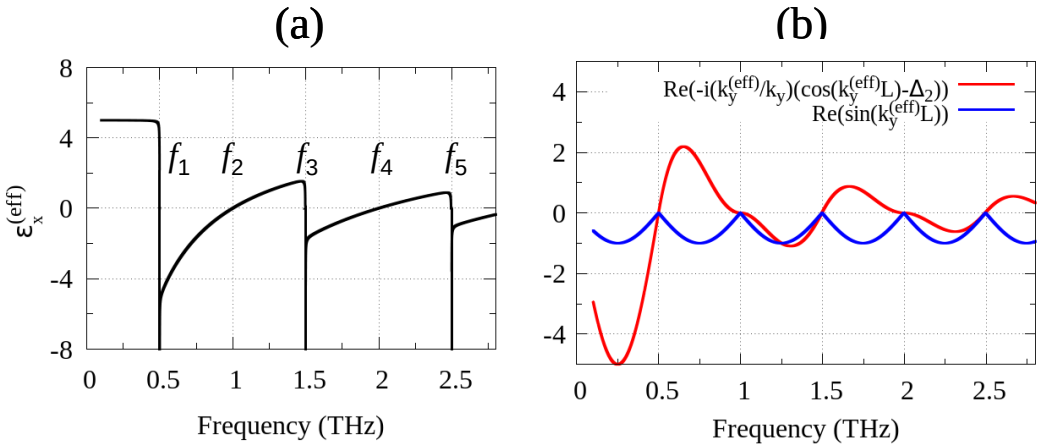

Fig. 5.15. (a) $\varepsilon_x^{(\mathrm{eff})}$ as a function of frequency of N=2 stacked grating/dielectric layers whose grating parameters are the same as those in Fig. 5.5. The FP resonant frequencies of the all-connected gratings with length $L'=150N=300\ \mu$m are indicated in the figure. (b) Numerator (red line) and denominator (blue line) of $\varepsilon_x^{(\mathrm{eff})}$ from Eq. (5.12) which is used to compute $\varepsilon_x^{(\mathrm{eff})}$ in Fig. 5.15 (a).

Now we can show the results of $\varepsilon_x^{(\mathrm{eff})}$ as N increases. Fig. 5.16 (a) shows that the increasing of N affects the $\varepsilon_x^{(\mathrm{eff})}$ due to the excitations of higher order FP resonances. Only the negative $\varepsilon_x^{(\mathrm{eff})}$ below the frequency about 1 THz and above its one-order-lower FP resonance are approximately constant. For example, the FP resonance at the frequency about 1 THz is the 40th-order FP resonance of the all-connected gratings N=40, and the one-order-lower FP resonance of this structure is the 39th-order which is at the frequency about 0.975 THz. This frequency range is narrower by further increasing N because the frequency difference between the FP resonances decrease. Therefore, we can estimate this region by considering the frequency difference between the FP resonances. For example, if N=250,

then $L' = 37.5\ \text{mm}$, and thus $\Delta f = c/2L' = 0.004$ THz. Therefore, the negative $\varepsilon_x^{(\text{eff})}$ of this structure in the narrow frequency range [0.9947,0.9987] THz are the same as the converged negative $\varepsilon_x^{(\text{eff})}$ in the structures with shorter length (0.9987 THz is the FP resonance). Fig. 5.16 (b) shows the $\varepsilon_x^{(\text{eff})}$ as a function of N at the working frequency 0.997 THz. The $\varepsilon_x^{(\text{eff})}$ converges by increasing N at this frequency. The $\varepsilon_x^{(\text{eff})}$ is converged at N=70 with the value $\varepsilon_x^{(\text{eff})} = -8.95\times10^{-3}$ with the error 0.01%. The reason that we stop at N=70 is that each parameter Ω_{disp}, N_{T}, and N_{R} obtained by the closed-form solutions become extremely large and it cannot be handled by the computer. This problem is called the overflow problem. Fortunately, the ratios $N_{\text{T}}/\Omega_{\text{disp}}$ and $N_{\text{R}}/\Omega_{\text{disp}}$ are finite. Therefore, this problem can be solved by calculating the 0th-order reflection and transmission coefficients from the single matrix equation with the LAPACK subroutine (partial-pivoting method).

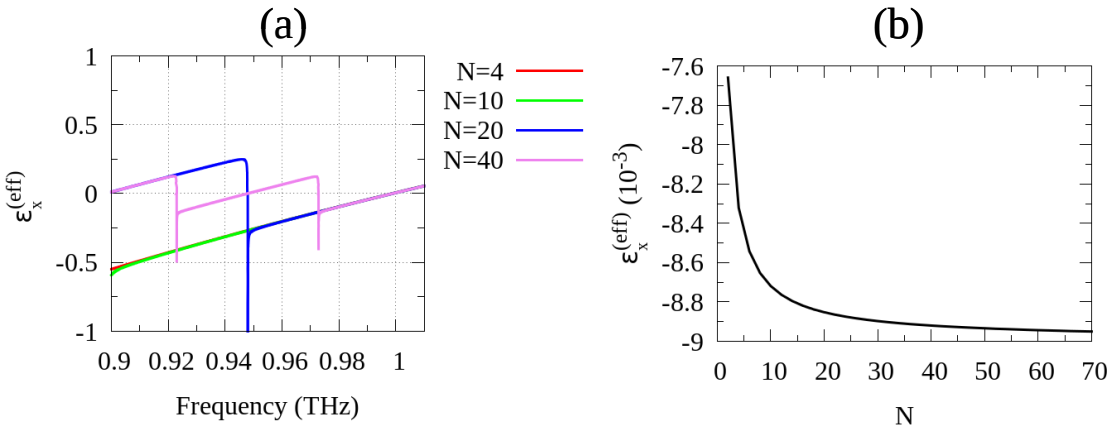

Fig. 5.16. (a) $\varepsilon_x^{(\text{eff})}$ as a function of frequency of the stacked grating/dielectric layers with four different N indicated in the figure. The grating parameters are the same as those in Fig. 5.5. (b) $\varepsilon_x^{(\text{eff})}$ as a function of N at 0.997 THz.

Next, we show the results of the effect of N on $\mu_z^{(\text{eff})}$ in Fig. 5.17 (a). The behaviour of $\mu_z^{(\text{eff})}$ can be explained in similar manner as $\varepsilon_x^{(\text{eff})}$ taking into account that $\mu_z^{(\text{eff})}$ is negative if $\varepsilon_x^{(\text{eff})}$ and $k_y^{(\text{eff})}$ are both negative, but $\mu_z^{(\text{eff})}$ is positive if $\varepsilon_x^{(\text{eff})}$ is negative and $k_y^{(\text{eff})}$ is positive. The frequency range in which $\mu_z^{(\text{eff})}$ is independent on large N is the same as that of $\varepsilon_x^{(\text{eff})}$. Fig. 5.17 (b) shows the $\mu_z^{(\text{eff})}$ as a function of N at the working frequency 0.997 THz. For $N<7$, $\mu_z^{(\text{eff})}$ is negative and the structure behaves as type-I HMMs where $\mu_z^{(\text{eff})}<0, \varepsilon_x^{(\text{eff})}<0, \varepsilon_y^{(\text{eff})}>0$. For $N\geq 8$, $\mu_z^{(\text{eff})}$ is positive and the structure can behave as type-II HMMs if $\varepsilon_x^{(\text{eff})}$ is negative that is $\mu_z^{(\text{eff})}>0, \varepsilon_x^{(\text{eff})}<0, \varepsilon_y^{(\text{eff})}>0$. The $\mu_z^{(\text{eff})}$ is converged at N=70 with the value $\mu_z^{(\text{eff})} = 7.47\times10^{-5}$ with the error 0.30%.

Next, we show the result of the effect of N on $\varepsilon_y^{(\text{eff})}$ at the working frequency 0.997 THz which is obtained by fitting the EFC corresponding to each N from $k_x^{(\text{eff})} = -0.25\pi/p$ to

$k_x^{(\text{eff})} = +0.25\pi / p$ covering our target wavevector $k_x^{(\text{eff})} = \pm 0.20\pi / p$. The orders of $k_y^{(\text{eff})}$ are corrected if they are greater than the zero-order $k_y^{(\text{eff})}$ within this range of $k_x^{(\text{eff})}$. The $\varepsilon_x^{(\text{eff})}$ and $\mu_z^{(\text{eff})}$ are taken from Fig. 5.15 (b) and 5.16 (b), respectively. The fitted $\varepsilon_y^{(\text{eff})}$ as a function of *N* is shown in Fig. 5.18. We see that the $\varepsilon_y^{(\text{eff})}$ is positive for any *N* and drops as *N* increases. The $\varepsilon_y^{(\text{eff})}$ is converged at *N*=70 with the value $\varepsilon_y^{(\text{eff})} = 1.94 \times 10^3$ with the error 0.05%.

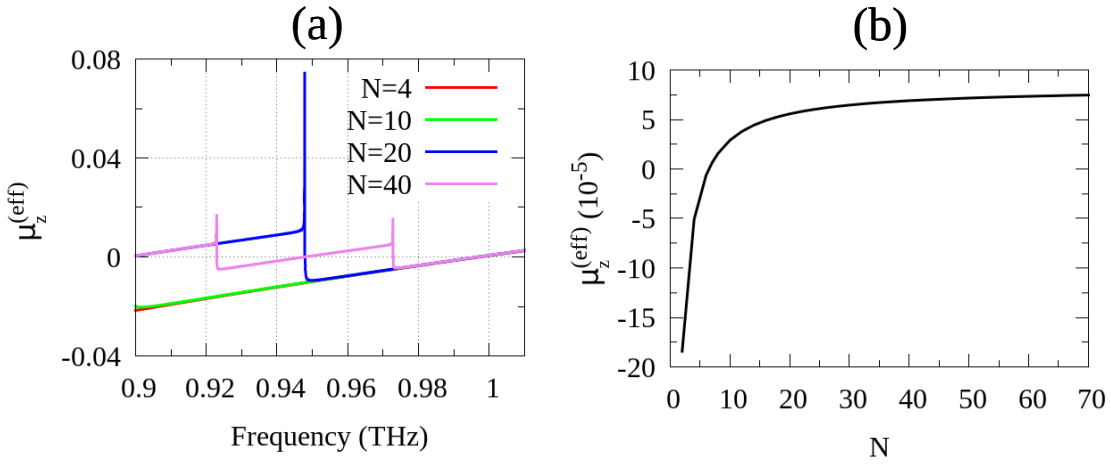

Fig. 5.17. (a) $\mu_z^{(\text{eff})}$ as a function of frequency of the stacked grating/dielectric layers with four different *N* indicated in the figure. The grating parameters are the same as those in Fig. 5.5. (b) $\mu_z^{(\text{eff})}$ as a function of *N* at 0.997 THz.

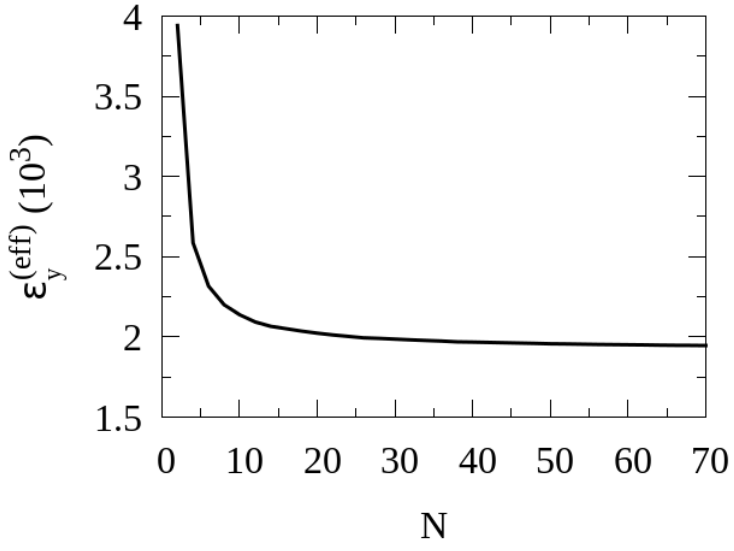

Fig. 5.18. $\varepsilon_y^{(\text{eff})}$ as a function of *N* at 0.997 THz. The grating parameters are the same as those in Fig. 5.5.

Lastly, we can also show the effect of *N* on the critical angle of the propagation direction of electromagnetic waves with the wavevectors having specifically the tangential component $k_x^{(\text{eff})} = \pm 0.2\pi / p$, which is denoted by α_c, and the critical angle of the Poynting vectors, which is

denoted by θ_c, corresponding to these electromagnetic waves. These critical angles must be carefully calculated. That is the order of the normal component $k_y^{(\text{eff})}$ at $k_x^{(\text{eff})} = \pm 0.2\pi / p$ must be corrected considering the presence of the band gaps, and the $k_y^{(\text{eff})}$ must be propagating waves (locate outside the band gaps). If one didn't take this into account, one would obtain the oscillating critical angles as

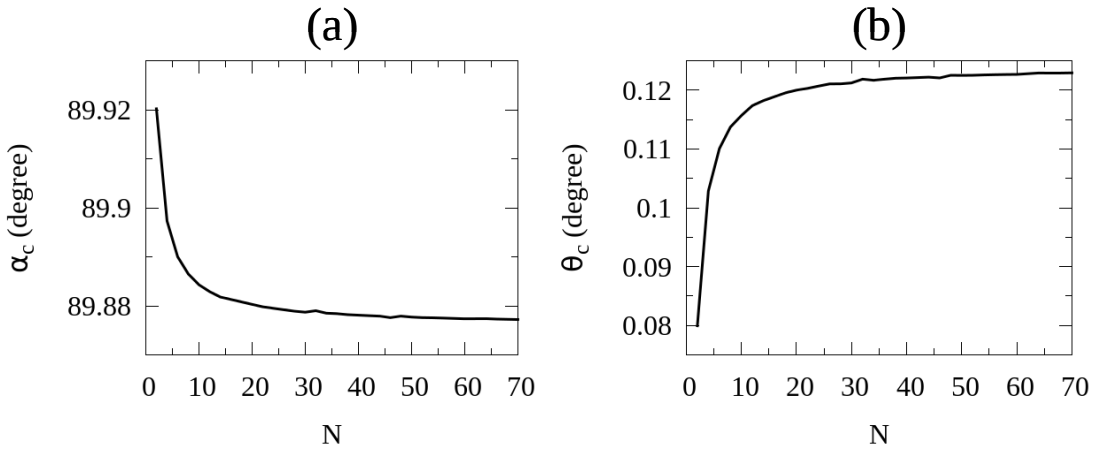

Fig. 5.19. (a) The critical angle of the propagation direction of the electromagnetic waves with the wavevectors having $k_x^{(\text{eff})} = \pm 0.2\pi / p$ as a function of *N* at the frequency 0.997 THz. (b) The critical angle of the Poynting vector corresponding to the wavevectors with $k_x^{(\text{eff})} = \pm 0.2\pi / p$ as a function of *N* at the frequency 0.997 THz. The grating parameters are the same as those in Fig. 5.5.

a function of *N* which are not converged even at *N*=70. Fig. 5.19 (a) shows that the positive α_c decreases by increasing *N* and become converged at large *N*. The small peaks at *N*=32 and *N*=48 occur because the wavevectors are close to the edges of the band gaps. The α_c is converged at *N*=70 with the value 89.9772 degree with the error 0.00004%. Fig. 5.19 (b) shows that the positive θ_c increases by increasing *N*. It is converged at *N*=70 with the value 0.1229 degree with the error 0.02%. This means that the critical angle of the Poynting vector in the long-length structure dose not perfectly parallel to the *y*-axis, and it can be estimated as 0.1229 degree at the working frequency 0.997 THz within the given errors.

5.5 Conclusion

We have shown that the stacked grating/dielectric layers are HMMs working in the THz radiation band by using the new effective medium model based on the closed-form solutions of the reflection and transmission coefficients of these structures. The types of HMMs depend on the frequency and the geometry of the structures. The type-I HMMs have $\varepsilon_x^{(\mathrm{eff})} < 0$, $\mu_z^{(\mathrm{eff})} < 0$, $\varepsilon_y^{(\mathrm{eff})} > 0$, and the type-II HMMs have $\varepsilon_x^{(\mathrm{eff})} < 0$, $\mu_z^{(\mathrm{eff})} > 0$, $\varepsilon_y^{(\mathrm{eff})} > 0$, both exist below the FP resonance in which the SSPs are excited. The Poynting vectors in both structures have opposite sign along the propagation axis as that of the phase velocity, and only the backward travelling waves send the energy to the image plane due to the causality. The critical angle of the Poynting vectors from the effective medium model can satisfyingly explain the formations of the images behind the structures obtained by the analytical solutions. We have discussed the effect of the number of gratings N on the EFC and the effective parameters. The effective parameters $\varepsilon_x^{(\mathrm{eff})}$, $\varepsilon_y^{(\mathrm{eff})}$, $\mu_z^{(\mathrm{eff})}$, and also the critical angle of the Ponyting vector are converged by increasing N below the FP resonance about 1 THz where $\varepsilon_x^{(\mathrm{eff})}$ is negative.

Summary

The non-ionizing radiation energy of the terahertz (THz) allows us to explore the microscopic worlds without harm if we can go beyond the diffraction limit that restricts the optical resolution to approximately the wavelength of the THz light. The diffraction limit is caused by the decay of the electromagnetic waves with large wavevectors called the evanescent waves or the near-fields so that only the far-fields with small wavevectors exist on the image plane. The hyperbolic metamaterials (HMMs) can support the propagation of the near-fields, and they can transform the decaying near-fields into the propagating far-fields if they are bent into the cylindrical shape called the hyperlens. This thesis gives the new structures that behave as the HMMs in the THz radiation band, and we also gives the analytical solutions of the hyperlens which can be applied to the new HMMs. Therefore, this thesis may lead to the practical structures and the physical limit of the THz hyperlens that can transform the near-field signal from the microscopic worlds into the far-field signal that we can detect with the conventional instruments.

We have organized the thesis in the chronological order. First, we are inspired by the invention of the hyperlens in the optical band. Then, we have learned that the FDTD simulation is slow and inaccurate when the wavelength is much longer than the size of the hyperlens. We cannot definitely work in the nanoscale with the THz if we keep using the FDTD simulation, and therefore we develop the new analytical solutions which allow us to efficiently optimize the imaging performance of the hyperlens in the chapter 2. We always check the analytical solutions with the FDTD simulation using the simple structures, and then we apply the analytical solutions to the structures which are impossible to solve with the FDTD. The hyperlens in the chapter 2 are made by alternating metal and insulator layers with finite dielectric constants. By giving the finite dielectric constants of the metals, we have shown in the chapter 2 that the subwavelength focal spot and the magnifying resolution can be optimized. As we try to apply these analytical solutions to the THz band, however, the dielectric constants of the metals become infinity because they are highly electrical conducting, and thus the transmittance is exactly zero. However, we can imitate the surface plasmons which exist naturally on the surface of the metals in the optical band by perforating the metals with holes to create the spoof surface plasmons (SSPs). We use the SSPs on the surface of the metallic grating, combine the grating with the dielectric layer to form the unit cell, and then stack the unit cell to make the new HMMs for the THz. We explain the analytical solutions of the stacked grating/dielectric layers in the chapter 4. The analytical solutions allow us to demonstrate the deep-subwavelength imaging, to explain the excitations of the quasi-waveguide resonances that can affect the image's intensity, and to show the deep-subwavelength imaging over the long distance. Our analytical solutions are general, and they may lead to the novel structures. However, these solutions cannot be accomplished without the solutions of the simpler structures : dielectrics/grating/dielectrics structures. Therefore, we explain the analytical solutions of the dielectrics/grating/dielectrics structures in the chapter 3 before the analytical solutions of the stacked grating/dielectric layers in the chapter 4. These analytical solutions also lead to the novel structures for subwavelength sensing which rely on the perfect absorption and the ultrahigh Q-factor of the SSPs. By monitoring the frequency shift of the resonant peak or the drop of the absorbance, the

subwavelength film with film thickness down to a few nanometre can be detected with the THz radiation. The chapter 3 is the good example of the novel structure which is realized from our analytical solutions. In order to clarify that the stacked grating/dielectric layers are HMMs, we develop new and simple effective medium model in the chapter 5 by taking into account the reflection and transmission coefficients of these structures. We can draw the contour between the components of effective wavevectors, and therefore we can show that the stacked grating/dielectric layers are indeed the HMMs in the particular frequency band. The type of HMMs depend on the frequency and the separation distance between the gratings. The effective medium model predicts that the direction of the energy propagation in these HMMs is bent from the normal axis, and it can satisfyingly explain the image formations from the analytical solutions.

It is not straightforward to apply the analytical solutions of the hyperlens developed in the chapter 2 to the stacked grating/dielectric layers explained in the chapter 4 and 5. Fortunately, it is also not too difficult. We need to change the forms of the electromagnetic fields inside the hyperlens by considering the hyperlens as the homogeneous hyperbolic medium described by the effective parameters given in the chapter 5. The electromagnetic fields in the core region and the outer region remain the same. The new field coefficients are then easily obtained by applying the boundary conditions on the innermost and the outermost interfaces of the homogenized hyperlens. The experiment would be challenge but we encourage the experimenters to pursue these structures as they make no loss in the structures and thus allowing the magnification over the long distance.

This thesis can be readily extended to the two-dimensional imaging by replacing the grating with the circular or rectangular hole arrays. The analytical solutions will not change their forms, and only the four coupling parameters : one parameter in the input region, two parameters between the two gratings, and one parameter in the output region will change their forms. These coupling parameters are determined by the scalar products between the two-dimensional diffraction waves and the waveguide modes in the hole arrays. Although the analytical solutions can be extended into the infrared and the optical band by taking into account the surface impedance boundary conditions of the metals, but the intrinsic loss in the metal will always hamper the magnifying resolution in these radiation bands. Therefore, the dielectric structures and metasurfaces may be more suitable than the bulk noble metals in the infrared and the optical bands.

Appendix

Here, we explain the computer programs of the analytical solutions used in each chapter. All computer programs are written in FORTRAN language which can be simply compiled by the command *"gfortran file.f90 -o output"*. Then, the program can be run by the command *"./output"*. All output files are written in GNUPLOT formats which are just the column containing the independent and dependent variables. The meaning of each column can be seen in the output writing statement which is always near the end of the main program, and the meaning of each variable can be seen in the comment of that variable in the section of the variable declaration. Note that one file may contain many columns for convenience of the author in the analysis. The programs explained in this appendix are given in the CD-ROM. All codes can be edited as wishes. But please cite our original paper which is related to that computer code if you use the code for your publication. The questions can be sent directly to the author via an unofficially e-mail : p_epsilon@yahoo.com.

A1. Chapter 2

A1.1 Focusing process

The name of the computer program for the focusing hyperlens is *"hypfocus.f90"*. The input variables such as the wavelength, the geometry of the hyperlens, the dielectric constants, and the maximum number of order *m* are defined in the beginning of the main program. The main program also contains the section of obtaining field coefficients. All field coefficients are stored in the *aj* (for the Hankel function of the first kind) and *bj* (for the Bessel function) variables. The ranges of these field coefficients and the region in the hyperlens corresponding to them can be seen in the variable declaration section. The intensity distribution is obtained by calling the "*splane*" subroutine, and the intensity profile is obtained by calling the "*scurve*" subroutine. In the optimization process, we usually calculate the intensity profiles along the desired curve by calling the "*scurve*" subroutine. After obtaining the sharp focusing, we then obtain the intensity distribution by calling the "*splane*" subroutine in order to accompany our discussion. The output files are declared in the subroutines.

A1.2 Magnifying process

The name of the computer program for the magnifying hyperlens is *"hypmagfy.f90"*. This program has the same structure as the *"hypfocus.f90"*. The only difference is the section of obtaining field coefficients. The locations of the point sources in the magnifying process are in the core region while the locations of the point sources in the focusing process are in the outer regions. Therefore, the scattering parameters in both processes are different as described in the main text.

If we use these programs in the extreme cases such as very small thickness of the CCL, vey small inner radius, and very large number of the CCL, we need to be very careful about the underflow (too small) and overflow (too large) of the special functions and the fields coefficients. Therefore, it is better to always check the behaviour of the special functions and the field coefficients within these extreme cases.

A2. Chapter 3

The codes in this chapter take only the fundamental waveguide mode of the slit into account. Therefore, they are valid in the regime where the slit width is much more smaller than the wavelength of light. How small is not addressed in this chapter. More works are needed in order to quantitatively answer this problem. As far as we can tell, the smaller the slit width, the sharper the resonant peak. Therefore, if one wants to make a structure for broadband sensing, one needs wider slit width (or smaller rod), and the analytical solutions in this chapter are definitely not useful unless we can find the truly analytical solutions by including all waveguide modes into one single expression.

A2.1 Comparison with FDTD simulation

The analytical transmission spectrum in Fig. 3.3 (a) is obtained by using the computer program "*hybridlens_spectra.f90*". The reflection and transmission coefficients are computed in the main program. At the beginning of the main program, the parameters of the structures are defined, and the meaning of each parameter is given by the comment in the variable declaration section. The coupling parameters $G_{\infty s}^{(\mathrm{in})}$ and $G_{\infty s}^{(\mathrm{out})}$ are obtained by calling the subroutines *"ginf_s_in_1layer_sub"* and *"ginf_s_out_1layer_sub"*, respectively.

The amplitude of the electric field in Fig. 3.4(a)-(c) is obtained by using the code "*hybridlens_field.f90*". All field components are computed in the main program. The parameters of the structure are defined at the beginning of the program.

The dispersion relation in Fig. 3.5 is obtained by using the code "*hybridlens_disp.f90*". In the main program, the user is required to define the parameters of the structure and then the range of the interested frequency. After running the program, the user needs to specify the tangential component of the wavevector in the unit of π / p. Then, the program will find the frequencies within the specified frequency range that satisfy the resonant condition that is the dispersion function is zero. The program does this by checking the change of the sign of the real part of the dispersion function when the frequency increases a little bit. If the program succeeds, both real part and imaginary part of the dispersion function will be shown up, and the user can check whether the mode is allowed or not by looking at the imaginary part of the dispersion function. The non-allowed mode has zero real-part of the dispersion function, but large imaginary-part of the dispersion function. The allowed mode will have small numbers of both real and imaginary parts of the dispersion function. When the user computes the dispersion relation, we do not encourage to compute it automatically. The computation of the dispersion relation should be as careful as possible, and the result should be compared with the far-field spectra.

A2.2 Perfect absorbers for subwavelength sensing

The absorption spectra of the back-perfect absorbers (back-PAs) in Fig. 3.10 (a) are obtained by using the code *"hybridlens_backPA.f90"*. The structure of this code is exactly the same as the "*hybridlens_spectra.f90*". We only change the $G_{\infty s}^{(\mathrm{in})}$ and $G_{\infty s}^{(\mathrm{out})}$ parameters. Moreover, the reflection coefficients will take the new form as defined in the main program. The program computes the reflectance from the reflection coefficient, and the absorbance is directly obtained from the reflectance via the relation A=1-R because the transmittance is zero.

The electric field distributions inside the spacer between the grating and the metallic plane in Fig. 3.10 (a) and (b) are obtained by using the code *"hybridlens_backPA_spacer.f90"*. The electric field distribution in front of the grating of the back-PA in Fig. 3.11 is obtained by using the code *"hybridlens_backPA_input.f90"*.

The absorption spectra of the front-perfect absorbers (front-PAs) in Fig. 3.12 are obtained by using the code "*hybridlens_frontPA.f90"*. The structure of this code is exactly the same as *"hybridlens_backPA.f90"* but the $G_{\infty S}^{(\mathrm{out})}$ is infinite for the front-PAs and it can be eliminated from the expression of the reflection coefficient. The exact form of the reflection coefficient of the front-PAs is given in the main program. The distributions of the electric field in front of the grating of the front-PAs in Fig. 3.12(c)-(e) and Fig. 3.13 are obtained by using the code *"hybridlens_frontPA_input.f90"*.

A2.3 Sensitivities of perfect absorbers as subwavelength film sensors

Fig. 3.14 (b) is obtained by the code *"hybridlens_frontPA_sens1.f90"*. This code is just the extension of the code "*hybridlens_frontPA.f90"* where the $G_{\infty S}^{(\mathrm{in})}$ is changed to the case of M=2 due to the presence of the thin film next to the front-PA. Fig. 3.14 (c) is obtained by using the code *"hybridlens_frontPA_sens2..f90"*. Fig. 3.14 (d) is obtained by using the code *"hybridlens_frontPA_sens3..f90"* that considers the frequency shift of the Wood's anomaly. Fig. 3.14 (e) and (f) which show the decrease of the absorbance at the resonant frequency as a function of the variation in refractive index and the film thickness, respectively, are obtained by the codes *"hybridlens_frontPA_sens4.f90"* and *"hybridlens_frontPA_sens5.f90"* , respectively.

A3. Chapter 4

The analytical solutions developed in this chapter take into account all waveguide modes. However, we mostly use the code taking just the zero fundamental waveguide mode because we work in the deep-subwavelength regime, the slit width is 1,500 times smaller than the working wavelength. Therefore, only the fundamental waveguide mode is sufficient in our case.

A3.1 Comparison with FDTD simulation

Fig. 4.3 (a) can be obtained by both the general code taking into account all waveguide modes and by the closed-form code taking into account only the fundamental waveguide mode. The Fig. 4.3 takes only the fundamental waveguide mode into account, and we obtain the great consistent spectra with the FDTD simulation. The name of the general code is *"hybridlens_1wvg_gen.f90"*, and the name of the closed-form code is the *"hybridlens_1wvg_closed.f90"*. These two codes can be applied to only the case where the number of the waveguide in the superlattice of the front grating (G_0 grating) is one. The position of the waveguide within the superlattice can be varied via the variable xj. In the case of any number of waveguide inside the superlattice such as in Fig. 4.3, we use the general code namely *"hybridlens_nwvg_gen.f90"* to compute the optical spectra. We always check that the absorbance from the analytical solutions has to be zero because there is no loss in the structure.

A3.2 Subwavelength imaging with one grating/dielectric metamaterial

The electric field behind the grating in Fig. 4.6 is obtained by using the code *"hybridlens_image_1g_field.f90"* taking into account only the fundamental waveguide mode. The transmission spectra in Fig. 4.7 (a) is calculated by using the code *"hybridlens_image_1g_spectra.f90"*.

The electric field inside the gap between the object (G_0) and the grating (G_1) in Fig. 4.8 (b) is obtained by using the code *"hybridlens_image_1g_field_QWR.f90"*.

A3.3 Subwavelength imaging over long-distance with stacked grating/dielectric layers

The electric field distributions behind the stacked grating/dielectric layers in Fig. 4.9 are obtained by using the code *"hybridlens_longimage_field.f90"* and their optical spectra can be obtained by using the code *"hybridlens_longimage_spectra.f90"*. The field profile in Fig. 4.10 can be easily obtained by using the code *"hybridlens_longimage_field.f90"*.

A4. Chapter 5

Even though the formulae for obtaining the effective parameters look simple, but they require careful consideration to obtain the correct results. The correct results mean that they are consistent with the analytical solutions, FDTD simulation, or the experiments that one performs. We show in the chapter 5 that our effective medium model gives the consistent results with the analytical solutions, at least in the particular frequency range. Therefore, it is worthy to give the codes for the further consideration in the future.

A4.1 Method of retrieving effective parameters

The code for Fig. 5.2 is given in the file named *"efm_fig52.f90"*. Notice that *"efm"* stands for effective medium model and the word after the underscore refers to the figure in the main text with the "." neglected. We use this notation to call all codes in this chapter. The EFC in Fig. 5.3 is obtained by using the code *"efm_fig53.f90"*, and the effective reflection and transmission coefficients are obtained by using the code *"efm_fig54.f90"*. These codes are very straightforward. First, we obtain the reflection and the transmission coefficients of the stacked grating/dielectric layers by using the closed-form formulae, and then we convert these coefficients into the effective reflection and transmission coefficients by using the effective medium model. The more technical details are referred to the main program.

A4.2 Method of retrieving effective parameters

The code for Fig. 5.5 (b) is given in the file named *"efm_fig55b.f90"*. The EFCs of the *N=10* stacked grating/dielectric layers at some frequencies shown in Fig. 5.6 are obtained by using the code named "*efm_fig56.f90*". This code can be used for any number of grating layer. The order-corrected EFC in Fig. 5.7 (c) is obtained by using the code named *"efm_fig57c.f90"*. The effective dielectric constant as a function of frequency in Fig. 5.10 (a) is obtained by using the code named *"efm_fig510a.f90"*, and the effective magnetic permeability in Fig. 5.10(b) is obtained by using the code named *"efm_fig510b.f90"*. These two codes can be applied to any number of grating layer.

Publications

(Papers)

[1] P. Tapsanit, M. Yamashita, C. Otani, "Analytical solutions of electromagnetic waves in focusing and magnifying cylindrical hyperlenses: Green's function approach," Opt. Express **22**, 229-238 (2014).

[2] P. Tapsanit, M. Yamashita, C. Otani, "Hybrid-lens for Terahertz Subwavelength Focusing beyond the Diffraction Limit," Engineering Journal **20**, 61-70 (2016).

[3] P. Tapsanit, M. Yamashita, C. Otani, "Tunable hybrid-platform comprising metallic grating with subwavelength width and stacked-dielectric layers for terahertz sensing," (in preparation)

(Conferences)

[4] P. Tapsanit, M. Yamashita and C. Otani, "Analytical solutions of the perfect absorber for the terahertz sensing," in *The 40th International Conference on Infrared, Millimeter, and Terahertz Waves*, Hong Kong, 2015.

[5] P. Tapsanit, M. Yamashita and C. Otani, "Analytical Theory of Metamaterial-Hybrid-Platform for Terahertz Sensing of Subwavelength Objects," in *The 3rd international symposium on microwave/terahertz science and applications)*, Okinawa, Japan, 2015.

[6] P. Tapsanit, M. Yamashita and C. Otani, "FDTD simulation of a planar hybrid-hyperlens for sub-wavelength focusing of terahertz light," in *The 7th Thailand-Japan International Academic Conference*, Tokyo, Japan, 2014.

[7] P. Tapsanit, M. Yamashita and C. Otani, "Theoretical demonstration of subwavelength focusing using hybrid-hyperlens," in *the 13th international conference of Near-field Optics and Nanophotonics*, Salt Lake City, Utah, USA, 2014.

[8] P. Tapsanit, M. Yamashita and C. Otani, "Hybrid-lens for terhaertz subwavelength focusing beyond the diffraction limit," in *The 4rd Advanced Laser and Photon Sources (ALPS'2014)*, Yokohama, Japan, 2014.

[9] P. Tapsanit, M. Yamashita and C. Otani, "Terahertz Subwavelength Focusing Hybrid-hyperlens," in *The 2nd Symposium on RIKEN Center for Advanced Photonics*, Sendai, Japan, 2014.

[10] P. Tapsanit, M. Yamashita and C. Otani, "Simulation of sub-wavelength focusing hyperlens for visible and terahertz light," in *The 1st Symposium on RIKEN Center for Advanced Photonics*, Wako, Japan, 2013.

[11] P. Tapsanit, M. Yamashita and C. Otani, "Sub-wavelength focusing by cylindrical hyperlens," in *The 6th Thailand-Japan International Academic Conference*, Osaka, Japan, 2013.

References

[1] http://galileo.rice.edu/sci/instruments/telescope.html

[2] A. J. M. Wollman, R. Nudd, E. G. Hedlund and M. C. Leake, "From Animaculu to single molecules: 300 years of light microscope," Open Biol. **5** (2015).

[3] L. Rayleigh, "XXXI investigations in optics, with special reference to spectroscope," Phil. Mag. Ser. 5 **8**, 261-274 (1879).

[4] G. Mie,"Beiträge zur Optik trüber Medien, speziell kolloidaler Metallösungen," Ann. Phys. **25**, 377 (1908).

[5] S. A. Maier, "Localized surface plasmons," in *Plasmonics: Fundamentals and Applications*, Springer, (Academic, 2007), p. 65-97.

[6] DW. Pohl, W. Denk, and M. Lanz, "Optical stethoscopy : image recording with resolution λ/20," Appl. Phys. Lett. **44**, 651-653 (1984).

[7] M. A. Seo, H. R. Park, S. M. Koo, D. J. Park, J. H. Kang, O. K. Suwal, S. S. Choi, P. C. M. Planken, G. S. Park, N. K. Park, Q. H. Park, and D. S. Kim, "Terahertz field enhancement by a metallic nano slit operating beyond the skin-depth limit," Nat. Photon. **3**, 152-156 (2009).

[8] L. Novotny and S. J. Stranick, "Near-field optical microscope and spectroscopy with pointed probes," Annu. Rev. Phys. Chem. **57**, 303-331 (2006).

[9] Y. Inouye and S. Kawata, "Near-field scanning optical microscope with a metallic probe tip," Opt. Lett. **19**, 159-161 (1994).

[10] F. Zenhausern, M. P. O'Boyle, and H. K. Wickramasinhe, "Apertureless near-field optical microscope," Appl. Phys. Lett. **65**, 1623 (1994).

[11] A. Hartschuh, E. J. Sanchez, X. S. Zie, and L. Novotny, "High-resolution near-field raman microscopy of single-walled carbon nanotubes," Phys. Rev. Lett. **90**, 095503 (2003).

[12] T. Ichimura, N. Hayazawa, M. Hashimoto, Y. Inouye, and S. Kawata, "Tip-enhanced coherent anti-stokes raman scattering for vibrational nanoimaging," Phys. Rev. Lett. **92**, 220801 (2004).

[13] A. J. L. Adam, "Review of near-field terahertz measurement methods and their applications," J. Infrared Milli Terahz Waves **32**, 976-1019 (2011).

[14] T. X. Huang, S. Huang, M. H. Li,Z. C. Zeng, X. Wang, B. Ren, "Tip-enhanced raman spectroscopy: tip-related issues," Anal Bioanal Chem **407**, 8177-8195 (2015).

[15] J. B. Pendry, "Negative refraction makes a perfect lens," Phys. Rev. Lett. **85**, 3966-3969 (2000).

[16] R. A. Shelby, D. R. Smith, and S. Schultz, "Experimental verification of a negative index of refraction," Science **292**, 77-79 (2001).

[17] V. G. Veselago, "The electrodynamics of substance with simultaneously negative values of ε and μ," Sov.Phys. Usp. **10**, 509-514 (1968).

[18] N. Fang, H. Lee, C. Sun, and Xiang Zhang, "Sub–Diffraction-Limited Optical Imaging with a Silver Superlens," Science **308**, 534-537 (2005).

[19] Z. Jacob, L. V. Alekseyev, and E. Narimanov, "Optical hyperlens: far-field imaging beyond the diffraction limit," Opt. Express **14**, 8247–8256 (2006).

[20] Z. Liu, H. Lee, Y. Xiong, C. Sun, and X. Zhang, “Far-field optical hyperlens magnifying sub-diffraction-limited objects,” Science **315**, 1686 (2007).

[21] S. Ishii, A. V. Kildishev, E. Narimanov, V. M. Shalev, and V. P. Drachev, “Sub-wavelength interference pattern from volume plasmon polaritons in a hyperbolic medium,” Laser Photon. Rev. **7**, 265–271 (2013).

[22] A. Poddubny, I. Iorsh, P. Belov and Y. Kivshar, "Hyperbolic metamaterials," Nat. Photon. **7**, 958-967 (2013).

[23] L. Ferraria, C. Wub, D. Lepaged, X. Zhangb, Z. Liu, "Hyperbolic metamaterials and their applications," Prog. in Quan. Elec. **40**,1-40 (2015).

[24] P. Tapsanit, M. Yamashita, C. Otani, "Analytical solutions of electromagnetic waves in focusing and magnifying cylindrical hyperlenses: Green’s function approach," Opt. Express **22**, 229-238 (2014).

[25] A. A. High, R. C. Devlin, A. Dibos, M. Polking, D. S. Wild, J. Perczel,N. P. de Leon, M. D. Lukin, and H. Park, "Visible-frequency hyperbolic metasurface," Nature **522**, 192-196 (2015).

[26] E. Yoxall, M. Schnell, A. Y. Nikitin, O. Txoperena, A. Woessner, M. B. Lundeberg, F. Casanova, L. E. Hueso, F. H. L. Koppens, and R. Hillenbrand, "Direct observation of ultraslow hyperbolic polariton propagation with negative phase velocity," Nat. Photon. **166** (2015).

[27] S. Dai, Q. Ma, T. Andersen, A.S. Mcleod, Z. Fei, M.K. Liu, M. Wagner, K. Watanabe, T. Taniguchi, M. Thiemens, F. Keilmann, P. Jarillo-Herrero, M.M. Fogler, and D.N. Basov, "Subdiffractional focusing and guiding of polaritonic rays in a natural hyperbolic material," Nat. Commun. **6**, 6963 (2015).

[28] P. Li, M. Lewin, A. V. Kretinin, J. D. Caldwell, K. S. Novoselov, T. Taniguchi, K. Watanabe, F. Gaussmann, and T. Taubner, "Hyperbolic phonon-polaritons in boron nitride for near-field optical imaging and focusing," Nat. Commun. **6**, 7507 (2015).

[29] A. Andryieuski, A. V. Lavrinenko, and D. N. Chigrin, "Graphene hyperlens for terahertz radiation," Phys. Rev. B **86**, 121108 (2012).

[30] A. Tuniz, K. J. Kaltenecker, B. M. Fischer, M. Walther, S. C. Fleming, A. Argyros, and B. T. Kuhlmey, "Metamaterial fibres for subdiffraction imaging and focusing at terahertz frequencies over optically long distances," Nat. Commun. **4**, 2706 (2013).

[31] S. J. Oh, S. H. Kim, Y. B. Ji, K. Jeong, Y. Park, J. Yang,D. W. Park,S. K. Noh, S. G. Kang, Y. M. Huh, J. H. Son, and J. S. Suh, "Study of freshly excised brain tissues using terahertz imaging," Bio. Opt. Express **5**, 2837-2842 (2014).

[32] B. Ferguson and X. C. Zhang, "Materials for terahertz science and technology," Nat. Mat. **1**, 26-33 (2002).

[33] Y. S. Lee, "Generation and detection of broadband terahertz pulses," in *Principles of terahertz science and technology*, Springer , (Academic, 2008).

[34] B. S. Williams, "Terahertz quantum-cascade lasers," Nat. Photon. **1**, 517-525 (2007).

[35] N. J. Karl, R. W. McKinney, Y. Monnai, R. Mendis, and D. M. Mittleman, "Frequency-division multiplexing in the terahertz range using a leaky-wave antenna," Nat. Photon. **9**, 717-720 (2015).

[36] A. A. Gowen, C. O'Sullivan, and C. P. O'Donnell, "Terahertz time domain spectroscopy and imaging: Emerging techniques for food process monitoring and quality control," Trends in Food Sci. & Tech. **25**, 40-46 (2012).

[37] T. Ouchi, K. Kajiki, T. Koizumi, T. Itsuji,Y. Koyama, R. Sekiguchi, O. Kubota, and K. Kawase, "Terahertz Imaging System for Medical Applications and Related High Efficiency Terahertz Devices," J. Infrared Milli Terahz Waves **35**, 118-130 (2014).

[38] Y. Ogawa, S. Hayashi, C. Otani, and K. Kawase, "Terahertz Sensing for Ensuring the Safety and Security," PIERS Online **4**, 396-400 (2008).

[39] M. C. Kemp, "Explosives Detection by Terahertz Spectroscopy—A Bridge Too Far?," IEEE Trans. on THz Sci. & Tech. **1**, 282-292 (2011).

[40] A. G. Davies, A. D. Burnett, W. Fan, E. H. Linfield, and John E. Cunningham, "Terahertz spectroscopy of explosives and drugs," Mat. Today **11**, 18-26 (2008).

[41] C. A. Schmuttenmaer, "Exploring Dynamics in the Far-Infrared with Terahertz Spectroscopy," Chem. Rev. **104**, 1759-1779 (2004).

[42] E. Hecht, "Diffraction," in *Optics* 4th ed., Addison Wesley, (Academic, 2002).

[43] C. Kittel, "Plasmons, polaritons, and polarons," in *Introduction to solid state physics* 8th ed., John Wiley & Sons, (Academic, 2005), p. 398.

[44] M. Dressel and G. Gruner, "Metals," in *Electrodynamics of Solids*, Cambridge, (Academic 2002), p. 93

[45] M. A. Ordal, L. L. Long, R. J. Bell, S. E. Bell, R. R. Bell, R. W. Alexander, Jr., and C. A. Ward, "Optical properties of the metals Al, Co, Cu, Au, Fe, Pb, Ni, Pd,Pt, Ag, Ti, and W in the infrared and far infrared," Appl. Opt. **22**, 1099-1120 (1983).

[46] W. L. Barnes, A. Dereux, and T. W. Ebbesen, "Surface plasmon subwavelength optics," Nature **424**, 824-830 (2003).

[47] J. Homola, S. S. Yee, and G. Gauglitz, "Surface plasmon resonance sensors : review," Sensors & Actuators B **54**, 3-15 (1999).

[48] S. A. Maier and S. R. Andrews, "Terahertz pulse propagation using plasmon-polariton-like surface modes on structured conductive surfaces," Appl. Phys. Lett. **88**, 251120 (2006).

[49] T. W. Ebbesen, H. J. Lezec, H. F. Ghaemi, T. Thio and P. A. Wolf, Nature **391**, 667-669 (1998).

[50] F. J. Garcia-Vidal, L. Martin-Moreno, T. W Ebbesen, and L. Kuiper, "Light passing through subwavelength apertures," Rev. Mod. Phys. **82**(1), 729-565 787(2010).

[51] F. Miyamaru, S. Hayashi, C. Otani, and K. Kawase, "Terahertz surface-wave resonant sensor with a metal hole array," Opt. Lett. **31**,1118-1120 (2006).

[52] F. D'Apuzzo, P. Candeloro, F. Domenici, M. Autore, P. Di Pietro, A. Perucchi, P. Roy, S. Sennato, F. Bordi, E. M. Di Fabrizio, S. Lupi, "Resonanting terahertz response of periodic arrays of subwavelength apertures," Plasmonics **10**, 45-50 (2015).

[53] K. A. Willets and R. P. V. Duyne, "Localized surface plasmon resonance spectroscopy and sensing," Annu. Rev. Phys. Chem. **58**, 267-297 (2007).

[54] P. Tapsanit, " Near field enhancement of optical transition in carbon nanotubes," master thesis (unpublished) (2012).

[55] S. Kawata, Y. Inouye, and P. Verma, "Plasmonics for near-field nano-imaging and superlensing," Nat. Photon. **3**, 388-394 (2009).

[56] A. I. Fernández-Domínguez, F. J. García-Vidal, and L. Martín-Moreno,"Resonant transmission of light through finite arrays of slits," Phys. Rev. B **76**, 235430 (2007).

[57] F. J. Garcia-Vidal, L. Martin-Moreno, and J. B. Pendry, "Surfaces with holes in them: new plasmonic metamaterials," J. Opt. A:Pure Appl. Opt. **7**, S97-S101 (2005).

[58] S. A. Maier, S. R. Andrews,L. Martin-Moreno, and F. J. Garcia-Vidal, "Terahertz Surface Plasmon-Polariton Propagation and Focusing on Periodically Corrugated Metal Wires," Phys. Rev. Lett. **97**, 176805 (2006).

[59] J. B. Pendry, L. Martin-Moreno, and F. J. Garcia-Vidal, "Mimicking Surface Plasmons with Structured Surfaces," Science **305**, 847-848 (2004).

[60] P. Yeh, "Optical waves in layered madia," (1988).

[61] A. F. Oskooi, D. Roundy, M. Ibanescu, P. Bermel, J. D. Joannopoulos, and S. G. Johnson, "MEEP: A flexible free-software package for electromagnetic simulations by the FDTD methods," Comput. Phys. Commun. **181**,687–702 (2010).

[62] S. A. Ramakrishna, J. B. Pendry, M. C. K. Wiltshrine, and W. J. Stewart, "Imaging the near field," J. Mod. Opt. **50**, 1419–1430 (2003).

[63] D. Lu and Z. Liu, "Hyperlenes and metalenses for far-field super-resolution imaging," Nat. Commun. **3**, 1–9 (2012).

[64] C. Ma and Z. Liu, "A super resolution metalens with phase compensation mechanism," Appl. Phys. Lett. **96**, 183103 (2010).

[65] S. Thongrattanasiri and V. A. Podolskiy, "Hypergratings: nanophotonics in planar anisotropic metamaterials," Opt. Lett. **34**, 890–892 (2009).

[66] G. Li, J. Li, and K. W. Cheah, "Subwavelength focusing using a hyperbolic medium with a single slit," Appl. Opt. **50**, G27–G30 (2011).

[67] H. Liu and K. J. Webb, "Resonance cones in cylindrically anisotropic metamaterials: a Green's function analysis," Opt. Lett. **36**, 379–381 (2011).

[68] E. N. Economou, "Time-independent Green's functions," in Green's Functions in Quantum Physics, 3rd ed.Heidelberg, Germany: Springer, (Academic, 2006), pp. 13.

[69] National Institute of Standard and Technology (NIST), (2015, August 7). Graf's and Gegenbauer's Addition Theorems (Online). Available : http://dlmf.nist.gov/10.23

[70] J. P. Moreau, (2009, April 23). Bessel programs in fortran 90 (Online). Available : http://jeanpierre.moreau.pagesperso-orange.fr/.

[71] E. Anderson, Z. Bai, C. Bischof, S. Blackford, J. Demmel, J. Dongarra, J. D. Croz, A. Greenbaum, S. Hammarling, A. McKenney, and D. Sorensen, LAPACK Users guide, 3rd ed. Philadelphia: Society for Industrial and Applied Mathematics (1999)

[72] S. Foteinopoulou, J. P. Vigneron, and C. Vandenbem, "Optical near-field excitations on plasmonic nanoparticlebased structures," Opt. Express **15**, 4253–4267 (2007).

[73] A. Mary, S. G. Rodrigo, L. Martin-Moreno, and F. J. Garcia-Vidal, "Holey metal film: From extraordinary transmission to negative-index behavior," Phys. Rev. B **89**, 165431 (2009).

[74] D Grischkowsky, S. Keiding, M. V. Exter, and C. Fattinger, J. Opt. Soc. Am. B **7**(10), 2006-2015, 1990.

[75] Y. S. Jin, G. J. Kim, and S. G. Jeon, JKPS **49**(2), 513-517 (2006).

[76] H. Räther, *Surface Plasmons on Smooth and Rough Surfaces and on Gratings*, Springer-Verlag, Berlin, (1998).

[77] A. P. Hibbins and J. R. Sambles, Phys. Rev. Lett. **92**(14), 143904 (2004).

[78] D. M. Pozar, *Microwave Engineering*, Wiley, USA, (2012).

[79] J. Jung, L. Martin-Moreno, and F. J. Garcia-Vidal, "Light transmission properties of holey metal films in the metamaterial limit : effective medium theory and subwavelength imaging," New J. of Phys. **11**, 123013 (2009).

[80] J. Jung, F. J. Garcia-Vidal,L. Martin-Moreno, and J. B. Pendry, "Holey metal films make perfect endoscope," Phys. Rev. B **79**, 153407 (2009).

[81] Y. Todorov, L. Tosetto, J. Teissier, A. M. Andrews, P. Klang, R. Colombelli, I. Sagnes, G. Strasser, and C. Sirtori, Opt. Express **18**(13), 13886-13907 (2010).

[82] R. Singh, W. Cao., I. Al-Naib, L. Cong, W. Withayachumnankul, and W. Zhang, Appl. Phys. Lett. **105**, 171101(2014).

[83] A. Mary, S. G. Rodrigo, L. Martin-Moreno, and F. J. Garcia-Vidal, "Holey metal film: From extraordinary transmission to negative-index behavior," Phys. Rev. B **89**, 165431 (2009).

[84] C. Garcia-Meca, J. Hurtado, J. Marti, and A. Martinez, "Low-loss multilayered metamaterial exhibiting a negative index of refraction at visible wavelengths," Phys. Rev. Lett. **106**, 067402 (2011).

[85] T. Okita and H. Tanaka, "Resonant transmission through a multiple periodic scattering system," J. of Opt. **14,** 085103 (2012).

[86] A. Castanie, J. F. Mercier, S. Felix, and A. Maurel, "Generalized method for retrieving effective parameters of anisotropic metamaterials," Opt. Exp. **22**, 29937-29953 (2014).

[87] Z. H. Jiang, J. A. Bossard, X. Wang, and D. H. Wemer, "Synthesizing metamaterials with angularly independent effective medium properties based on an isotropic parameter retrieval technique coupled with a genetic algorithm," J. Appl. Phys. **109**, 013515 (2011).

[88] E. Feigenbaum, N. Kaminski, and M. Orenstein, "Negative dispersion : a backward wave or fast light? Nanoplasmonic examples," Opt. Exp. **17**, 18934-18939 (2009).

[89] W. Sarrazin, J. P. Vigeron, and J. M. Vigoureux, "Role of Wood anomalies in optical properties of thin metallic films with bidimensional array of subwavelength holes," Phys. Rev. B **67**, 085425 (2003).

[90] D. Lu and Z. Liu, "Hyperlenses and metalenses for far-field super-resolution imaging," Nat. Commun. 3, 1205 (2012).

[91] A. O. Pinchuk, "Size-dependent Hamaker constant for silver nanoparticles," J. Phys. Chem. C **116**, 20099-20102 (2012).